YEARBOOK
2022

INSTITUTE OF TECHNICAL PHYSICS AND MATERIALS SCIENCE
CENTRE FOR ENERGY RESEARCH
PART OF EÖTVÖS LORÁND RESEARCH NETWORK

http://www.mfa.kfki.hu/

Published by
Institute of Technical Physics and Materials Science
Centre for Energy Research
Part of Eötvös Loránd Research Network

EK MFA Yearbook 2022

Content

GENERAL INFORMATION

Director's foreword

As the director of MFA, it is my pleasure to welcome the reader. I recommend browsing the present yearbook which continues the series of the former ones and contains results achieved in 2022.

2022 was the third whole year what we spent as the member of Eötvös Loránd Research Network (ELKH). As previously the network administration set up a system which provided financial support to member institution not only to cover the running cost, but also a part of the budget was distributed based on the qualification of the staff, based on the publication and citation records. The whole Centre for Energy Research and MFA as one of its member institutions gained increased support via that system. I used to say to my colleagues already science became a production income. After I reported on that a year ago, in 2022 we could buy some scientific instruments from which the most valuable one was a new XPS photoelectron spectrometer. A Thermo Fisher Scientific Escalab Xi+ system was selected and installed with XPS, UPS, ISS, EELS and IPES (inverse photoelectron spectroscopy) options equipped with a cluster ion gun. In the same year another attachment of an electron gun for making Auger electron spectroscopy was bought and installed.

Unfortunately we lost couple of our former colleagues, Dr. Pál Sviszt, Dr. András Hegedűs and emeritus professor György Kozmann. For the memory of Prof. József Gyulai our former institute director, we could set up a relief with his face at the gate of our main building in which he did work.

In 2022 we faced a new challenge, what was the elevated price of gas heating increased by a magnitude of order. Therefore, we started to select and order heat pumps for the two buildings of MFA, the investment will be finished in 2023.

MFA could continue to pay publication award for the young authors of the best publications.

After the pandemic period already in 2022 some of our colleagues achieved successful scientific qualification. György Sáfrán and András Deák got the Doctor of Academy title, and we had also three successful PhD candidates, namely: Dániel Szekrényes, Ágoston Nagy and Tamás Gerecsei. We are very proud of them.

I congratulate to my colleagues Prof. István Bársony (our former director) who got the honorary professor title at Debrecen University and Prof. Miklós Fried who became professor at Óbuda University. Our Róbert Horváth was awarded by the Physics Prize Hungarian Academy, Physics Section of Sciences for his development of the label free biophysics methods, while Péter Vancsó got the Zoltán Gyulai prize from Eötvös Loránd Physics Society for his results achieved in the field of 2D materials. I am also pleased to inform you that the Officer's Cross of the Hungarian Order of Merit was donated to our Péter Petrik and to Tivadar Lohner as well. Our Attila Szolnoki received already fourth time the Highly Cited Researcher title from Clarivate. The World Academy of Ceramics recognized the outstanding scientific contribution of our Dr. Csaba Balázsi by the academician title.

The home applications of MFA were successful and the institute could gain three TKP (Thematic Excellence Programme) projects in the following subjects: new semiconductors, innovative biosensing processes for health applications and emergency monitoring sensors.

We are also proud of the scientific results achieved by our colleagues, I hope you will enjoy learning them in this book. Here I note that the former MFA Yearbooks are available electronically at http://www.mfa.kfki.hu/hu/yearbook.

Béla Pécz, corr. member of HAS., deputy general director of Centre for Energy Research, MFA director

Organizational structure

Director: Dr. Béla Pécz, corr. member of HAS

Scientific departments	
Thin Film Physics Department	Katalin BALÁZSI, Ph.D.
Complex Systems Department	Géza ÓDOR, D.Sc.
Photonics Department	Péter PETRIK, D.Sc.
Nanobiosensorics Department	Róbert HORVÁTH, Ph.D.
Microsystems Department	Péter FÜRJES, Ph.D.
Nanosensorics Laboratory	János VOLK, Ph.D.
Nanostructures Department and "Lendület" group - 2D Materials	Levente TAPASZTÓ, Ph.D.
"Lendület" group - Topological Nanostructures	Péter NEMES-INCZE, Ph.D.

Directly supervised functions	
Head of Scientific Advisory Council	Levente TAPASZTÓ, Ph.D.
Scientific secretary, projects and PR	Krisztina SZAKOLCZAI, Ph.D.
Quality control, patents, MTMT, REAL admin	Andrea BOLGÁR
Technical support	Károly BODNÁR
Financial administration	Zsuzsanna KELEMEN
Informatics	Gergely TAMÁS
Technology transfer (IPR)	Antal GASPARICS, Ph.D.

Key Financial Figures of MFA

The domestic subsidies changed in 2020, not long after the centre left the MTA network and became part of the Loránd Eötvös Research Network (ELKH). It has been adjusted partly to the number and salary of the researchers as well as excellence and output of the centre. Moreover, thanks to the excellence and output indicators of the centre it was further increased. Since 2015 MFA is part of the Centre of Energy Research. The financial operation is only partly transparent, therefore the data shown here for 2015-2022 for MFA are based upon our own estimates.

The subsidy of the institute is still around 40% of the annual budget. It means strong financial dependence on the amount of income the research grants could provide. The number of researchers together with the research supporting staff dropped from ca. 140 to 100, but started to raise a bit after COVID, currently around 120. The fluctuation is although still high because of the brain drain and also double payment from industrial partners.

MFA budget 2003-2022 (million HUF)
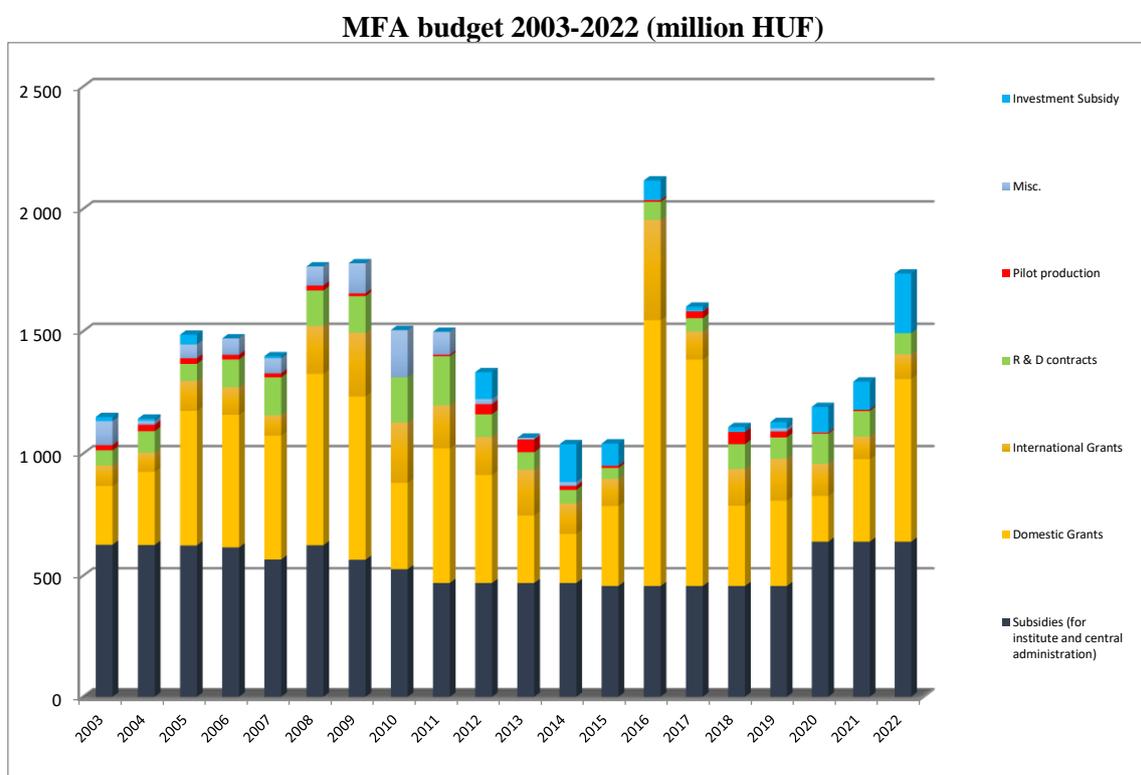
The institute and its administration handles approximately 50 grants and 25 other R&D contracts each year. Exactly half of the project are fundamental research grants (NKFIH OTKA), rest implements industrial and application driven ideas. Despite all the efforts of colleagues R&D grants require stable strong and research motivated SMEs, which is hard to find in Hungary. Three new and large thematic excellence grants (TKP2021) started from the first months of 2022, which provides some sort of stability for the upcoming 3 years. Also after few years of break new MSCA fellowship and Korean R&D grant started at the end of the year. The excellence "Lendület" grants ran out in 2022, so our researchers are aiming for Horizon Europe proposals.

The Research Centre used part of the increased support for investment. For MFA (and other Labs in the Centre) Escalab Xi+ XPS surface chemical analysis instrument was purchased.

MFA 2003-2022 restoration and investment spendings (million HUF)
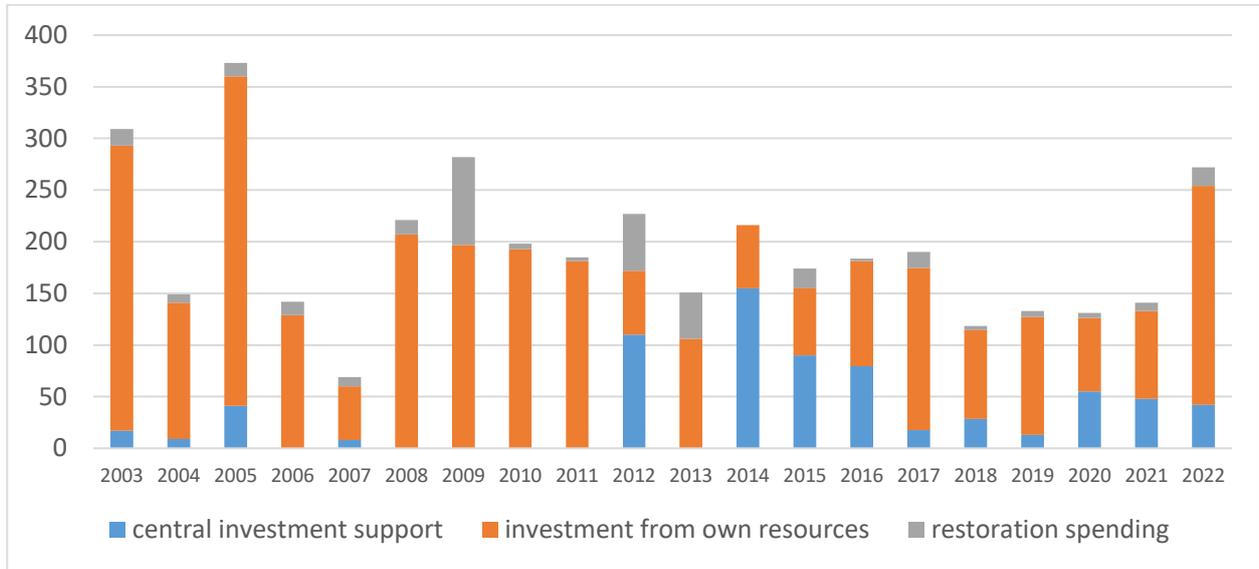
Publications and Citations of MFA

According to the Thomson-Reuters ISI "Web of Knowledge", and MTMT2 databases, the Institute has an average publication activity of ca. 100 scientific papers in IF journals a year. The number decreased a bit in the last years, but recently MFA researchers publich in journals with higher impact factor.

MFA and its predecessor's publications per year since 1998
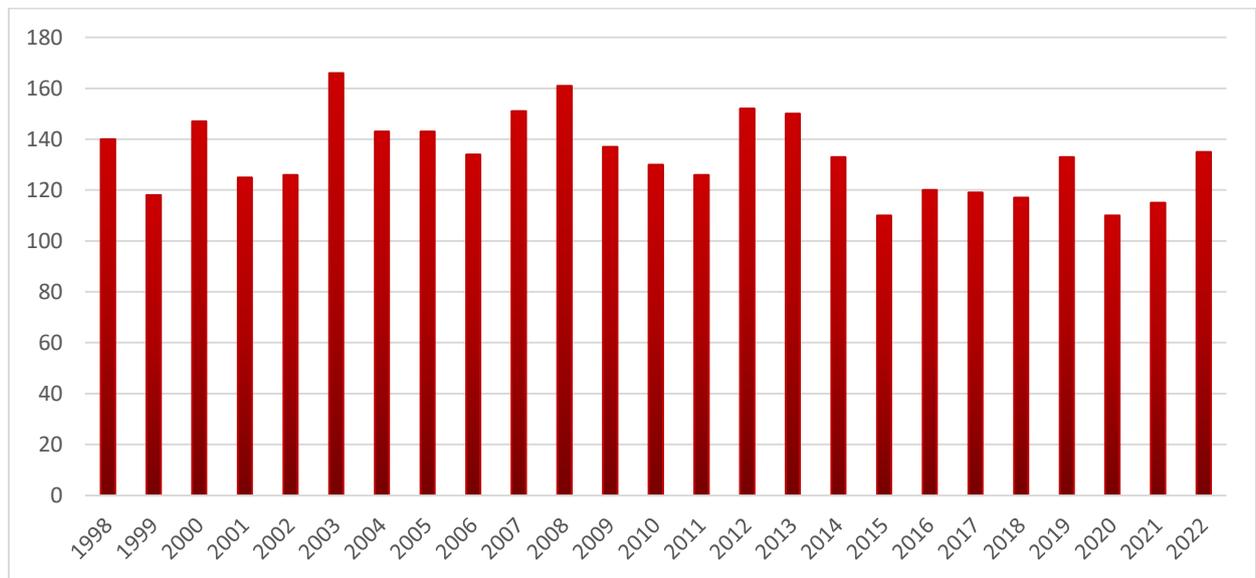
MFA and its predecessor's independent citations number per year
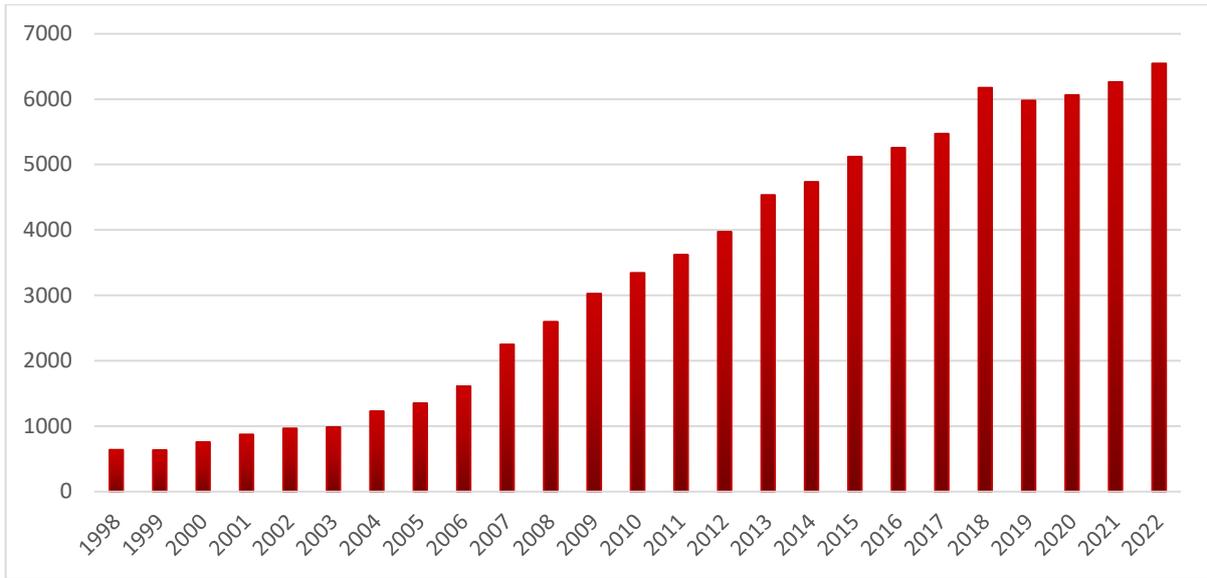
Prizes and Distinctions

PETRIK, Péter   Officer's Cross of the Hungarian Order of Merit

LOHNER, Tivadar   Officer's Cross of the Hungarian Order of Merit

HORVÁTH, Róbert   Physics Prize from Hungarian Acadaemy of Sciences

BÁRSONY, István   honorary professor at Debrecen University

VANCSÓ, Péter   Zoltán Gyulai prize from Eötvös Loránd Physics Society

SZOLNOKI, Attila   Top 1% Highly Cited Researcher at Clarivate

BALÁZSI, Csaba   academician of the World Academy of Ceramics

NEMES-INCZE, Péter   MFA institute prize

KOVÁCSNÉ KIS Viktória   MFA postdoc researchers prize

SZABÓ, Zoltán

MFA postdoc researchers prize

BÁNYAI, Anita

MFA young researchers prize
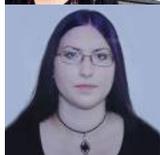
FARKAS, Enikő

MFA young researchers prize

SZÁSZ, Noémi

MFA research support prize

Prof. István Bársony was awarded with Honorary Doctor title by the rector of the University Debrecen (image source: unideb.hu)
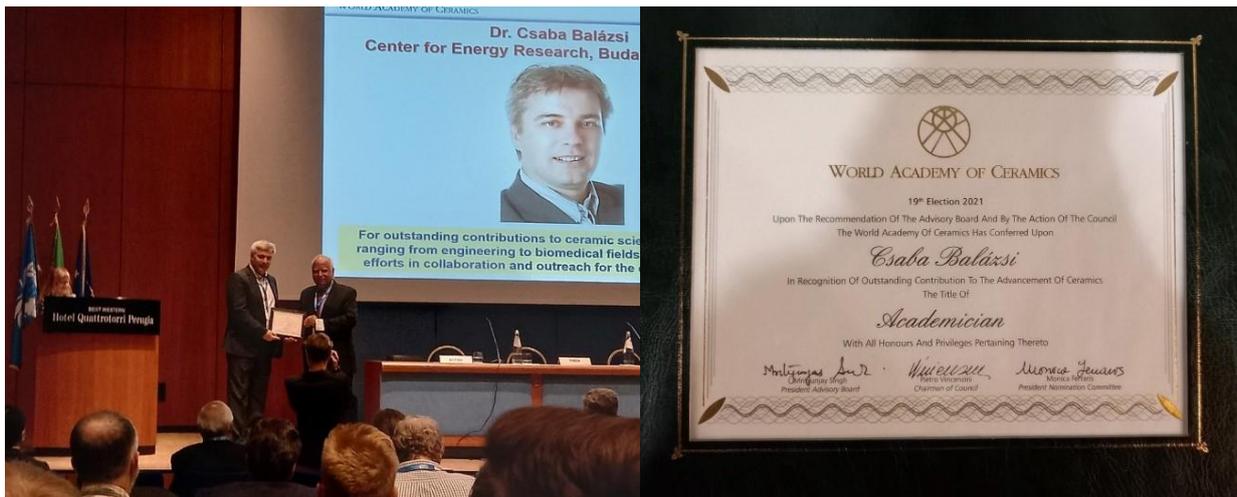
Dr. Csaba Balázsi was elected as academician of World Academy of Ceramics.

Oxygan workshop
Álmok álmodói

Dr. Miklós Fried accepted his appointment as a university professor at Óbuda University from the president of Hungary Katalin Novák.

SCIENTIFIC REPORTS

Nanostructures Laboratory

Head: Dr. Levente TAPASZTÓ, Ph.D., research fellow

Research Staff:
- Zsolt Endre HORVÁTH, D.Sc., Deputy Head of Laboratory
- Prof. László Péter BIRÓ, Member of the HAS
- Gergely DOBRIK, Ph.D.
- Krisztián KERTÉSZ, Ph.D.
- Antal Adolf KOÓS, Ph.D.
- Géza István MÁRK, Ph.D.
- Péter NEMES-INCZE, Ph.D.
- Zoltán OSVÁTH, Ph.D.
- András PÁLINKÁS, Ph.D.
- Gábor PISZTER, Ph.D.
- Péter SÜLE, Ph.D.
- Péter VANCSÓ, Ph.D.

Ph.D. students:
- Konrád KANDRAI, Ph.D. student
- Soma KESZEI
- Péter KUN, Ph.D. student
- Krisztián MÁRITY, Ph.D. student
- Márton SZENDRŐ, Ph.D. student

The research activity of the Nanostructures Laboratory is based on the two-decade-long expertise in the synthesis, characterization and engineering of various nanostructures using scanning probe microscopy as the main experimental technique. Since more than a decade, our research efforts are focused on the investigation of two-dimensional materials. Besides graphene, in the last couple of years, novel 2D materials, mainly form the family of transition metal chalcogenides (TMC) have been intensely studied. Recently, we have further extended our activity with the investigation of layered topological insulator crystals. We have also successfully continued our research on bioinspired photonic nanoarchitectures.

Ultra-small Pt nanoclusters on 2D MoS2 for highly efficient hydrogen evolution

*T. Ollár, A. Koós, P. Kun, P. Vancsó, P. Nemes-Incze, J. S. Pap, L. Tapasztó*

Large-scale and environmentally friendly production of hydrogen requires highly active, stable and cost-efficient catalysts. While platinum is known as the most efficient catalyst for hydrogen evolution, its high costs and scarcity strongly limit its practical use in large-scale applications. To overcome this, extensive efforts have been focused on replacing platinum with cheaper, more abundant materials, as well as on reducing the Pt content of catalysts, while maintaining the outstanding activity and stability. Among the most successful approaches are those based on improving Pt atom utilization efficiency through improving dispersion, which is maximized in Pt single atom catalysts (SACs). Indeed, such catalysts were able to reach the activity of commercial Pt/C catalysts, with two orders of magnitude lower Pt loadings of order of $\mu g/cm^2$. However, SACs represent the end of the road in terms of catalyst design for approaches relying on dispersion. To further reduce the Pt loading, without losing activity, one needs to design Pt structures that outperform the intrinsic activity of conventional Pt nanoparticles and Pt SACs.
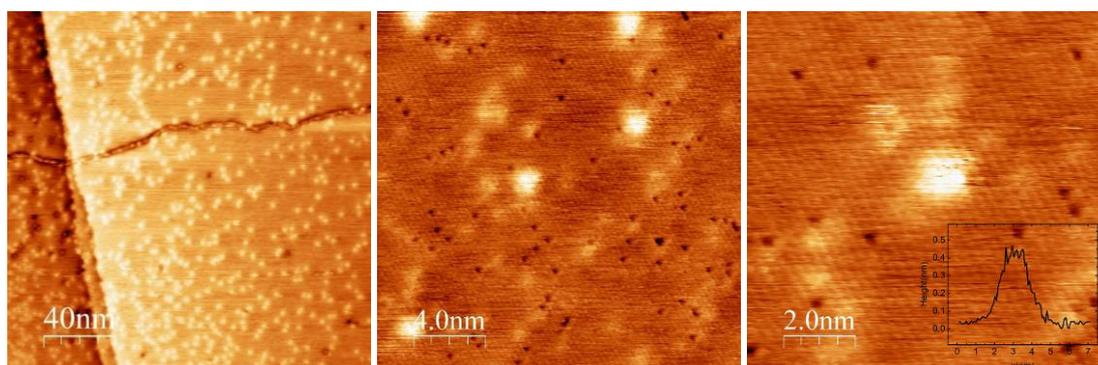
Figure 1.1. *Scanning tunneling microscopy images of small (~ 1 nm) Pt clusters (bright dots) deposited on 2D MoS₂ crystals. The dark spots in the atomic resolution STM images correspond ot S atom vacancies of the MoS₂ support, acting as anchor sites for Pt clusters.*

Distorted Pt structures were shown to host reaction sites of increased intrinsic activity. However, this comes at the price of a substantially reduced stability. Therefore, engineering novel Pt structures is a continuous compromise between increasing activity and preserving stability. Metal-support interaction emerged as an efficient tool for engineering catalytic performance. Enhanced metal-support interactions clearly boost the stability and durability of supported metal catalysts, and it can also substantially influence their activity and selectivity. Pt/MoS₂ systems emerge as a promising candidate for realizing an increased metal-support interaction, due to the strong affinity between Pt and S. This, combined with a relatively large lattice mismatch can give rise to novel Pt structures emerging from the competition of adhesion (Pt-S) and cohesion (Pt-Pt) that holds the promise for a simultaneous enhancement of activity and stability. We have observed that the catalytic performance of the Pt/MoS₂ system can be substantially improved by realizing small Pt clusters that interact more strongly with the MoS₂ support. Such small Pt clusters were grown by an electrochemical deposition on CVD grown MoS₂ single and few layers, grown on graphite. STM investigation reveal a high-density decoration of MoS₂ surface by ultra-small (~1 nm) Pt clusters, as well as a high density of sulphur vacancy type defects in the 2D MoS₂ crystals. Such defect sites act as

anchors for Pt clusters hindering their aggregation and enabling the stabilization of ultra-small Pt clusters at high density (Fig. 1.1).
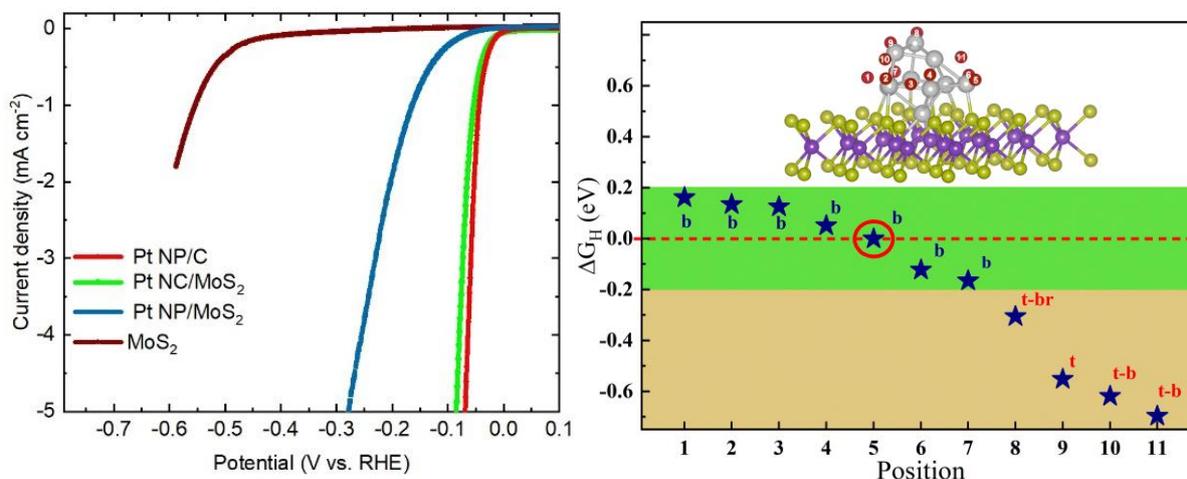
Figure 1.2. *Linear sweep voltammetry measurements on various samples revealing the Pt nanoclusters on MoS₂ can closely approach the activity of commercial Pt-C catalysts at orders of magnitude lower Pt content (left). Theoretical model of Pt nanoclusters on MoS₂ and the corresponding H adsorption free energies, indicating the presence of highly active sites at the interface/perimeter of the Pt cluster.*

2D MoS₂ crystals decorated with such small Pt clusters display exceptionally high catalytic activity towards hydrogen evolution. Such ultra-fine clusters perform much better than larger (~5 nm) Pt nanoparticles deposited on MoS₂, even though the Pt content is three orders of magnitude lower for samples comprising small Pt clusters (Fig 1.2.a). Most importantly small Pt clusters on MoS₂ samples closely approach the activity of commercial Pt-C catalysts, again a three orders of magnitude lower Pt content. We attribute the observed outstanding efficiency of our catalyst to a strongly increased Pt/MoS₂ interaction, leading to: (1) the stabilization of ultra-fine Pt clusters all over the MoS₂ basal plane, (2) deformation of Pt clusters morphology into a quasi-flat (bilayer) structure, in order to take better advantage of Pt-S interactions, and (3) a spectacular increase of the intrinsic activity of Pt sites, allowing a four orders of magnitude reduction of Pt loading, compared to commercial Pt/C catalysts, without losing activity or stability. Detailed simulations of hydrogen adsorption free energies revealed that the most active sites are on the Pt atoms directly adhering to the MoS₂ surface (Fig 1.2b), indicating strong synergistic effects at the origin of the outstanding catalytic performance.

Identifying stacking faults and domain walls in rhombohedral graphite by scanning tunneling microscopy

K. Kandrai, K. Márity, Z. Tajkov, M. Szendrő, A. Pálinkás, P. Kun, P. Vancsó,
L. Tapasztó and P. Nemes-Incze

Materials having a flat band [Ref. 1.1] at the Fermi level can host a variety of emergent many body ground states. One such system is rhombohedral graphite (RG), which is a rare form of graphite (Figure 1.3.a). Previously we have shown that rhombohedral graphite hosts strong interactions [Ref. 1.2], in its surface flat band. Being one of the simplest materials with a flat surface band, we have a chance to understand the complete defect structure of the material. In most experiments one can disregard vacancies and other point defects [Ref. 1.3], because their density is smaller than 10^9 cm^{-2}. This leaves lateral domains walls and stacking faults as the main defects we need to consider.

We have explored both types of defects using scanning tunneling microscopy (STM) measurements on thick (>6 graphene layers) RG samples. In Figure 1.3 we present a representative measurement on a 17-layer thick sample showing a domain wall between the hexagonal and rhombohedral areas. The rhombohedral region is apparent only if we measure the tunneling conductance at the Fermi level and plot it on a map (Figure 1.3.d).
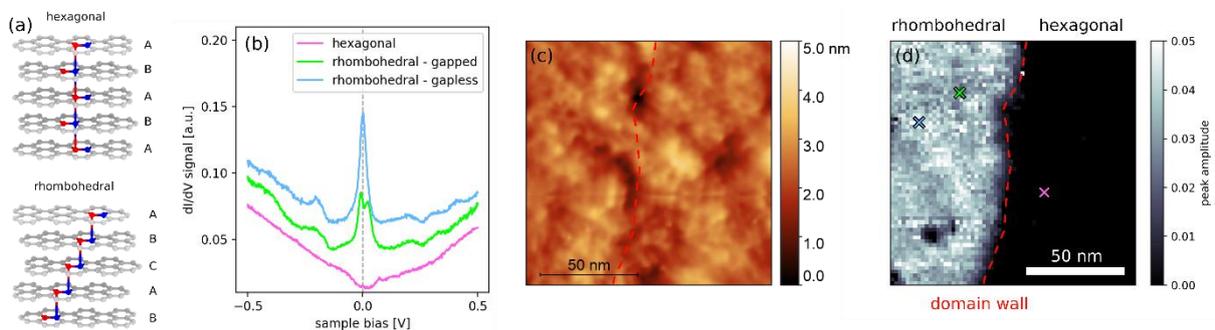

Figure 1.3 (a) *Stacking arrangement of the graphene layers in hexagonal and rhombohedral graphite. (**b**) Characteristic tunneling spectroscopy measurements of the LDOS on the surface of the two graphite phases. The surface flat band shows up as a large LDOS peak at 0 V sample bias and hosts a gapped and gapless, degenerate ground state at low temperature (9 K). (**c**) STM topographic map of a 17-layer RG surface. (**d**) Map of the surface state peak intensity in the same area as (c). The surface shows a lateral domain wall between rhombohedral / hexagonal regions, made clear by the presence / absence of the surface state.*

Besides lateral domain walls, graphite samples can have stacking faults, where one layer switches the stacking configuration of the crystal, from hexagonal to rhombohedral or vice versa. Raman spectroscopy is well suited [Ref. 1.3, Ref. 1.4] to identify areas of RG in exfoliated samples, but is not particularly sensitive to small perturbations of the stacking sequence, such as twins.

In our STM investigation of RG we have identified that the bulk bands of RG can be used to identify the number of rhombohedrally stacked graphene layers in a sample. By measuring the top surface of an RG crystal, the bulk bands show up as peaks in the dI/dV signal, which is a measure of the local density of

states (LDOS). The energy spacing between these peaks decreases monotonically as the number of graphene layers increases in the crystal. An example of this can be seen in Figure a, with the calculated LDOS in Fig.1.4.b. Thus, by measuring the LDOS of the top layer we gain information on the crystal structure deep inside the sample. This allows us to ensure that the sample we are measuring does not contain stacking faults within the measured area, because such a defect will change the energy of the bulk bands in a stepwise fashion. In the area presented in Fig. 1.4.d, the bulk band shows a smooth modulation over the surface, in correlation with the local doping (Fig.1.4.c).

These results are the starting point to explore the local electronic structure of lateral domain walls. Furthermore, STM measurements of the bulk bands in the surface LDOS will allow for an unprecedented understanding of the defect structure of RG, aiding further exploration of this exciting quantum material.
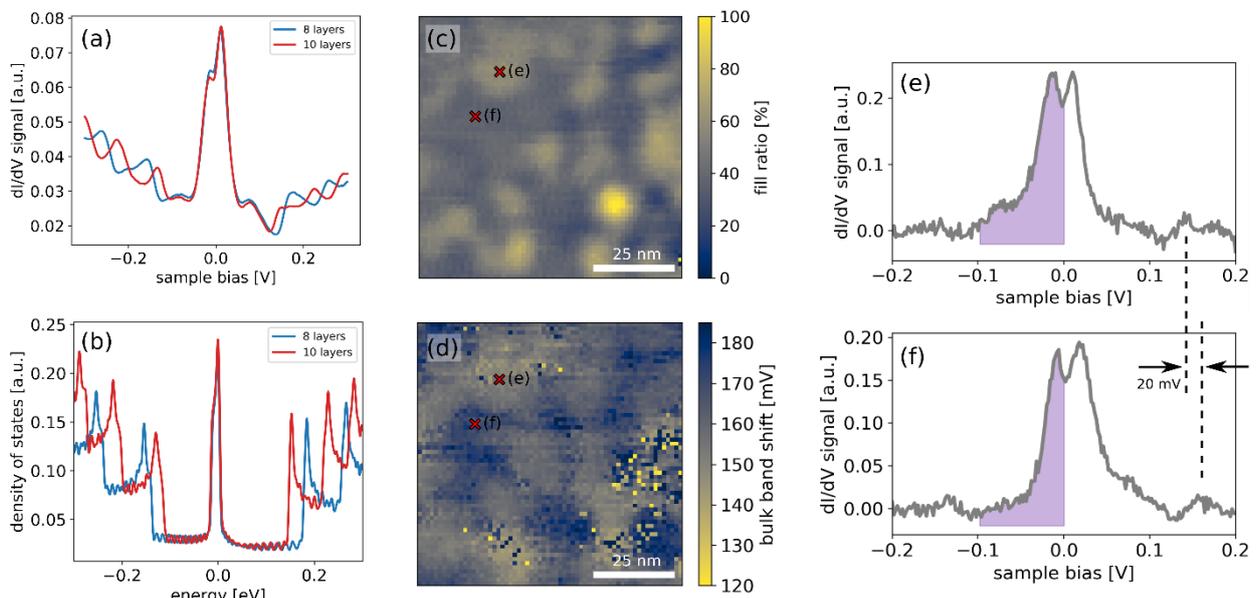
Figure 1.4. (a) *Tunneling spectroscopy measurement on an 8-layer and 10-layer RG crystal on SiO2.* ***(b)*** *Calculated LDOS.* ***(c)*** *Map of the spectral weight below the Fermi level (0 sample bias), as a measure of the local doping of the sample.* ***(d)*** *Position in sample bias of the first bulk state of the sample, tracked across the same area as in (**c**), shows no step-like changes. Individual spectra shown in (**e, f**) are marked by red crosses. The spectra in (**e**) and (**f**) show a 20 mV shift in the first bulk state due to changes in the local doping.*

Topological phase diagram of ZrTe5 mono and bilayers

Z. Tajkov, D. Nagy (ELTE), K. Kandrai, J. Koltai (ELTE), L. Tapasztó and P. Nemes-Incze

The concept of time reversal invariant topological insulators has been a paradigm shift in solid-state physics and the controllable topological phase transition in two-dimensional materials has been a long-sought goal. The transition-metal pentatelluride $ZrTe_5$ lies at the boundary of the weak and strong topological phases, making tuning by mechanical deformation a viable avenue to realizing transitions between topological phases. This material has received substantial interest due to its numerous exotic properties, such as the planar Hall effect, anomalous Hall effect and chiral magnetic effect. However, most studies have focused on the bulk material, with very few [Ref. 1.5] experimental results on monolayers, even though in the single layer the crystal is predicted to be a large gap 2D topological insulator.[Ref. 1.6]
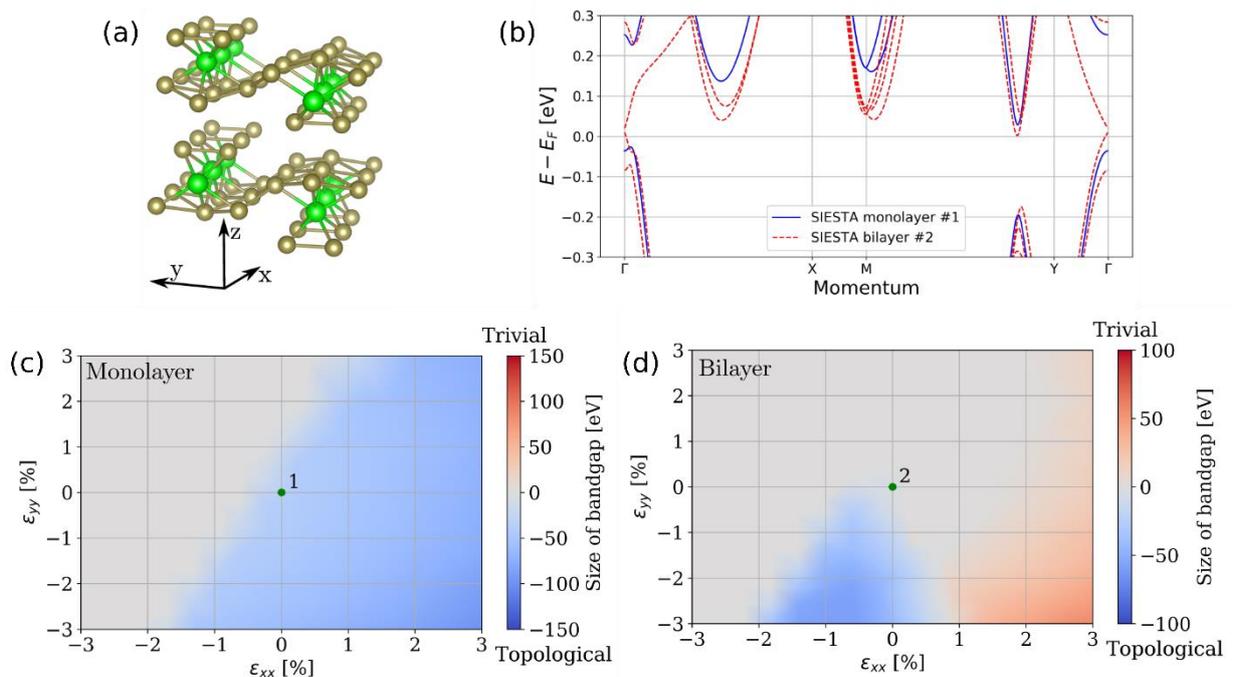

Figure 1.5. *Topological phases of mono and bilayer $ZrTe_5$. **(a)** Crystal structure of ZrTe5, showing two van der Waals monolayers, extending along the x, y plane. **(b)** Band structure of the monolayer and bilayer. Density plot of the band gap for the monolayer **(c)** and bilayer **(d)**. Red and blue colors represent the topological character of the gap (see also ref. **Error! Bookmark not defined.**) as a function of biaxial in plane (ε_{xx}) and out of plane (ε_{xy}) strain.*

Previously, we have examined the topological phase transition in a bulk crystal, via STM measurements and *ab initio* calculations. [Ref. 1.7] Here we explore the topological phase diagram of monolayer and bilayer $ZrTe_5$ crystals under mechanical deformations, using *ab initio* calculations. The band structure of mono- and bilayers of $ZrTe_5$ is plotted in Figureb, showing a 70 meV topological gap for the monolayer, in agreement with the previous prediction by Weng et al[Error! Bookmark not defined.]. In the bulk, changes to the interlayer spacing are a key parameter in shaping the topology of the band structure. This is reflected in the topological phase diagrams shown in Figure.5, where the gap closes for modest strain in the van der Waals

interlayer separation. As a function of in-plane biaxial deformation, the bilayer shows a transition from a trivial insulator to a topological insulator at experimentally achievable strains of a few %. At the same time, in the monolayer case there is no trivial-topological phase transition, only a closure of the topological gap for small (<1%) compressive strain. Thus, from a perspective of tuning topological phases via strain, bilayers of $ZrTe_5$ represent a unique platform realizing the topological-trivial insulator transition.

Since the preparation of monolayers and bilayers is still a challenge, we also examine the exfoliation of $ZrTe_5$ onto gold substrates (see Fig. 1.6.). We conclude that this method is unviable, as opposed to other 2D tellurides [Ref. 1.8] due to strong attraction of the first layer to gold which destroys its crystalline structure. Thus, in future experiments it is worth exploring the exfoliation of $ZrTe_5$ onto other clean metal surfaces [Ref. 1.9] , where the adhesion to the metal does not compromise the crystal structure of the material.
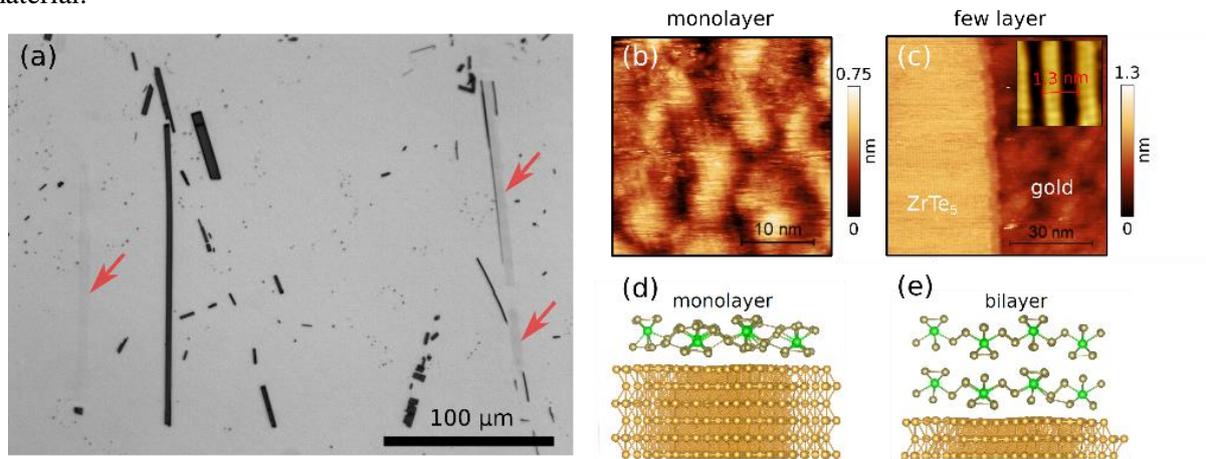
Figure 1.6. (a) Optical microscopy image of exfoliated $ZrTe_5$ on a gold substrate. Red arrows mark areas with the smallest optical contrast, possibly monolayers. (b) Representative STM topographic image of a low contrast area, showing a disordered structure with only slight hints of unit cell periodicity. (c) STM topographic image of a few-layer area, showing a well resolved atomic contrast on top of the crystal. (d) Relaxed ab-initio model of an adsorbed $ZrTe_5$ layer on a gold (111) surface. (e) Calculation for a bilayer $ZrTe_5$. The crystalline structure of the monolayer is destroyed by the strong adhesion to the gold substrate, while in the bilayer case the top monolayer is unaffected.

Graphene-encapsulated silver nanoparticles for plasmonic vapor sensing

### *OTKA K134258, MTA János Bolyai Research Scholarships*

G. Piszter, Gy. Molnár, A. Pálinkás, Z. Osváth

Noble metal nanoparticles (NPs) are widely used for chemical and biological sensing because of their local surface plasmon resonance (LSPR) and surface-enhanced Raman scattering properties. The LSPR produces sharp spectral absorption, which can be used to detect changes in the molecular environment near the surfaces of NPs by spectral shift detection. In this work, we fabricated Ag NPs and graphene–silver nanoparticle hybrids directly on highly oriented pyrolytic graphite (HOPG) substrates as follows. Ag films of 7 nm thickness were evaporated onto HOPG and then covered with CVD-grown graphene. The transfer process yielded a graphene coverage of 40-50%. To form nanoparticles, both bare and graphene-covered Ag thin films were annealed at 400 °C under an inert gas atmosphere for 1.5 h. The obtained samples (samples #1 and #2) were characterized by tapping-mode atomic force microscopy (AFM), as well as scanning electron microscopy (SEM), see Fig. 1.7.
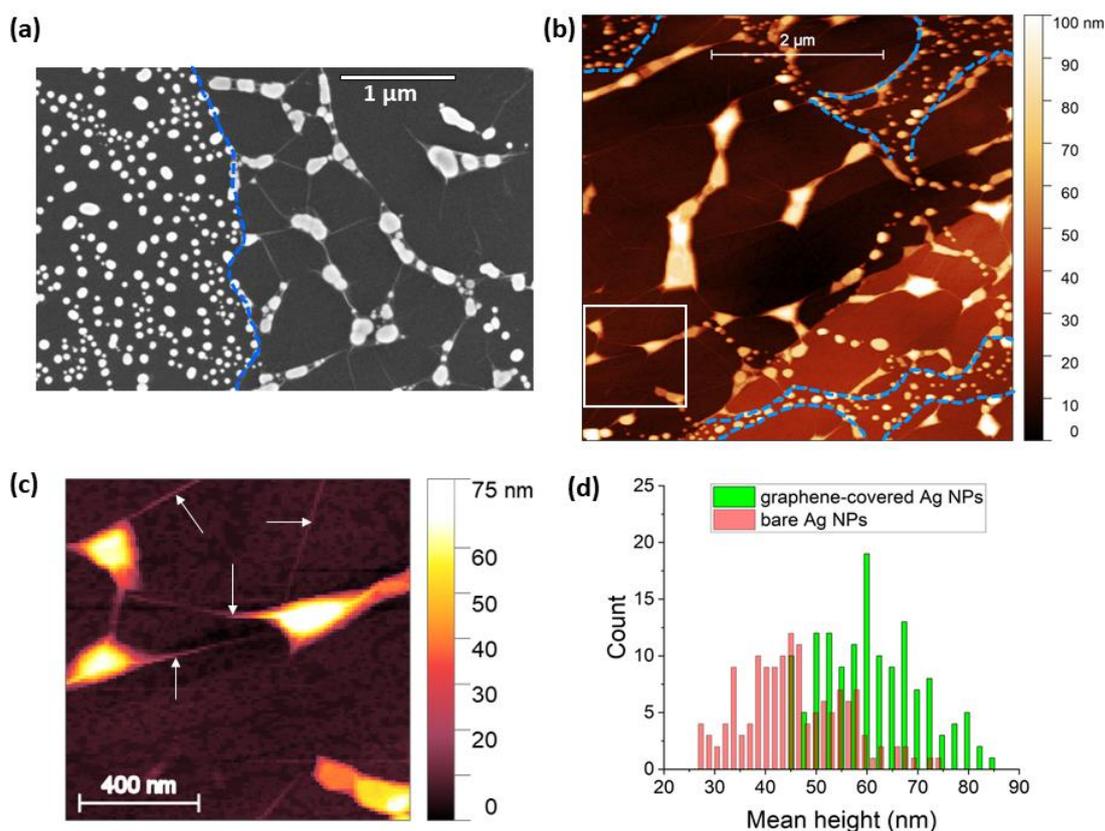
Figure 1.7 (*a*) *SEM image of bare Ag NPs (left) and Ag NPs covered with graphene (right). The edge of graphene is marked with a blue dashed line as a guide for the eye. (**b**) AFM image of graphene-encapsulated Ag NPs. Discontinuities in the graphene overlayer and areas with bare Ag NPs are demarcated with blue dashed lines. Several graphene-covered nanoparticles are demarcated with a white square and shown in the enlarged image in (**c**). Here, wrinkling of the graphene overlayer is observed (arrows). (**d**) The mean height distribution of graphene-covered (green) and bare Ag NPs (red) was measured on 142 NPs in both cases.*

We investigated the effect of point defects on the sensing properties of graphene-covered Ag NPs. Therefore, we introduced defects in sample #2 by exposing it to O_2 plasma for 5 seconds. Such plasma treatment induced individual, point-like defects (vacancies) in the graphene overlayer, located several nanometers apart from each other. UV-Visible reflectance spectroscopy was used to measure the shift of the LSPR upon exposure to acetone, ethanol, 2-propanol, toluene, and water vapors. Since the LSPR shifts are rather small changes compared to the LSPR intensity, it is more convenient to use the *reflectance change* spectra (Fig. 1.8) defined as $\Delta R = (R/R_0) \times 100\%$, where R_0 is the initial reflectance in synthetic air.
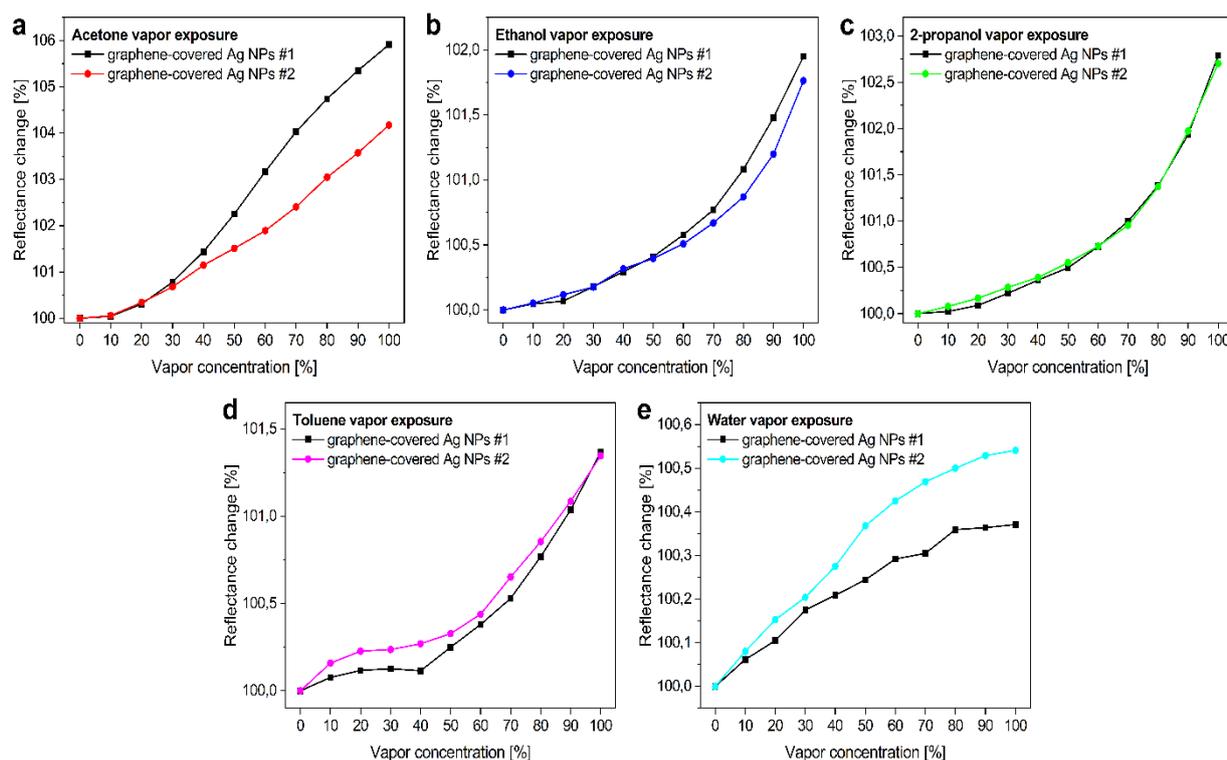
Figure 1.8. *Maximal peak intensities in the reflectance change spectra as a function of vapor concentration. For each applied vapor, the optical responses of samples #1 and #2 are compared. (a) acetone, (b) ethanol, (c) 2-propanol, (d) toluene, and (e) water vapors were applied.*

We showed that the prepared hybrid nanostructures displayed pronounced optical responses upon exposure to organic vapors. The observed concentration-dependent shifts in the LSPR were substance-specific, as demonstrated in Figure 2. One can observe that there are differences in the maximal responses of the two samples, especially for acetone, water, and toluene. The defected graphene overlayer (sample #2) increases the sensitivity to water and toluene. This agrees with recent calculations showing that toluene and water molecules adsorb better to graphene with defects. In comparison, exposure to ethanol and 2-propanol results in similar optical responses, while acetone even gives a reduced signal on defected graphene. These findings can be useful in tuning the selectivity in sensing volatile organic compounds.
***The paper was published in Nanomaterials 12, 2473 (2022).***

Spectral Engineering of Hybrid Biotemplated Photonic/Photocatalytic Nanoarchitectures

G. Piszter, K. Kertész, D. Kovács, D. Zámbó, Zs. Baji, L. Illés, G. Nagy, J. S. Pap,
Zs. Bálint, and L. P. Biró

Heterogenous photocatalysis is a light driven process that enables transformation of the abundant and environmentally safe sunlight into much needed chemical processes to achieve, for example, water purification. For this purpose, supported catalysts are needed, which can be used in a continuous-flow regime. To enhance the efficiency of the purification process, the properties of the used catalysts have to be tunable in a way to fit the characteristics of the pollutant to be removed. For this type of application, the photocatalyst has to be cheap and, in order to allow avoidance of the use of UV transparent materials with prohibitive prices, preferably, able to operate with visible light.

Due to their nanostructure, butterfly wings offer a support with a large specific surface that can be produced in a cheap and environmentally safe way, onto which different nanoparticles (NP) can be immobilized and eventually coated by a few nanometers of semiconductor material to enhance their photocatalytic effect. An additional benefit may arise from the photonic-crystal-type (PhC) structures in the butterfly wings.
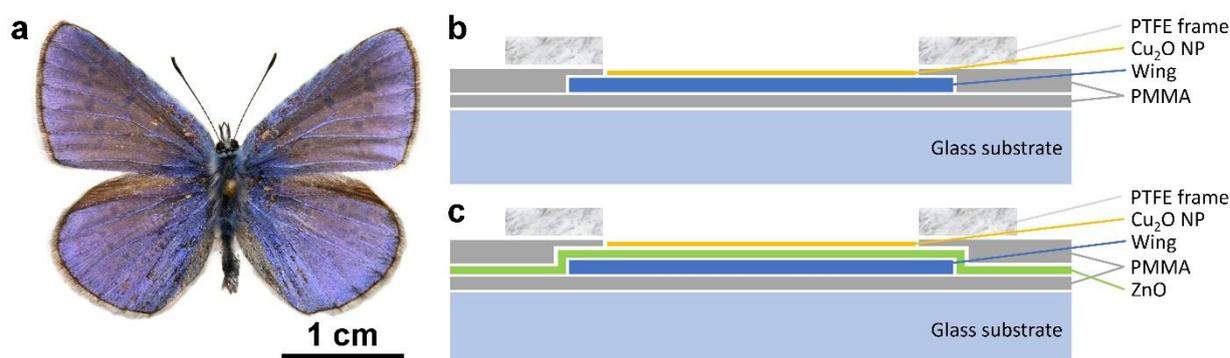
Figure 1.9. *Common Blue butterfly and typical sample structures used. (**a**) Dorsal wing surfaces of a male specimen; (**b**) Type-1 sample structure without 15 nm ZnO layer on the butterfly wing before the Cu_2O deposition; (c) Type-2 sample structure with 15 nm ZnO layer deposited by ALD on the butterfly wing before the Cu_2O deposition.*

Here, photonic nanoarchitectures of biological origin with hierarchical organization from nanometers to centimeters were applied as biotemplates. The blue wing surface of laboratory reared male Common Blue (*Polyommatus icarus*) butterflies were used in combination with atomic layer deposition (ALD) of conformal ZnO coating and deposited octahedral Cu_2O NPs to explore the possibilities of engineering the optical and photocatalytic properties of hybrid photonic nanoarchitectures (Fig. 1.9).

Type-1 and type-2 samples were prepared similarly, the only difference was the additional base layer of 15 nm ZnO under the Cu_2O NPs: the wings were glued to glass substrates, were pretreated in ethanol overnight, then the different amounts of Cu_2O sols were added carefully to the dry samples. Half of the samples were coated with an additional 5 nm ZnO cover layer to immobilize the Cu_2O NPs.
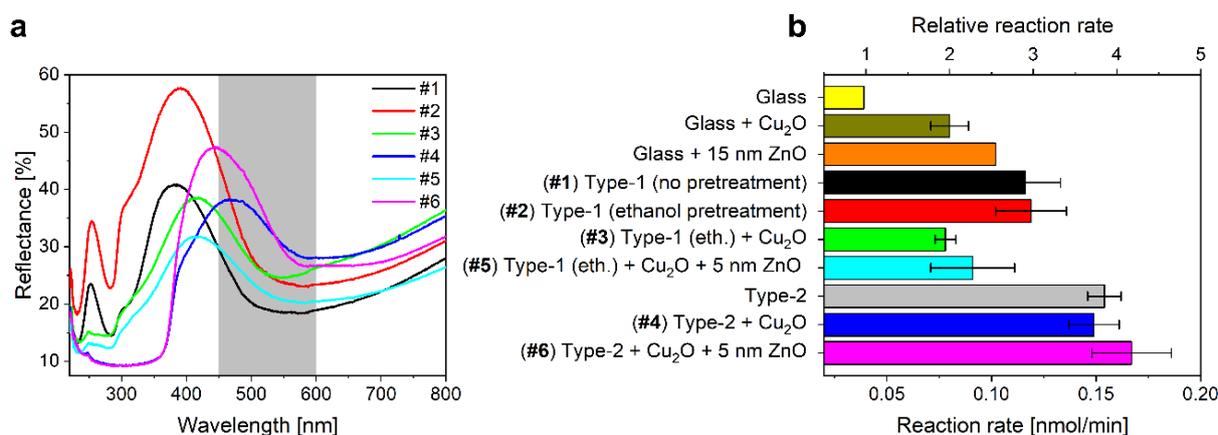
Figure 1.10. (a) *Reflectance spectra of the wing samples used in the photocatalytic experiments in as prepared state: (**1**) type-1 sample, without ethanol pretreatment; (**2**) type-1 sample with ethanol pretreatment; (**3**) type-1 sample with 120 µl of Cu₂O sol drop dried; (**4**) type-2 sample with 120 µl of Cu₂O sol drop dried; (**5**) type-1 sample with 120 µl of Cu₂O sol drop dried followed by the deposition of 5 nm of ZnO; (**6**) type-2 sample with 120 µl of Cu₂O sol drop dried followed by the deposition of 5 nm of ZnO. The grey-shaded area marks the rhodamine B absorption band. (**b**) Absolute and relative reaction rates of the samples used to characterize the photocatalytic efficiency of the biotemplated photonic/photocatalytic nanoarchitectures.*

The samples were characterized by UV-visible reflectance spectroscopy, and their photocatalytic performance was benchmarked by comparing the initial decomposition rates of rhodamine B (Fig. 1.10) under visible light illumination. The relative reaction rates may be helpful in comparing the individual effects of the various components of the more complex biotemplated photonic nanoarchitectures that proved to have the best efficiency in the photodegradation of the dye. The reaction rate on bare glass was taken as unity.

Cu₂O NPs alone or on the butterfly wings, covered by 5 nm thick layer of ZnO, showed poor performance. Butterfly wings, or ZnO coated butterfly wings with 15 nm ALD layer showed a 3 to 3.5 times enhancement as compared to bare glass. The best performance of almost 4.3 times increase was obtained for the conformally coated wings by 15 nm ZnO, deposited with Cu₂O NPs followed by conformal coating with an additional 5 nm of ZnO by ALD. The above results demonstrate that properly chosen photonic nanoarchitectures of biologic origin—from the large "library" of such structures—in combination with well-chosen photocatalyst(s) can significantly enhance the efficiency of complex, hybrid biotemplated photonic/photocatalytic surfaces. Taken together, our findings suggest that the reason for the enhanced efficiency is complex; both the fast carrier separation at Cu₂O–ZnO p-n heterojunctions and the slow light effect of the photonic nanoarchitecture are contributors.

Effect of Plasmonic Au and Ag/Au Nanoparticles and Sodium Citrate on the Optical Properties of Chitin-Based Photonic Nanoarchitectures in Butterfly Wing Scales

K. Kertész, G. Piszter, Z. E. Horváth, D. Zámbó, A. Deák, and L. P. Biró

Photocatalysis on non-toxic, stable metallic nanoparticles (NPs) such as Au or Ag/Au alloys, which offer the possibility to tune the wavelength range where photoexcitation is occurring, is ideal to be used for clean and safe technology. To be able to exploit this advantage, the metallic NPs must be supported on a substrate which will provide a large specific surface area, possibly by micro- and nanostructuring, and can be produced in a cheap and environmentally friendly way. Photonic-crystal-type (PhC) structures, in particular inverse opal type nanoarchitectures, are used to host various catalytic NPs. These hybrid nanoarchitectures (PhC + NP) exhibit a lot of potential for harnessing solar radiation for catalytic purposes. PhC-type nanoarchitectures of biologic origin can be found on the wings of butterflies exhibiting structural coloration. Using this cheap substrate, the simplest way of producing nanocomposites of metallic NPs in PhC nanoarchitectures in butterfly wing scales is the application of colloidal sols of metallic NPs on the flat butterfly wing. In this process, the effect of three major sol components has to be taken into account: the effect of water, the metallic Au and alloyed Ag/Au NPs, and the sodium citrate used for the formation/stabilization of the NPs. Here, the impact of these three components on the optical properties of the natural photonic nanoarchitectures is discussed.
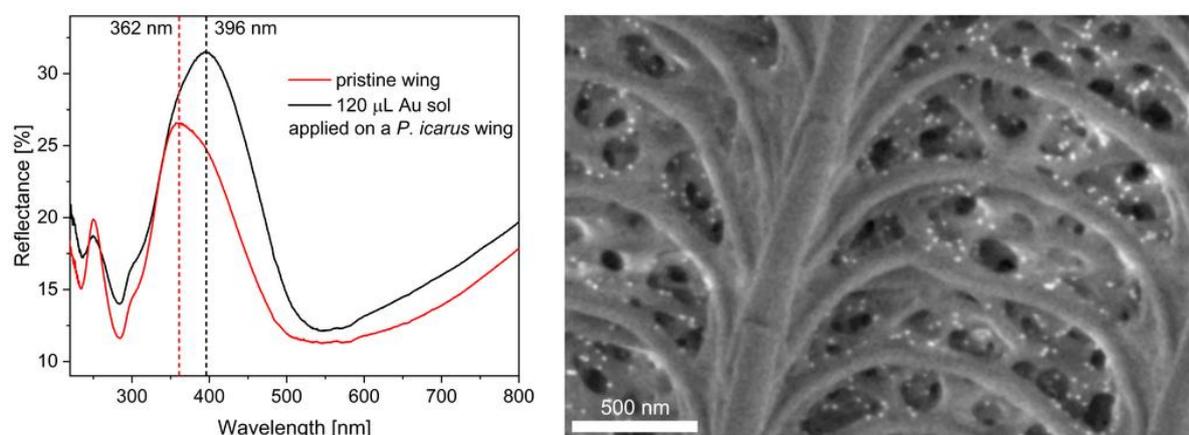
***Figure 1.11** (**a**) Integrating sphere reflectance measurements of the Polyommatus icarus wing in pristine state before the application of the sol and after the application of 120 µL of Au sol and complete drying; (**b**) Scanning electron micrograph of a scale of the Polyommatus icarus wing after the application of 120 µL of Au NP sol and complete drying. One may note the presence of bright dots in the image, which represent the Au NPs.*

The butterfly wing scales, with the NPs, integrated into the photonic nanoarchitecture, as seen in Fig. 1.11.b, behave like a complex nanocomposite which inherits its properties from both components. As the composite is made up dominantly of the chitin-based biologic photonic nanoarchitecture, its properties are primarily determined by photonic nanoarchitectures of the butterfly wing scales. See pristine and shifted reflectance in Fig. 1.11.a.

For a detailed analysis, a total of 40 samples were prepared and subjected to different treatments. One may observe that PLA gluing produced a slight blueshift in the spectral position of the reflectance maximum, but on average, the amplitude of the reflectance maximum in normal incidence did not change significantly (Fig. 1.12.b). The subsequent water immersion for 8 h, followed by overnight drying, did not

produce modifications of the spectral position and the amplitude of the reflectance maximum. The drop-drying of sodium citrate solution returned the spectral position of the reflectance maximum to that of the pristine state (redshift) but produced a significant increase in the amplitude of the normal incidence reflectance. The removal of the dried citrate by immersing the samples for 8 h in water and measuring them after overnight drying in air eliminated the redshift in the spectral position but preserved the increased amplitude of the reflectance.
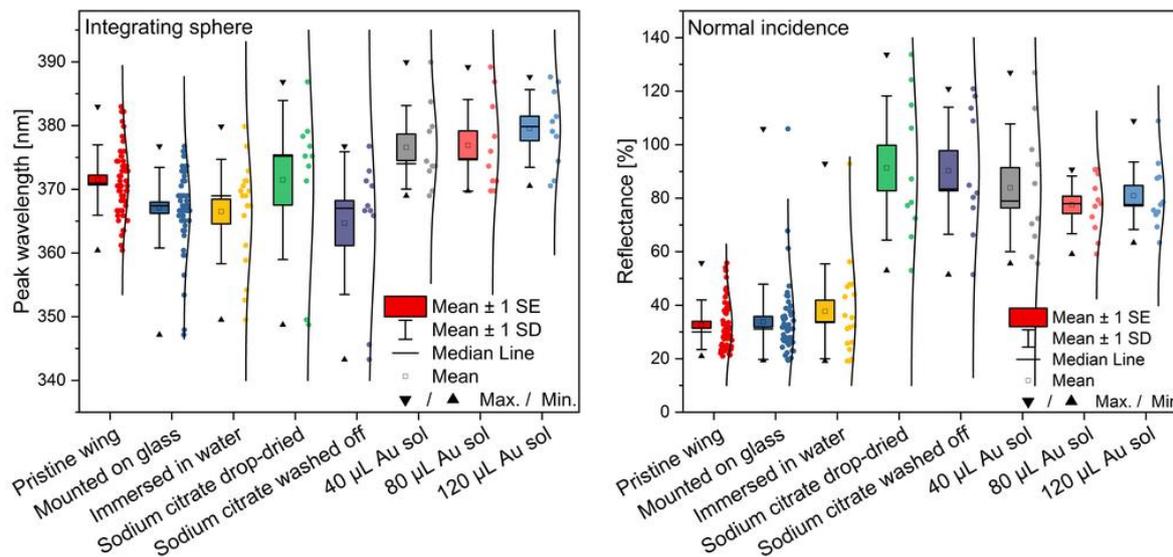
Figure 1.12. *Statistical presentation of the changes in optical properties of male Polyommatus icarus wings mounted on glass substrate by PLA. (**a**) Integrating sphere measurement of the spectral position of the blue reflectance maximum after the different treatments of the wings; (**b**) normal incidence measurement of the amplitude of the blue reflectance maximum after the different treatments of the wings.*

When Au NP sol in sodium citrate solution was applied on the water-immersed and dried butterfly wings, the observed effects presented the characteristics of the citrate solution application, but an additional redshift was produced, and the increase in the amplitude of the normal incidence reflectance maximum was slightly smaller.

In addition, we used ethanol to facilitate the penetration of deionized water inside the photonic nanoarchitecture, the major effect measured after drying is the increase of normal incidence reflectance caused by the flattening of the wing scales towards the wing membrane which is a persistent effect.

Photonics Department

Head: Dr. Peter PETRIK, D.Sc., scientific advisor

Research Staff:
- Miklós FRIED, D.Sc., Head of Ellipsometry Laboratory
- András DEÁK, Ph.D., Head of Chemical Nanostructures Laboratory
- Antal GASPARICS, Ph.D.
- Norbert NAGY, Ph.D.
- Zoltán LÁBADI, Ph.D.
- Ferenc RIESZ, C.Sc.
- Dániel ZÁMBÓ, Ph.D.
- Alekszej ROMANENKO
- Miklós SERÉNYI, D.Sc., retired
- Gábor VÉRTESY, D.Sc. , Prof. emeritus
- György KÁDÁR, D.Sc., Prof. emeritus
- Tivadar LOHNER, D.Sc., Prof. emeritus
- János MAKAI, C.Sc., retired
- András HÁMORI, dr. univ., retired
- György JUHÁSZ, dr. univ., retired

Students:
- Deshabrato Mukherjee, Ph.D.
- Berhane Nugusse, Ph.D.
- Noor Taha Ismael, Ph.D.
- Csaba Bakos,
- Áron Fogarasy,
- Dávid Kovács,
- Rita Némedi,
- Máté Szűcs,
- Gergely Südi,
- Dániel Takács

The Photonics Department develops unique methods and tools for non-destructive optical and magnetic measurement of surface nanostructures and materials (spectroscopy; magnetic material testing; biosensors; surface curvature measurement; surface testing; water contamination). One of the most important tasks of the Department is patenting and application of the methods in international projects with partners representing the industry and the high technology.

Key achievements of the Photonics Department in 2022:

- Non-destructive magnetic methods have been developed for the investigation of structural materials in nuclear power plants. A correlation is sought between the sample parameters determined by non-destructive magnetic measurements and the dose of neutron irradiation. It is extremely important that these tests can be performed on cladded surfaces. The measurements performed can play an important role in the non-destructive testing of the pressure tank of nuclear power plants, which is currently one of the most important tasks in nuclear technology. Their results make it possible in the future to replace the labor-intensive, costly and destructive testing with the magnetic method they have developed.
- A micro-combinatorial mapping method was used for high-resolution composition-dependent optical analysis of materials used in solar cell technology and sensing.
- Surface nanoparticles were generated in a controlled way that can be used in sensing, medicine, and solar cell technology, among others. Using a self-built single-particle spectrometer, we investigated the role of the exchange of molecules inherently present in the surface of gold nanorods (due to the synthesis method) in interactions by examining individual nanoparticles.

- We develop cryoaerogels electrochemical and catalitic applications. We have demonstrated the importnce of nanoscale design in the charge carrier transport properties of CdSe/CdS/metal cryoaerogels.
- We developed a capillary probe method for high-precision testing of hydrophobic and hydrophilic surfaces. Computational and experimental investigation of hydrophobic surfaces based on previous measurements and in collaboration will be of paramount importance. We investigated the novel possibilities of the method for the determination of solid-liquid adhesion work and surface free energy.
- Taking advantage of the high sensitivity and the nondestructive nature of spectroscopic ellipsometry, interface processes were investigated in highly relevant research topics. It has been shown that the hot electrons created by plasmon excitation in gold occupy the top few nanometers of the layer, and they have a different dispersion than the thermalized electrons of the bulk layer. Hydrocarbon adsorption on the surface of highly oriented pyrolytic graphite was measured by spectroscopic ellipsometry
- on time scales of more than two months, showing the kinetics of monolayer adsorption.
- We developed an optical sensor structure that shows resonant surface amplification in a controllable way, depending on the properties of the biological materials to be tested. We applied combinatorial plasmonic materials for Kretschmann-Raether sensing at solid-liquid interfaces.Electrochemically grown gold nanoparticles were used to create sensor surfaces suitable for electrochemical measurements. We optimized the adsorption of the filaments by monitoring optical measurements on the surface of the sensors. Cyclic voltammetry measurements detect contaminants in natural waters and drinking water.
- We developed the method of Makyoh topography into new directions. It was also shown that front-face deformations of semiconductor wafers induced by localised backside contamination particles during polishing can also be well approximated by the Gaussian curve, thus making the analysis more transparent.

Contact angle determination by the Capillary Bridge Probe method: from perfect wetting to hydrophobic surfaces

OTKA FK 128901

N. Nagy

The developed indirect Capillary Bridge Probe method combines the accuracy of the Wilhelmy method and the general usability of the sessile drop method without their limitations. The method is based on the use of a liquid bridge as a probe: the capillary bridge of the test liquid is stretched between the base of a cylinder and the investigated surface under equilibrium conditions. The advancing contact angle on the sample can be measured during the stepwise or slow (quasi-static) decrease of the bridge length. The receding contact angle is determined during the retraction of the cylinder (Fig. 2.1).
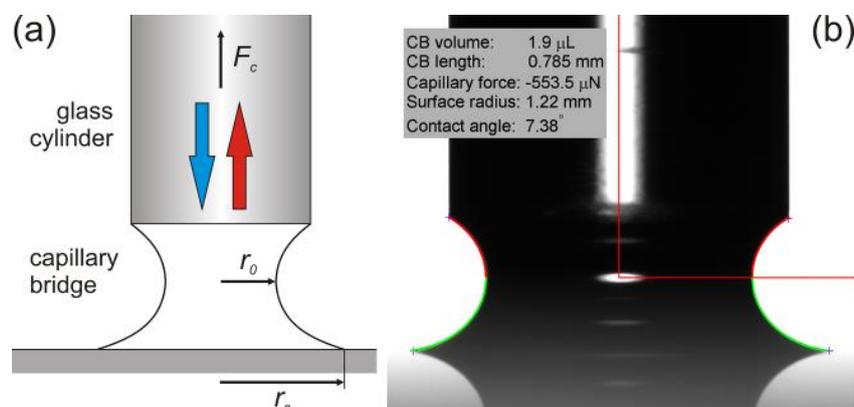

Figure 2.1. a) Schematics of a capillary bridge (Fc: capillary force; r0: neck radius; rs: contact line radius on the sample surface). b) Captured and evaluated image of a water capillary bridge on a glass surface. The diameter of the glass cylinder is 2 mm. The blue crosses designate the corners of the bridge's silhouette, the red and green curves show calculated profile.

The contact angle is calculated from Delaunay's analytical solution, while the three necessary parameters are the measured capillary force (F_c), the radius of neck or haunch (r_0), and the radius of the contact line (r_s) on the investigated surface. The latter two parameters are obtained from the automated analysis of the captured image of the liquid bridge. The radius of the upper contact line (r_c) is constant since it pins on the rim of the cylinder.

A typical measured graph and determined contact angles are plotted in Fig. 2.2. The measurement was carried out on a clean stoichiometric Si_3N_4 surface. The attractive (negative) capillary force decreases with the decreasing bridge length, and it shows hysteresis (Fig. 2.2.a). This hysteresis results in the contact angle hysteresis in Fig. 2.2.b. The advancing contact angle is stable, while the receding values show decreasing character (similarly to the results of evaporating drop measurements).

As a demonstration of a unique property of the method, perfect wetting situations were also characterized. The graphs shown in Fig. 2.3. were measured on a super hydrophilic acid-treated glass surface. The capillary force and the contact angle do not exhibit hysteretic character. However, a novel phenomenon can be observed in Fig. 2.3.b. The contact line starts to advance again during the retraction and the corresponding (readvancing) contact angles are much lower than the advancing and receding values.

In this phase, the readvancing contact line finds prewetted surface, this is the reason of the low determined values. [Ref. 2.1]
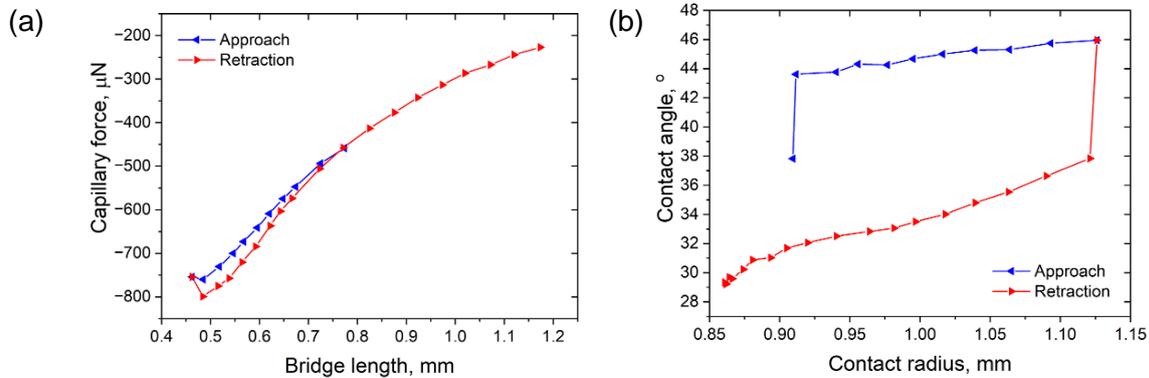
Figure 2.2. *(a) Capillary force as a function of bridge length measured on a hydrophilic Si_3N_4 surface. (b) Determined contact angles as a function of the contact radius. The force hysteresis results in contact angle hysteresis.*
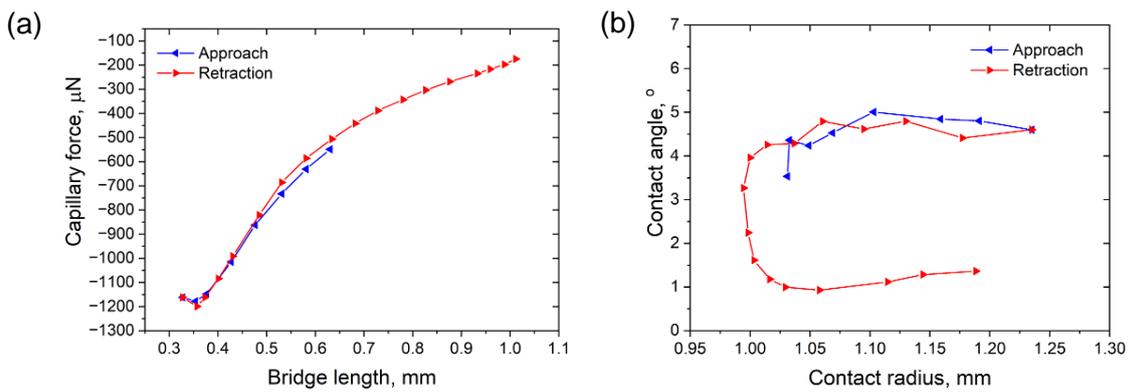
Figure 2.3. *(a) Capillary force as a function of bridge length measured on an acid-treated superhydrophilic glass surface. (b) Contact angles vs. the contact radius. The contact line starts to advance again during the retraction and the readvancing contact angles are much lower.*

Hydrophobic surfaces can be characterized with high sensitivity, as it was demonstrated on PTFE surfaces. The graphs in Fig. 2.4 show hysteresis of capillary force and contact angle, as well. Sessile drop measurements did not show any contact angle hysteresis. [Ref. 2.2]
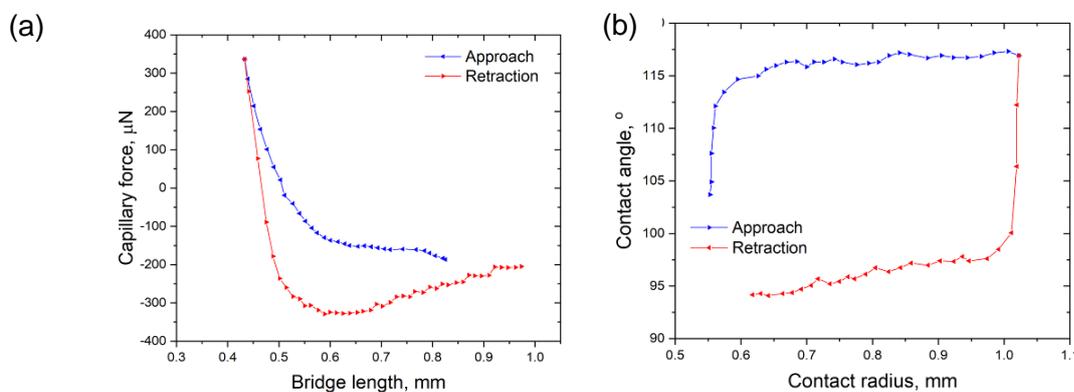

Figure 2.4. *(a) Capillary force vs. bridge length measured on a hydrophobic PTFE surface. The capillary force changes its sign during the approach and retraction. (b) Contact angles as a function of the contact radius.*

Mapping and modeling of the optical properties of thin films developed on ferrite grains by color etching

TKP2021-EGA-04, OTKA K 131515, EMPIR POLight

J. B. Renkó, A. Romanenko, P. J. Szabó, A. Sulyok, P. Petrik, A. Bonyár

Etching methods in metallography are used to develop the grain structure at the surface. The etchant reacts with the material at the surface to change its topography, making individual grains visible. Color etchants are less common than chemical etchants, mainly because the saline solutions used in color etching are less aggressive. The layer grows in both directions relative to the original plane of the sample. As the film grows, each grain undergoes a cyclic color change. Although these color etching methods are widely used, the chemical processes involved are not or only partially explored. In this investigation we have mapped the individual grains using focused-beam ellipsometry, and compared the results with complementary methods (Fig. 2.5). We have shown that the refractive index varies depending on the crystallographic orientation of the grains in the same way as the etching speed. The refractive index is inhomogeneous in depth with larger values at the interface between the layer and the substrate. This finding correlates well with compositional depth profile revealed by X-ray photoelectron spectroscopy. This work was a significant contribution to relate the colors to the crystallographic orientations of the individual grains. [Ref. 2.3]
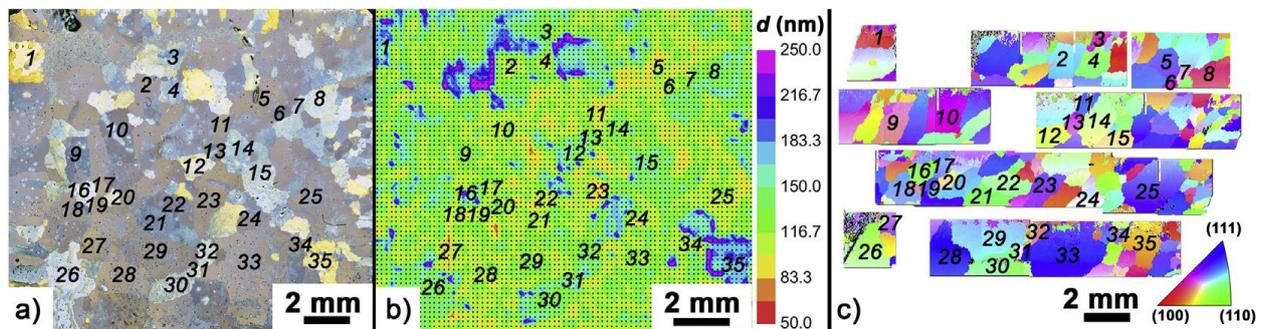
Figure 2.5*. a) Optical microscope image of the color etched ferritic steel specimen (60 s in Beraha-I). The numbers represent labels of the grains for further investigation. b) The layer thickness map determined by spectroscopic ellipsometry (using a Cauchy dispersion). c) The inverse pole figures of the same area from electron backscatter diffraction (EBSD).*

High-sensitivity ellipsometry for in-situ characterization of interface phenomena

TKP2021-EGA-04, OTKA K 131515, EMPIR POLight

P. Petrik

Taking advantage of the high sensitivity and the nondestructive nature of spectroscopic ellipsometry, interface processes were investigated in highly relevant research topics. It has been shown that the hot electrons created by plasmon excitation in gold (Fig. 2.6.a) occupy the top few nanometers of the layer, and they have a different dispersion than the thermalized electrons of the bulk layer [Ref. 2.4].

Hydrocarbon adsorption on the surface of highly oriented pyrolytic graphite was measured by spectroscopic ellipsometry on time scales of more than two months (Fig. 2.6.b) and a few hours (not shown here, see [Ref. 2.5]). It was shown that monolayer adsorption can be followed by this technique, as verified and analyzed by tapping mode methods.
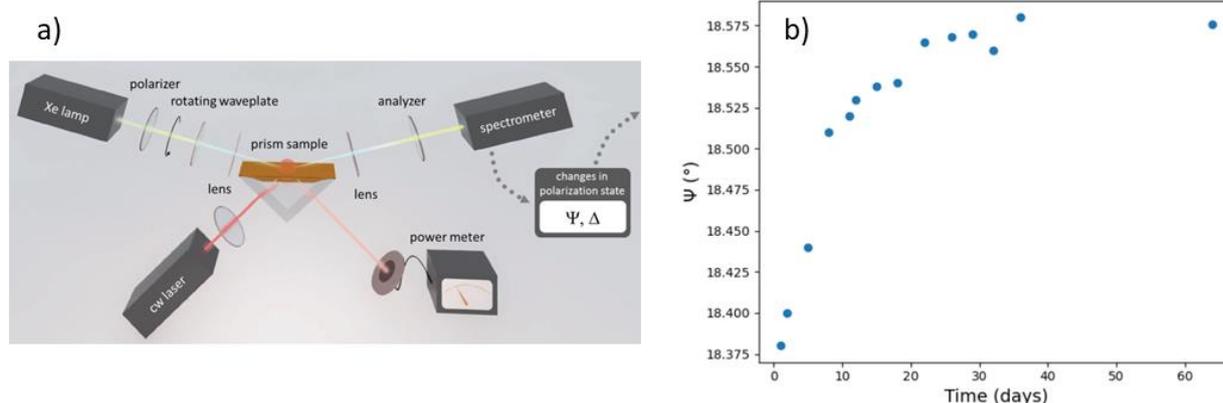
Figure 2.6. *a) Experimental setup to measure hot electrons during plasmon excitation in a thin gold layer. The plasmons are generated by a laser illumination the layer from the substrate side, whereas the ellipsometry measurement it performed at the gold/air interface during the excitation. b) Ellipsometry measurement during hydrocarbon adsorption on highly oriented pyrolytic graphite. ($\Psi=tan^{-1}(|r_p/r_s|)$, where r_p and r_s denote the complex reflection coefficients of light polarized parallel and perpendicular to the plane of incidence, respectively.)*

Ellipsometry monitoring of sensor processes based on gold nanoparticle bonded proteins

OTKA K 131515 and OTKA NNE131269

Z. Labadi, C. Bakos, M. Szucs, A. Bonyar, D. Mukherjee, H. Jankovics, F. Vonderviszt and P. Petrik

Monitoring and reducing pollution is one of the most important challenges. To achieve this goal, techniques that allow accurate and easy measurement of pollutants are essential. Unfortunately, in the case of heavy metal pollutants, there are currently no inexpensive, field-applicable methods available that let us easily and accurately determine the concentration of ions that pose a health risk.

In this work we examine selective heavy metal sensor structures based on specific modified proteins deposited onto conductive surface and the sensing process itself is based on electrochemistry. Our previous results [Ref. 2.6-2.7] show the feasibility of the modified protein-based sensor structures for ppm range monitoring of Ni and As contaminations in natural waters. Combining SEM, and voltammetry data with in-situ Spectroscopic Ellipsometry (SE) measurements provides deeper understanding of the sensing processes.

The first step of the process is the preparation of proteins with genetic modification that introduces selective nickel or arsenic binding domains. For this purpose, bacterial flagellar filaments were used. These are natural protein nanotubes, which are formed by self-assembly from thousands of flagellin subunits. Their variable middle portion that forms the D3 domain exposed on the surface of the filaments and was engineered to create a metal-binding site. This work was done at University of Pannonia, and details are given in [Ref. 2.6]

SE is a sensitive non-destructive method to monitor interfaces. Three consecutive steps of the building of the sensor structure are monitored by SE: (1) the deposition of gold nanoparticles onto a gold substrate, (2) the binding of modified proteins on gold nanoparticles and (3) selective binding of Ni or As contaminant on the modified proteins. These processes are monitored by independent physical and chemical characterization methods (SEM, AFM, cyclic voltammetry) as well while SE gives independent in situ monitoring data. The main advantage of SE is its sub-nanometer thickness sensitivity together with spectroscopic data in the 190-1700 nm range (i.e., 0.7-6.5 eV photon energy), plus second-range time resolution.
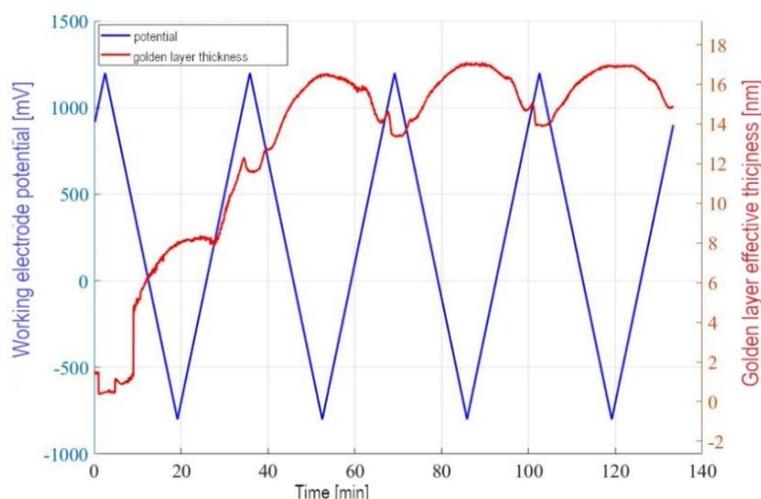

Figure 2.7. *Equivalent layer thickness of Au nanoparticles determined by SE as a function of time (red curve). Blue graph represents the applied potential as a function of time.*

Deposition of gold nanoparticles took place from 0.2mmol/l HAuCl4 solution in 10mM/L HEPES (4-(2-hidroxietil)-1-piperazin-ethaensulphonic acid) pH=7.0 buffer while the substrate electrode went through potential cycles between -0,6 and 1,2V versus saturated calomel electrode. Simultaneous SE spectra were measured throughout the cycles. Evaluation of SE spectra was made using a three-layer optical model (vacuum evaporated gold, followed by a surface roughness layer and a nanoparticle layer, both characterized as mixture of water and gold using the Sellmeier model). Fig. 2.7. shows the measured Au nanoparticle layer thicknesses. Golden nanoparticle deposition takes place in cycles synchronous with the potential change and the deposition takes place in the 0. – 1V potential range. Fig. 2.8 shows the SEM micrographs of the surface after10 cycle deposition. Full coverage with an approx. 100nm surface roughness is observable. This surface was used to immobilize the protein filaments.
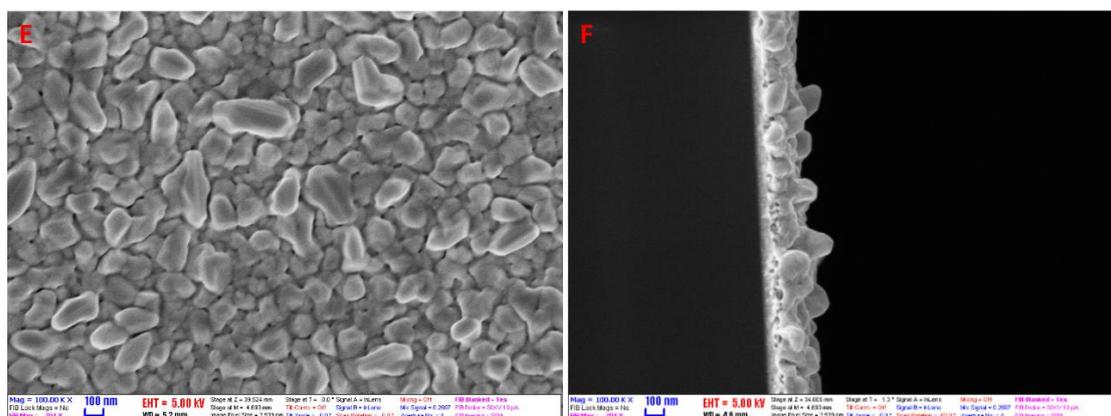
Figure 2.8. SEM micrographs of golden nanoparticles deposited onto evaporated gold in 10 cycles and cross-sectional view of sample

Protein immobilization was carried out from 1mM/L protein solution in 10mM/L HEPES pH=7.0 buffer applying potential cycles between -0.6 – 0.7V. Fig. 2.9. shows the protein filament coverage on the surface after 10 cycles. It has to be noted that the protein coverage remained relatively low, and preferably should be increased by the cycle number and/or the protein concentration.
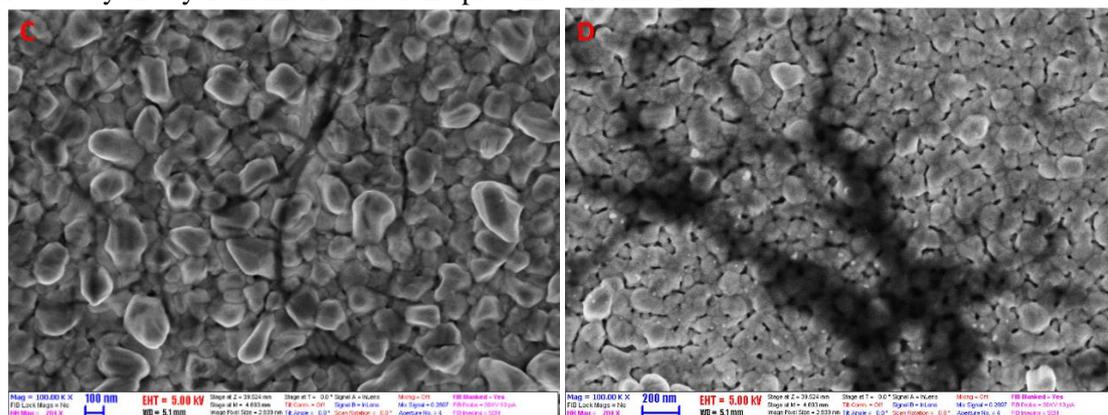
Figure 2.9. Protein filament coverage on the surface after 10 cycles

The protein immobilization was also followed by SE using a three-layer model (gold nanoparticle layer, rough surface layer and a protein/solvent layer characterized by different Au, water and protein contents respectively. Fig 2.10. shows the amount of accumulated protein at the surface as a function of time (cycles). The protein irreversibly accumulates in the middle layer (rough gold) and its amount increases with time.
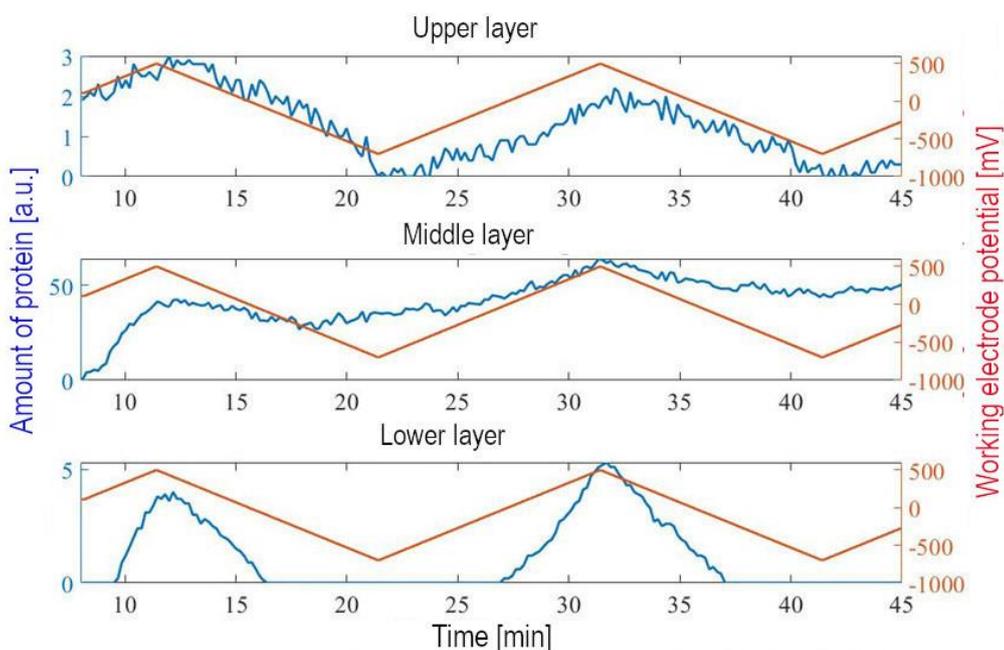
Figure 2.10*. Protein content calculated from three-layer ellipsometry model (blue curves). Red curves represent the potential cycles*

The sensor surfaces prepared with immobilized protein were characterized for Ni ion interaction. 150mM HEPES solution was contaminated with increasing concentration of Ni ions and cyclic voltammograms were measured on them using our electrode covered with filaments. Fig. 2.11. shows the voltammograms taken at increasing amount of Ni. As it can be seen in Fig. 2.11. a redox process is observable in the presence of Ni.
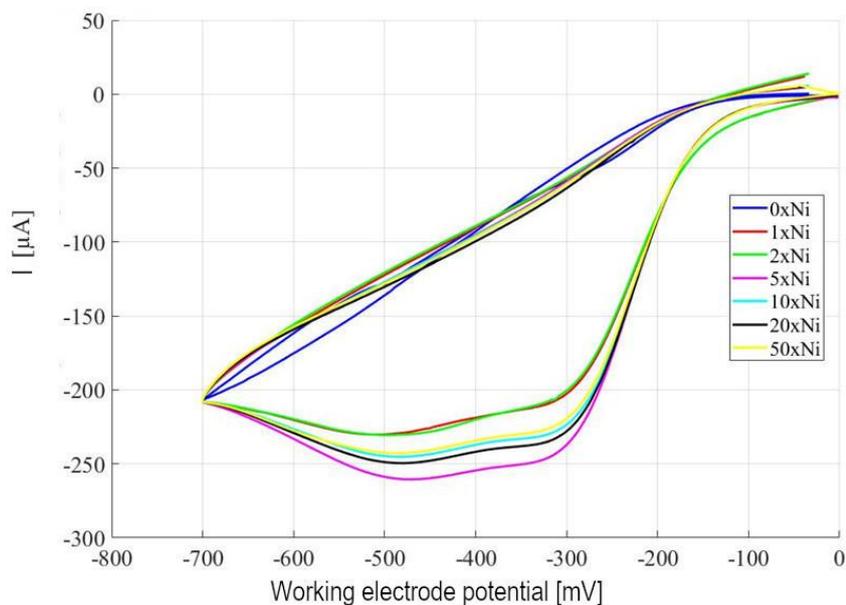
Figure 2.11. *Cyclic voltammograms of filament covered golden surfaces in the presence of Ni contamination. Ni concentrations are expressed in the multiples of 1µmol/L concentration (i.e at the EPA health limit for tap water)*

Figure 2.12. shows the integral of the peaks as a function of the Ni concentration. (curve belonging to Ni free sample was chosen as baseline) The integral values show only slight increasing tendency with increasing Ni which can be explained by the low partial coverage of the surface and the saturation of Ni binding points.
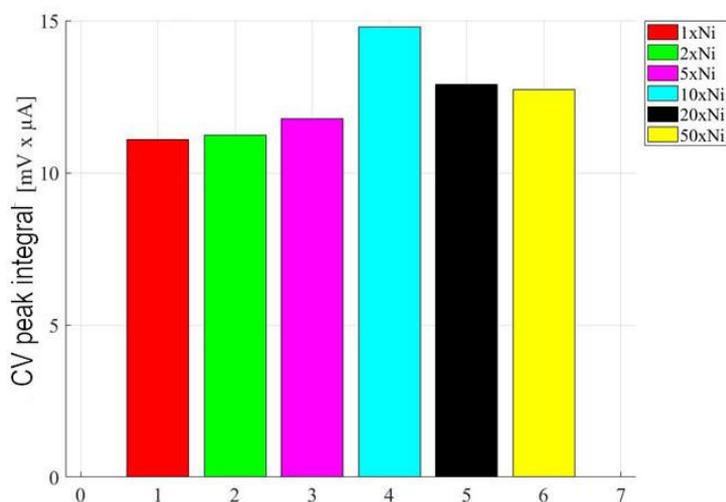
Figure 2.12. Integral of the curves measured on Ni contaminated samples as a function of the Ni concentration.

Protein flagellar filaments were successfully immobilized on golden nanoparticle covered electrode surface. The golden nanoparticle formation and the protein binding was successfully monitored by in situ Spectroscopic Ellipsometry. Genetically engineered bacterial flagellar filaments were successfully tested as sensor layers for measuring Ni concentration in aqueous solution at 1μmol concentration.

Surface sodification and self-assembly of gold nanoprisms

OTKA FK FK128327

A. Deák

Controlled surface modification of nanoparticles could enable the preparation of nanoscale objects that feature different surface-regions on the same particle, covered by different types of molecules. Such "multifunctional" particles have application potential especially in the fields of biomedicine and sensorics. In our recent work we investigated the controlled surface modification of gold nanoprisms with the aim to cover the tip/edge and face regions of the particles with different types of molecules. [Ref 2.8]
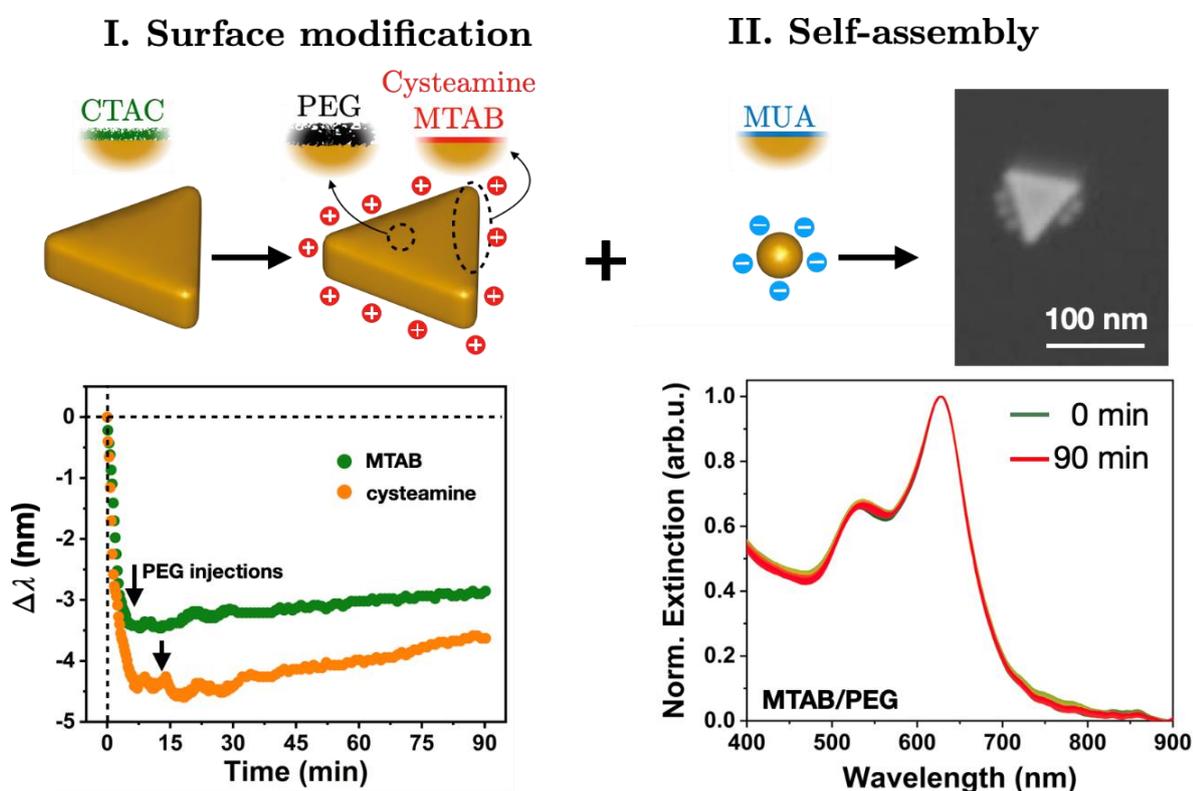
Figure 2.13. *Sketch of the binary surface modified gold nanoprisms and the blueshift of the dipolar plasmon resonance mode upon sequentially adding the thiol and the thiolated PEG (left). Self-assembly of the MTAB/PEG binary surface modified nanoprisms with MUA coated nanospheres - only minor spectral changes are observed, but spheres accumulate at the prism edges (right)*

The prisms were prepared *via* a seed-mediated wet chemical synthesis route, surface modification was achieved using thiolated molecules, as thiols show high affinity towards gold surfaces. The original CTAC capping ligand layer is partially replaced by cysteamine or MTAB when their respective concentration is kept low. By monitoring the time-evolution of the dipolar plasmon resonance mode of the gold nanoprisms, concentration levels could be identified where the thiols preferentially bind to the edges/tips of the prisms. In a second step the remaining surface of the prisms was covered by a thiolated PEG moiety. Whereas the tip/edge replacement of the original CTAC capping layer by the thiols induced a significant blueshift of the dipolar plasmon resonance as a result of decreasing effective refractive index in the optical near-field, PEG

injected into the same system results only in a minor redshift. This indicates the successful preparation of binary, thiol/PEG surface modified nanoprisms.

The self-assembly behavior of the prisms was also tested, using MUA surface modified nanospheres. MUA renders the nanospheres negatively charged, while both cysteamine and MTAB provide a positive surface charge. As PEG is a neutral polymer, it is expected that the oppositely charged nanoparticles will heteroaggregate as dictated by the electric double layer interaction between them. When performing such a heteroaggregatation experiment, no plasmon coupling related clear indication of the the heteroaggregation is found, but SEM images reveal that spheres preferentially accumulate at the sides of the prisms.

Importance of the nanoscale design on the charge carrier transport in CdSe/CdS/metal cryoaerogels

TKP2021-NKTA-05

D. Zámbó

Beside the outstanding optical properties of cadmium chalcogenide nanocrystals closely related to the radiative recombination of the photoexcited electrons and holes, the separation of these carriers is also of great interest particularly in electrochemical processes. Combining CdSe quantum dots and CdS shell (as a form of a nanorod) endows the semiconductor with the possibility to separate the holes in the core QD, while the electrons are being immobilized in the elongated CdS shell. These electrons are able to be transferred towards other semiconductor nanorods or even metal domains/nanoparticles. The benefit of the accumulation of the electron in a metal domain lays in the fact that the radiative recombination pathways are suppressed and the electron's lifetime can be extended. The latter technically means an enhanced efficiency to utilize them in catalytical processes. Due to the nonradiative nature of these processes, spectroelectrochemical techniques need to be applied to monitor them.

In case of CdSe/CdS dot-in-rods and core/crown nanoplatelets, the combination of the semiconductor part with metals (*e.g.* Au, Pt) can be obtained *via* two strategies: (i) wet-chemical growth of the metal domain onto each semiconductor nanoparticle or (ii) mixing the components in liquid phase. However, the resulting interparticle connections will be fundamentally different which alter the charge carrier dynamics. Upon cryogelating the multicomponent solutions, differences in the microstructure of the gels as well as their spectroelectrochemical properties are observed as a consequence of the different interparticle contacts (Fig. 2.14).
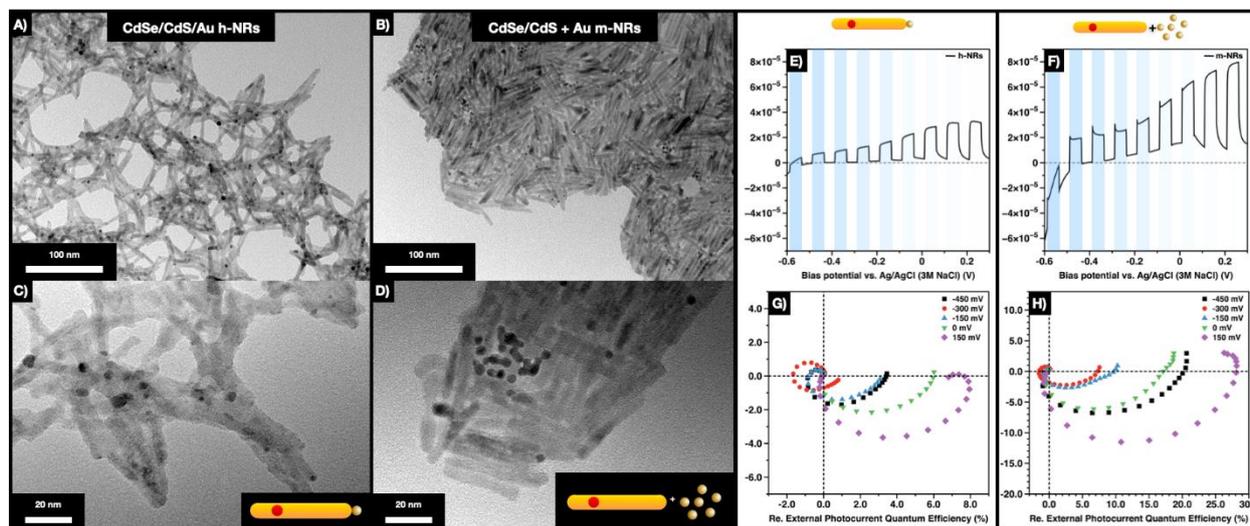
Figure 2.14. *TEM images representing the structure of the hybrid and the mixed semiconductor/metal nanoparticle cryoaerogels (A-D). Linear sweep voltammograms and IMPS Nyquist plots of the cryoaerogels (E-H).*

While growing the metal domains onto the semiconductor builindig blocks provides a homogeneous metal particle distribution, mixing leads to aggregation and inhomogenous accumulation of the metal particles. Based on spectroelectrochemical measurements (linear sweep voltammetry and intensity modulated photocurrent spectroscopy), competing charge transfer processes were identified: electron transfer from the semiconductor towards the ITO electrode, transfer from one semiconductor nanoparticle to the neighbouring one as well as electron transfer towards the metal domains and further to the solution. It was found, however, that the transfer of the photoexcited electrons towards the metal domains (and to the solution) dominates the spectroelectrochemical response of the gels consisting of semiconductor particles with on-grown metal domains leading to a negative photocurrent. This enables the use of such structures in e.g. hydrogen-evolution reaction (HER). [Ref 2.9]

Makyoh imaging and topography

F. Riesz

Makyoh imaging, named after the Japanese 'magic mirror', denotes an optical imaging mechanism, where a plane (or, more generally, spherical) wave is reflected from a nearly flat mirror, causing intensity variations in a far-field screen image because of the local deflections. The intensity distribution reflects the mirror height map. The first application of this principle was probably the Oriental magic mirror; a modern application is Makyoh topography, used mostly for the visualization of surface defects or texture of semiconductor wafers. In the ancient magic mirror, but often also in semiconductor technology, the flatness deviations of the mirror surface are caused by mechanical pattern transfer of the back relief of the mirror plate (or wafer) see Fig. 2.15.a. We have modelled the role of this pattern transfer in Makyoh imaging [Ref. 2.10]. Following the earlier studies, the convolution by a Gaussian was used for modelling the process mechanically; it was also shown that front-face deformations of semiconductor wafers induced by localized backside contamination particles during polishing can also be well approximated by the Gaussian curve, thus making the analysis more transparent (Fig. 2.15.b). Because of the convolution, the front face topography will have specific properties, which are reflected also in the Makyoh image. The Makyoh image formation was modelled by a full theory incorporating the effects of surface gradients on the intensity and Gaussian curvature, unlike previous approaches which used the linear approximation (Laplacian contrast). The main global features, inferred from our model, are the following: (1) the amplitude parameter of the Gaussian has a linear scaling effect on the front-face topography, this is equivalent to the scaling of the screen distance; (2) the convolution has a symmetrizing effect on the shapes as well as decreases the astigmatism of the reflected beams, this effect is characterized by the width of the Gaussian; (3) the nonlinearity of the imaging is reduced and (4) a minimum (local) focal distance (caustic limit) is imposed.
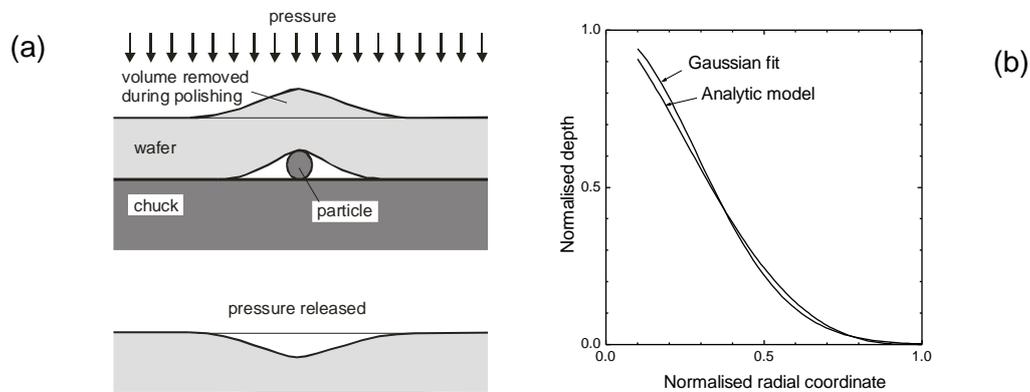
Figure 2.15. *a) Scheme of the formation of a front-face depression induced by a contaminant particle in a semiconductor wafer during polishing. b) Deformation profile of the depression: analytic plate-theory modelling and the Gaussian fit.*

In the linear case (valid if the screen distance is much larger than the front surface's local curvature radii) the whole optomechanical process is equivalent to the convolution by a LoG (Laplace of Gaussian) function; this is a standard edge-detection method in image processing. Another result of the past year is the proposal of a novel approach for the imaging of the ancient mirror: the *visual image* of the back relief pattern, rather than its topography is compared to the Makyoh image. The visual image depends on the environmental illumination conditions and surface reflection properties, but it can be stated the both images are essentially emphasise edges (gradient changes) of the back relief, thus their correspondence can be established, especially if the Makyoh imaging is in the nonlinear region (that is, the bright areas are strongly focused and their width is reduced).

Thin Film Physics Department

Head: Dr. Katalin Balázsi, Ph.D., senior scientist

Research Staff
- Csaba BALÁZSI, D.Sc.
- Haroune R. BEN ZINE
- Ildikó CORA, Ph.D. (from November)
- Zsolt CZIGÁNY, D.Sc.
- Zsolt FOGARASSY, Ph.D.
- Mónika FURKÓ, Ph.D.
- Tamás KOLONITS
- Viktória KOVÁCSNÉ-KIS, Ph.D.
- Béla PÉCZ, corr. member of HAS., deputy general director of Centre for Energy Research, MFA director
- György Zoltán RADNÓCZI, Ph.D.
- Adél RÁCZ, Ph.D.
- György SÁFRÁN, C.Sc.
- Attila SULYOK, Ph.D.
- Dheeraj VARANASI, Ph.D.
- Péter B. BARNA, D.Sc., Prof. emeritus
- Miklós MENYHÁRD, D.Sc., Prof. emeritus
- György RADNÓCZI, D.Sc., Prof. emeritus
- János LÁBÁR, D.Sc, Prof. emeritus

Ph.D. students
- Dániel OLASZ
- Erzsébet DÓDONY
- Klára HAJAGOS-NAGY
- Nikolett HEGEDÜS
- Mohamed AFROIU (Hungaricum stipendium)
- Maroua H. KAOU (Hungaricum stipendium)

Technical Staff
- Andrea JAKAB-FENYVESINÉ
- Andor KOVÁCS
- Valéria OSVÁTH (maternity leave)
- Noémi SZÁSZ
- Viktor VARGA

The scientific results of the Thin Film Physics Department are related to thin film and ceramic fields. The main research topics are in line with modern trends of material science with the respect to a 50 years long history of the department.

The development of the 2D semiconductor, multicomponent thin films and technical ceramics were the important base research fields supported by several international basic scientific projects and collaborations in 2022. The uniqueness of the Department in national and international level as well was the structural investigation of various materials by transmission electron microscopy (TEM). The effect of the structure on the developed material´s properties was demonstrated by TEM. It was demonstrated that the optimal structure can be directed in a controlled way. All topics were supported by methodical developments based on electron diffractions. In 2022, 55 papers (11pc D1, 23pc Q1) appeared in refereed journals with a cumulative impact factor of 290. In addition, 24 papers were published with no impact factor conference proceedings. Members of the group presented 16 invited lectures, 50 oral talks and 19 posters at national and international conferences. The group received 3610 independent citations in the examined interval of the last two years.

Research members of the group lectured some courses at universities and held few laboratory practices. All courses were for full semester (Eötvös Lóránd University - ELTE, and Budapest University of Technology and Economics - BME, and University of Pannonia- UP and Óbuda University - OE). In addition, 6 PhD students were supervised. Social activity of the group is landmarked by 15 memberships in different committees of the Hungarian Academy of Sciences and in boards of international societies (European and American Ceramic Society, International Ceramic Society, International Union for Vacuum Science). In addition, Béla Pécz, D.Sc. was elected as a corresponding member of the Hungarian Academy of Sciences (MTA) and Csaba Balázsi, D.Sc. as a full member of the World Academy of Ceramics (WAC).

Structural investigation of wide bandgap semiconductors prepared by sputtering

M. Gajdics, B. Pécz

Recently wide bandgap (Eg > 4 eV) semiconductors, such as AlN and Ga_2O_3 have received considerable interest. These materials have a wide range of potential applications, i.e. electronic devices, such as diodes and transistors, optoelectronic devices, such as UV photodiodes and photodetectors, and gas detection systems. The aim of this research is the structural investigation of sputter deposited AlN and Ga_2O_3 thin films.

Gallium oxide films were deposited on sapphire substrates by radio frequency sputtering at room temperature (Fig. 3.1.). The applied pressure was $p = 2 \cdot 10^{-2}$ mbar and the DC potential was 1400 V. Sputtering was carried out using Ar, Ar^+O_2 and Ar^+H_2 gas mixtures, the gas flow for O_2 and H_2 was 1 sccm. The AlN films were prepared by HiPIMS (High-Power Impulse Magnetron Sputtering) using an average power of 200 W, frequency of 1 kHz and pulse width of 100 µs. The N_2 concentration was varied during deposition to create a microcombinatoric film with changing composition. The structure of the films was studied by X-ray diffraction and transmission electron microscopy. The composition and refractive index was determined by energy dispersive spectroscopy and spectroscopic ellipsometry, respectively. The as-deposited Ga_2O_3 films were found to have an amorphous structure and a slightly sub stoichiometric composition ($Ga_2O_{2.9}$ for Ar and Ar^+H_2, $Ga_2O_{2.95}$ for Ar^+O_2). In order to have a crystalline material, the samples were annealed at 900 °C for 1 hour in air, using 5 °C/min heating rate. As a result of the heat treatment, X-ray diffraction peaks of the crystalline β-Ga_2O_3 phase appeared on the diffractograms (Fig. 3.1.a). The reflections can be indexed as (-201) and its multiples, which indicates that the film has preferential texture.
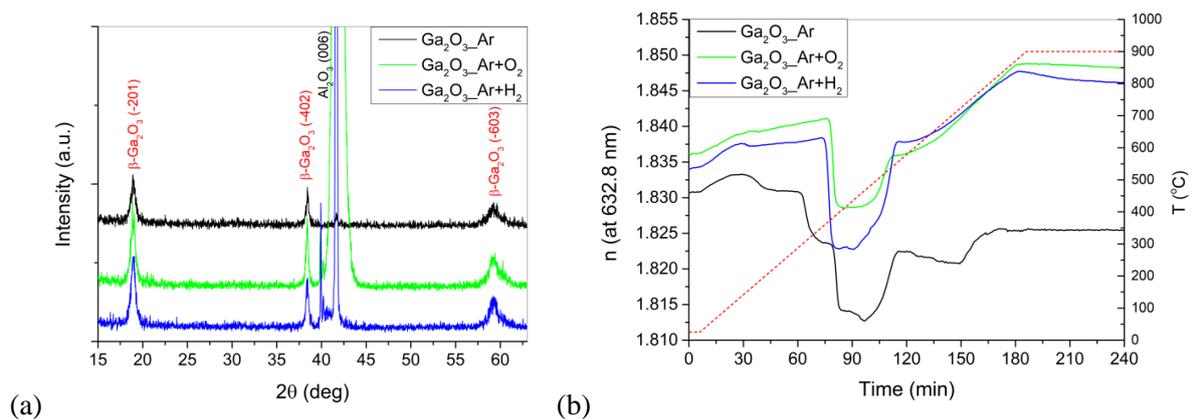
Figure 3.1. *(a) X-ray diffraction patterns of the annealed Ga_2O_3 films showing peaks of β Ga_2O_3. (b) Variation of the refractive indices (at 632.8 nm) during annealing determined by in-situ ellipsometry measurement*

The applied gas mixture apparently does not influence the crystallization of the material. After the annealing in air the films show the Ga_2O_3 stoichiometry. Variation of the refractive index was observed during the heat treatment (Fig. 3.1.b), which may be indicative to phase transformations. Temperature dependence of the refractive index is similar to all the studied samples, i.e. changes occur in the same temperature ranges. Composition of the gas mixture only has a minor effect on the value of the refractive

index. To further study the phase transitions additional annealing experiments and X-ray measurements are currently underway. EDS measurements of AlN thin films prepared using different N_2 flow rates show that samples with excess nitrogen cannot be manufactured under these conditions.

   Nevertheless, sub-stoichiometric films can be prepared and the N concentration has a significant effect on the structure of the sample. The stoichiometric film is made up of crystalline AlN phase, with the decrease of the N concentration the fraction of the crystalline phase decreases, and at some point a completely amorphous film forms. With further decrease of N concentration, crystalline Al appears in the sample (Fig. 3.2).
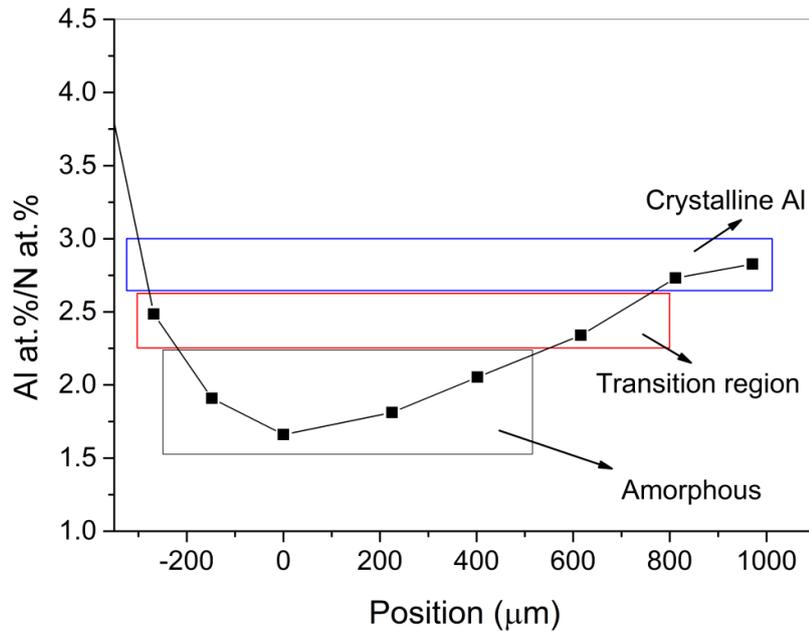
Figure 3.2*. Al/N atomic ratio as a function of position on a microcombinatoric AlN film. Different composition results in different crystal structures, the rectangles show the different composition regions with different structure.*

Role of TEM in the development of Qubits. SIQUOS: Superconducting Silicon Qubit in CMOS Technology

2019-2.1.7-ERA-NET-2022-00032

J. L. Lábár, B. Pécz, F. Chiodi (2C2N-Paris Saclay), F. Nemouchi (CEA-Grenoble), Z. Zhang (Uppsala University), S. Zhang (Uppsala University), F. Lefloch (CEA-Grenoble)

Qubits are the basic units of quantum computing and communication. Physical implementation of a qubit needs a system with *two energy levels* that can be manipulated separately. One of the several implementations is based on usage of superconductors. A superconducting qubit is an *artificial atom*, where the energy levels are assessed by the quantized resonance frequencies of an LC resonator. The qubit consists of a capacitively shunted inductor, where the inductance is provided by a *superconducting weak link (*Josephson junction: JJ, controlled by microwave signal). In an *anharmonic* oscillator the energy level spacings are different, so we can manipulate the *first two, independently* from the others. One variant of the superconducting qubits is a *Gatemon*, where energy levels are controlled by electrostatic potential of gate. Anharmonicity is introduced by the JJ.

The aim of SIQUOS is to realise and study a Si gatemon qubit, a gate tuneable transmon qubit composed of a Si Josephson field-effect transistor (JoFET) coupled to a microwave resonator. It represents a valid integrable and scalable alternative to fully metallic superconducting qubits.

SIQUOS focuses on the Si JoFET, i.e., a Si transistor with superconducting source and drain (S&D) contacts, whose non-dissipative supercurrent can be modulated by an electrostatic gate. CMOS-compatible metal silicides as well as heavily boron (B) doped Si will be used as the superconducting S&D contacts. A comprehensive investigation of the superconductor/Si (S/Sm) interface by means of structural, chemical and low-temperature electronic transport characterisation is being performed. The first and foremost objective of SIQUOS is to optimise the S/Sm interface transparency so as to allow for the transfer of correlated charge carriers from the superconducting contacts into the Si channel and to reach large, reproducible supercurrents. The second objective is to realise Si JoFETs, demonstrating the gate tuneability of the Josephson supercurrent. Thereupon, the third and final objective is to integrate Si JoFETs in a transmon geometry including on-chip capacitors and resonators, and to realise the manipulation of quantum states in Si-gatemon devices.

The heart of a CMOS Si gatemon is a Josephson field effect transistor (**JoFET**) that has superconducting source and drain (Fig. 3.3). The superconductor can be a metal-silicide (PtSi in the figure) or a highly boron-doped Si.
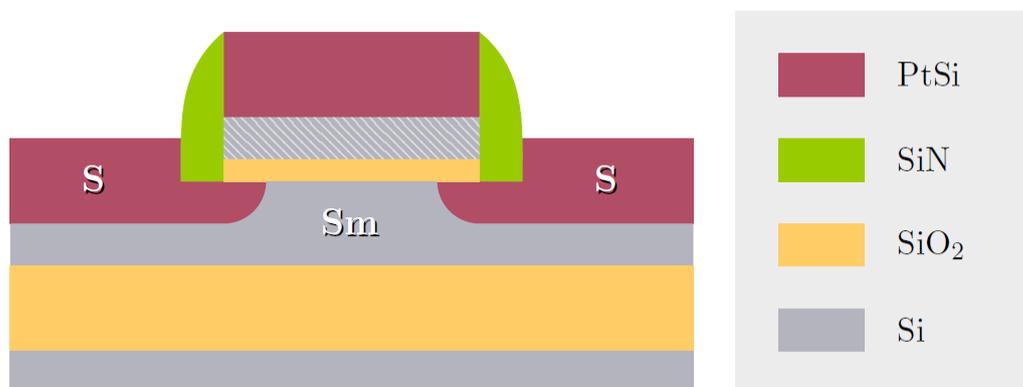
Figure 3.3. A Josephson field effect transistor (JoFET) that has superconducting source and drain.
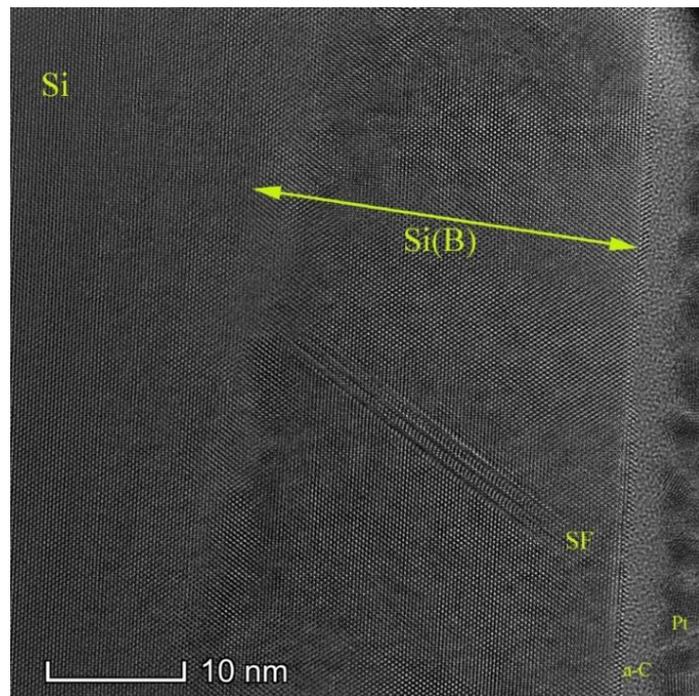
Figure 3.4*. HRTEM image of a supersaturated, Boron doped Silicon (Si:B) layer.*

Quality depends on exact sizes, on crystallographic phases and their orientation and on the crystallographic quality of the interface at the *atomic level*. Here comes *electron microscopy (TEM) for characterization*. Si(B) needs a boron concentration above the equilibrium level. It is reached by a special technique: gas immersion laser doping. There is a *need to check* the depth of doping, the flatness of the interface and the concentration of B in Si. Cross section samples were prepared by FIB for HRTEM. Concentration of substitutionally positioned B was determined from the strain measured from HRTEM images (Fig. 3.4).

A new method was also developed for the measurement of strain from 4D-ED. The first tests seem to be useful for determining connection between strained state (measured at room temperature) and superconductivity (measured at a few tens of mK temperature). Publication of the results is expected in 2023.

# Combinatorial mapping of microstructure and morphology in Cu-Mn films

K. Hajagos Nagy, F. Misják, Gy. Radnóczi

The scaling down of advanced semiconductor devices is a serious challenge for industrial technologies. Size reduction amplifies the effects of various diffusion related problems (e.g. electromigration) and some previously well-functioning solutions (e.g. TaN diffusion barriers) cannot be integrated in the new technologies. In interconnect design the use of self-organized processes has emerged as a solution, which involves the formation of a diffusion barrier from the interconnect material i.e. an alloyed Cu layer at the Cu/dielectric interface as a result of annealing or chemical reaction. The Cu-Mn alloy is a promising candidate for a number of diffusion barrier applications needed for Cu interconnects [Ref. 3.1].

Mapping the Cu-Mn thin film system may help in the search for optimal technological parameters. Previously, we found three one-phase regions in the system at room temperature: fcc Cu(Mn) solid solution, amorphous Cu-Mn alloy and α-Mn(Cu) solid solution. Between these intervals two phase regions exist, where an amorphous grain boundary layer covers the solid solution grains [Ref. 3.2]. For the successful application of Cu-Mn films the changes of microstructure and morphology within the phase regions has to be known in more detail. This can be effectively investigated using combinatorial samples, where one of the growth parameters changes continuously as a function of distance on the sample.

50 nm thick Cu-Mn combinatorial films were grown by DC magnetron sputtering on amorphous carbon foils using Sáfrán's micro-combinatorial method [Ref. 3.3]. The composition changed linearly between 0-100 at% Mn. The microstructure of the films was investigated in a Philips CM-20 transmission electron microscope by light and dark field imaging and selected area electron diffraction. The composition was verified by EDS measurement. Diffraction patterns were evaluated using the Process Diffraction program.

Combinatorial samples offer an effective way of investigating the effect of composition on microstructure and morphology. Fig. 3.5. shows the characteristic microstructure and morphology of the five phase regions in lateral bright field images and SAED patterns. The grain size of the fcc Cu(Mn) solid solution is bimodal, it decreases from 10-50 nm to 5-10 nm in the 0-35 at% Mn content interval. The α-Mn(Cu) solid solution has a more uniform grain size, it decreases from 10-20 nm to 5-10 nm from pure Mn to 70 at% Mn content. Calibrating the diffraction patterns by an internal standard (MnO) allowed us to determine the correlation between the composition and lattice parameter of the α-Mn(Cu) solid solution. The lattice parameter increases linearly with Cu content: $a_{\alpha-Mn(Cu)} = a_{Mn} + c_{Cu} \cdot 1,046$ (in Å), where $a_{Mn} = 8,912$ Å and c_{Cu} is the Cu concentration in at%. In the amorphous region, two types of short-range order are likely: fcc Cu(Mn) based below 50 at% Mn content and α-Mn(Cu) based over 50 at% Mn content.
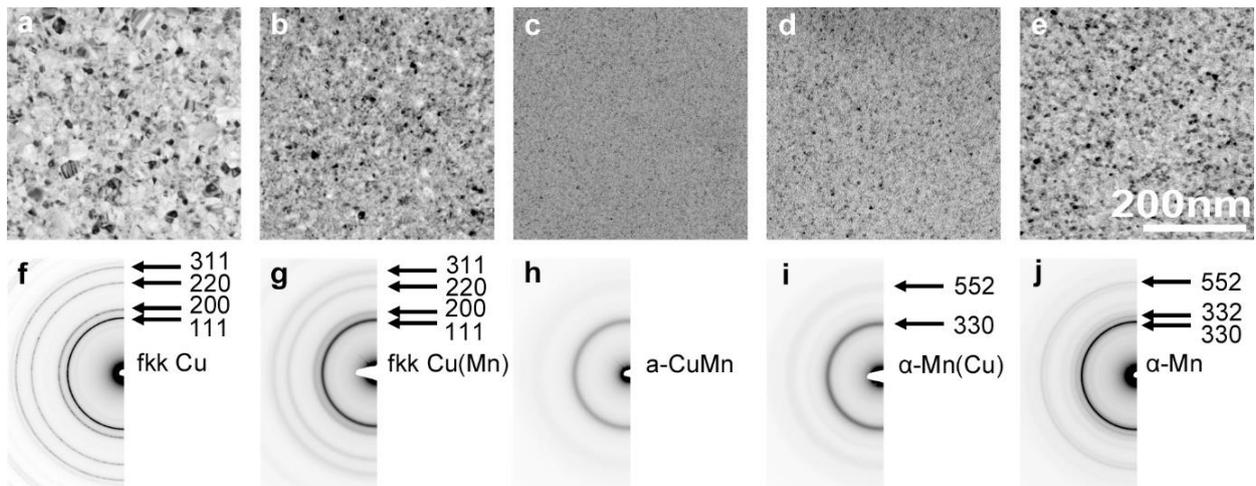
Figure 3.5. *Morphology and microstructure of Cu-Mn films in each phase interval in lateral bright field images (a-e) and SAED patterns (f-j). Pure Cu film (a,f), Cu-based two-phase film (30 at% Mn) (b,g), amorphous film (50 at% Mn) (c,h), Mn-based two-phase film (80 at%Mn) (d,i) and pure Mn film (e,j).*

Bactericidal and Virucidal Properties of ZrN-Cu Nanostructured Coatings Deposited by an Industrial PVD System

Zs. Czigány, K. Balázsi, S. Behrangi (Masaryk University), I. Sedláček (Masaryk University), J. Štěrba (University of South Bohemia), G. Suková (Masaryk University), V. Buršíková (Masaryk University), P. Souček (Masaryk University), V. Sochora (SHM, s.r.o.) and P. Vašina (Masaryk University)

Pathogenic microbes such as bacteria and viruses spread through contaminated surfaces. Most of these microorganisms are viable for a long time, so they spread from surfaces to the living organism and cause disease. ZrN-Cu nanocomposites with different Cu content were produced in a PVD device and their ability to kill bacteria and viruses (SARS-CoV-2) was investigated as a function of Cu content and exposure time. The layers were grown in an industrial equipment (SHM s.r.o. Šumperk, Czech Republic) using a hybrid process, combining electric arc evaporation (Zr) and magnetron sputtering (Cu) in a reactive medium. The Zr target is made of Zr702 alloy (99.2 wt% Zr; 4.5 wt% Hf; 0.8 wt% Fe, Cr, O, C).

The cylindrical copper target (99.95 wt%) was 96 mm in diameter and 445 mm long. We varied the power of the magnetron between 0.5 kW and 3 kW to control the Cu content. Additional growth parameters: N_2 pressure 1.5 Pa, substrate bias 50 V, heating current 150 A, substrate temperature 400°C, layer growth time 60 min. Below 6 at% copper content, only fcc ZrN phase is present, which suggests that copper is incorporated into the ZrN structure on the Zr sites. At higher copper content, however, copper forms a separate crystalline phase, which can be observed both in electron diffraction patterns and elemental maps (Fig. 3.6). Hardness and elastic constant decreased with increasing copper content. The copper content also affected the antibacterial properties. The antibacterial effect was excellent against Escherichia coli and Pseudomonas aeruginosa, especially in the case of 12 at%Cu content and treatment longer than 40 minutes. However, the antiviral effect of the coatings was not significant.

In conclusion, hard and wear-resistant ZrNCu coatings may be suitable for the development of antibacterial coatings that prevent the spread of pathogens on surfaces that people often touch. The optimal Cu content can be set between 12 and 25at%, taking into account the trade-off between antibacterial effect and mechanical properties [Ref. 3.4].
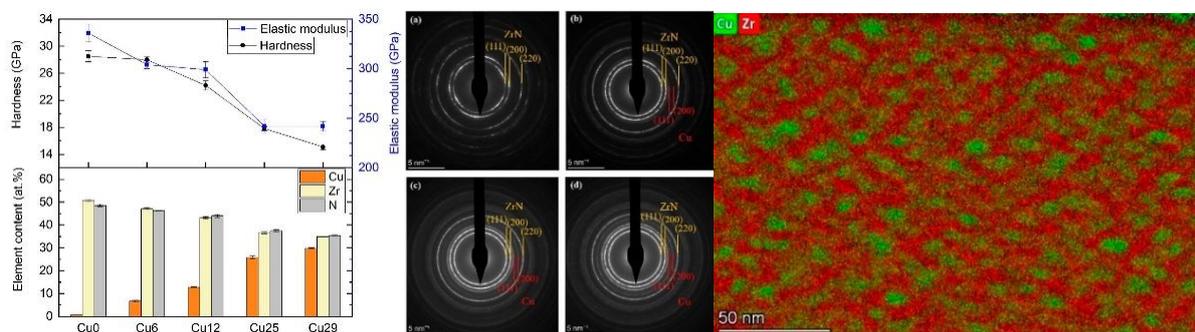

Figure 3.6. *Left panel: composition and mechanical properties of ZrN-Cu nanocomposites. Middle panel: SAED patterns of (a) Cu6; (b) Cu12; (c) Cu25; and (d) Cu29 samples. Right panel: Combined Zr and Cu elemental maps of ZrN-Cu29 film.*

Synthesis and characterization of the ceramic refractory metal high entropy nitride thin films from Cr-Hf-Mo-Ta-W system

Zs. Czigány, K. Balázsi, T. Stasiak (Masaryk University), P. Souček (Masaryk University), V. Buršíková (Masaryk University), N. Koutná (TU Wien), P. Vašina (Masaryk University)

High entropy alloys (HEA) and their nitrides were produced by reactive sputtering using Cr, segmented Mo-W and Hf-Ta targets. The purpose of the study is to determine the effect of the production parameters on the microstructure and mechanical properties of these innovative, multi-component layers. The layers were grown in pure and N_2-containing Ar gas at room temperature and at 750°C. The combined concentration of the metallic elements was stabilized with a saturation value below 50% as a function of the nitrogen injection, with a high nitrogen injection. In the case of the layers grown in argon, a single-phase body-centered cubic (bcc; a0 = 3.174 Å) structure was created (Fig. 3.7.).

An amorphous structure was obtained at a low nitrogen injection, while a NaCl-type face centred cubic nitride phase (fcc; a0 = 4.186–4.268 Å) was formed at a high N_2 injection (Fig. 3.7.). The lattice parameter of the fcc nitride phase increases with increasing nitrogen flow, in agreement with the values predicted by ab-initio calculations. The experimental lattice parameters of the RT samples lie between the values calculated for the composition $(CrHfMoTaW)N_{0.75}$ and $(CrHfMoTaW)N_{0.5}$, where the former composition is energetically more advantageous.
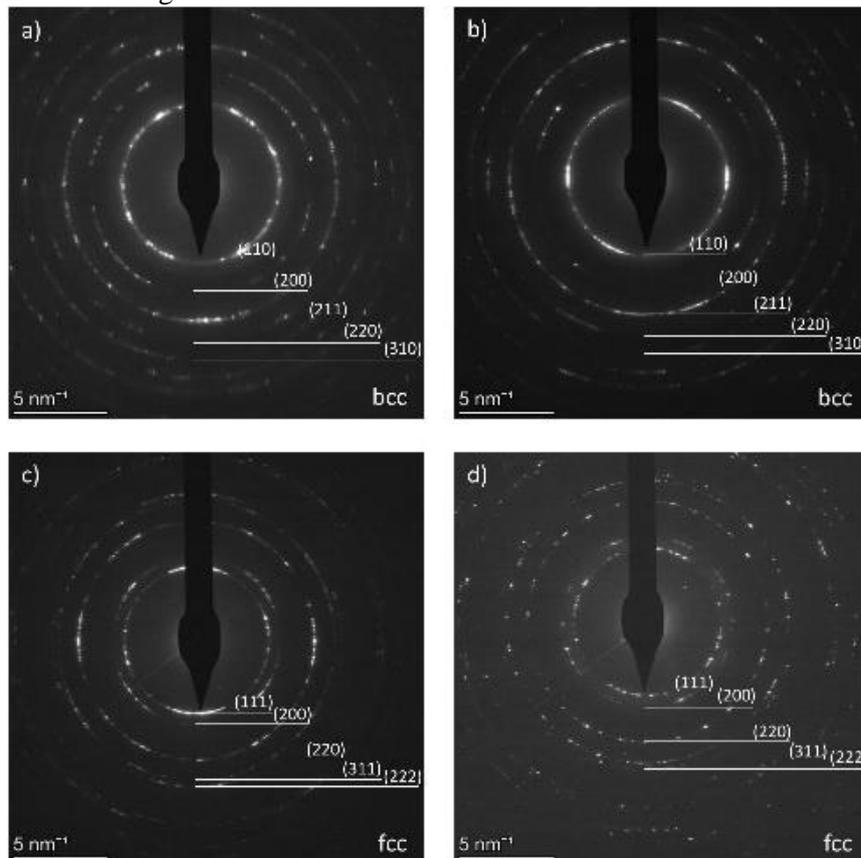
Figure 3.7. *SAED patterns of coating. (a) RT without nitrogen flow, (b) HT without nitrogen flow, (c) RT under 20 sccm nitrogen flow, (d) HT under 20 sccm nitrogen flow.*

The cross-sectional morphology of the amorphous sample was homogeneous, while the samples with the majority fcc nitride phase showed a characteristic columnar morphology (Fig. 3.8.). In addition, the elemental maps show a multilayered structure (due to rotation of the sample holder) and that the columns are separated by amorphous walls that are poor in molybdenum and nitrogen. The values of hardness and Young's modulus were 20.3 GPa and 471 GPa, respectively, for the fcc nitride coating. The experimental values of the Young's modulus showed a good agreement with the values of the Young's modulus in the [100] direction obtained by ab-initio calculations. The results of our research showed that coatings consisting of bcc and fcc phases with favourable mechanical properties (e.g. high Young's modulus) can be produced by magnetron sputtering.

Furthermore, the results contribute to the understanding of the effect of nitrogen flow on microstructural characteristics (such as crystallite size, vacancy formation, and lattice parameter change) [Ref. 3.5].
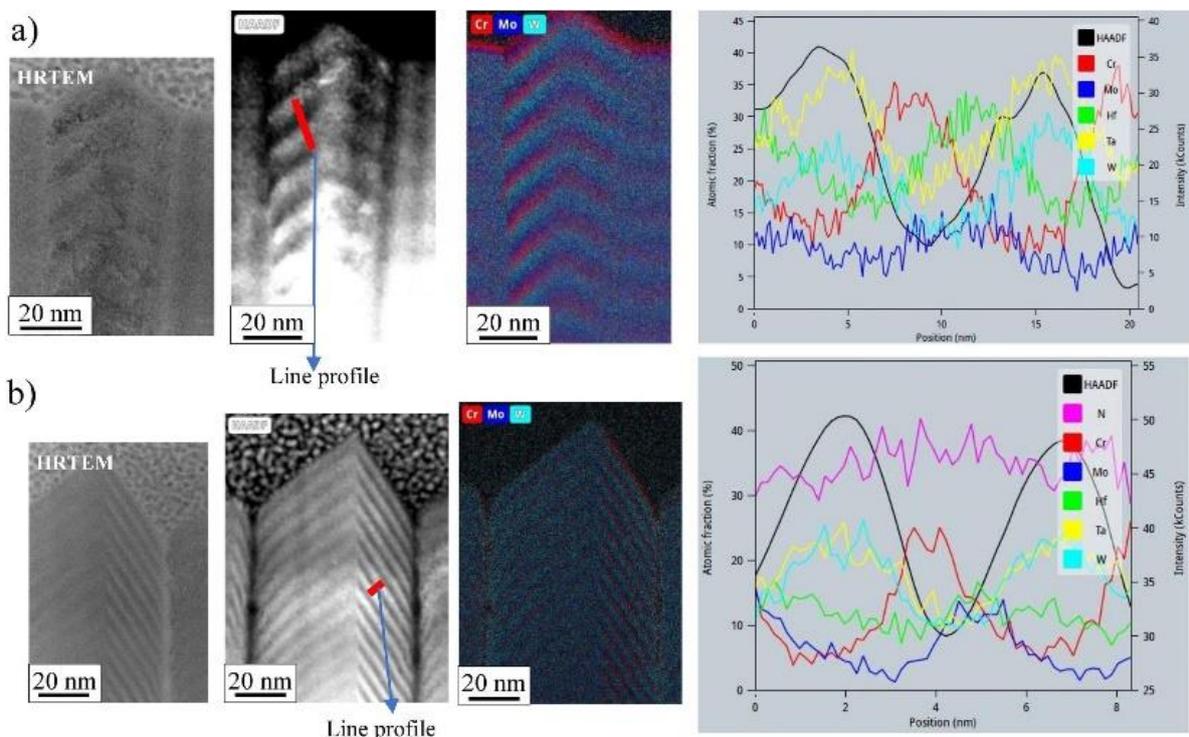
Figure 3.8. HRTEM and STEM HAADF images combined with EDX elemental map (Cr, Mo, W) and line profile of layer showing all elements. (a) metallic coating deposited at RT without nitrogen flow, (b) nitride coating deposited at HT under 20 sccm nitrogen flow.

The first promising experimental experience obtained on the Cr-Hf-Mo-Ta-W system confirm the possibility of the formation of multi-component metallic bcc and multi-component fcc nitride phases and represent a starting point for further optimization of the growth conditions and chemical composition in order to achieve excellent mechanical properties.

Probing the onset of wurtzite phase formation in (V,Al)N thin films by transmission electron microscopy and atom probe tomography

Zs. Czigány, M. Hans (RWTH Aachen), D. Neuß (RWTH Aachen), J. A. Sälker (RWTH Aachen), H. Rueß (RWTH Aachen), J. Krause (RWTH Aachen), G. K. Nayak (Montanuniversität Leoben), D. Holec (Montanuniversität Leoben), J. M. Schneider (RWTH Aachen)

The thermal decomposition mechanisms of single-phase, metastable cubic (V,Al)N thin films grown at 440 °C by high-power pulsed magnetron sputtering were systematically investigated by vacuum heat treatment at 600-900 °C after deposition [Ref. 3.6]. During growth, a columnar microstructure was formed in the layers. The beginning of the spinodal phase separation, during which cubic AlN separates into V- and Al-rich cubic nitride phases with the same structure, can be detected after heat treatment at 700 °C. Furthermore, both transmission electron microscopy and atom probe tomography measurements provide evidence for diffusion of aluminium to grain boundaries and triple junctions at this temperature.

According to ab initio calculations, the activation energy of volume diffusion of aluminium is 25% lower than that of vanadium, which explains the formation of Al-rich regions. It is reasonable to assume that these Al-rich regions are precursors for the formation of wurtzite AlN, which can be clearly identified after heat treatment at 800 °C by both microscopy (Fig. 3.9.) and tomography. The significantly larger equilibrium volume of wurtzite AlN compared to the cubic AlN phase explains that the formation of the wurtzite phase is limited exclusively to the triple junctions and grain boundaries. In contrast, twin boundaries are rich in vanadium.

Interestingly, the formation of the wurtzite phase at grain boundaries and triple junctions can be detected by resistivity measurements, while X-ray diffraction and nanoindentation are less sensitive to the formation of the minority phase. Thus, the latter methods clearly confirm its formation only after heat treatment at temperatures above 900 °C. Therefore, it is evident that previously reported formation temperatures for wurtzite AlN in transition metal aluminium nitrides, determined by non-nanometer-scale chemical and structural methods, are overestimates.
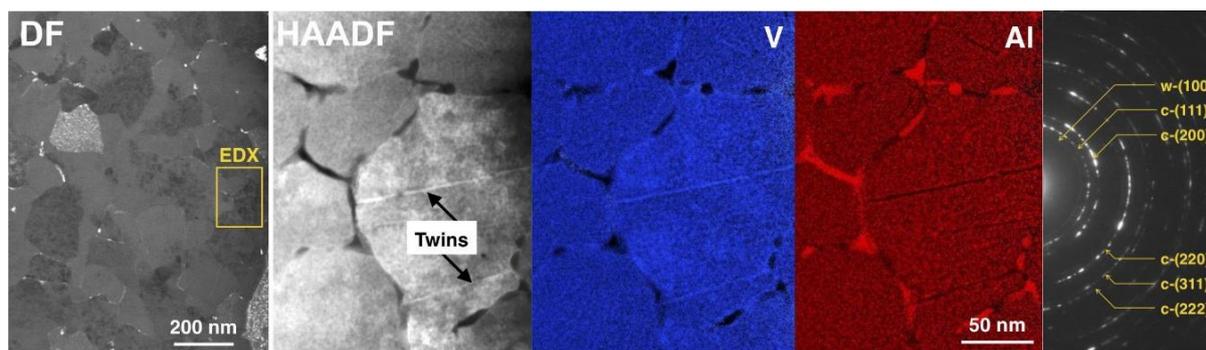
Figure 3.9. *Plan-view DF image of VAlN film annealed at 800°C, taken with the wurtzite (100) reflections. HAADF and STEM-EDX elemental maps (Al and V) of the region of interest indicated in the DF. Elemental maps indicate Al diffusion into grain boundaries and triple junctions. In contrast, twin boundaries are rich in vanadium. The electron diffraction pattern (right) proves formation of wurtzite phase that is located at grain boundaries and triple junctions in DF.*

Investigation of lithium niobate nanocrystals synthesized on different routes

T. Kolonits, L. Kocsor (Wigner, ELTE), G. Dravecz (Wigner), L. Péter (Wigner)

Within the framework of a collaboration between the Thin Film Physics Department, the Wigner Research Centre for Physics and the Eötvös University (ELTE), the synthesis of lithium niobate nanocrystals was investigated. Lithium niobate is an excellent optical material with outstanding electro- and acousto-optical, nonlinear optical, and photorefractive properties. Since its first single crystal growth realized more than 50 years ago, also a progress has been made in the production of nanopowders in the last decades. In the present study two synthetisation routes were investigated: solvothermal synthesis (a bottom-up method) and wet condition ground milling (a top-down one).

The solvothermal synthesis using different organic media is an easy and effective way for producing nanoparticles at relatively low temperature. The organic medium, acting as stabilizer can control the growth of the particles and prevent their agglomeration. In our study [Ref. 3.7] four polyol media were used: ethylene glycol, diethylene glycol, triethylene glycol and glycerol. The reaction was performed through the following process:

$$Nb_2O_5 + 2LiOH \rightarrow 2LiNbO_3 + H_2O \qquad (1)$$

Our results [Ref. 3.7] suggest that the reaction goes through two consecutive steps. First, LiOH reacts with Nb_2O_5 on the surface of the nanoparticles, forming the Li-rich Li_3NbO_4 phase:

$$Nb_2O_5 + 6LiOH \rightarrow 2Li_3NbO_4 + 3H_2O \qquad (2)$$

Then, the secons step is that the Li_2O already incorporated to the peripheral Li_3NbO_4 phase penetrates further into the Nb_2O_5 particle and forms lithium niobate:

$$Li_3NbO_4 + Nb_2O_5 \rightarrow 3LiNbO_3 \qquad (3)$$
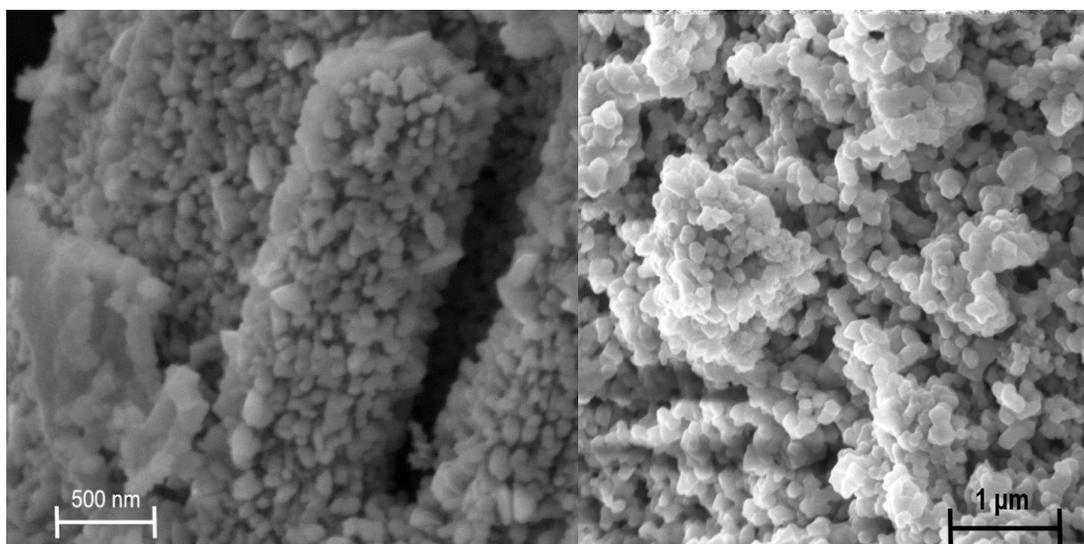
Figure 3.10. *End product of the solvothermal reaction. Left without- and right with pre-milling of Nb_2O_5.*

Nb_2O_5 was pretreated by milling the raw material down to 300-500 nm in particle diameter using a planetary mill. Without this treatment, the product retained the original columnar structure of Nb_2O_5 and the LN formation could only be completed on its surface as it can be seen on Fig. 3.10. The effects of the polyol media, the reaction time and the Li excess were investigated. As a conclusion, the best yield and the most homogeneous lithium niobate phase could be prepared by using diethylene glycol medium with a Li/Nb ratio of 1.5 and a 72-hour reaction time.

Planetary milling as a top-down method was also investigated. During this study [Ref. 3.8] congruent lithium niobate prepared by sintering was grounded under wet conditions in a planetary mill in order to produce nanocrystals. The aim was to prove that this method is more efficient than using a shaker mill. The particle size was monitored by SEM and dynamic light scattering with a good correspondence.
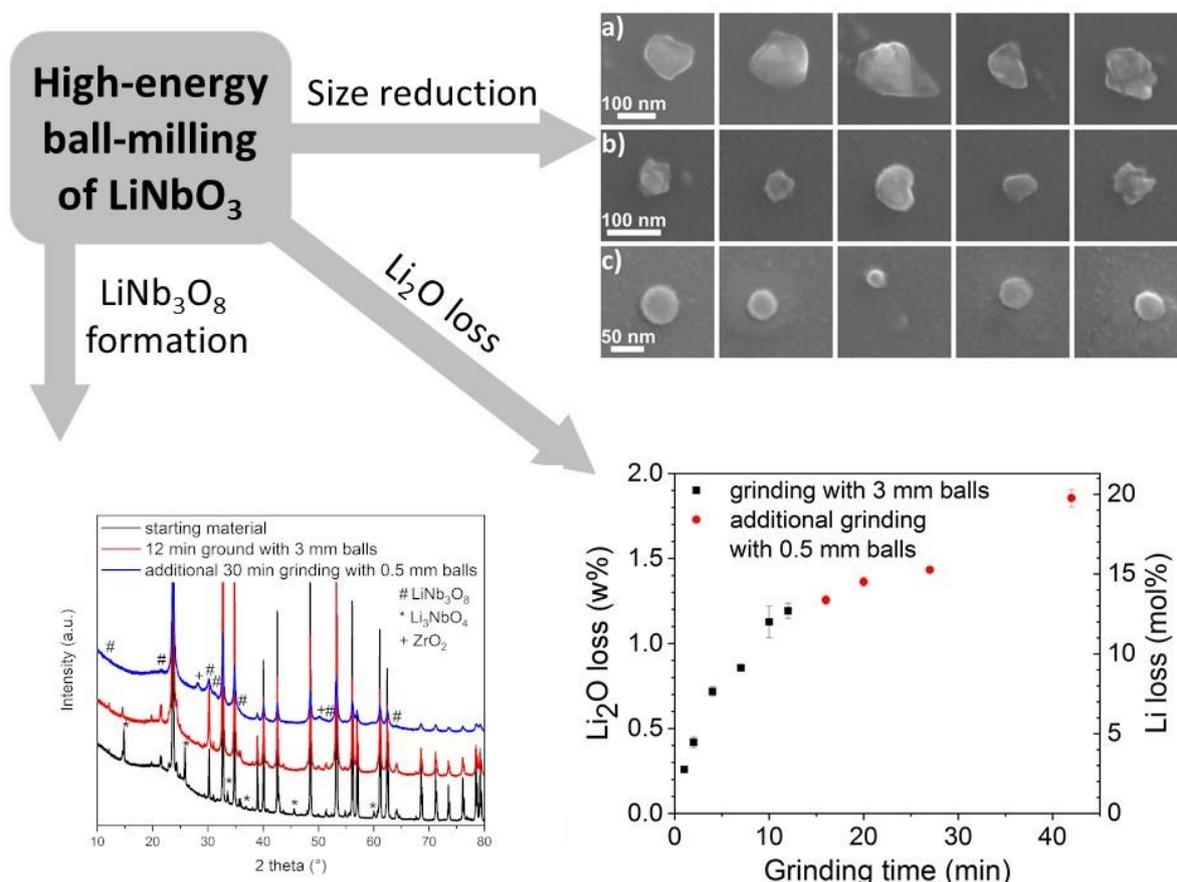
Figure 3.11. *The morphology of the ball-milled LiNbO₃ nanoparticles, the X-Ray diffraction phase analysis and the calculated LiO₂ loss*

It was shown, that already the first phase of ball-milling in the planetary mill by using balls of 3 mm diameter resulted in particles with 100 nm < D <150 nm after 12 min effective milling time, as opposed to the shaker mill where the minium diameter was several hundred nanometer after several hours. X-Ray diffraction has shown, that the final size of the crystals could be reduced to about 12–15 nm. Hence, it is obvious that the particles seen in the SEM images (Fig. 3.11) are composed of several crystallites.

As a correlation with the particle size reduction, X-ray diffractometry revealed the formation of a lithium-deficient $LiNb_3O_8$ phase (Fig. 3.11) as a Li_2O loss during the milling process. The presence of $LiNb_3O_8$ was confirmed by means of Raman spectroscopy. The amount of Li_2O loss was also determined by titration in a good agreement with the other methods. Correlation was revealed between the composition change of the nanopowder and the total surface area of the particle assembly calculated from dynamic light scattering measurements (Fig. 3.11).

Design and corrosion resistance of tungsten carbide-rich coating layers

A. S. Rácz, Zs. Fogarassy, Zs. Kerner, M. Menyhard

Tungsten carbide is known for its superior hardness and good chemical resistance. In this work tungsten-carbide-rich coating layers have been produced by irradiating C/W multilayer of various structures (with individual layer thicknesses from 10 to 20 nm) by argon and xenon ions. The range of energies and fluences varied between 40-110 keV, and 0.07 - 6x10^{16} ions/cm^2, respectively. The component in-depth distributions have been determined by Auger-electron spectroscopy (AES) depth profiling.
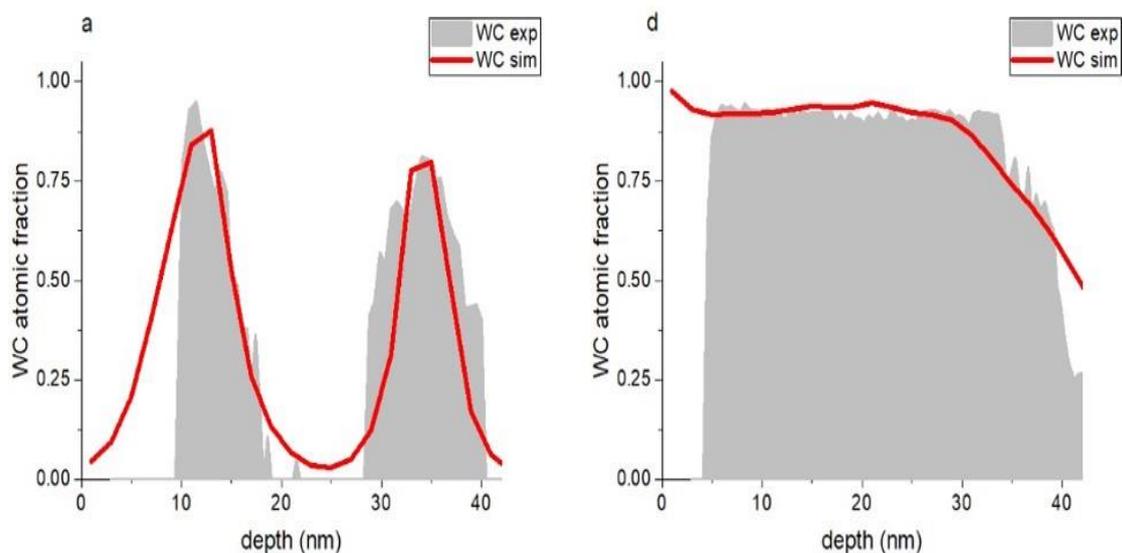
Figure 3.12. *Comparison of measured WC distribution with that of calculated for sample of C 10nm / W 24.5 nm / C 9.1 nm // Si substrate, irradiated by 120 keV Xe$^+$ applying various fluences.*

It has been shown that the growth of the WC-rich layer started at the interfaces and with increasing fluence the separately growing layers coalesced. For predicting the WC in -depth distributions TRIDYN simulation has been applied. This simulation is based on the description of binary collisons and describes the ballistic mixing, which is usual for systems having low average atomic number (<20). We show that adapting parametrizations the simulations were able to estimate the in-depth distribution of the elements after ion irradiation.

The amount of carbide has been calculated applying a simple model. The agreement between the experimental and simulated depth profiles has been tested for a rich dataset differing in layer structures, projectiles, ion fluences and energies. An example is shown in Fig. 3.12. The good agreement enables the design of the WC-rich layers and also enables the significant decrease of the experimental work [Ref. 3.9].
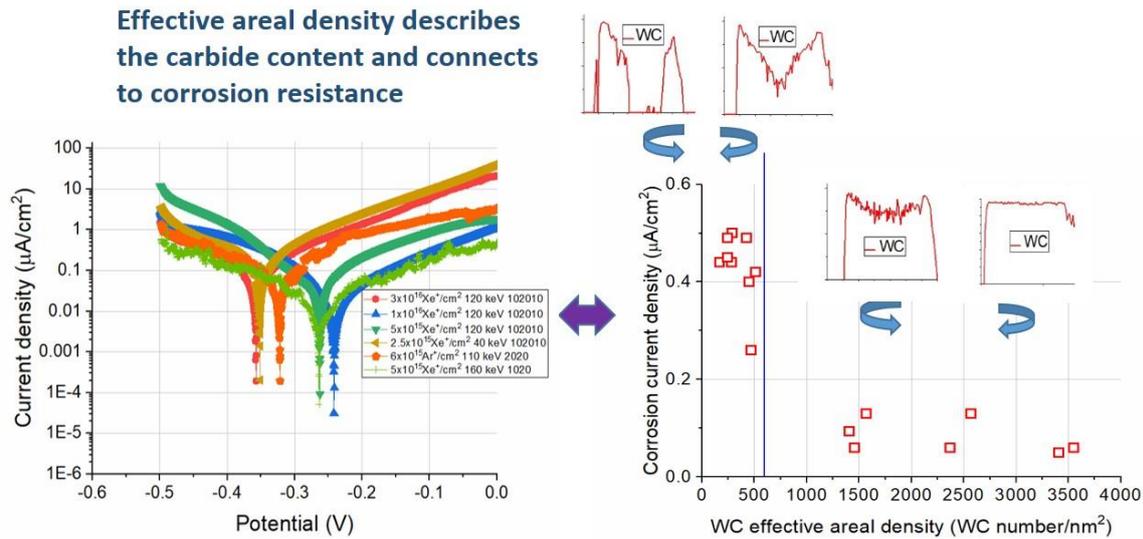
Figure 3.13. *The measured Tafel curves in 3.5 wt% NaCl solution and the connection between the WC effective areal densities and corrosion current densities.*

The corrosion resistance of the samples has been tested by potentiodynamic corrosion test in 3.5 wt% NaCl solution. The test has shown that the irradiated samples had better corrosion resistive properties than that of a WC cermet. For quantifying the protectivity of the systems the term WC effective areal density has been introduced which can be calculated from the carbide in-depth distributions.

If the effective areal density was in the range of 0–550 WC (number /nm2) the corrosion current density was 0.5 (μA/cm2) $\pm$ 35%, while if the effective areal density was higher than 1200 WC (number/nm2) the corrosion current density was 0.08 (μA/cm2) $\pm$ 36% (Fig. 3.13).

As the effective areal density values can be calculated also from the TRIDYN simulations the fast and cheap design of these corrosion protective layers is possible.

A combinatorial study of the RF sputtering process and the properties of silicon-oxynitride thin film system under variable reactive gas injection

OTKA K143216, KDP 2021 Cooperative Doctoral Programme

N. Hegedüs, Cs. Balázsi, T. Kolonits, D. Olasz, Gy. Sáfrán, M. Serényi, K. Balázsi

Pure silicon dioxide (SiO2) and silicon nitride (SiN) have long been used in electronics technology and are produced by a number of proven technologies such as RF sputtering. In its complex form, amorphous silicon oxynitride (SiON) is a chemically very stable material with a refractive index of between 1.45 and 2.05, depending on the oxygen and nitrogen content. This wide range of refractive index is very useful in optoelectronic applications. The application of SiON technology is limited because the composition of the composite layer and thus its refractive index is particularly sensitive to small changes in sputtering parameters, especially the oxygen content of the plasma gas [Ref. 3.11].

Our aim is to efficiently investigate the sputtering process itself and the properties of the Si-O-N thin film system over the whole compositional range. To achieve this, we have developed and applied a combinatorial layer growth method with variable reactive gas-injection [Ref. 3.3, 3.12]. Instead of producing and testing a large number of individual samples with different compositions, we have therefore chosen a more efficient combinatorial solution. In a single 25 mm long sample, an amorphous silicon-oxynitride layer of variable properties was grown by reactive RF sputtering, that included the complete transition from oxide to nitride. Two different target voltages (1.62kV and 1.95kV) were used to sputter layers of different thicknesses. The variation of optical properties and layer thickness was investigated by spectroscopic ellipsometry (SE) measurements, while the elemental composition was studied by energy dispersive spectrometry (EDS).
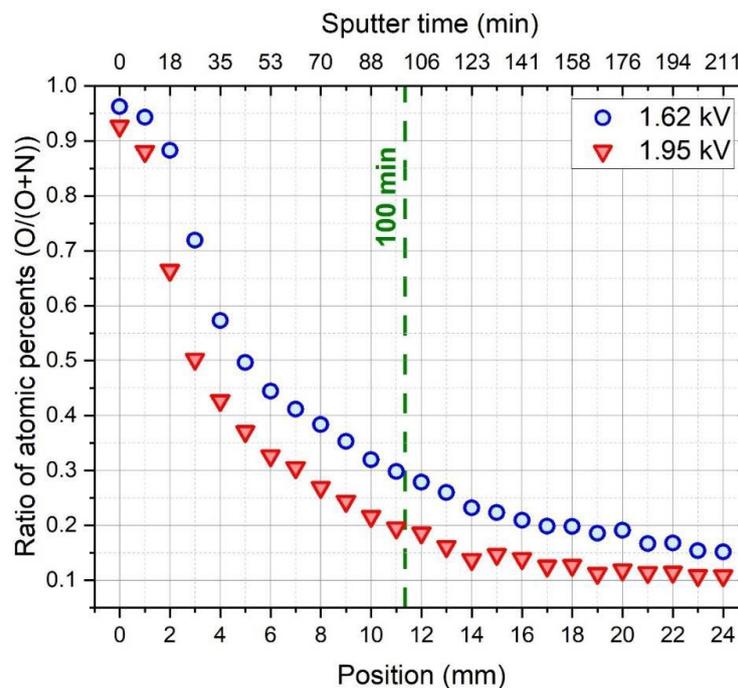
Figure 3.14. *Atomic concentrations (O/O+N) measured by EDS in Si-O-N samples of varying composition sputtered at 1.62 and 1.95 kV as a function of distance along the sample.*

Fig. 3.14. clearly shows a remarkable effect of partial pressures of O and N reactive gases on the layer composition. O/O+N decreases with the oxygen depletion in the reactive gas mixture and as well with the DC voltage as measured along the sample.
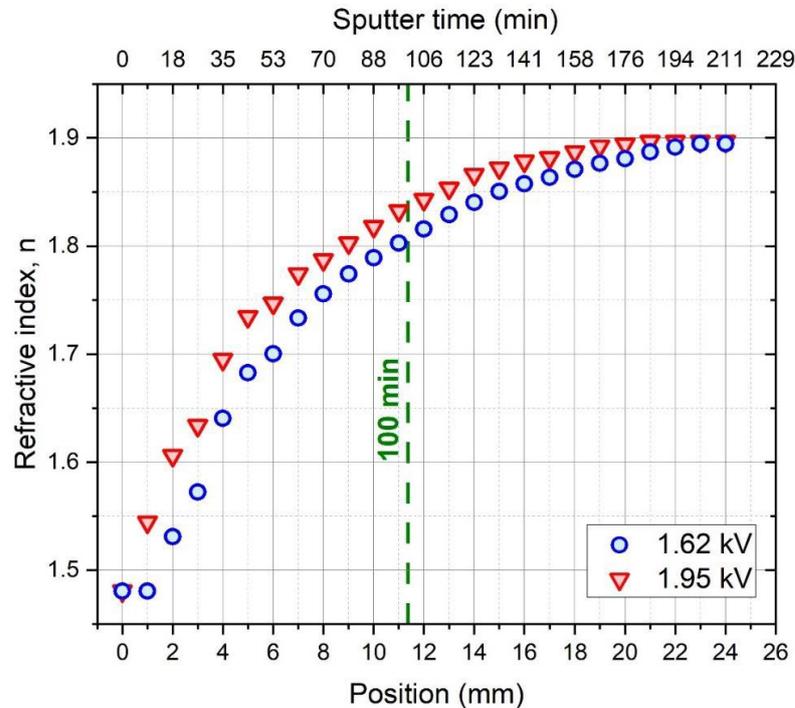
Figure 3.15. *Refractive index (n) variation of samples sputtered at 1.62 and 1.95 kV of varying O/O+N composition measured along the substrate by spectroscopic ellipsometry.*

In Fig. 3.15, we have shown that the refractive index (n) of the layer can be tuned in the range 1.48-1.89 by varying the partial pressure of oxygen injected into the chamber, in accordance with the compositional variation. It is clear that the refractive index increases as the O content decreases, indicating an SiOx–SiOxNy–SiNx transition in the composition-spread samples. From the data on the composition of the layer, the typical physical parameters of the process were determined using the Berg model [Ref. 3.13, Ref. 3.14] developed for reactive sputtering. A new approach was introduced in the modelling - a metallic Si target sputtered with a uniform nitrogen and variable oxygen gas flow was considered as an oxygen gas sputtered SiN target [Ref. 3.15]. According to the calculations detailed in the publication, the sputtering gas temperature can increase by up to 40 °C during the growth of the oxygen-rich layer due to the exothermic nature of the oxidation.

Our variable gas-induced combinatorial layer growth method and the correlations found between sputtering parameters, layer composition and refractive index, in agreement with the model developed, allow us to produce silicon-oxynitride layers with exactly the designed optical properties. This experimental technique, moreover, allows the growth of thin films with gradient refractive indexes required for some specific applications.

Indentation size effect in exceptionally hard AlCu thin films

D. Olasz, Gy. Sáfrán, N. Szász, G. Huhn (ELTE), N. Q. Chinh (ELTE)

We investigated the correlations between the structure and mechanical properties of the AlCu thin film system by efficient combinatorial methods: in a single experiment, 15 adjacent bands of 12x1 mm², ~1.7 um thick samples of varying composition representing the whole concentration range (Al_xCu_{1-x}, $0 \leq x \leq 1$) were deposited on a 25x12 mm² Si substrate using dual DC magnetron sputtering. Composition-dependent mechanical properties of the samples, such as hardness and deformation mechanisms, have been determined by nanoindentation, and composition, structure and morphology by microscopic methods (SEM, TEM) [Ref. 3.16].
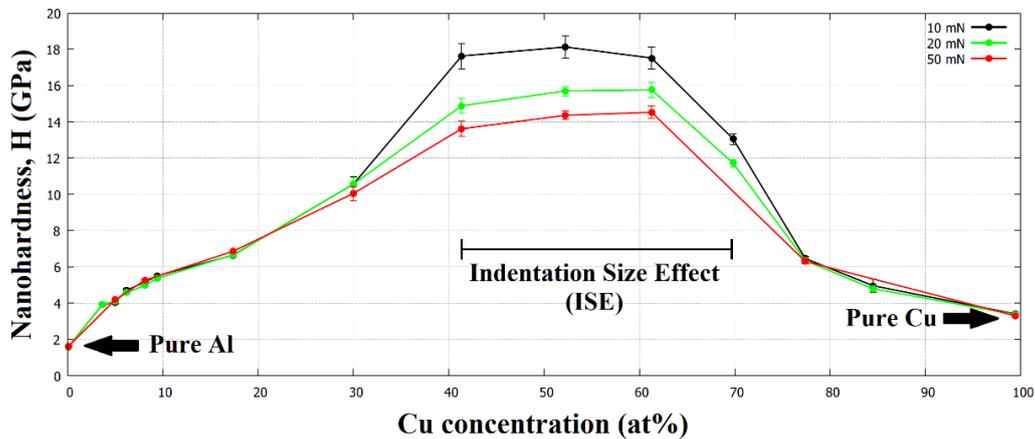
Figure 3.16. *Hardness of AlCu alloy thin films as a function of composition, measured at three maximum indentation forces (10, 20 and 50 mN).*

Fig. 3.16. shows the hardness (H) of the layers as a function of copper concentration. It is observed that the hardness of pure Al layer is 1.6 GPa, which is significantly higher than the hardness of bulk Al (~0.3 GPa). Even in the presence of a low alloying concentration of 3.7 at% Cu, the strength of the layer increases significantly to 3.9 GPa. The maximum strength value of ~16 GPa, which is 10 times harder than the pure Al thin film, is reached in the concentration range of ~40-60 at% Cu. This extraordinary strength is not only twice that of the hardest AlCu thin film reported in the literature, H=8 GPa [Ref. 3.17], but also comparable to that of the hard coating materials used in industry. Fig. 3.16. shows that at the edges of the diagram, at low alloy concentrations, different indenation forces - 10, 20, 50 mN - result in practically identical H values, while in the medium ~40-70 at% Cu concentration range, lower indentation forces are associated with higher H values. This phenomenon is the Indentation Size Effect (ISE), which is well-known for pure bulk Al and Cu materials. In contrast, our measurements showed the absence of ISE in the pure- and low alloying concentration materials.

The absence of ISE at low alloying concentrations can be explained by the microstructure. In our present films, even the pure Al and Cu layers are characterized by very fine grain size (~ 100 nm), which brings to the fore another deformation mechanism, grain boundary sliding. AFM and SEM measurements revealed

the formation of pile-ups around the indentation marks (Fig. 3.17.), what also confirms the enhanced activity of the grain boundary sliding.
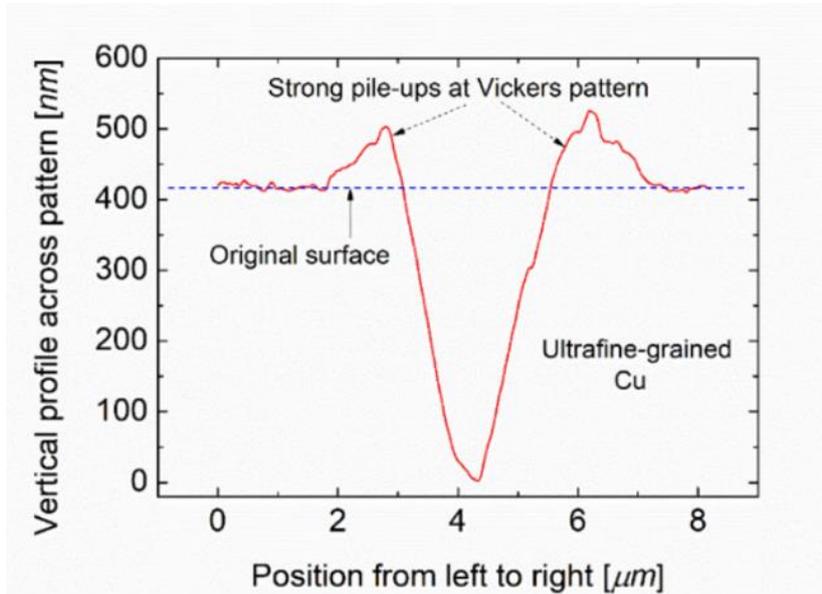
Figure 3.17. *For a pure Cu layer, the vertical profile of the indentation trace determined by AFM. The "pile-up" phenomenon is clearly visible at the edge of the trace.*

On the other hand, in the ~40-70 at% Cu range, the nanoindentation load-displacement (P-h) curves (Fig. 3.18.a) at a maximum indentation force of 50 mN clearly show a step-like behaviour, indicating a non-continuous deformation.
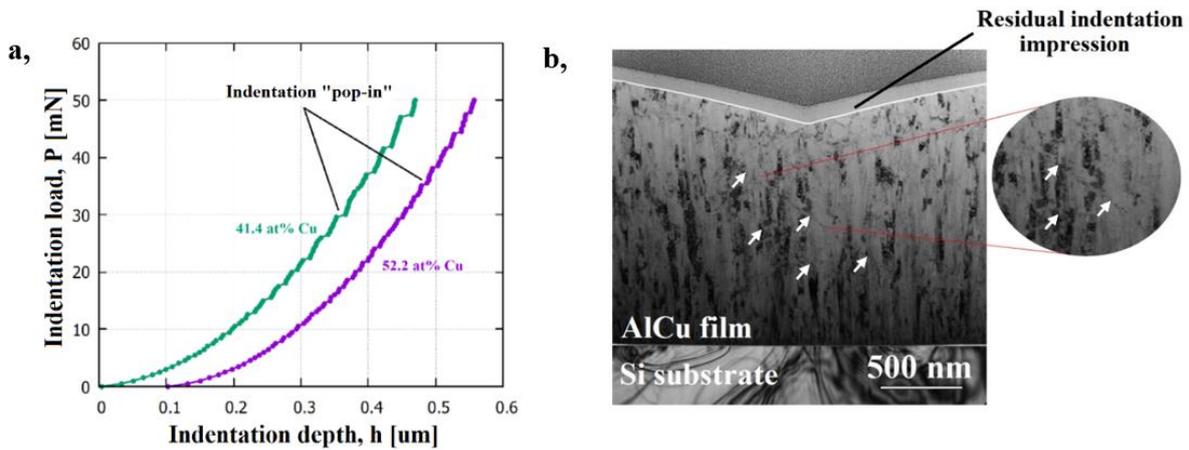
Figure 3.18*: (a) "Step-like" indentation curves showing a "pop-in" phenomenon at a maximum indentation force of 50 mN. (b) Cross-sectional TEM image of an indented layer containing 52.2 at% Cu. Arrows indicate the two deformation bands around the indentation.*

The cross-sectional TEM image in figure Fig.3.18.b shows the layer with 52.2 at% Cu exhibiting a fine columnar morphology. Arrows mark deformation bands found under the indentation, running at an angle of about 45°. The measured step-like indentation behaviour ("pop-in") can be explained by the formation and propagation of these shear bands. [Ref. 3.16, Ref. 3.17]

Structure determination using corrected diffraction intensities: Extension of the Ewald correction method

E. Dódony, B. Rudd, I. Dódony (NanoLab) and Gy. Sáfrán

Today, with the development of nanotechnology, it is increasingly important to understand the materials of modern devices at the atomic level. Transmission electron microscopy (TEM) is one of the most important tools for this. The structure of the sample is determined by a combined analysis of high-resolution (HRTEM) images and electron diffraction (ED) patterns obtained by TEM. The HRTEM images and ED patterns require a preliminary correction for deviations from the projected charge density and the structure factor (F_{hkl}^2) squared as determined by scattering theory. The deviation between the high-resolution images and the projected-charge-density is due to the signal transfer characteristics of the electron microscope. The detected intensities differ from the ideal F_{hkl}^2 proportional values if, due to experimental conditions, the Ewald sphere is deflected from the detector plane. To determine a crystal structure, it is necessary to know the square of the structure factors (F_{hkl}^2), so the diffracted intensities $I_{exp_{hkl}}$. In the ED pattern, the intensity of the reflections differs from this as a function of the distance between the Ewald sphere at the given reflections and the reciprocal plane. Cowley described the equation in 1992 [Ref. 3.18] for the effect of the Ewald sphere on the diffraction intensities:

$$I_{exp_{hkl}} = I_{hkl} * E_{w_{hkl}}$$

$$E_{w_{hkl}} = \frac{\sin\frac{\pi\lambda t}{2d_{hkl}^2}}{\frac{\pi\lambda t}{2d_{hkl}^2}}$$

,where $I_{exp_{hkl}}$ is the experimentally measured intensity of the reflection at the Miller index hkl, $I_{hkl} = F_{hkl}^2$ and $E_{w_{hkl}}$ is the Ewald sphere effect on the intensity I_{hkl} at a given value of d_{hkl} as a function of λ wavelength and sample thickness t.

Thus, the intensities measured in the experimental image can be corrected by the reciprocal of $E_{w_{hkl}}$ to obtain the theoretical F_{hkl}^2 values ($I_{hkl} = \frac{I_{exp_{hkl}}}{E_{w_{hkl}}}$).

While several computer programs (e.g. CRISP) are available for the correction of HRTEM images, no such program has been developed for the Ewald correction of diffraction patterns. When correcting diffraction patterns in some cases up to a few hundred reflections have to be corrected separately, which is a very time consuming task. To ease this task, a computer program has been developed that performs the correction for the whole diffraction image, given the wavelength λ, the microscope constant K, the center of the Laue zone, the position of the direct beam, and the d-value of the reflection in the zero-order Laue zone furthest from the direct beam. By extending Cowley's theory [Ref. 3.18, Ref. 3.19], we provide a solution for the case when the center of the Laue zone is not on the optical axis. The method also works for cases that are a few degrees off the zone axis (~0.8° in cases ~5° depending on the structure). It is of great advantage, for example, when working with radiation-sensitive material and there is no time for precise orientation of the crystal. Fig. 3.19.a and 3.19.b illustrate the oriented and the missaligned cases.
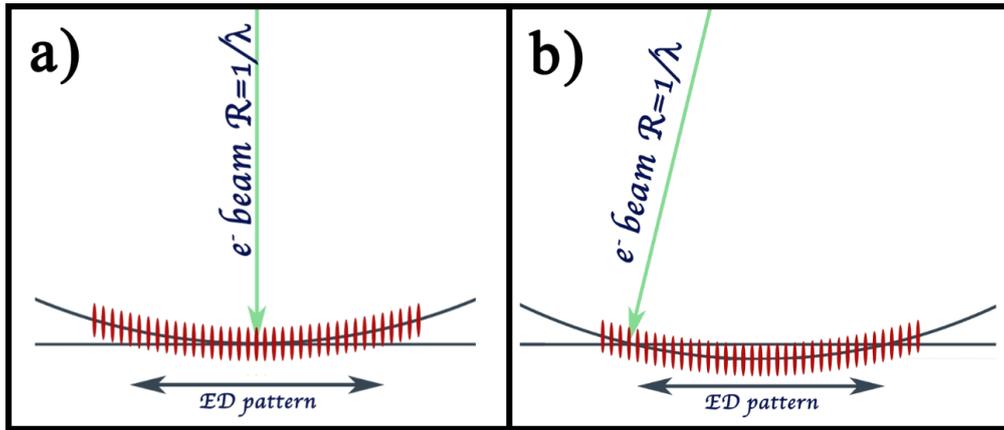
Figure 3.19. *(a) In the oriented case the detector plain is tangent with the Ewald sphere, the center of the Laue-zone coincides with the location of the direct beam. Correction is done by applying $\frac{1}{E_{w_{hkl}}}$ on the diffracted intensities. (b) In the slightly misaligned case the detector plain intersects the Ewald sphere, the center of the Laue zone (at the lowest point of the sphere) doesn't coincides with the location of the direct beam.*

For the correction we have to use a different function from $\frac{1}{E_{w_{hkl}}} \rightarrow \frac{1}{E_{w,tilt_{hkl}}}$

The $\frac{1}{E_{w_{hkl}}}$ correction function was extended to the slightly misaligned case through a simple idea. When searching for the new $\frac{1}{E_{w,tilt_{hkl}}}$ function we had an idea, that the same correction is applicable at a given reciprocal space in the misaligned case as in the aligned, where the distance between sphere and plane are the same. So we related every reciprocal lattice point $d^*_{hkl,tilt}$ in the misaligned case to the d^*_{hkl} in the aligned case where the distance between the Ewald sphere and the detector plane are the same and used the correction calculated with d^*_{hkl} for the aligned case at the place $d^*_{hkl,tilt}$. The correctness of the new procedure was verified on diffraction images that are deviated from the zone axis.
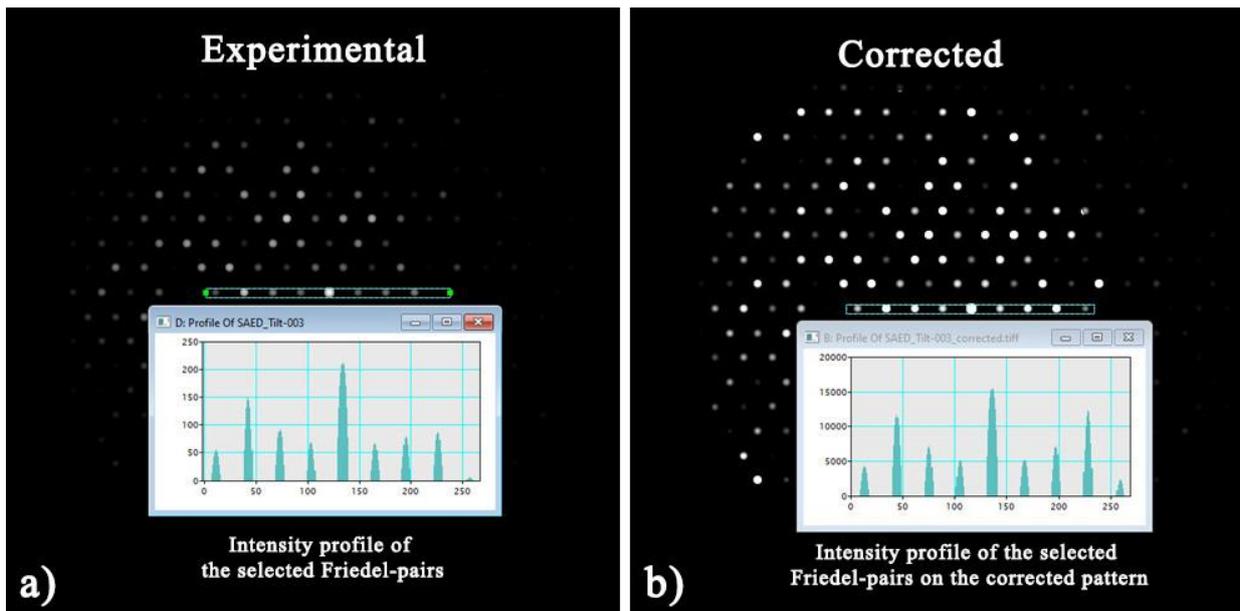
Figure 3.20. *(a) The intensity ratios of the Friedel pairs in the experimental diffraction pattern are different from 1 (misaligned orientation), (b) the intensities of the Friedel pairs in the software corrected pattern are nearly identical. As a result, the Ewald correction can be extended to the misaligned cases.*

We examined the intensity ratios of the Friedel pairs before and after correction. In the well-oriented case, the Friedel pairs have the same intensity, so if the ratio of Friedel pairs approaches 1 by applying the new correction function, we know that the correlation is correct. This check was performed for different orientations of apatite, of which the case tilted out of the [001] zone axis is shown in Fig. 3.20. It clearly shows that after the correction the ratio of the Friedel pair intensities is close to one, while before the correction it was far from one. (This was true for all the orientations tested.) So we can conclude that the extended procedure works.

With the computer program we have developed, it is possible to perform a fast Ewald correction of the experimental electron diffraction petterns, thus ensuring that the I_{hkl} theoretical intensity dataset needed to determine unknown structures is easily accessible. The program can also be applied to cases with small deviations from the zone axis (~0.8° in cases up to ~5°). This is an advantage when working with beam-sensitive materials or in post-processing if the sample is not perfectly oriented but you want to use the I_{hkl} intensity set of the SAED pattern.

Microstructure Investigation of Nanocrystalline Materials Using Electron Diffraction Based Rietveld Analysis – Approximation of Instrumental Broadening

V. Kovács Kis, Zs. Czigány, Zs. Kovács (ELTE)

Rietveld analysis [Ref. 3.20] is commonly used for the evaluation of XRD and neutron powder diffraction patterns providing quantitative data on phase composition, crystal structure and microstructure parameters, such as crystallite size, anisotropic shape, preferred orientation, microstrain. However, this full pattern fitting method is less used for electron powder diffraction (EPD) patterns, mostly because the contribution of dynamical scattering of electrons to the detected intensity distribution hampers direct interpretation of diffraction pattern. Another difficulty is concerning the large variability of electron optics, which requires standardized measurements to control e.g. instrumental broadening in electron diffraction. So far, the number of papers presenting results based on Rietveld analysis of EDP does not exceed 25, however, this method has a great potential in nanoparticle and thin film analysis, as yields quantitative and statistically representative information on nanostructured materials. Indeed, to achieve accuracy and reproducibility of EPD similar to that of the other diffraction methods, and to obtain as small instrumental broadening of diffraction peaks as possible, strict control on lens currents of the electron microscope is needed [Ref. 3.21].
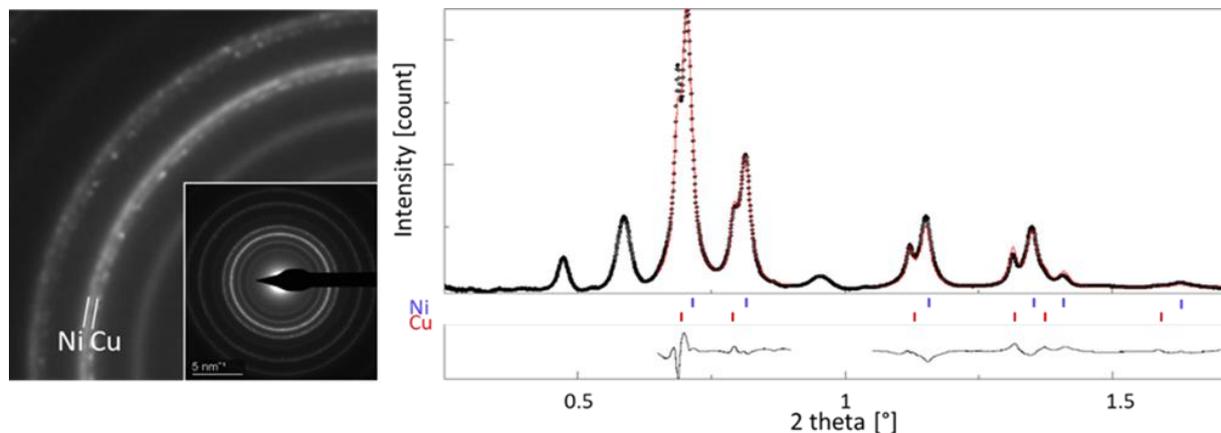
Figure 3.21. *SAED of a Cu-Ni thin film deposited at 150 °C using DC magnetron sputtering (left) and corresponding integrated intensity profile (right). Black dots are measurement data and red line is fitted curve. Bragg positions of Cu and Ni, and difference curve of the fitted regions are also plotted.*

To measure and reproduce the instrumental broadening parameters for EPD Rietveld analysis, a three-step procedure was proposed [Ref. 3.22], which comprises subsequent XRD and EPD measurements of two different calibration samples. We propose a novel, single step in-TEM (transmission electron microscope) procedure, which allows to obtain the instrumental broadening function of the TEM directly from a single measurement, without the need of an additional X-ray diffraction measurement. Using graphene calibration standard and applying properly controlled acquisition conditions on a spherical aberration corrected microscope, we achieved an instrumental broadening of ± 0.01 Å in terms of interplanar spacing. The shape of the diffraction peaks is modelled as function of scattering angle using the Caglioti relation [Ref. 3.23],

and the obtained parameters for instrumental broadening can be directly applied in Rietveld analysis of electron diffraction data of the analysed specimen. During peak shape analysis, instrumental broadening parameters of the TEM are controlled separately from nanostructure related peak broadening effects, which contributes to a higher reliability of nanostructure information extracted from electron diffraction patterns. The potential of the proposed procedure is demonstrated through the Rietveld analysis of hematite nanopowder and two-component Cu-Ni nanocrystalline thin film specimens (Fig. 3.21).

Biphasic iron uptake from nano-haematite particles by roots

V. Kovács Kis , Z. Klencsár, Á. Keresztes (ELTE), F. Pankaczi (ELTE), F. Fodor(ELTE), Á. Solti (ELTE)

Nanoscale Fe containing particles can penetrate the root apoplast. Nevertheless, cell wall size exclusion questions that for Fe mobilisation, a close contact between the membrane integrating FERRIC REDUCTASE OXIDASE (FRO) enzymes and Fe containing particles is required. Haematite nanoparticle suspension, size of 10–20 nm, characterized by 57Fe Mossbauer spectroscopy, TEM, ICP and SAED was subjected to Fe utilisation by the flavin secreting model plant cucumber (*Cucumis sativus*). Alterations in the structure and distribution of the particles were revealed by 57Fe.
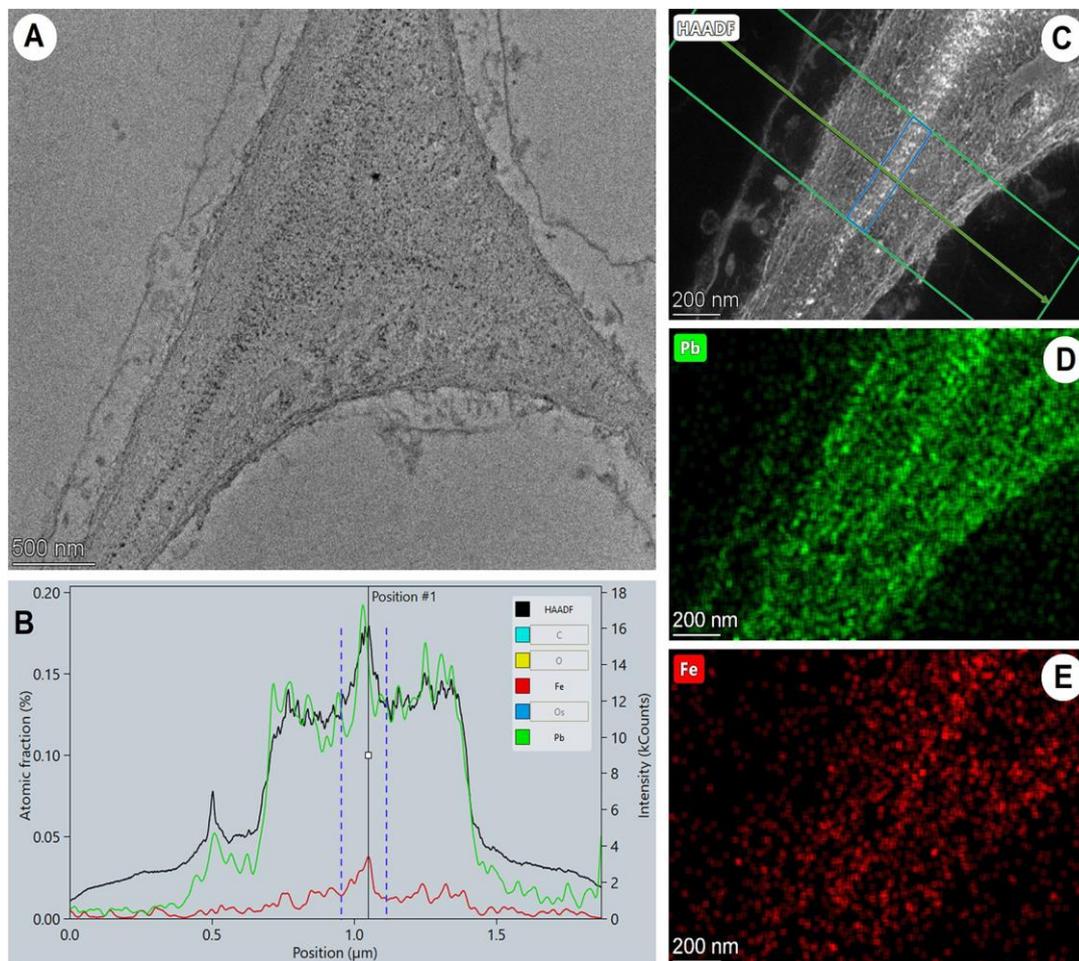
Figure 3.22. *Transmission electron micrograph of a three-cell junction (A) and high-angle annular dark-field (HAADF) image (B) of the root tip meristem cells of NH treated plants. Energy dispersive X-ray spectroscopy (EDS) line profile analysis (B) performed by merging data applying a 300 pixel integration width perpendicular to the line indicated on (C). Elemental distribution maps of Pb as for contrasting material (D) and Fe (E) was created based on the Pb Lα1 and Fe Kα peaks (10.55 and 6.40 keV, respectively). Area of the line profile between dashed lines on (B) is the region marked by blue box on (C), which coincides with the middle lamella in the two-cell junction. In this area large number of high atomic number particles (bright spots) are seen, and, according to EDS line profile analysis, besides the contrasting material Pb, is characterized by elevated concentration of Fe.*

TEM analysis revealed aggregates of electron dense particles in the middle lamellae between adjacent cell walls in the nanohaematite (NH) treated sample (Fig. 3.22.a-c) with elevated iron content (Fig. 3.22). EDS elemental mapping (Fig. 3.22.b, Fig. 3.22.d-e) revealed that abundance of both Fe and Pb (this latter originated from the contrasting material) was higher in the middle lamella between the adjacent cell walls across the root tip. In contrast to NH treated samples, accumulation of Fe was not observed in the control samples.
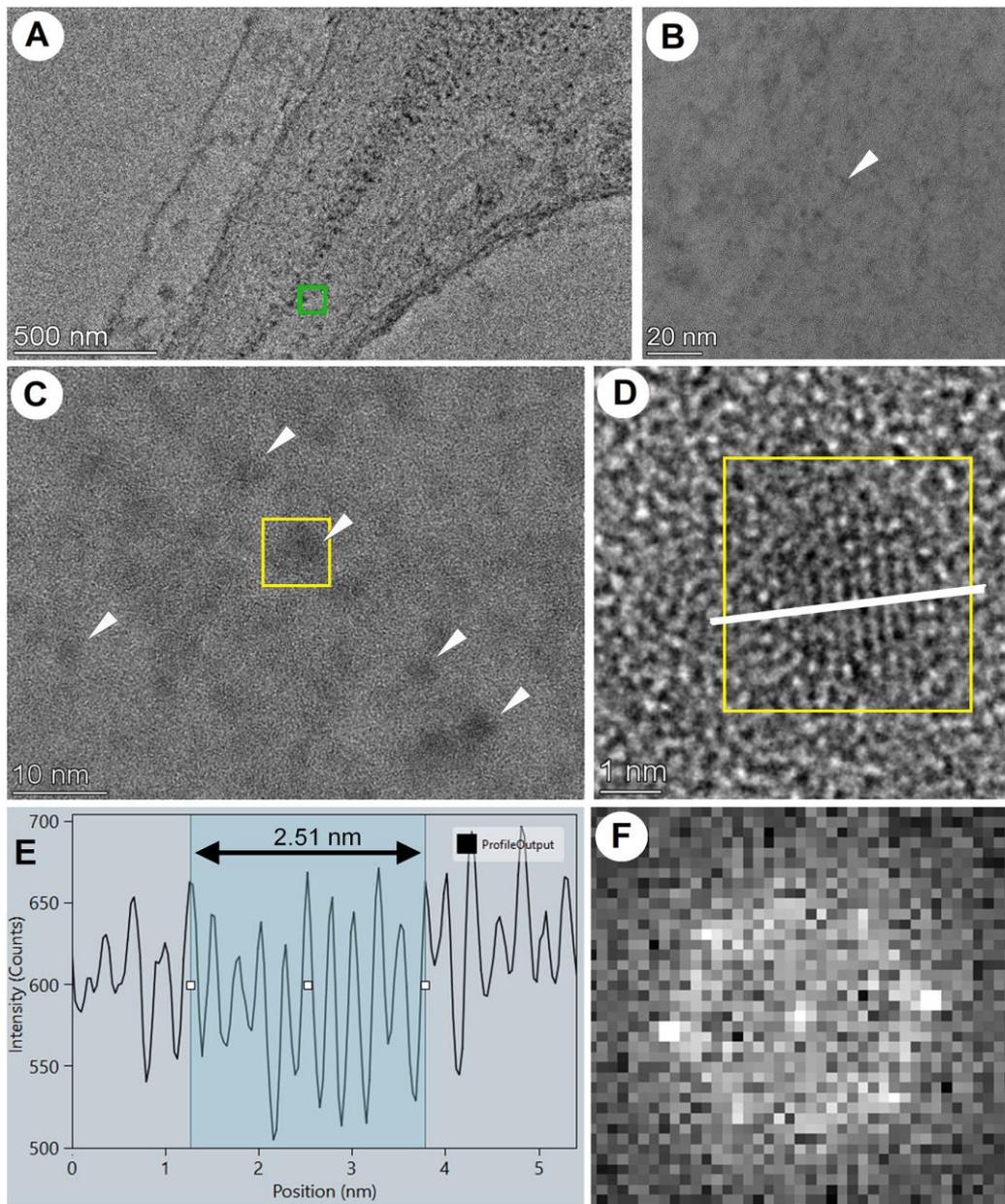
Figure 3.23. *High-resolution transmission electron micrographs (HRTEM; A–C) of the root tip meristem cells of NH treated plants. Subdivision B is a high-resolution site indicated by a green square on subdivision A (sample is identical to 3A). Bar on (A) equal to 500 nm. Electron dense particles, pointed by arrowheads, accumulated in the middle lamella of the cell wall at two-cell junctions. HRTEM indicate the presence of several separate electron dense particles (C). Atomic resolution image of an individual particle proves crystalline structure (D), the measured periodicity is 2.51 nm, typical to haematite d(110) interplanar spacing (E). Fourier transform support unambiguously haematite nanoparticle in [001] zone axis orientation (F).*

HRTEM analysis of NH treated roots indicates accumulation of particles at the interfaces of the middle lamella and the adjacent walls (Fig. 3.23.a-c), which corresponds to the linearly arranged high average atomic number particles observed on the HAADF images (Fig 3.23.c). Based on the interplanar spacing values measured on the Fourier transforms, these nanoparticles were identified as haematite (Fig. 3.23.d-f). Size analysis of the particles indicated a diameter of 1.96 ± 0.28 nm for the particles, where no particles were detected above the diameter of 2.85 nm.

Biological utilisation of Fe resulted in a suppression of Fe deficiency responses (expression of *CsFRO 1, 2 & 3* and *RIBOFLAVIN A1*; *CsRIBA1* genes and root ferric chelate reductase activity). Haematite nanoparticles were stacked in the middle lamella of the apoplast. Fe mobilisation is evidenced by the reduction in the particle size. Fe release from nanoparticles does not require a contact with the plasma membrane. Parallel suppression in the *CsFRO 1&3* and *CsRIBA1* transcript amounts support that flavin biosynthesis is an inclusive Fe deficiency response involved in the reduction-based Fe utilisation of *Cucumis sativus* roots. CsFRO2 is suggested to play a role in the intracellular Fe homeostasis [Ref. 3.24].

Bioresorbable and biocompatible biomineralized carbonated amorphous calcium phosphate loaded biopolymer composites

OTKA PD131934

M. Furko

The aim of this research work is to develop biomineralized bioceramic/biopolymer composite coatings onto implant materials. Amorphous or nanocrystalline calcium phosphates (ACPs) and their combination with biopolymers are innovative types of resorbable coatings for load bearing implants that can promote the integration of metallic implants into human bodies. In addition, they are advantageous form of the various calcium phosphate phases since they have faster dissolution rate than that of crystalline hydroxyapatite. Owing to the biomineral additions (Mg, Zn, Sr) in optimized concentrations, the base CP particles became more similar to the mineral phase in human bones (dCP). We investigated the effect of bioactive mineral addition on the morphology and chemical characteristic of the powder, as well as we prepared cACP-PCL composite thin layers to implant surfaces and studied their biodegradability characteristic by corrosion measurements.

Fig. 3.24. shows the difference in morphology of cACP powder and the biomineralized cACP powder. The biomineralization caused a slight decrease in the particle size and the particles tended to agglomerate into larger blocks, while in the cACP, disordered, mainly needle-like microstructure formed.
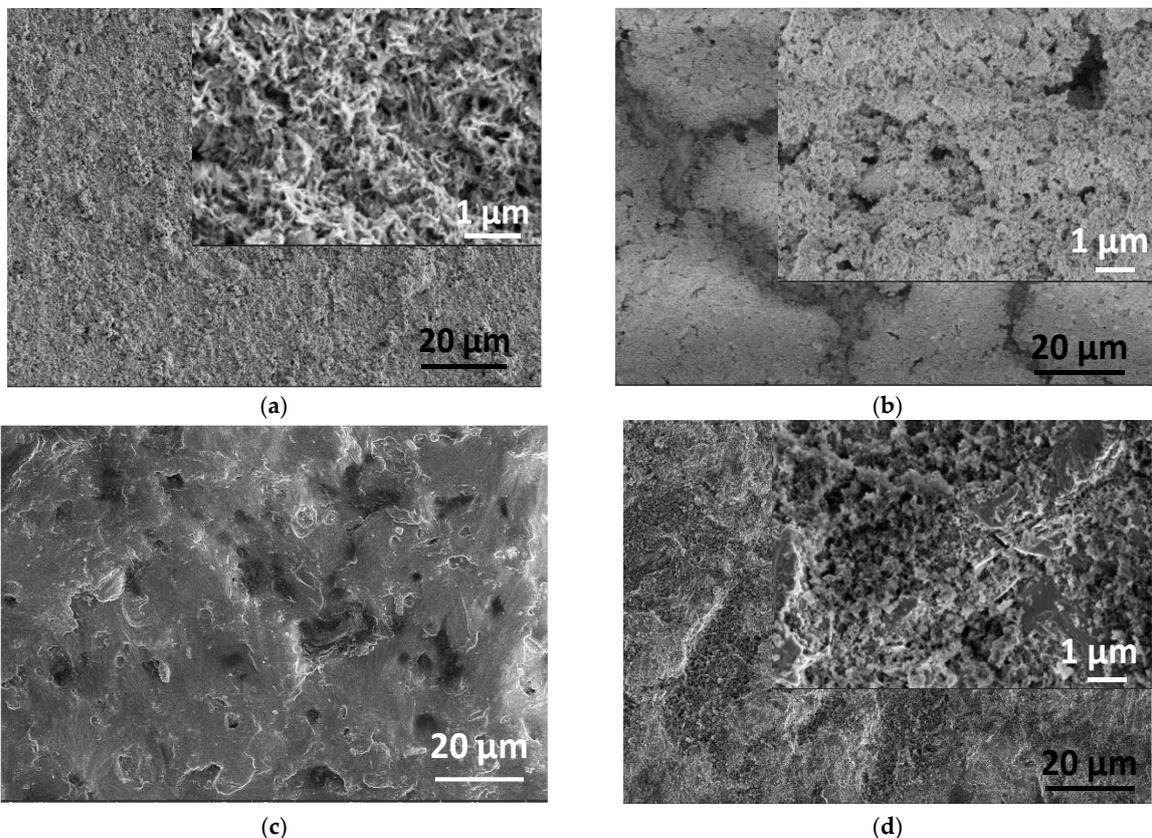
Figure 3.24. *SEM images of calcium phosphate cACP powder coating (a) biomineralized cACP powder coating (b) PCL thin layer (c) biomineralized cACP-PCL thin layer (d)*

The SEM image of PCL coating (Fig. 3.24.c) reveals that the layer is very thin and contains numerous holes through which the substrate surface emerges. The surface of polymer layer is smooth and the polymer particles has glass-like amorphous feature. Incorporating the cACP particles into PCL matrix increased the adherence of the coating since it acts as a natural bioadhesive on the surface. The microstructure of cACP added PCL thin film noticeably differ from the powder coatings. It contains larger agglomerates and blocks along with smaller particles such causing rougher surface with larger surface area that is advantageous to the bone cell attachment. The biodegradable properties of different thin layers were evaluated by potentiodynamic polarization curves.

As it is visible in Fig. 3.25, the shape and characteristic of the curves is quite similar in all cases and did not change noticeably over time. The difference appears in the values of corrosion currents and corrosion potentials of different samples which corresponds to their corrosion rates.
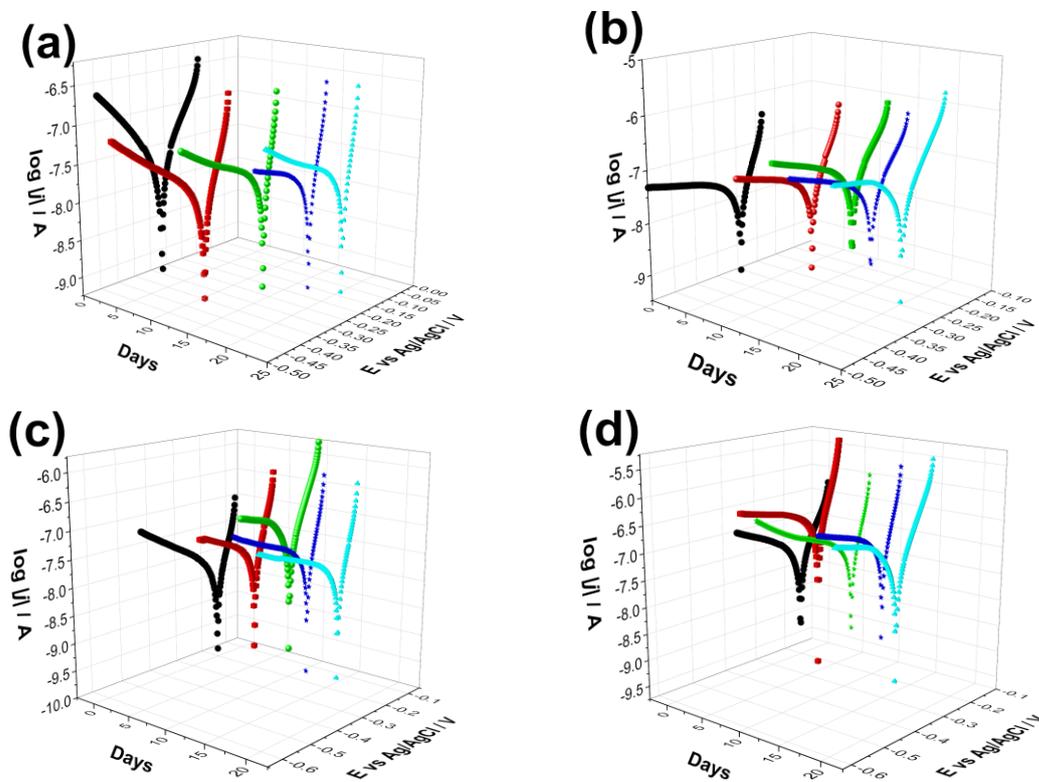
Figure 3.25. *Potentiodynamic polarization curves recorded on uncoated Ti6Al4V alloy (a) on CP thin coating (b) on dCP thin coating (c) as well as on dCP-PCL composite thin layer. The measurements were repeated several times over a two-week period in PBS solution in ambient condition. The potential scanning rate is 1 mV s⁻¹ in each case.*

(a)   (b)
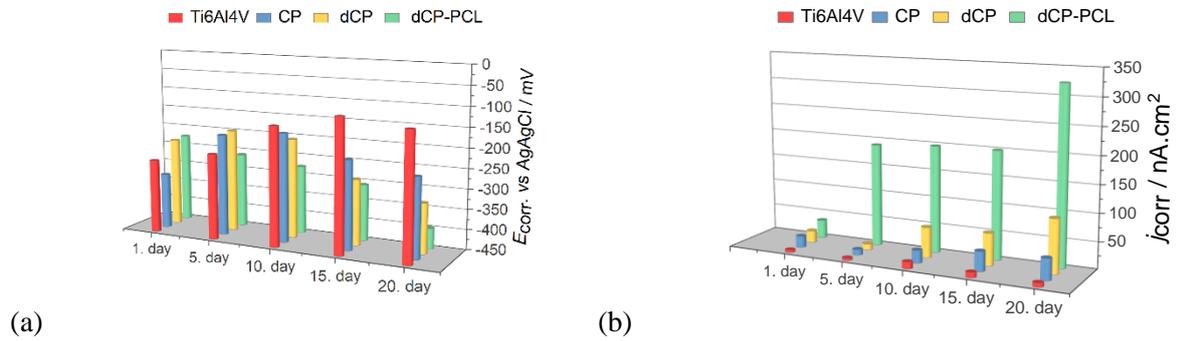
Figure 3.26. *Electrochemical parameters: E_{corr} (a) j_{corr} (b) derived from the potentio-dynamic curves in Figure 3.25.*

The corrosion potential ($E_{corr.}$) values shifted to slightly more positive potentials as time passed for the substrate material, which indicates surface passivation. The corrosion potentials of cACP and biomineralized cACP thin coatings slightly decreased over the whole immersion period. The corrosion current density values hardly changed with immersion time in the case of uncoated implant, however, in the cases of powder and composite thin layers, the j_{corr} showed a steady and slightly slow increasing tendency over the investigated immersion time. The highest j_{corr} values were measured for the cACP-PCL composite layer, that supports its increased biodegradability.

Al$_2$O$_3$ prepared from the oxidized AlN powder by hot isostatic pressed and pressureless post-sintering

K. Balázsi, D. Varanasi, M. Furkó, Cs. Balázsi

Aluminum nitride (AlN) is an alternative refractory ceramic material being used in various range of applications such as optics, electronics and computer circuits for its unique thermal and electrical properties. It has a really high degree of thermal stability and wear resistance while exhibiting a low density. The effect of the pressureless post-sintering in hydrogen on the structural and mechanical properties of the hot isostatic pressed alumina (Al$_2$O$_3$) ceramics prepared by oxidized AlN powder has been studied as the potential substrates for integrated circuits.

The micrometer size AlN powder (H.C. Starck GMBH, Berlin) has been oxidized in air at 900° C and sintered by hot isostatic pressing (HIP) at 1700 °C, 20 MPa nitrogen atmosphere for 5 h (Fig. 3.27). Pressureless sintering (PS) has been applied for all HIP sintered samples in H$_2$ gas at 1800° C for 10 h. Transmission (TEM, Jeol 3010) and scanning (SEM, Thermo Fisher) electron microscopy were used fir detailed structural analysis. HIT300 (Anthon-Paar) nanoindenter was used for the nanomechanical testing.

Based on the structural characterizations, the oxidation caused a core–shell AlN/Al$_2$O$_3$ structure and the amount of Al$_2$O$_3$ increased with increasing of the oxidation time of the AlN powder. AlN powder before oxidation showed mainly globular character with average grain size of~1 µm The processing method is influencing the obtained microstructure, reduces the grain size and increases the densification of final sintered ceramic. Te increasing of the oxidization time above 10 h caused the formation of pores on the surface of the AlN, indicating the creation of Al$_2$O$_3$ oxide phase. Hot isostatic pressing (HIP) has unique advantages in promoting the compactness of parts, eliminating void defects, reducing segregation and improving the mechanical properties of the ceramics. The presence of α-Al$_2$O$_3$ phase has been only observed. The subsequent PS sintering effected the grain growth from 1 µm to ~ 5 µm at 1800 °C for 10 h. The PS sintered Al$_2$O$_3$ has been consisted from the non-uniform morphology and the grain size has been still around 5 µm. The structure of oxidizes ceramics compared to non-oxidized reference showed the smoother surface. The improvement of the mechanical properties of Al$_2$O$_3$ can be expected potential ceramics for novel engine or other applications. The hardness values of post-sintered samples have been increased to 17–18 GPa having apparent densities between 3.11 and 3.39 g/cm^3.

Bulk sintered Al$_2$O$_3$ has been prepared by oxidization of AlN powder and combined sintering process, the hot isostatic pressing (HIP) in N$_2$ and pressureless sintering (PS) in the atmosphere. Both sintering methods (HIP followed by PS) of oxidized AlN powder without sintering additives has been successfully developed for the first time [Ref. 3.25]. The micrometer sized AlN has been oxidized between 3 and 20 h in ambient atmosphere. The volume of Al$_2$O$_3$ phase increased with the increasing of oxidation time of AlN powder. High temperature HIP sintering transformed θ-Al$_2$O$_3$ and only two major phases α-Al$_2$O$_3$ and minor AlN have been stabilized. PS post-sintering in 1800 °C for 10 h caused the phase transformation to α-Al$_2$O$_3$ which had effect on the apparent density and hardness of PS sintered ceramics. The highest apparent densities 3.11–3.39 g/cm3 (78–85% relative densities) and highest hardness values (17–18 GPa) have been measured for PS sintered α-Al$_2$O$_3$ prepared from base powder oxidized between 3 and 10 h.
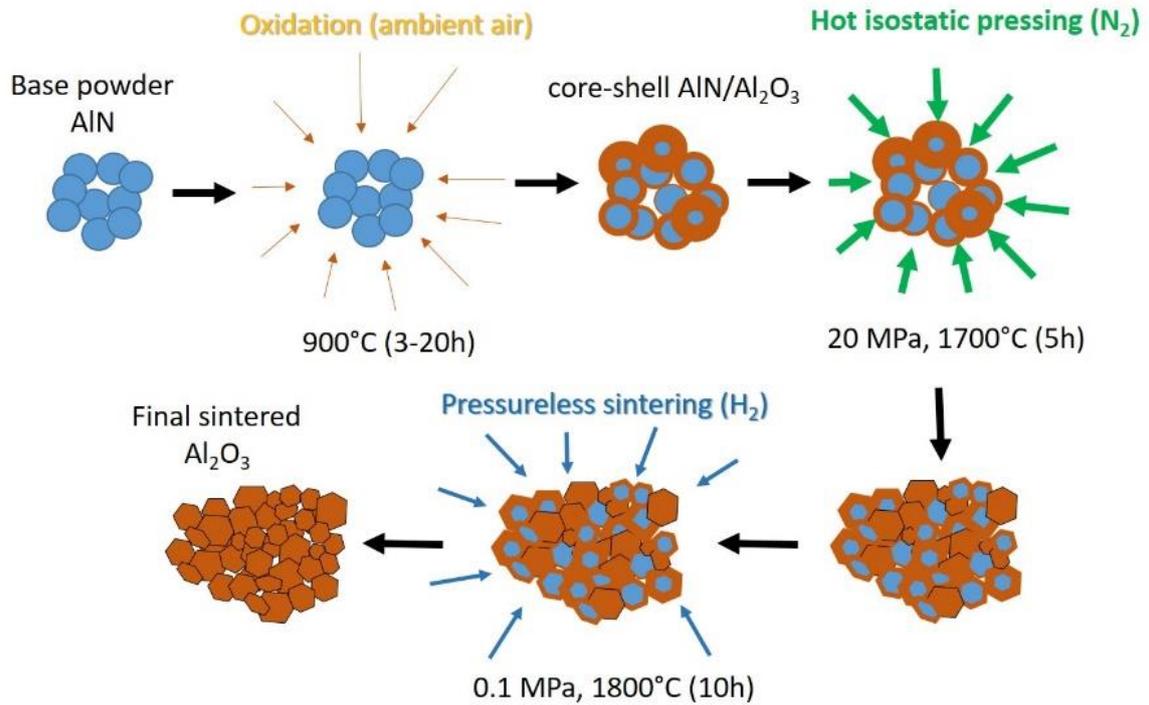
Figure 3.27. *Experimental procedure of Al₂O₃ sintered sample preparation from AlN powder.*

Nanosensors Laboratory

Head: Dr. János VOLK, Ph.D., senior research fellow

Research Staff:
- Gábor BATTISTIG, D.Sc.
- Zsófia BAJI, Ph.D.
- Nguyen Quoc KHÁNH, Ph.D.
- György MOLNÁR, D.Sc.
- Péter Lajos NEUMANN, PhD
- László PÓSA, Ph.D.
- János RADÓ, PhD
- Zsolt ZOLNAI, Ph.D.

Technical Staff:
- Ferenc BRAUN, engineer
- János FERENCZ, engineer
- Levente ILLÉS, engineer
- Attila NAGY, technician
- Erika TUNYOGI, engineer
- Zoltán KOVÁCS, Ph.D. engineer

Ph.D. students / Diploma workers:
- Sadaf ARJMANDABASI, MSc student
- Péter HORNUNG, B.Sc./M.Sc student
- Axel KATONA, B.Sc student
- Silvia A. STÁGL, B.Sc student
- Anett SZELEDI, B.Sc student
- Tímea Nóra TÖRÖK, Ph.D. student
- Mátyás VOLOM, B.Sc student
- Tamás ZEFFER, PhD student

Nanosensors Laboratory was established at the beginning of 2019 from the former Department of Microtechnology. The core infrastructure, having two semiconductor clean rooms, is shared and operated together with the Microsystems Laboratory. The mission of the Lab is to utilize the emerging results of nanotechnology and materials science for novel physical sensors, particularly for micro- and nanometer sized electromechanical systems (MEMS/NEMS). In the following sections eight selected topics are presented, which relate to i) characterization of functional thin films; ii) nano- and micrometer sized electronic and sensor devices; and iii) novel force sensor systems.

This year, the highlight is on the VO_2 phase changing material based devices and on the novel applications of packaged 3D piezoresistive force sensors. These research topics are conducted mainly in the framework of three domestic and two international projects (TKP2021-NVA-03: Environmental monitoring sensors for emergency and extreme conditions; OTKA: Atomic layer deposition and applications of functional sulfide nanolayers (OTKA FK 139075); OTKA: Development of Nanometer Scale Resistive Switching Memory Devices (OTKA K 143282); TéT: Atomic layer deposition and application of functional VO_2 thin films (2019-2.1.11-TÉT-2020-00189); TéT: Fabrication, characterisation and development of semiconductor devices for energy conversion, sensing and electronics (2019-2.1.11-TÉT-2019-00066). Besides, the Nanosensors Laboratory provided electronmicroscopy services for several industrial partners (Lighttech, Technoorg Linda, Bosch, Visola), nanofabrication infrastructure for the Quantum Information National Laboratory (QNL), and was engaged in university education as well (University of Debrecen, Budapest University of Technology and Economics).

VO2 layers with high resistive switching ratio by atomic layer deposition

2019-2.1.11-TÉT-2020-00189

Zs. Baji, L. Pósa, Gy. Molnár, Z. Szabó, M. Volom, A. K. Kjara Surca*, G. Drazic*, J. Volk
*National Institute for Chemistry, Ljubljana, Slovenia

The atomic layer deposition of vanadium oxides has been in the focus of much research effort. Vanadium oxides are much-researched materials due to the wide range of applications from microelectronics, smart electrochromic and thermochromic windows, metamaterials, gas sensors, programmable critical thermal sensors to battery energy storage. VO_2 is in the centre of most research due to its reversible transition at 68°C, where the crystalline structure of the material reorganises from monoclinic to tetragonal rutile structure coupled by dramatic changes both in the electrical and optical properties. Therefore, all the optical and electrical properties of the material may be controlled through this SMT transition. This quality makes VO_2 an excellent material for resistive switching.

The atomic layer deposition of vanadium oxides has been in the focus of much research effort. With atomic layer deposition, a number of precursors and different reactions can be used for this purpose, but there are some substantial difficulties with all of them. The present work aims at the comprehensive investigation of the atomic layer deposition of VO_2 with the TEMAV precursor. Water, formalin and oxygen plasma were used as oxidants at deposition temperatures between 200°C and 350°C.

All the deposited films were examined with AFM SEM and XRD, and they all proved to be very smooth with RMS roughness's between 2-5 nm. The XRD showed no peaks typical of vanadium oxide, therefore they all the layers were amorphous. According to the results of the structural and electrical characterisation, the deposition with water vapour at 200°C was ideal for the preparation of resistively switching VO_2. The crystallinity of the layers was improved with annealing, for which procedure oxygen, nitrogen and hydrogen atmospheres were investigated, and different temperatures and annealing lengths were examined. The optimal layers were prepared with the post deposition annealing of 3 hours in oxygen rich atmosphere at 500°C. This layer is shown in Fig. 4.1.b, and it can be seen, that the layer is dense with large crystallites.
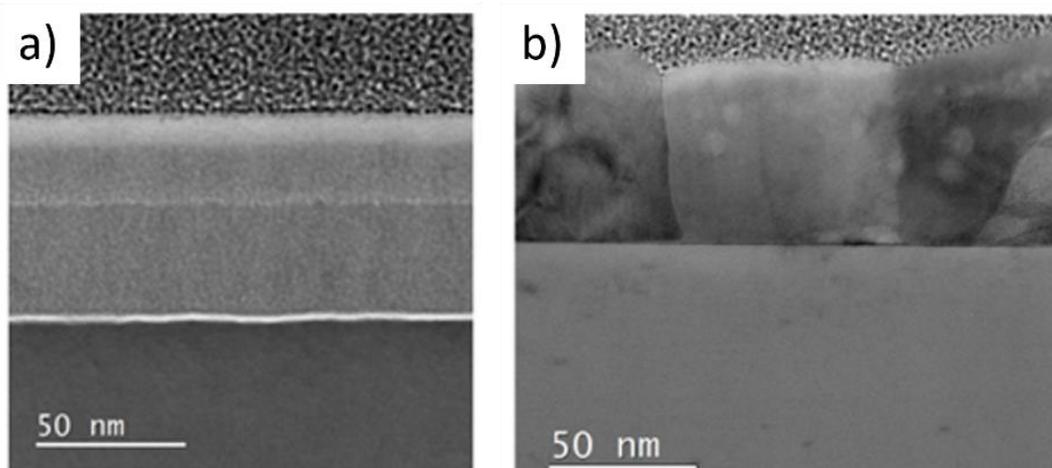
Figure 4.1. *STEM image of as deposited vanadium oxide (200°C) film with water as an oxidant before (a) and after (b) annealing in O_2 for 3 hours at 500°C*
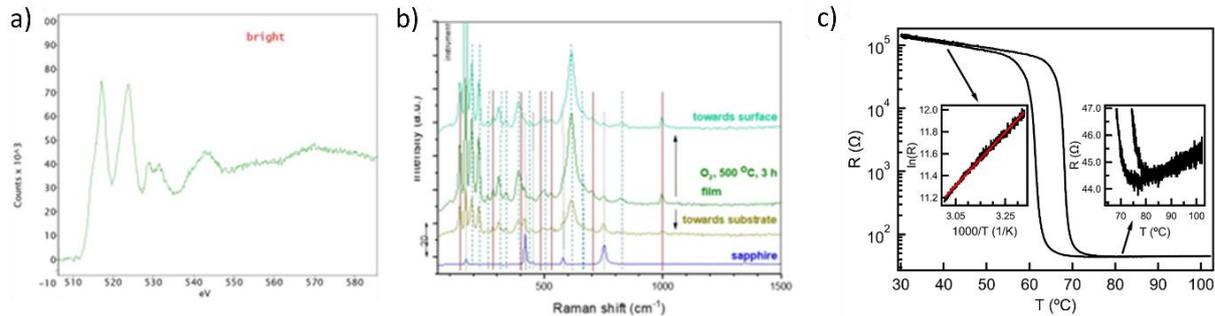
Figure 4.2. *Electron energy loss spectroscopy (EELS) (a), Raman (b) and temperature dependent resistance (c) spectrum of the VO₂ film.*

Electron energy Loss Spectroscopy (EELS) and Raman measurements also proved that the films are monoclinic VO_2. The EELS spectrum showed the typical shoulder for VO_2 at the Vanadium peak at 515 eV, and the characteristic double peak of the Oxygen around 530eV (Fig. 4.2.a). The Raman measurement also found only the peaks corresponding to VO_2 (Fig. 4.2.b). The electrical properties of the films were measured by Hall technique at room temperature, and after being heated to the phase transition temperature. The optimal layer showed the required phase transition, with its resistance dropping by three orders of magnitude at the transition temperature. The free electron mobility rose from 0.18 cm^2/Vs to 15.4 cm^2/Vs, while the carrier concentration increased from $3.5 \cdot 10^{18}\,cm^{-3}$ to $2.9 \cdot 10^{19}\,cm^{-3}$. Therefore, the drop in resistivity in our layers is due to a combination of increasing mobility and carrier concentration. It is widely stated that the phase transition is a result of the rearrangement of the V-V bond lengths, which are alternately shorter and longer in the monoclinic structure, to the equidistant shorter lengths of the rutile phase, thus the sharp decrease of the V-O distance and the overlapping of the oxygen $2p$ and vanadium $3d$ orbitals resulting in both the d and π orbitals being partially occupied at the Fermi level, and ultimately in a metallic behaviour.

The temperature dependent resistance was measured between 1 mm diameter Ti/Au ohmic contacts dots separated by 2mm. During the electrical resistance measurement triangular voltage signal was applied with 20 mV amplitude, while the current was monitored by a current amplifier. The layer showed ohmic behaviour with linear I(V) characteristics, thus the resistance could be determined by linear fit. The R(T) trace shows a several orders of magnitude jump around Tc=68 °C, characteristic to VO_2 (Fig. 4.2.c). The resistance switching ratio between 30 °C and 100 °C exceeds 3100. At low temperature, the layer exhibits semiconducting behaviour with a E_{gap}=418 meV band gap energy (see left inset), which is in good agreement with the literature values. Above the phase transition temperature, the sample shows an increasing resistance with the temperature, referring to metallic phase (see right inset). Due to the hysteretic behaviour, the layer transforms back to the semiconductor state at lower temperature (T_c=61 °C) during the cooling process. In summary, vanadium-oxide layers with the desired stoichiometry (VO_2) were successfully synthesized by atomic layer deposition and a post-annealing step. The layer showed a distinct switching property around the critical temperature with an R_{OFF}/R_{ON} ratio of over 3000 providing an attractive active layer for volatile memristor devices.

Interplay of thermal and electronic effects in the Mott transition of ultrasmall VO$_2$ phase change memory devices

L. Pósa, P. Hornung, N. T. Török*, S. Arjmandabasi, Gy. Molnár, Zs. Baji, A. Halbritter*, and J. Volk
*Department of Physics, BME, Budapest, Hungary

VO$_2$ has been studied for decades due to its metal-insulator (MIT) transition at T ≈ 68 °C. This first order phase transition is accompanied by the structural transformation from low-temperature, semiconducting monoclinic to high-temperature, metallic tetragonal phase. This near room temperature phase transition was exploited in the field of neuromorphic computing, taking advantage of the volatile resistive switching characteristics of VO$_2$ devices. However, the underlying switching mechanism exhibits remarkable complexity both in the temporal and spatial domain. The description of these phenomena mostly requires complex modelling tools, like a percolation network model. We aimed to lessen the complexity of the physical operation in VO$_2$ resistive switches by focusing the switching to a nanometer-sized well defined active volume. We established devices with an ultra-small (≈ 30 nm) spacing between the contacting electrodes and anticipate that these devices are already describable by the formation and disappearance of a single metallic spot instead of more complex spatial patterns. This simplified arrangement facilitates the device modelling, providing further insight into the details of the local electronic and thermal processes.

Our devices were fabricated in lateral arrangement by depositing Ti/Au metal electrodes onto a Si/SiO$_2$ substrate covered by VO$_x$ layer (see the SEM image in Fig. 4.3.a). The gold top electrodes (light grey) were patterned by electron beam lithography, realizing an asymmetric structure with triangular electrode on one side and rectangular one on the other. At the narrowest spot the separation of the two electrodes is ≈ 30 nm. The VO$_2$ layer (dark grey) was produced by the thermal oxidation of a pure, 100 nm thick V layer at 400 °C for 4.5 h under 0.1 mbar sparse air. According to EELS measurements the topmost 30-50 nm thick part of the oxidized VO$_x$ layer contains VO$_2$ grains, whereas the bottom 170-190 nm thick part is V$_2$O$_5$. The presence of VO$_2$ at the surface region is also supported by the temperature dependent electrical resistance measurement. The device shows pronounced phase change characteristic, shown in Fig. 4.3.c. The resistance switching ratio between 30 °C and 100 °C exceeds 600. We anticipate that the discrete jumps in the R(T) curve during the transition are related to the involvement of only a few VO$_2$ grains in the electrical transport. The electrically induced phase transition could be also triggered by applying triangular voltage signals to the device.

To identify the contribution of the thermal and electronic effects in the device operation, we studied the scaling of the switching parameters as well as the detailed evolution of the device resistance with the base temperature and bias voltage. Fig. 4.3.d shows I(V) characteristics recorded at different temperatures between 30.4 °C and 66 °C. The set voltages (V$_{set}$) show a very clear decreasing tendency as the temperature increases, whereas the current right before the switching (I$_{set}$) is nearly temperature independent. Accordingly, the switching power (P$_{set}$=V$_{set}$·I$_{set}$) also shows decreasing trend, however, it does not reach the zero power value at Tc=66.2 °C. Consequently, these trends can not be qualitatively described by either the pure thermally or electrically triggered MIT.

To gain further insight the underlying physical mechanisms performed a detailed analysis of the R(V) curves to determine the conduction phenomena. The high electric-field induced carrier generation can produce a finite slope of the R(V) curve around zero bias, which is presented in the measured data (see dashed linen in Fig 4.3.e. Several conduction mechanisms were applied to describe the nonlinear I(V) behavior of VO_2 layers, which all can be summarized in the following form:

$$R(V_{bias}, T) \approx R_0(T) \cdot \exp \left[-(V_{bias}/V_c)^\alpha \right] ,$$

where $R_0(T)$ is the temperature dependent low voltage resistance shown in Fig. 4.3.c, V_{bias} is the voltage drop on the device, V_c is a characteristic voltage, whereas the α exponent specifies the conduction mechanism. The dominant conduction mechanism was determined by fitting the $\ln(-\ln(R/R0))$ vs. $\ln(V_{bias})$ curves to a line (see inset of Fig. 4.3.e), whose slope, the α parameter were close to unity at all temperatures referring to Zener conduction.
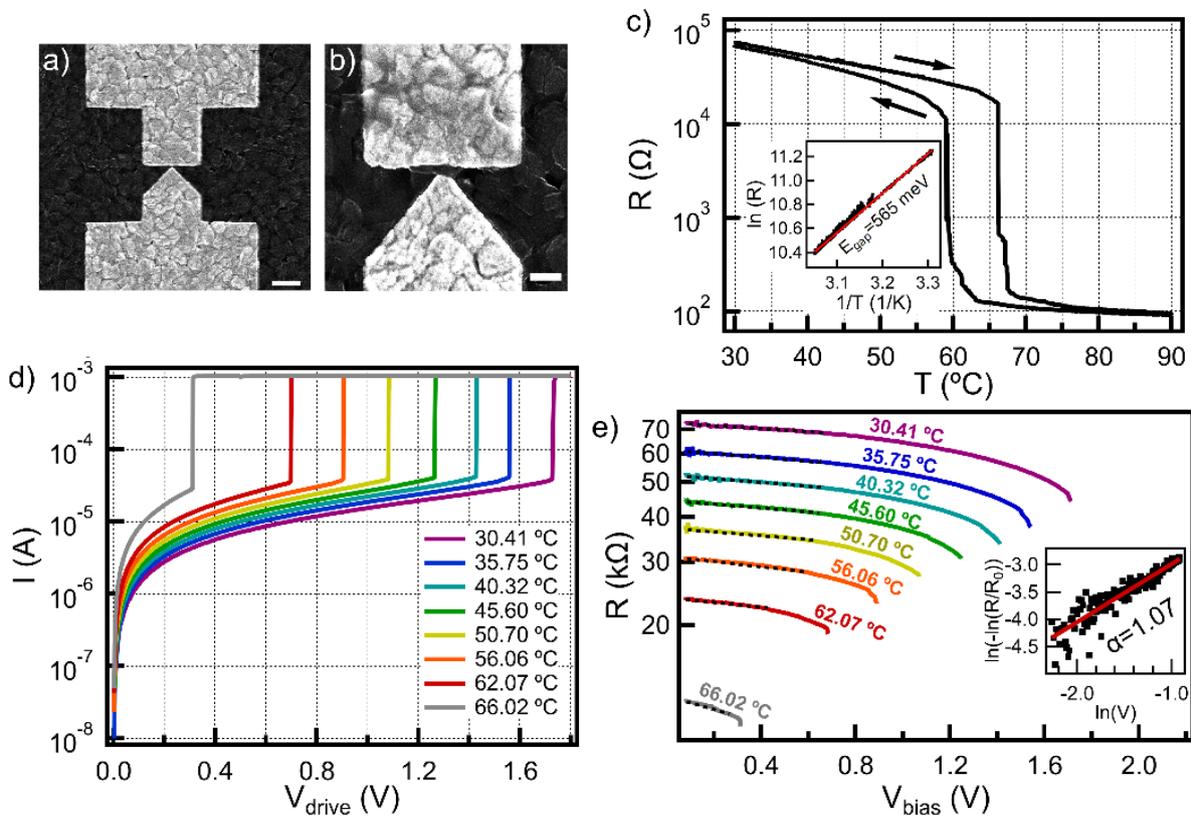
Figure 4.3. *Scanning electron microscopy (SEM) image of the device before (a) and after (b) performing the electrical measurements. The scale bar in the initial a) SEM image indicates 500 nm, whereas in panel b) it indicates 200 nm. c) Temperature dependent resistance shows very sharp phase transition, characteristic to VO_2. The arrows indicate the direction of the hysteresis loop. d) Current-voltage characteristics recorded at different base temperatures. The resistive switching occurs at decreasing voltages as the temperature increases. a) R(V) traces measured at different temperatures. All traces show the similar nonlinear current behaviour at low bias voltage (see dashed lines). The inset shows the $\ln(-\ln(R/R_0))$ vs. $\ln(V)$ relation at 56.06 °C base temperature whose slope determines the α exponent, introduced in the equation above.*

To better understand the contribution of nonlinear electronic phenomena to switching mechanism, we performed steady-state finite element simulations in COMSOL Multiphysics implementing the exact geometry of the device. The layer structure of the model with the most relevant dimensions is schematically presented in Fig. 4.4.a, mimicking the result of the TEM and EELS measurements. Fig. 4.4.a also shows

the considered heat conduction mechanisms (marked by coloured arrows) and thermal boundary conditions (marked by dashed black line). We considered a thermal boundary conductance at the VO$_2$/Ti interface (h$_{th}$, purple arrow).

To demonstrate that neglecting either the thermal or the electronic phenomena leads to insufficient description, we plotted a measured R(V) trace at 35.75 °C (black curve) with its best fittings with either a purely thermal or purely electronic model, (Fig. 4.4.c). The red trace shows the result when the field dependence was eliminated from the model (i.e. $\rho(E,T) = \rho_0(T)$) and the resistance changes solely due to the self-heating effect. Similarly, we simulated the field dependent resistance, assuming no self-heating effect (blue curve). Both models give a poor fit to the measured data. In contrast, Fig. 4.4.d shows the results of the electrothermal simulation at different base temperatures (black circles with line) using the temperature and electric field dependent resistivity. The measured R(V) curves (coloured curves) are well fitted by the simulation, all of them have correct slope at low bias and follow the same high bias nonlinearity due to the self-heating. The combined electrothermal simulation gives a remarkably precise agreement with the experimental observations. [Ref. 4.1]
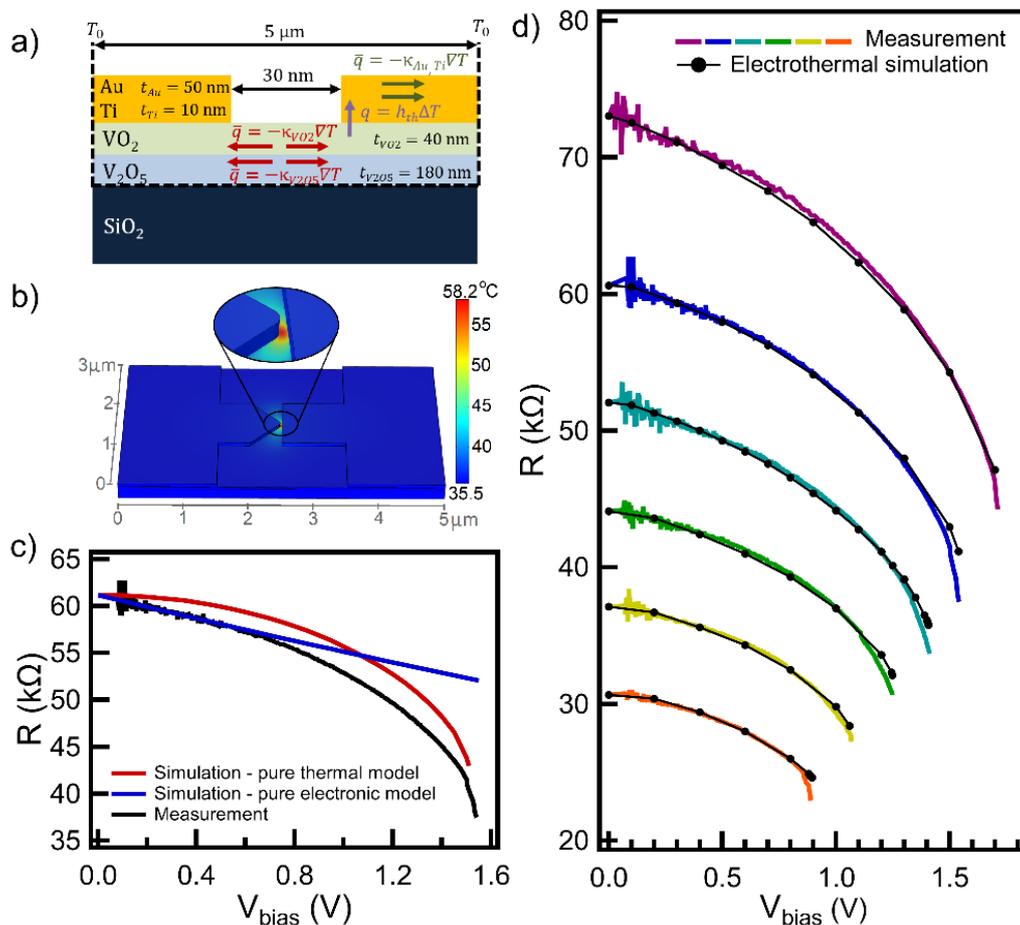
Figure 4.4. *a) Schematic of the thermal model of the device, introducing the most relevant geometry parameters and the heat transfer mechanisms with the corresponding heat equations. b) The simulated temperature profile with V$_{bias}$ = 1.5 V and T$_0$ = 35.75 °C, showing the realistic device geometry. The magnified view of the gap shows the focused ultra-small active region. c) Results of pure thermal and pure electronic simulation. The thermal model (red curve) cannot reproduce the initial decreasing tendency of the R(V) curve due to the negligible Joule heating. The pure electronic model (blue curve) has a constant nonlinearity due to the lack of Joule heating and diverges from the measured R(V) curve (black) at higher bias. d) Measured (coloured curves) and simulated R(V) characteristics (black curves) using the electrothermal model. The simulated traces show very good agreement with the measurement at each base temperature between 30.41 °C and 56.06 °C.*

AlGaN/GaN Heterostructure Based 3-Dimensional Force Sensors

TKP2021-NVA-03

P. L. Neumann, J. Radó, J. M. Bozorádi, J. Volk

Tactile sensing is an essential physical-electrical gateway in sensing technology. Creating such sensors is a complex challenge if the goal is to reproduce human-like sensations. Classical MEMS tactile sensor solutions in typical environmental conditions exist few types, but harsh conditions such as space technology or high-temperature range are not solved yet. One proposed material complex is the GaN/AlGaN system.

In this project, a novel AlGaN/GaN heterostructure-based 3D force sensor is proposed. The principle of operation is similar to its Si counterpart: a thin membrane is deformed upon applying a loading force on the Si micro-stick formed on the backside of the membrane (Fig. 4.5.a). Local strains in four positions of the membrane are measured by semiconductor gauges (Fig. 4.5.b). By collecting the electrical signals, both the magnitude and the direction of the force can be determined. However, in contrast to conventional Si piezoresistive devices, mechanical strain influences the density of the 2-dimensional electron-gas (2DEG) at the AlGaN/GaN interface by changing the magnitude of the discontinuity in the polarisation vector between the AlGaN barrier and GaN channel layer, that means the external strain could be a proportional modulation factor to the density of the carrier concentration.
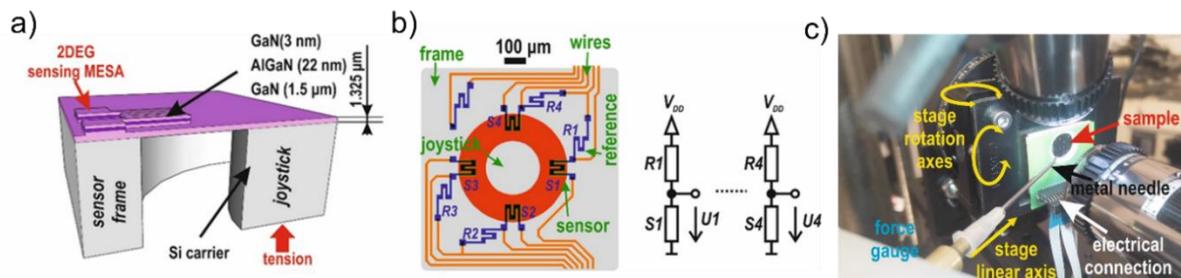
Figure 4.5. *The cross-section shows the quarter of the prepared MESA structure containing the 2DEG layer (a). Top view of the 2DEG force sensor with the sensor elements (S1-S4), the reference elements (R1-R4) and its equivalent circuit (b). Wire-bonded force sensor mounted on a three degrees of freedom vertical sample stage and loaded from the actuator side with a load cell needle and monitored by a USB camera (c).*

The mechanical and electromechanical measurements were carried out using a purpose-built system with three degrees of freedom sample holder (Fig. 4.5.c). The external loading was performed with a medical needle mounted on a force gauge (Andilog Centor Easy). During the alignment and testing, the position of the force gauge and the needle was precisely controlled by translational actuators (ThorLabs) and visually monitored by a USB camera (Dino-Lite Edge). A LabView software-controlled data acquisition module (NI USB 6211 DAQ) was used to power (V_{DD}) the wire-bonded 2DEG force sensor and to collect its response signals (U_1-U_4). The signals were filtered to reduce the noise.

Numerical simulation was carried out by COMSOL Finite Element Method to determine the volumetric strain map in the AlGaN/GaN membrane, which predicts the possible 2DEG modulation to sense the force strength and direction. The simulated object geometry was the same as the original design. Fig. 4.6. shows the analytically calculated volumetric strain under an applied load of 10 mN. In normal loading direction, pointing to the centre of the Si microstick, the resulting strain is circularly symmetric and shows absolute

minimum (ε_{min}=-296 ‰) and maximum (ε_{max}=311 ‰) values close to the outer edge and to the root of the microstick, respectively (Fig. 4.6.a). That can assume the sensor elements on the membrane will show conformity between its output signals' directions and values. In contrast, for a load force at an oblique angle φ= 45° (where φ is the angle with respect to the normal direction), the simulation result shows a significant asymmetry of the volumetric strain building up in the membrane (Fig. 4.6.b). The simulation results predict that the asymmetric out voltage will be on the sensor element in the force direction and symmetrical one in the perpendicular direction, but the lower 2DEG modulation effect will be lower.
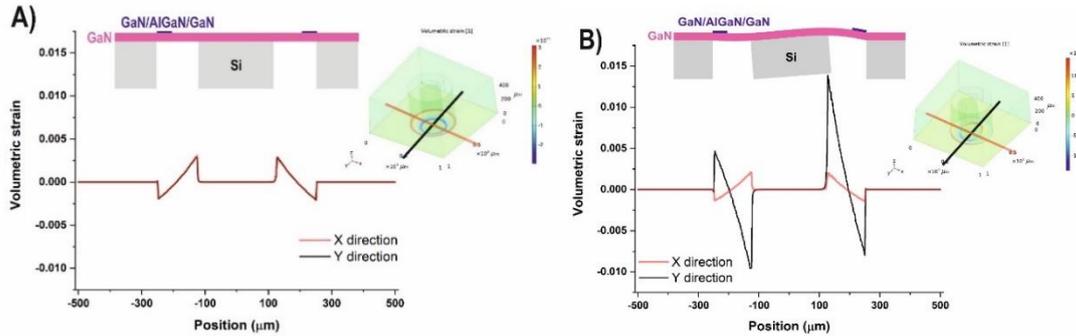
Figure 4.6. *Simulation results of the volumetric strain for normal (φ= 0°) (A) and oblique (φ= 45°) (B) load force, where φ is the angle with respect to the normal direction. The inset shows the simulation results of the deflection and the volumetric strain, indicating the locations of the line cuts.*

In the electromechanical experiment, the sensitivity of the force sensor on normal force load was investigated (Fig. 4.7.a). All four bridges show almost the same voltage response upon increasing load. The sensitivity from the plotted curves is approx. 100 mV/N/V. This value is more than one order higher than the Si base force sensor case, where this sensitivity was ~9 mV/N/V. The recorded voltage signals gave a fast response (< 0.2 s) on the applied load. The response examination was followed by a dynamic normal tension analysis, in which load pulses with increasing magnitude. The individual sensor bridges showed increasing voltage pulses with increasing load and ran roughly together since the stress and the arising strain at the position of the symmetrically arranged MESA elements are similar. In the next experiment, the load force angle was set to φ= 45° (Fig. 4.7.b) and increased, and then the measured signals trends split in the direction of load force as expected in the simulations. A further plan is to get an accurate tensile sensor for harsh environments is to investigate the temperature sensing and dependency, the direction decoding from the recognized response of the voltage divider, and the matrix arrangement of the sensors to obtain redundancy information for the precise touching information. [Ref. 4.2]
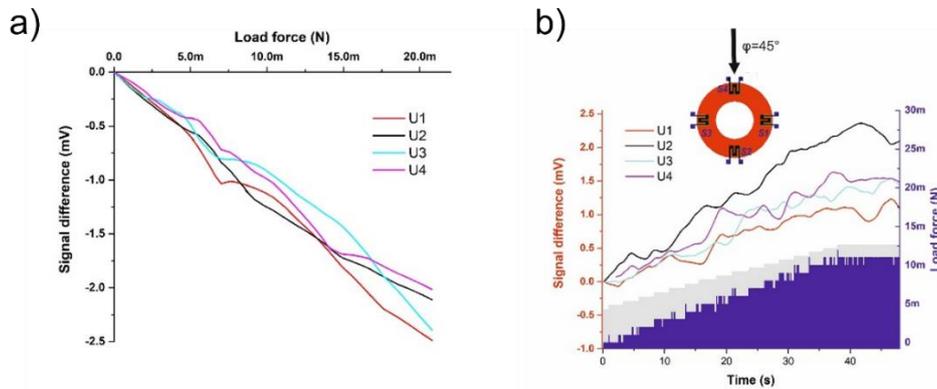
Figure 4.7. *Normal load force response signals of the sensor outputs (a). For a better visualization, at the beginning of the measurement, a reference voltage was taken for each bridge, and only the change as a function of time upon increasing load pulses is shown. Sensor output signal for increasing φ=45° load force as a function of time. The grey region represents the needle displacement (total step length ≈ 950 μm).*

Microsystems Laboratory

Head: Dr. Péter FÜRJES, Ph.D., senior research fellow

Researchers:
- István BÁRSONY, member of HAS
- Orsolya BÁLINT-HAKKEL, Ph.D.
- Barbara BEILER, Ph.D.
- Ferenc BÍRÓ, Ph.D.
- Csaba DÜCSŐ, Ph.D.
- Péter FÖLDESY, Ph.D.
- András FÜREDI, PhD., MSCA fellow
- Péter FÜRJES, Ph.D.
- Eszter LEELŐSSYNÉ TÓTH Ph.D.
- János RADÓ, Ph.D.
- Zoltán SZABÓ, PhD.

PhD Students:
- Anita BÁNYAI (ÓE Univ. Óbuda)
- Lilia BATÓ (ÓE Univ. Óbuda)
- Dóra BERECZKI (ÓE Univ. Óbuda)

Engineers / technicians:
- Gabriella BÍRÓ, technician
- János Márk BOZORÁDI, electrical engineer
- Tibor CSARNAI, electrical engineer
- Magda ERŐS, technician
- Petra HERMANN, bioengineer
- Róbert HODOVÁN, mechatronic engineer
- Csaba LÁZÁR, electrical engineer
- Margit PAJER, technician
- Zsuzsanna Brigitta SIK, bioengineer
- Zsombor SZOMOR, medical enginee

The main goal of the Microsystems Laboratory is to research and develop integrated sensors and sensor systems, MEMS and BioMEMS devices fabricated by silicon or polymer micro- and nanomachining technology. The activity covers the characterisation of materials, microsystems, development of technology solutions and sensing principles. The application of micromachining technology enables the miniaturisation of sensing and analytical systems and integration of various functions of sample preparation, sensing, readout, actuation or communication. The laboratory is focusing on the development of mechanical, physical, chemical (and biochemical) sensors, functional micro- and nanofluidic devices, implantable microsystems and infrared LED.

Our medium-term goal is to broaden the spectra of perspective research topics of MEMS systems and to develop a systematic organisation by forming a dynamic and growing research group in the Microsystems Laboratory. Considering the financial environment our research directions fit to the European and Hungarian strategic roadmaps and directives (S3 - National Smart Specialisation Strategy) by the following research topics:
- Health: BioMEMS, Lab-on-a-Chip, Organ-on-a-Chip, microfluidic systems, implantable, wearable devices, personal medicine, continuous monitoring, etc.
- Cutting-edge technologies: human-machine interaction and cooperation – sensors for robotics, quantum technologies (quantum computing, sensing), space technologies, biosensors, driving safety sensors, new materials and manufacturing technologies: advanced materials, nanotechnologies, 3D manufacturing
- Energy, climate: Low consumption electronics, sensors for energy industry, characterisation photovoltaic systems, energy harvesting, environment safety sensors (water monitoring), gas sensors (smart home, smart clothes)
- Healthy food: Food safety sensors, spectroscopy

Research group structure in the Microsystems Laboratory

The development of MEMS devices requires solid design capacity and advanced cooperation among the research and technical staffs for precise operation of the full micromachining fabrication line. Actually, 11 researchers, 10 engineers / PhD student and 3 technicians work for the Laboratory with close and flexible cooperation with the colleagues of the Nanosensors Laboratory.

- **MEMS / smart sensors (Csaba Dücső, Ferenc Bíró, János Radó):** The team's primary expertise is traditional MEMS sensor development, such as gas, environmental and mechanical sensors with an emphasis on the technology of 3D microstructure implementation.
- **BioMEMS, medical applications (Péter Fürjes, János Márk Bozorádi, Csaba Dücső, János Radó):** Silicon based sensor development and their electro-mechanical integration, specifically for medical applications, are the long-term goals in this topic. The medical field demands the development of tools in low numbers that have extensive added value, which also aligns with the European strategic directives. The topic includes Si and flexible integrated microstructure development as initiated in connection with the National Brain Programme.
- **Lab-on-a-Chip / Organ-on-a-Chip (Péter Fürjes, Anita Bányai, Lilia Bató, Dóra Bereczki, András Füredi, Orsolya Hakkel, Zsuzsanna Brigitta Sik, Zsombor Szomor):** The Lab-on-a-Chip and Organ-on-Chip systems are essential building blocks of Point-of-Care diagnostic and drug analytical tools in the medical field. We have vast experience in this topic, especially in microfluidics. Accordingly, we actively collaborate with companies, research institutes and universities in this field (77 Elektronika Kft., Aedus Space Kft., Micronit B.V., CSEM, University of Pécs) as well.
- **IRLED (Zoltán Szabó, Barbara Beiler, Ferenc Bíró):** We fabricate and develop a few thousand infrared LEDs per year (partners: Anton Paar GmbH, Senop OY). Additionally, we envisaged a larger scope spectroscopic development and application in the frame of an actual ECSEL grant. Environmental analytics and food safety applications could be important goals for IR spectroscopy and other optical developments.
- **Integrated systems / Heterogeous integration /IoT (Péter Földesy, János Márk Bozorádi):** Research grants ask for a certain level of preparedness, which usually includes demo systems (sometimes prototypes). Therefore, the requirements of developed instruments and their electro-mechanical integration are becoming a more and more important and complex tasks.
- **Technology, FEM / Multiphysics Modelling (Eszter Leelőssyné Tóth, Zsombor Szomor):** Modelling, such as digital twin, is a widely applied method in engineering practice. It speeds up development and manufacturing time of prototypes while also lowering costs. The application of these methods is not as straight forward for the development of microstructures due to the effects of microenvironments. However, the use of these simulations is indispensable. The group is effectively corroborating the research and development tasks.

Infrastructure and technological competencies

This is a unique infrastructure in Hungary, therefore its sustainable operation and development is a strategic goal. The infrastructure is open for academic and industrial partners to fabricate (and to characterise) complex, purpose-designed microsystems, nanocircuits, as well as Lab-on-a-Chip devices and to develop their technology solutions.

The high-tech microtechnology related fabrication and characterisation systems work in a class 10 cleanroom facility. The laboratory is dedicated for 3D processing of 3" and 4" Si / glass / polymer substrates with maximal resolution of 1µm, together with lithographic mask manufacturing. Electron beam lithography and focused ion beam (FIB) milling are also available with resolution of 20nm. Multi-domain Finite-Element Modelling (FEM), and process simulation also support the structural design and development. Wide spectra of characterisation techniques are also available: optical (fluorescent) and electron microscopy (SEM and EDS), atomic force microscopy (AFM), profilometry, optical and electrical measurements, electrochemical impedance spectroscopy, microfluidic characterisation, mechanical vibration and climate test chambers, UV / VIS / IR / FTIR spectroscopy, etc.

Available micromachining techniques:

- Patterning – mask design, laser pattern generator, photolithography, (double side) alignment, electron beam lithography (E-Beam), Focused Ion Beam processing – FIB milling, nanoimprinting
- Structured polymer layers – PMMA, PI, SU8 patterning, micromoulding, soft lithography – PDMS, hot embossing technique for polymers
- Wet chemistry – chemical wafer cleaning, isotropic and anisotropic etching techniques
- Dry etching – deep reactive ion etching, plasma etching techniques (DRIE, RIE)
- High temperature processes – thermal oxidation, diffusion, annealing, rapid thermal annealing (RTA)
- Physical thin film depositions – Thermal and electron beam evaporation, DC and RF Sputtering
- Chemical thin film depositions – Atmospheric and Low Pressure Chemical Vapour Deposition (CVD, LPCVD, LTO), thermal and plasma enhanced Atomic Layer Deposition (ALD)
- Liquid Phase Epitaxy of III-V compound semiconductors (LED manufacturing)
- Wafer bonding – Si-glass, glass-glass, polymer-glass anodic and thermal bonding
- Chip dicing, wire bonding especially for sensor applications
- Special packaging techniques and methods
- 3D printing and CNC milling for application-specific polymer packages or microfluidic structures

Cooperations

Apart from the European and bilateral international R&D projects wide cooperative and knowledge network was established by the large number of joint research projects with Hungarian universities and research centres (BME, DE, ÓE, PPKE, PTE, SE, HUN-REN-ATOMKI, HUN-REN-SZBK, HUN-REN-WIGNER, HUN-REN-TTK, HUN-REN-SZTAKI) or research groups to perform interdisciplinary research. We are supporting the National Quantum Technology Programme (HunQuTech), the National Brain Programme and National Laboratory on Human Reproduction Programme by our infrastructural background. Besides the scientific projects, the Lab offers technology development services for several industrial partners (SEMILAB, 77 Elektronika, Mirrotron, Trimble, Bay Zoltán Appl. Res., Anton Paar (Austria), FRK (Poland), Philips (The Netherlands), Senop (Finland), Z-Microsystems (Austria)) to achieve higher technology readiness levels (TRL 2 → 6).

The technological and scientific results are directly transferred into the higher education, by means of several lectures, laboratory practices, TDK, diploma and PhD works. Our researchers give lectures at various departments of TalTech (Estonia), BME, PPKE, ÓE, DE, ELTE.

Major research projects

The researchers of the Microsystems and Nanosensors Laboratories are involved in development, fabrication and integration micro- and nanosystems, sensor structures to open new perspectives in the field of medical diagnostics, Minimal Invasive Surgery techniques, energy-efficient autonomous systems (sensor networks, autonomous driving). Our interest covers the topics of optical analytics (spectroscopy), environmental and safety (gas detectors) sensors.

- Accelerating Innovation in Microfabricated Medical Devices – Moore4Medical, ECSEL Innovation Actions (IA), ECSEL-2019-1-IA-876190
- Advanced Aerosol Metrology for Atmospheric Science and Air Quality - AEROMET II, European Metrology Programme for Innovation and Research (EMPIR 9ENV08)
- Monitoring sensors deployed in emergency situations and in harsh environment, Thematic Excellence Programme - TKP2021 National Defence and Security, TKP2021-NVA-03
- Innovative biosensing technologies for medical applications – INBIOM, Thematic Excellence Programme - TKP2021 Health, TKP2021-EGA-04

- Development of a point-of-care microfluidic device for Therapeutic Drug Monitoring in cancer treatment (POC-TDM), Marie Skłodowska-Curie Actions - Postdoctoral Fellowships (HE MSCA PF101065044 - POC-TDM) – András Füredi, Péter Fürjes
- Integrated microfluidic / Lab-on-a-chip systems for Point-of-care medical diagnostics,Cooperative Doctoral Program –Anita Bányai (Univ. Óbuda), partner: 77 Elektronika Ltd., supervisors: Fürjes Péter and Varga Máté
- Low-dimensional nanomaterials for the optical sensing of organic molecules on liquid and gas interfaces - OTKA K 131515 (participant)
- IR spectroscopy of extracellular vesicles: from exploratory study towards IR-based diagnostics – OTKA K 131594 (participant)
- Thin film integrity check by capillary bridge test – OTKA FK 128901 (participant)

Scientific cooperation:
- Manufacturing optrode devices applied in the NKP_17 „National Brain Programme" - 2017_1.2.1-NKP-2017-00002 for Pámány Péter Catholic University
- Development Lab-on-a-Chip technology for detection nucleic acid content in extracellular vesicles for University of Pécs (cooperative partner: BME SZAKT)

Industrial cooperation:
- Development and optimisation polymer based autonomous microfluidic cartridge, its production technology and measurement methodology for high sensitive Point-of-Care detection of bacteria and blood biomarkers for 77 ELEKTRONIKA Ltd.
- Development CVD technology and equipment for deposition low roughness polycrystalline Silicon layers for MIRROTRON Ltd.
- Development and manufacturing specific calibration test samples for characterisation methods of semiconductor industry for the SEMILAB Co.
- Development and manufacturing Near InfraRed LED devices for spectroscopic applications for Senop Ltd. (Finland)

Wearable gas sensors for emergency and extreme conditions

## *Thematic Excellence Programme TKP2021-NVA-03*

F. Bíró, I. Bársony, Cs. Dücső

Gas sensor applications for wearable devices

In the „ Chemical gas sensors" workpackage of the TKP2021-NVA-03 „Environmental monitoring sensors for emergency and extreme conditions" project we plan to develop wearable gas sensors for detection dangerous gases carry high risk during natural or industrial disaster management (time frame: April 1. 2022 – March 31. 2026). Two families of gas sensors are considered: **1) low cost solid-state chemoresistive sensors** for simple alarming and development of sensor KIT to provide a standard tool fo characterize their gas sensing layers and **2) moderate cost optical sensor for more accurate concentration measurements**. The primary goal is the recognition of methane leakage; however, detection of other risky gases will also be investigated.

Microhotplates for chemoresitive sensor

We exploit our previously developed microhotplate structure as the carrier of the gas sensitive material. Regardless the operation principle, these sensors operate at elevated temperatures between $100 - 500°C$. The basis of the sensors is a newly developed small diameter (150µm) microhotplate exhibiting ±1% temperature uniformity on the heated area below 550ºC. The stability of the heater is 5000 hours at least at the operation temperature of 530°C, thereby in pulsed mode operation ca. 5 years operation can be achieved. The power dissipation at 500°C is 27mW/1.5V, so the chip can be utilized in portable or wearable devices for personal safety. A utility model protection was given for the microhotplate design in 2021 (*Microheater with uniform surface temperature,* U 20 001150, registration number 5279).
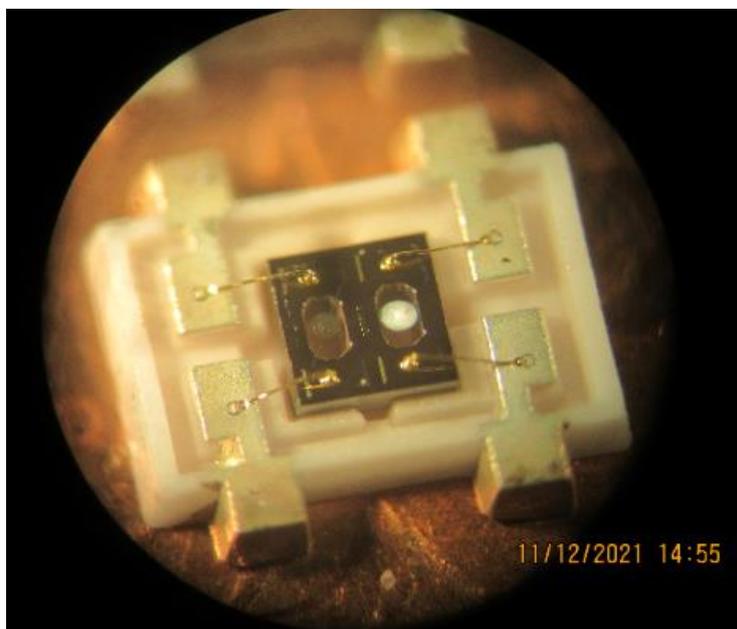
Figure 5.1. *Gas sensor chips in laser micromilled ceramic headers. In this sample the hotplate is covered with catalyst (black on the optical image) and reference suspensions (white) dropped on hotplates (The size of both chips is 1x1mm^2. The same hotplates structure forms the basis of the chemoresistive devices.*

The sensor KIT will be developed by the mid of the project. It comprises two chips: i) a three element sensor chip and a ii) dedicated masking element chip what enables the end-user laboratories to easy adapt their deposition technique by selectively form their sensing layers on the heated area and test its functionality. In 2022 we elaborated the concept and designed the appropriate processing technology including the necessary photomask set.

Optical gas sensing

We have been investigating the construction and capability of methane detection by non-dispersive operation principle in the mid infrared region. The goal is to develop a complete setup consists of MEMS elements, such as microheaters and reflectors for IR source, optical channels and detectors. Test setup was built from commercial components, whereas the electronics was constructed in modular form for **driving the IR source** and the **appropriate read-out**. Adequate optical systems was constructed to ensure high IR intensity projection on the detector and improve the achievable signal-to-noise ratio with the applied pathway (30mm). The preliminary results show that the construction is capable to detect methane in the 500 – 50000 ppm concentration range with the accuracy of 1-10%. Nevertheless, in order to minimize device size and eliminate the thermal effects, we plan to adapt digitized detector chips and elaborate the best sensing methodology. The final goal is to fabricate the smallest possible device composed of our micromachied components and a commercially available detector chip.

Microcalorimeters

Having in hand the **stable heaters** we now focus on other applications also. In cooperation with the University Debrecen we have already started to develop a **micro-calorimetric measuring method** to investigate thermally indicated physical-chemical phenomena in thin films. [Ref. 5.1- 5.3]

3D MEMS force sensor for tissue recognition

J. M. Bozorádi, Cs. Dücső, P. Fürjes

Laparoscopic devices have been widely used in the past decades during surgical procedures. Currently they are the golden standard in minimal invasive surgery. Combining these devices with robotic platforms, most notably the Da Vinci system, is more and more common. Minimally invasive (robotic) surgery (MIS) offers several advantages for the patients, although the lack of sensory feedback for the surgeon is also a barrier in its progress. Collecting immediate multi-parametric information about the physical and anatomic conditions of tissues is crucial for the operator to precisely control the robotic actions or support the tissue recognition and pathologic characterization. Smart devices with integrated MEMS force sensors can provide such feedback and improve the safety of these interventions or help in on-site pathologic decisions.

Our goal was to develop a novel device with integrated micromachined 3D force sensors to provide tactile information about the different organs and tissues touched. Piezoresistive force sensory units were integrated with dedicated readout electronics and precisely controlled linear motors solving the accurate tissue deformation to provide more information about the mechanical (elastic) parameters of the analysed materials. In the present work we demonstrate the complex, automatized measurement system – as well as hardware and software solutions – which is capable of implementing in vitro mechanical tissue characterization and thus provides elastomeric and pathological data (see Fig. 5.2).
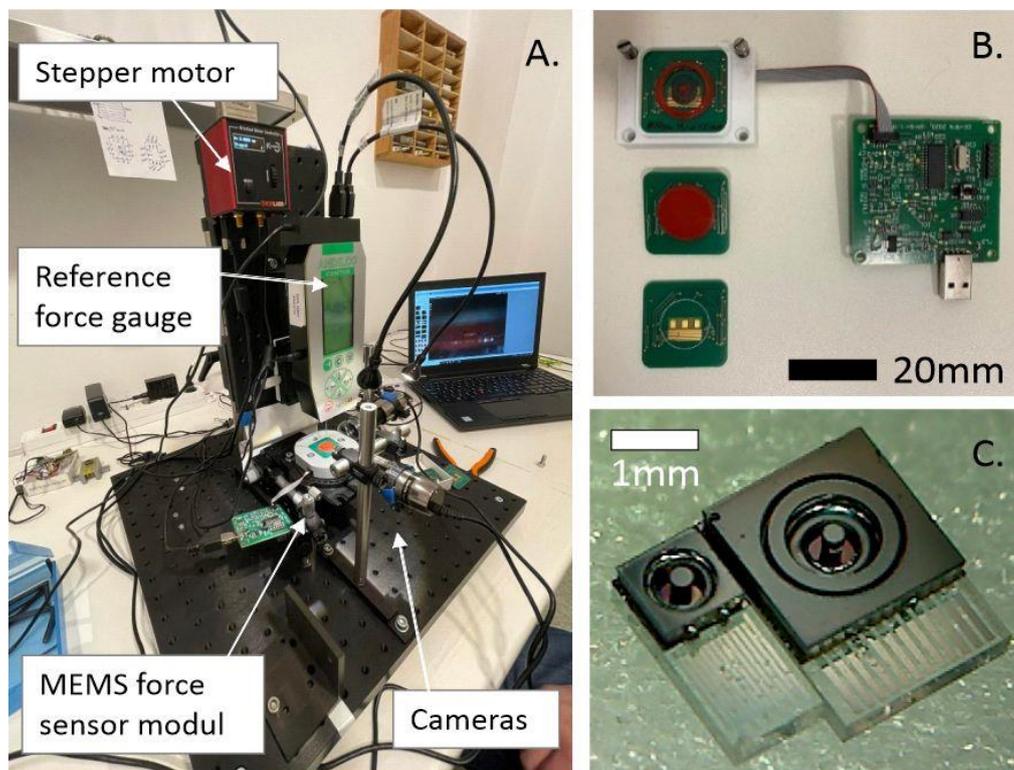
Figure 5.2. *Measurement setup developed for mechanical characterization of elastomers and tissues (A.). The device contains dedicated electronics (B.) for readout and processing the signals of the integrated piezoresistive MEMS 3D force sensors (C.).*

We designed and manufactured 3D piezoresistive force sensors by silicon micromachining technology and mechanically integrated in the appropriate biocompatible packaging and elastic coverage. Application specific readout electronics were also elaborated to solve the analog-digital signal conversion, initialization, noise filtering and the communication with a LabVIEW data acquisition user interface. A custom built Thorlabs stage equipped with a nanometre precision stepper motor and controlled by the LabVIEW based driver interface was used for actuation. Preliminary calibration tests were accomplished to evaluate and compare the force signals of the integrated MEMS sensors to a reference Andilog force gauge as the function of the material deformation.

Tactile measurements were implemented on artificial samples and real animal tissues to prove the feasibility of the device for biomechanical screening during Minimal Invasive Surgery or pathological analysis. The applicability of the setup was proved by differentiation the mechanical behaviour – calculated elastic parameters (Young-modulus) – of various PDMS (polydimethylsiloxane) elastomer samples as the function of their curing agent / elastomer mixing ratios. The elastic properties of the PDMS samples were similar to the commonly published values. After calibration and setup of the packaged MEMS sensors real bovine gastric samples were also characterised and its elastic parameters were also calculated (see Fig. 5.3).
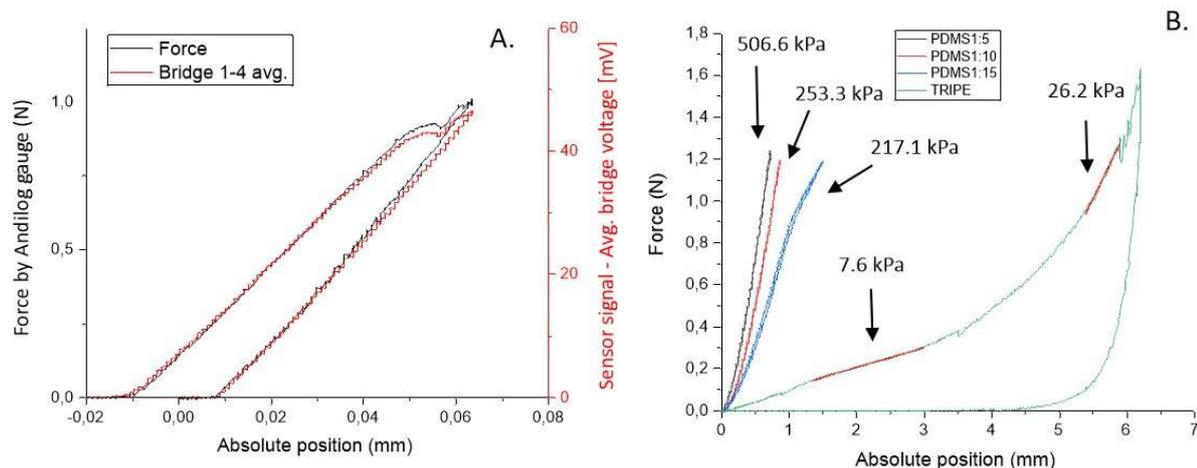
Fig. 5.3. *Deformation dependent signal of the piezoresistive MEMS sensors calibrated by reference force gauge (A.) and the measured force values during the deformation of different PDMS samples and real tissue material (bovine gastric) and the calculated elastic parameters (Young-modulus) (B.).*

The results also demonstrate the deformation dependent and hysteretic behaviour of the artificial viscoelastic and biological samples also, as the Young modulus is continuously changing during the loading procedure (between the values of 7,6 kPa and 26,2 kPa in case tripe). Both of these values was validated and confirmed by different literatures, which correlates with the hardening phenomena of real tissues experienced by surgeons during stapling procedures. On the basis of the results both a compact measurement setup and a prototype electronics were developed for in vitro human tissue measurements. [Ref. 5.4-5.6]

Microfluidic methods for particle and cell manipulation – filtering, sorting, capturing

### Thematic Excellence Programme TKP2021-EGA-04

A. Bányai, P. Hermann, O. Hakkel, E. L. Tóth, P. Fürjes

In several diagnostic applications, the main goal is to develop **microfluidic cartridge** for certain subtasks of **sample preparation and handling**, which then can be integrated into an optical or electro-chemical measurement instrument. The integrated Lab-on-a-Chip cartridge must include transport and filtration of the liquid sample, positioning of bacteria in the detection chamber over the sensing layer. Hydrodynamic principle based **microfluidic filters and lateral concentrating structures** were developed and evaluated by their filtration efficiency for different particle sizes; and by the target loss ratio in the size range of bacteria.

Filtration efficiencies of crossflow type microfilters for E.Coli separation

Crossflow filtration is a pressure-controlled separation method for size dependent segregation of fine particles, microorganism, spores or even micelles. It is a preferred technology in the food industry to remove bacteria or in healthcare for high-throughput plasma filtration. In contrast to dead-end filtration processes, the filter surface is parallel to the liquid flow in case of crossflow separation, thereby significantly reducing the possibility of clogging. The particle separation in these crossflow systems is based on the pore size, although the filtration process is sensitive to the flow rate, transmembrane pressure, membrane resistance, layer resistance, and particle size distribution in the suspension.

Crossflow microfluidic systems with parallel filter structure were parameterized and designed to optimize the separation efficiency and the amount of the target in the filtrate. For preliminary tests multi-disperse fluorescent beads (with 2µm, 6µm, 16µm diameters) were used as a model representing the particles and cells in urine. The target E.coli was initially modelled with 1.97µm diameter polystyrene beads before applying GFP-labeled E. coli bacteria. The trajectories of the fluorescent beads and GFP-E.colis, the developing compaction layer on the filter's surface and consequently the degree of target loss were characterized by fluorescent microscopy. The efficiency of the filtration was determined by particle counting by Bürker chamber and by Luna-II imaging based cell counter also. The columnar and weir type filter architectures were compared: the latter was considered more advanced.
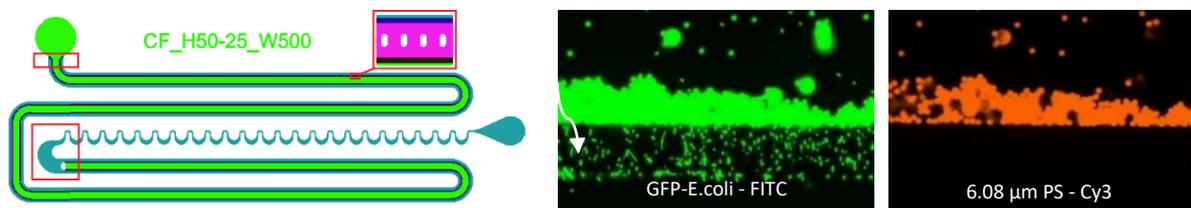
Figure 5.4. *Crossflow filter architecture (left) and the structure of the compaction layer during filtration (right)*

Lateral focusing modell particles and real cell samples

After filtering every larger component of the urine sample, the permeated bacteria must be vertically and possibly laterally focused in the detection chamber in order to achieve high trapping efficiency on the functionalized surface. The inertial focusing phenomenon was investigated, which can be used as a passive method for sample preparation and target manipulation in case of particulate suspensions. Asymmetric channel geometry was designed to apply additional inertial forces besides lift forces to promote laterally ordered particles to achieve sheathless focusing or size dependent sorting. In these channels secondary flow – counter rotating Dean vortices – also promotes lateral focusing further to a single point beside the inertial forces. The parameter dependence of the fluidics were determined with the ratio of particle size (a) and the hydrodynamic channel diameter (D_h): $a/D_h > 0.07$, above which successful focusing is expected. The evolving hydrodynamic forces were tailored with altered channel parameters (width and height), and different flow rates, to get a better understanding of smaller beads' lateral migration. The behaviour of the microfluidic system was tested by using artificial fluorescent beads with different sizes (diameter of 15.8 µm – 6.08 µm – 1.97 µm beads) and real samples as GFP-modified E. coli, red blood cells, yeast cells and HeLa tumour cells also.
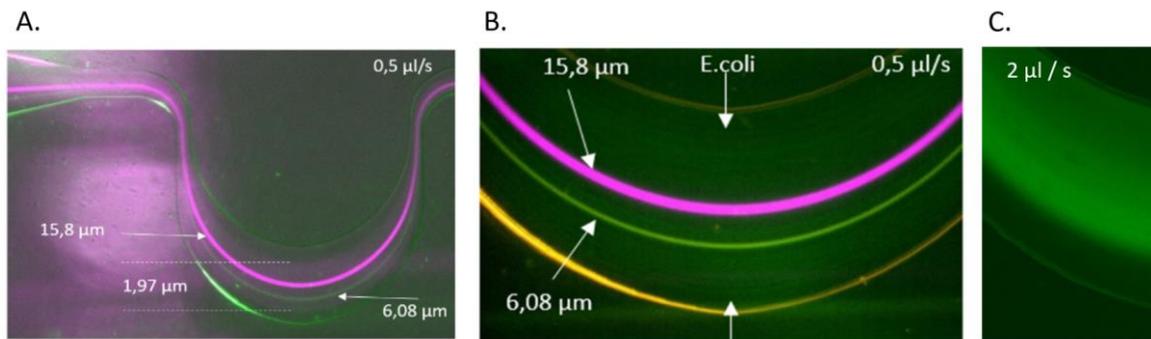
Figure 5.5. *Lateral focusing in pressurized flow with different particle sizes. A.) Lateral focusing of beads at 0.5 µl/s flow rate: 15.8 and 6.08 µm beads, and concentration of 1.97 µm beads at the end of the lateral focusing unit. B.) E.coli could not be focused in the very same structure, shape: stick, dimensions: 0.5 and 2 µm. C.) E.coli concentration at decreased channel height (15 µm), and increased flow rate (2µl/s).*

Computational fluid dynamics (CFD) simulation was also performed using COMSOL Multiphysics (version 5.3a) to analyse and predict particle movement in the specially designed microchannels. Finite Element Modelling (FEM) is applied to numerically calculate the Navier-Stokes equation considering laminar flow due to the low Reynolds number regime. Particle tracing module was used to calculate particle trajectories in the pre-solved velocity field. Dean vortices evolving in curvature are visualised in Fig. 5.6 and the Poincare map represents the calculated positions of the particles at the outer surface of the microfluidic systems.

The position and extent of the focused region were investigated using polystyrene fluorescent beads with different bead diameters (Ø = 0.5 – 16.5 µm) at flow rates 0.5 – 2 µL/s. Size-dependent focusing generated a precise map of the equilibrium positions of the spherical beads at the end of the periodically altering channels. Comparing them with the four types of living cells – E.coli – RBC – Saccharomyces cerevisiae – HeLa cells – they gave a good benchmark for focusing multi-dimensional particles and cells (see Fig. 5.7).
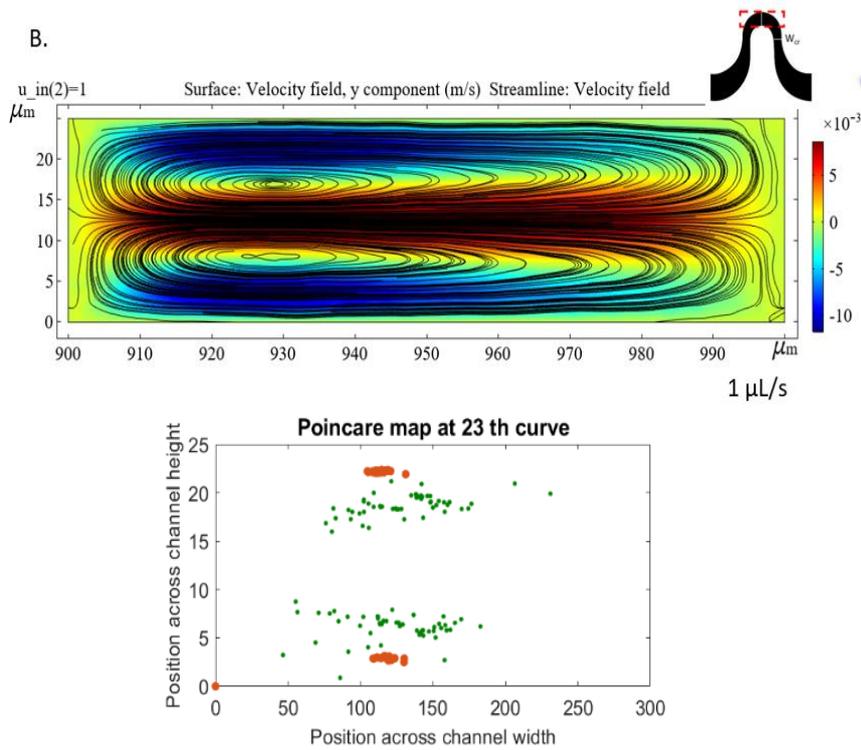
Figure 5.6. *Dean vortices evolving in the curvatures (up) can be visualised by Finite Element Modelling. The Poincare-map (down) shows the equilibrium positions of the modell beads (diameters: 15.8 μm and 6.08 μm) in the channel cross-section. The presence of the Dean vortices depicted in the smaller bend in the channel cross-section.*
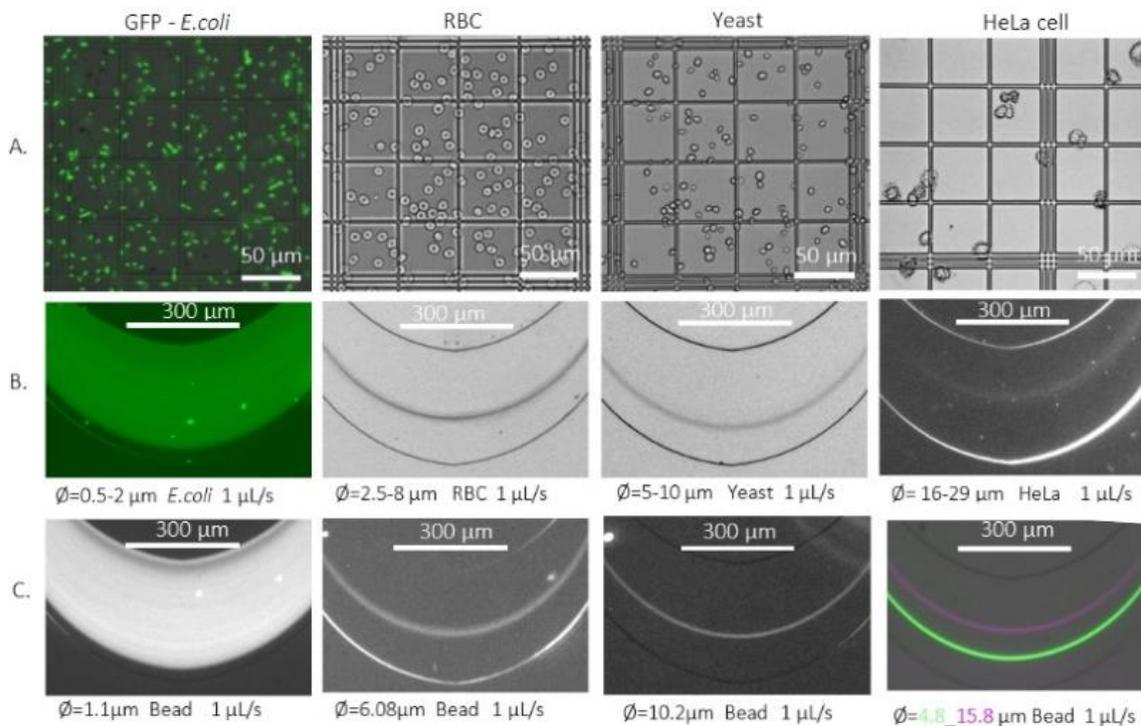
Figure 5.7. *Lateral focusing of biological cells and their rigid model beads at 1 μL/s flow rate. The size and morphology of the applied biological sample were studied (A), and their lateral positions (B). (C) is the polystyrene bead profiles that best describes the lateral focusing position and profile of the given cell sizes.*

Single cell trapping and viability testing

In vitro testing of cell populations or individual cells in artificial systems that model their real environment is highly prospective from a biomedical and environmental point of view. Specially designed microfluidic systems allow the development of such a controllable chemical environment that is comparable to the size of cells. The application of such Organ-on-chip devices, which integrate sensing functions, can be a significant step in the research of pharmaceutical agents, but also in facilitating the spread of personalized medicine. Cell trapping and fluorescent dying are powerful tools that enable the investigation of cell viability and proliferation in microfluidic structures.

A microfluidic system capable of trapping cells individually was created and the viability of yeast cells was investigated. The microfluidic chip had narrowing channels with the dimensions compatible with the size of cells and being capable of trapping yeast cells (diameter: 5-10 μm). The optimal concentration of cell suspension was determined to ensure the trapping of individual cells in the traps, thus conducting single-cell tests. After the cells were trapped a fungicide solution (50 mg/l Penconazole - $C_{13}H_{15}C_{l2}N_3$ - Syngenta TOPAS 100 EC) was injected into the fluidic channels and then the dead cells were dyed with propidium iodide fluorescent dye (see Fig. 5.8). Concentration dependent physiological effect on fungi was observed by fluorescent microscopy and compared to the results of optical spectroscopy. The established microfluidic system has been proved capable of trapping individual cells and observing their physiological processes in artificial chemical environment.
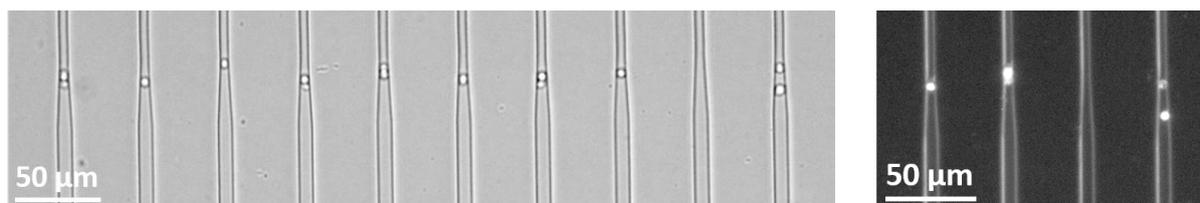
Figure 5.8. *Captured cells in microfluidic systems (left) and dyed with propidium iodide in fungicide chemical environment (right).*

Magnetophoretic trapping in microfluidic system

Immunomagnetic separation methods based MEMS systems are quite straightforward for high-volume particle separation for bioanalytical applications. In this work different microfluidic channel geometries and secondary morphological inhomogeneities were applied to modulate the local magnetic trapping efficiency. The effect of the combined magnetophoretic and hydrodynamic phenomena was analysed experimentally and by finite element modelling to optimise the trapping pattern and to increase the local distribution of captured beads at higher flow rates.

25μm_1μl/s_2.8μm_ H: 10x4x2 mm³_N52
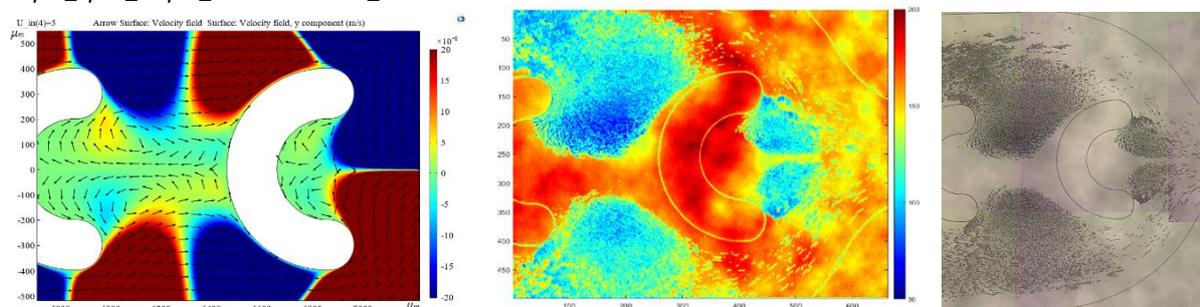
Figure 5.9. *Flow velocity distribution (left) determines the magnetophoretic trapping of ferromagnetic particles in the microfluidic systems (right).*

The high-volume flow-through magnetophoretic separation method was tested in specially designed microfluidic devices. Permanent neodymium magnets, attached from the bottom side of the channel ensured the magnetic flux. The applied channel heights (25, 50 µm) and morphological inhomogeneities – as secondary columns and walls (C-shape, D-shape, Zig-zag) in the middle of the channel – were varied to modulate the location dependent trapping efficiency and to form proposed lateral pattern of the magnetic beads (Ø= 2.8 µm) even at higher flow rates (0.5-1-2 µL/s).

The trapping pattern of magnetic beads were recorded, and the experimental results were compared to finite element (FEM) simulations performed by COMSOL Multiphysics software. The combined effects of the superpositioned magnetophoretic and hydrodynamic processes were investigated – considering the flow velocity field evolving in the chamber around the built in inhomogeneities. Based on the developing local concentration distribution of the magnetic beads the applicability of the multi-domain finite element model was proved to represent and predict the trapping behaviour of the magnetic beads realistically at even higher flow rates. [Ref. 5.7-5.12]

Development of near infrared LEDs and spectroscopic applications

B. Beiler, K. Pankász, F. Bíró, J. M. Bozorádi, Cs. Dücső, P. Fürjes, Z. Szabó

Infrared spectroscopy is a very popular measurement technique especially in food industry, pharmaceutical industry and agriculture for the detection and measurement of organic materials. The -OH, -NH and -CH functional groups found in organic substances can frequently be detected by spectroscopy through absorbance measurements at the resonance wavelength of valence-bond vibrations. The measured wavelengths are 4-2.5μm, while the signal to noise ratio of photon detectors is low due to thermal noise at room temperature. The 1st-3rd harmonic absorption bands are located in the range of the near infrared (NIR), where smaller signals can be measured effectively in practice. NIR LEDs have narrow wavelength, therefore they are suitable for measurements at given wavelength. Further advantages of LEDs compared to incandescent lamps are their small dimensions, high efficiency, and low power consumption, which is critical in small handheld devices.

GaInAsP/InP is an ideal material system for the fabrication of double heterostructure devices as the emission wavelength is easily tuneable between 950-1650 nm. As InP has higher bandgap than the lattice-matched GaInAsP active layer the absorption losses inside the device structure can be minimized. In order to tune the emission wavelength of the LED, the composition of the semiconductor light-emitting layer has to be properly set. Our high quality single peak LED chips (1220nm) have a stable market with a business partners as SENOP Oy (Fi) and Anton Paar Ltd. (At).

Development multiple wavelength or broadband IRLED

In the cases when a broader emission-peak is preferred for spectroscopic applications, multiple solutions are known. One of them is where the primary light coming from the active layer of the diode excites the second smaller band gap epitaxial layer producing secondary light by photoluminescence. The partly transmitted primary and the secondary light together result in a broader spectrum. Our research group has already demonstrated the method by integrating one active and one photoluminescent layer using liquid phase epitaxy (LPE). Specific InGaAsP/InP layer structures were grown by LPE to fabricate wide emission-spectrum near-infrared LEDs. The final multilayer structure could be achievable in two consecutive LPE growth steps: by growing 2 InGaAsP photoluminescent layers with the emission peaks of ca. 1320 nm and 1500 nm first and by growing other photoluminescent (1650 nm) and the active (1220 nm) layers in the second step.

Samples were characterized by optical transmittance and photoluminescence measurements right after each LPE growth steps. The derivative transmittance spectrum shows information about the optical band gap, thickness and quality of the grown layers. The photoluminescence-intensity of the layers depends on the thickness of the InP separation layers due to the optical and charge carrier coupling also. Scanning electron microscope was used to measure layer thicknesses and to verify epitaxial crystal formation. The LED chips were characterized electrically and optically as well. The I-V curves showed the expected diode characteristics while the 4 emission peaks appeared on the emission spectrum. The slightly unbalanced emission spectrum can be improved by precisely adjusted layer thicknesses. The integrated emitted optical power is ca. 1/3 of the optical power of the standard 1220 nm LED. This loss is due to the energy difference of the primary and secondary photons but implies high conversion efficiency. [Ref. 5.13]
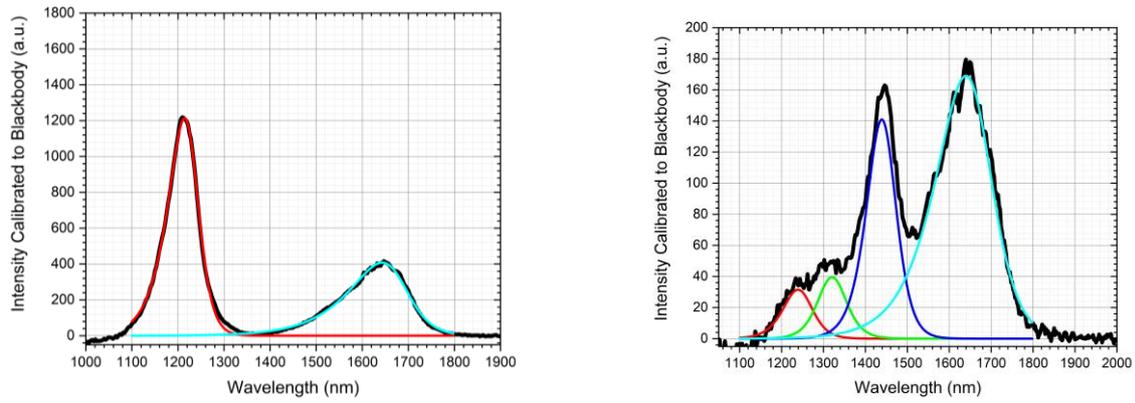
Figure 5.10. *Optical radiation spectra of different multi-layered IR-LED structures (combinations of 2 (left) and 4 (right) wavelengths).*

Plate reader-compatible microfluidic chambers for fluorescent spectroscopy

D. Bereczki, A. Füredi, P. Fürjes

Fluorescence spectroscopy is a widespread method to measure concentrations of specific drug molecules such as active pharmaceutical ingredients (APIs) or their impurities. It is also commonly used to determine the content of components in biological samples and to characterize the mechanism of reactions between proteins and small-molecule drugs. The emitted fluorescent wavelength and the intensity can be characteristic signals of a chosen molecule conformation and concentration by fluorescent spectroscopy. Plate readers or benchtop spectrophotometers are appropriate for screening these molecules. To analyze reduced sample volume, a device-compatible microfluidic cuvette should be applied. Considering UV-VIS range excitation, a proper material selection for the microfluidic system is crucial to ensure appropriate sensitivity. To reduce the sample volume a plate reader-compatible microfluidic system was designed and fabricated by soft lithography. For increased sensitivity, the geometric parameters of the microfluidic structure were optimized by modifying the chamber diameter and depth.

For VIS range excitation, the spectral fluorescent properties of the well-known Alexa Fluor 350 dye were screened by Tecan Spark Plate Reader in both microplate and the manufactured microfluidic chip. The applied glass window material was suitable for excitation above 350 nm. The signal intensity and linearity were tested by applying well-designed microfluidic chambers for 20 µl sample volume and compared to conventional microplate-based spectrophotometric methods. To characterize the applicability of the specific cuvette in the UV excitation range, window materials – glass and fused silica – were compared by analysing the fluorescent emission spectra of G-1™ PLUS (Vitrolife) cell culture media containing 5 mg/mL Human Serum Albumin (HSA). Consequently, advanced sensitivity and excellent linearity were achieved by using a well-designed microfluidic cuvette and the plate reader-compatible structure, what is appropriate to determine the concentration of APIs having fluorescent characteristics in the UV-VIS range. [Ref. 5.14-5.15]
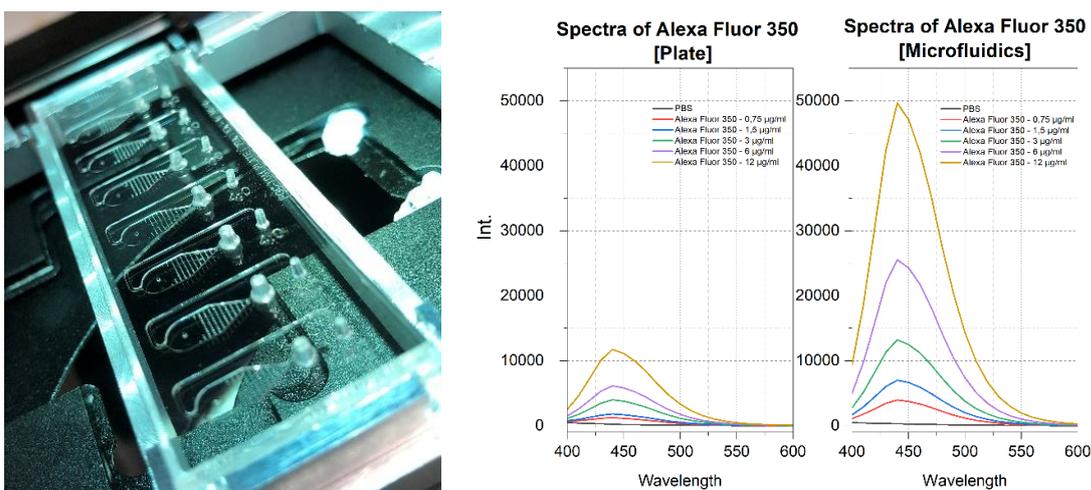
Figure 5.11. *Plate Reader-compatible microfluidic cuvette (A) and optical spectra of Alexa Fluor 350 dye (B) compared in a plate and in microfluidic chip – measured in 5 different concentrations (0,75-12 µg/ml).*

Nanobiosensorics Momentum Goup

Head: Robert HORVATH, Ph.D., Senior Scientist

Research Staff
- Robert HORVATH, Ph.D.
- Sándor KURUNCZI, Ph.D.
- Inna SZÉKÁCS, Ph.D.
- Beatrix PÉTER, Ph.D.
- Boglárka KOVÁCS, Ph.D.
- Zoltán SZITTNER, Ph.D.
- Enikő FARKAS, Ph.D
- Nicolett KANYÓ, MSc
- Beatrix MAGYARÓDI, MSc

Ph.D. students / Diploma workers
- Ágoston NAGY, Ph.D. student
- Tamás GERECSEI, Ph.D. student
- Kinga Dóra KOVÁCS, PhD student
- Bálint BÉRES, PhD student
- Imola RAJMON, BSc student
- Anna BALOGH, BSc student
- Szabolcs NOVÁK, MSc student
- Zsolt, JANKA MSc student
- Viktor Sándor KOVÁCS, BSc student
- Tamás HAJDŰ, MSc student
- Lili FARKAS, MSc student
- Igor SALLAI, MSc student
- Norbert PAP, BSc student
- Róbert TARR, BSc student
- Kinga TÓTH, BSc student
- Barbara MAJOROS, MSc student
- Péter JOÓ, MSc student
- Krisztina BORBÉLY, MSc student

The research profile of the Nanobiosensorics Group is the development and application of label-free optical biosensors, the mathematical modeling of the relevant biological and biophysical processes. Building on their broad national and international collaborative network the group conducts research in the fields of instrument development, monitoring of cell secreted extracellular vesicles, development of protein-based functional coatings, adhesion studies on human cancer and immune cells, and theoretical modeling. In 2014, the application for an ERC Consolidator Grant by the head of the research group received qualification category "A (fully meets the ERC excellence criteria and should be funded if sufficient funds are available)" after the interview in Brussels, but the funding line did not reach this proposal due to budgetary constraints. However, using this achievement the Group could successfully apply for funding from NKFIH in the framework of the ERC_HU call. In the framework of this project they aim single cell manipulation and label-free sensing. Building on this expertise, in 2018 they won an Élvonal (NKFIH) research project for single cell biosensing. In 2020, the research group won the Tématerületi Kiválósági Program (TKP) excellence project as well in collaboration with other groups of the MFA.

Characterization of the dissolution of water microdroplets in oil

LP2012-26/2012 Lendület, OTKA ERC_HU 117755, and OTKA KKP129936

T. Gerecsei, R. Ungai-Salánki, A. Saftics, I. Derényi (ELTE), R. Horváth, B. Szabó (ELTE)

The main objectives are to develop highly sensitive and reliable label-free high-content optical methods. Water in oil emulsions have a wide range of applications from chemical technology to microfluidics, where the stability of water droplets is of paramount importance. Here, using an accessible and easily reproducible experimental setup we describe and characterize the dissolution of water in oil, which renders nanoliter-sized droplets unstable, resulting in their shrinkage and disappearance in a time scale of hours. This process has applicability in creating miniature reactors for crystallization. We generated nanoliter-sized water droplets dispersed in oil and observed that they gradually shrank and disappeared in a few hours. Using an easily reproducible and low-cost setup based on a spinning Petri dish to generate the nanoliter scale droplets and an inverted microscope to observe them (Fig. 6.1), we monitored the contact radius and the volume of droplets, without the need for specialized droplet printing equipment [Ref. 6.1].
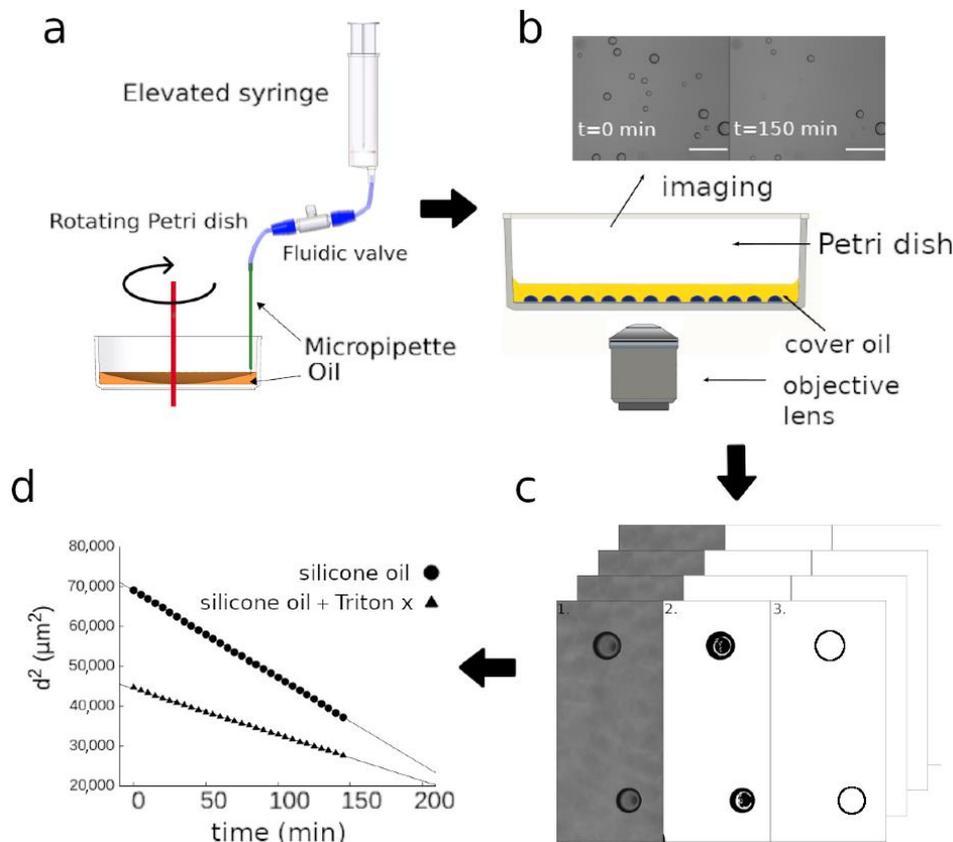
Figure 6.1*. The workflow of droplet diameter measurements. (a): The droplets are generated by a water filled micropipette immersed in a rotating Petri dish containing oil. (b): The Petri dish with the w/o emulsion is placed on an inverted microscope and images are taken in time-lapse mode. Scale bars indicate 100 μm. (c): Image stacks are segmented to detect and track the droplets. (d): Diameter of droplets is automatically measured to plot the curves of droplet dissolution*

Development and in-depth characterization of bacteria repellent and bacteria adhesive antibody-coated surfaces using optical waveguide biosensing

E. Farkas, R. Tarr, T. Gerecsei, A. Saftics, K. D. Kovács, B. Stercz (SOTE), J. Domokos (SOTE),
B. Péter, S. Kurunczi, I. Székács, A. Bonyár (BME), A. Bányai, P. Fürjes, Sz. Ruszkai-Szaniszló (77E),
M. Varga (77E), B. Szabó (77E), E. Ostorházi (SOTE), D. Szabó (SOTE), R. Horváth

Bacteria repellent surfaces and antibody-based coatings for bacterial assays have shown a growing demand in the field of biosensors, and have crucial importance in the design of biomedical devices. We described an OWLS-based method supporting the development of bacteria repellent surfaces and characterize the layer structures and affinities of different antibody-based coatings for bacterial assays (Fig. 6.2). The best performance in the biosensor measurements was achieved by employing a polyclonal antibody in combination with protein A-based immobilization and PAcrAM-P blocking of nonspecific binding. Using this setting, a surface sensitivity of 70 cells/mm^2 was demonstrated [Ref. 6.2].
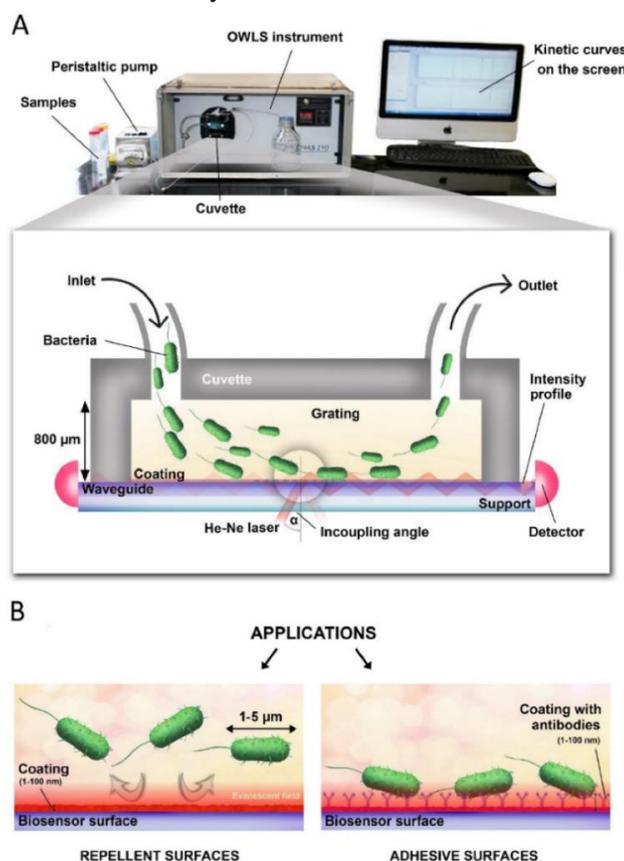
Figure 6.2. *(A) Cross-sectional view of the OWLS cuvette and the basics of optical detection. Laser light is coupled into an optical waveguide layer by a surface grating where it propagates by total internal reflection to a photodetector placed at the end of the waveguide. Adsorbing bacteria shift the resonant angle (α). (B) OWLS is an ideal tool for testing and developing both bacteria repellent and bacteria adhesive surfaces.*

Single-cell adhesivity distribution of glycocalyx digested cancer cells from high spatial resolution label-free biosensor measurement.

N. Kanyó, K. D. Kovács, S. V. Kovács, B. Béres, B. Péter, I. Székács, R. Horváth

The glycocalyx is a cell surface sugar layer of most cell types that greatly influences the interaction of cells with their environment. Interestingly, cancer cells have a thicker glycocalyx layer compared to healthy cells, but to date, there has been no consensus in the literature on the exact role of cell surface polysaccharides and their derivatives in cellular adhesion and signaling. In our study, a high spatial resolution label-free optical biosensor was employed to monitor the adhesivity of cancer cells both at the single-cell and population level (Fig. 6.3). Population-level distributions of single-cell adhesivity were first recorded and analyzed when ChrABC was added to the adhering cells. The presented results open up new directions in glycocalyx related cell adhesion research and in the development of more meaningful targeted cancer treatments affecting adhesion [Ref. 6.3].
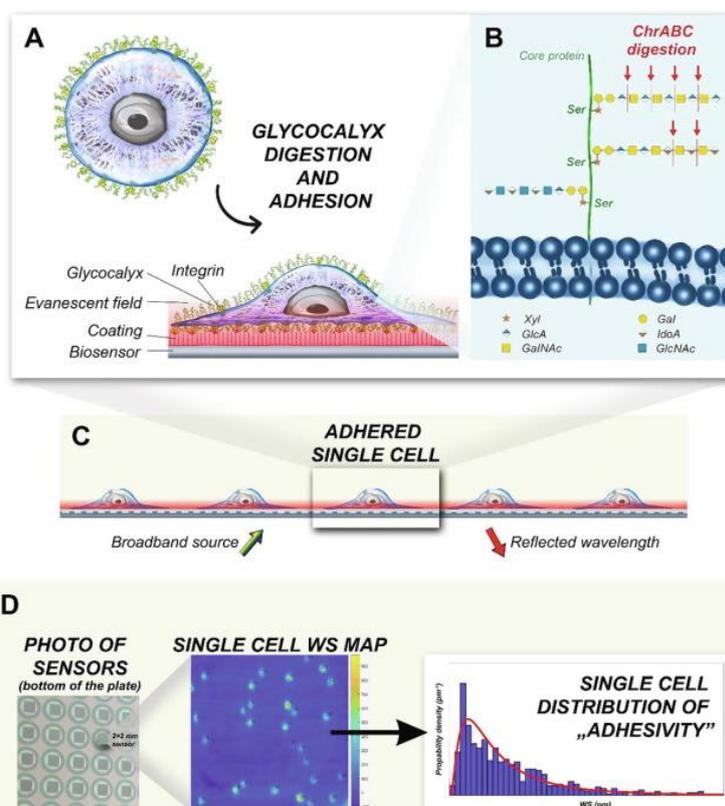
Figure 6.3. *chematic representation of the applied label-free method. (A) ChrABC enzyme digests the glycocalyx components of the HeLa cells. (B) Schematic illustration of the glycocalyx components. (C) With the RWG biosensor, even single-cells can be studied with high resolution. (D) The device works with 384-well microplates with 2×2 mm RWG biosensors in each well. The primary output of the device is the wavelength shift (WS) map in each well.*

Epigallocatechin-gallate tailors the cell adhesivity of fibronectin coatings in oxidation and concentration-dependent manner

B. Péter, N. Kanyó, I. Székács, A. Csampai (ELTE), Sz. Bősze (ELTE), R. Horváth

Fibronectin is an extracellular matrix component that plays a significant role in many physiological processes, such as cell adhesion, growth, differentiation, and migration. In our study, we revealed the interaction between this important protein and the widely studied natural active substance green tea polyphenol epigallocatechin-gallate (EGCG) and its oxidized form. Furthermore, we investigated the kinetics of cancer cell adhesion on the polyphenol-treated fibronectin coatings. We applied a high-throughput, label-free optical biosensor capable of monitoring the above processes in real time with an excellent signal-to-noise ratio (Fig. 6.4) [Ref. 6.4].
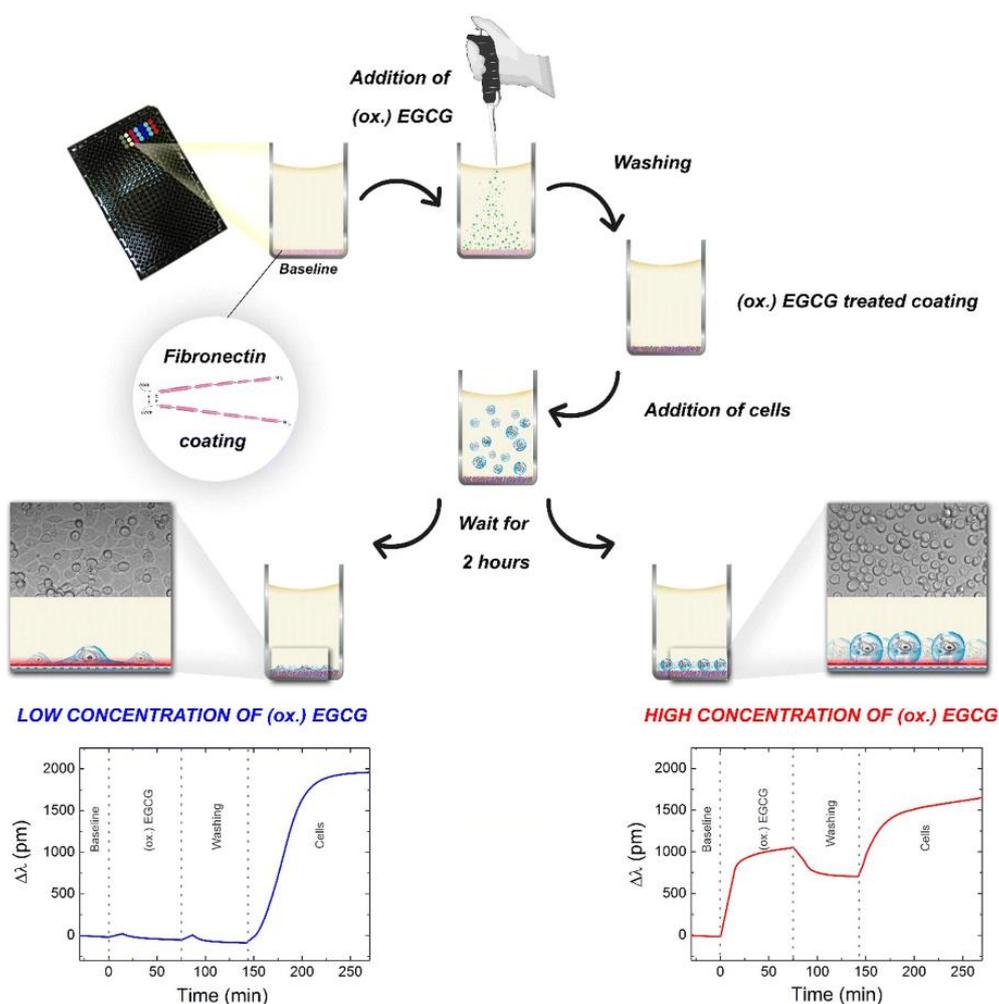
Figure 6.4. *Schematic illustration of the measurement procedure and the typical kinetic curves obtained on the fibronectin coating.*

Functional blood cell analysis by label-free biosensors and single-cell technologies

Z. Szittner, B. Péter, S. Kurunczi, I. Székács, R. Horváth

Our aim was to summarize the current state of methods for label-free identification and functional characterization of leukocytes (Fig. 6.5) with biosensors and novel single cell techniques in a review article. The emphasis is on techniques on the characterizations of single cells with special attention to surface sensitive technologies. Recent developments highlighted the importance of small cell populations and individual cells both in health and disease. Nonetheless techniques capable of analyzing single cells offer a promising tool for therapeutic approaches where characterization of individual cells is necessary to estimate their clinical therapeutic potential [Ref. 6.5].
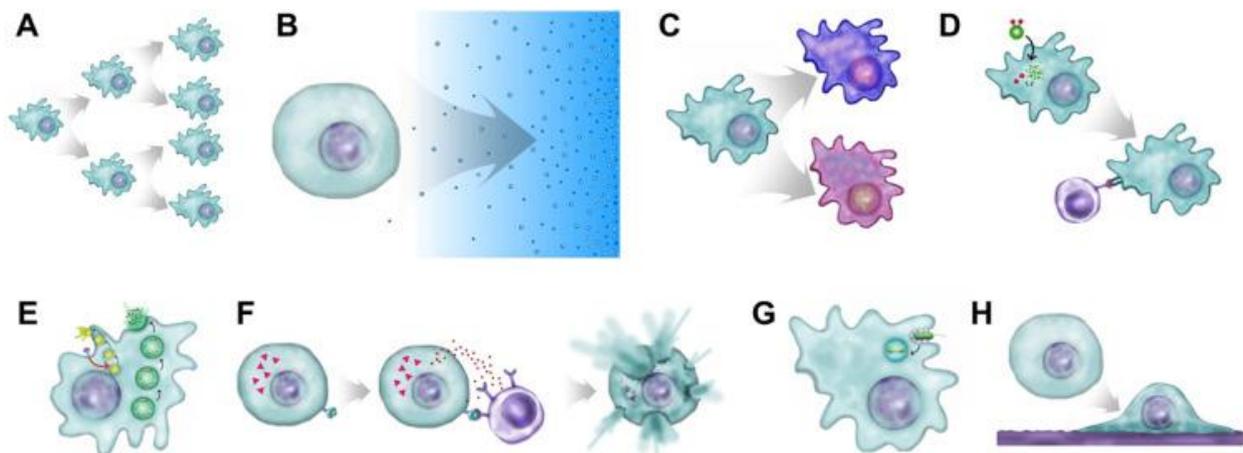
Figure 6.5. *Examples of leukocyte functions detectable by label-free biosensors (A) proliferation (B) chemotaxis (C) cell polarization and activation (D) antigen presentation (E) degranulation and secretion (F) cytotoxicity (G) phagocytosis and (H) adhesion.*

Population distributions of single-cell adhesion parameters during the cell cycle from high-throughput robotic fluidic force microscopy

LP2012-26/2012 Lendület, OTKA ERC_HU 117755, TKP2021-EGA-04 and OTKA KKP 129936

Á. G. Nagy, N. Kanyó, A. Vörös, I. Székács, A. Bonyár (BME), R. Horváth

Robotic fluidic force microscopy (FluidFM) was utilized to measure the adhesion parameters of cells in a high-throughput manner to study their population distributions in-depth. The investigated cell type was the genetically engineered HeLa Fucci construct with cell cycle-dependent expression of fluorescent proteins (Fig. 6.6). We first revealed that reticular adhesion can exert a higher force per unit area than canonical focal adhesions, and cells in this phase are significantly stiffer. The possible biological consequences of these findings were also discussed, together with the practical relevance of the observed population-level adhesion phenomena [Ref. 6.6].
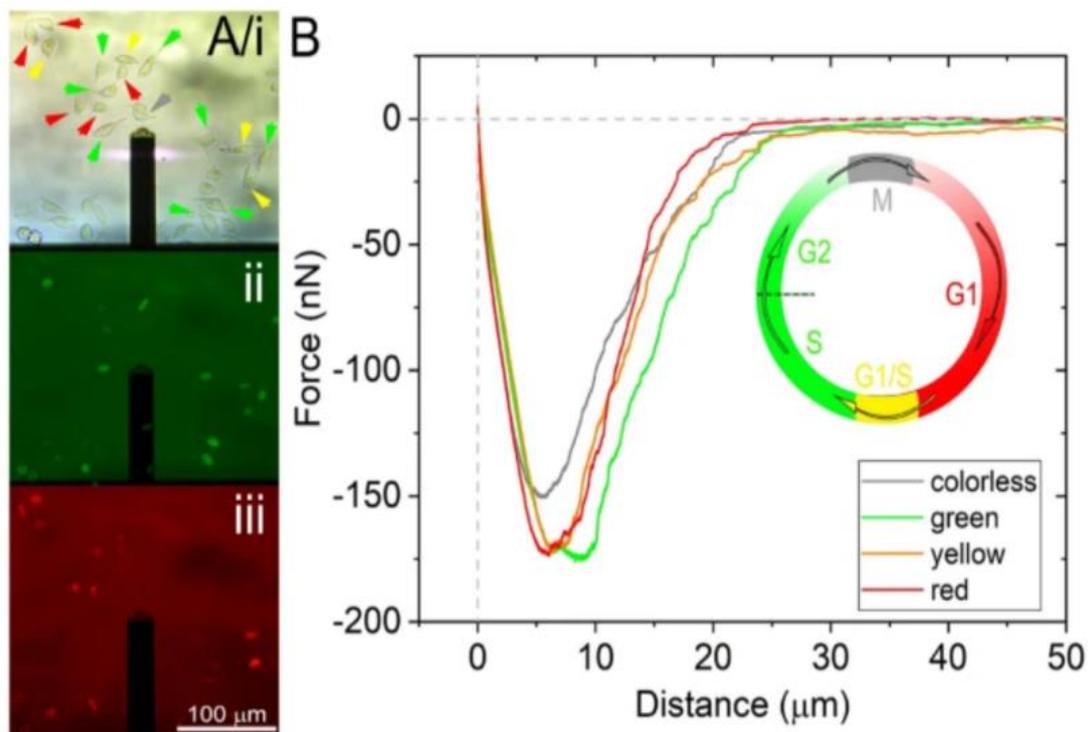
Figure 6.6. *The Fucci construct and the actual measurement when the FluidFM cantilever is approaching the targeted cell. (A) Schematics of the HeLa Fucci cycle indicate the colors visible during the different phases. Fluorescent images were taken during the measurements on the FluidFM platform. (B) Averaged characteristic curves were obtained from each measurement belonging to different color phases of HeLa Fucci cells.*

Cell-substratum and cell-cell adhesion forces and single-cell mechanical properties in mono- and multilayer assemblies from robotic fluidic force microscopy

Á. G. Nagy, I. Székács, A. Bonyár (BME), R. Horváth

We studied the cellular adhesion maturation of epithelial Vero monolayers by measuring single-cell force-spectra with FluidFM. We found that HeLa cells adhere significantly stronger to the tight Vero monolayer than cells of the same origin. Moreover, the mechanical characteristics of Vero monolayers upon cancerous HeLa cell influence were recorded and analyzed (Fig. 6.7) [Ref. 6.7].
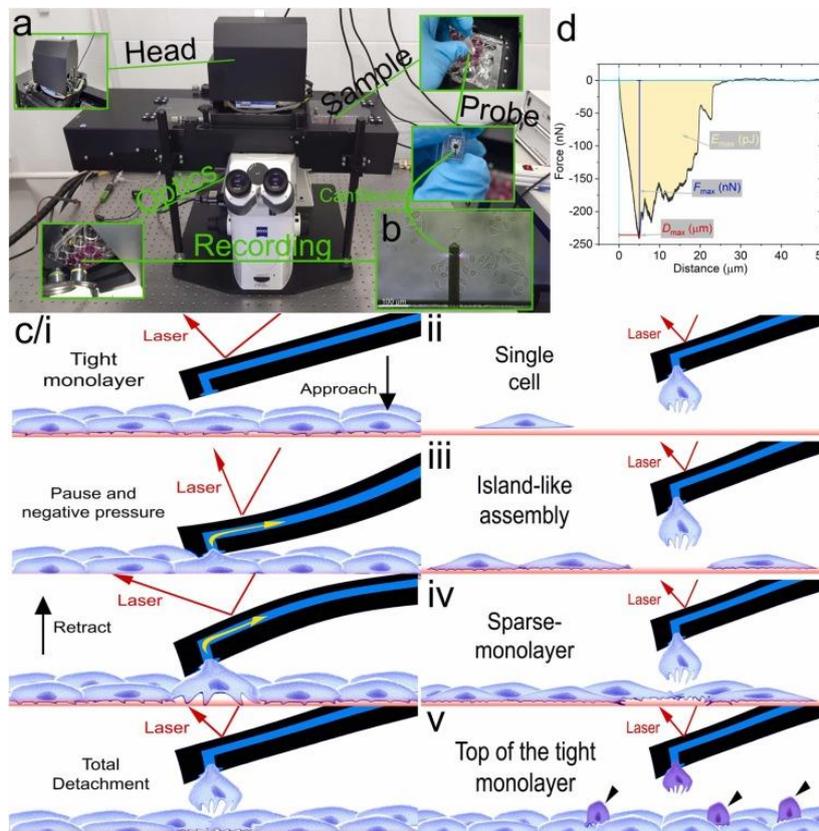
Figure 6.7. *Schematic representation of the robotic FluidFM measurement setup and procedure. Living cell cultures on the FluidFM (a) can be observed with an optical microscope (see insert b where the cantilever is clearly visible). Under the measurement head, the large area sample stage allows multiple cell targeting in mm-cm scale areas. c) During SCFS recording, the cell from a tight cellular monolayer (i), single cells (ii), cells from island-like assemblies (iii), cells from a sparse monolayer (iv), or cells seeded on top of the tight monolayer (v, black arrowheads) are approached with the hollow FluidFM cantilever, which pauses upon contact with the targeted cell. Subsequently, suction (vacuum) is applied to attach the cell to the aperture, and the cantilever is retracted from the substrate.*

Simple and automatic monitoring of cancer cell invasion into an epithelial monolayer using label-free holographic microscopy

Á. G. Nagy, I. Székács, A. Bonyár (BME), R. Horváth

The invasiveness of cancer cells describes the metastasizing capability of a primary tumor. The straightforward detection and quantification of cancer cell invasion are important to predict the survival rate of a cancer patient and to test how anti-cancer compounds influence cancer progression. Digital holographic microscopy based M4 Holomonitor (HM) is a technique that allows the label-free monitoring of cell morphological and kinetical parameters in real-time (Fig. 6.8). It was demonstrated that the invasion of single cancer cells is soundly observable and also quantifiable through monitoring parameters such as phase shift, optical volume, area, and motility, which parameters can easily be obtained and processed automatically. Based on the experimental data, the invasion speed of cancer cells entering the epithelial layer can be defined as the shrinking of detected single-cell volume per unit time. [Ref. 6.8].
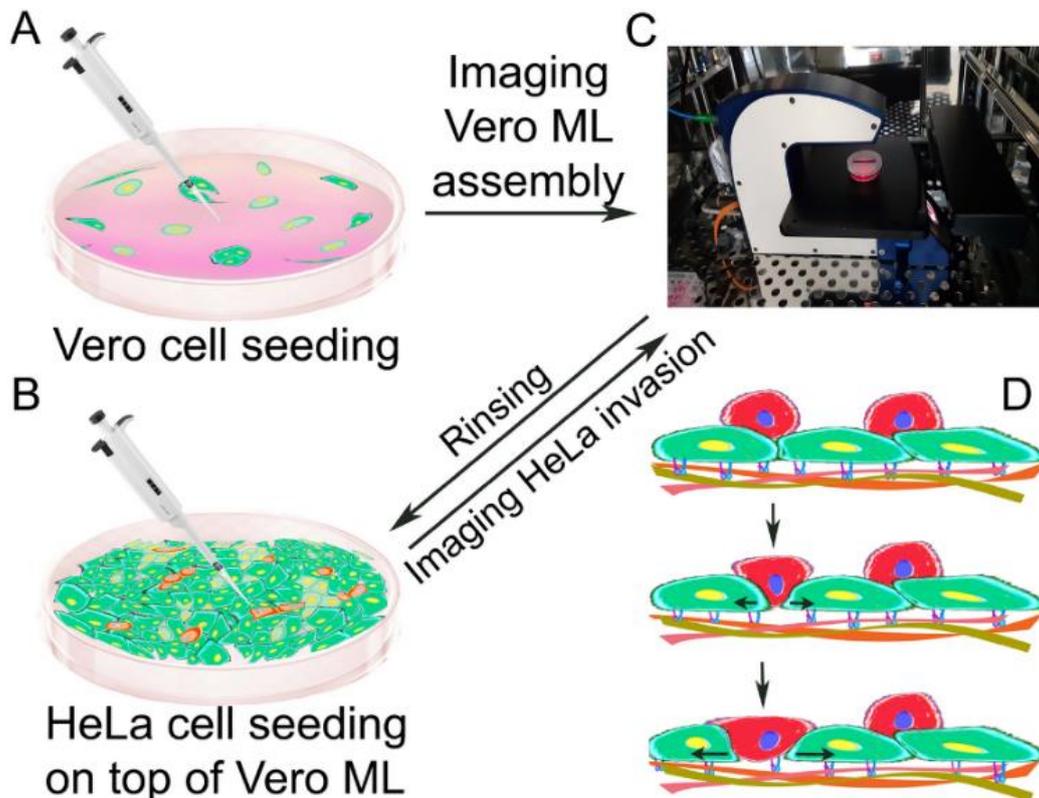
Figure 6.8. *Schematics of experimental design, execution, and results. (A) Seeding of Vero cells (green) on gelatin-coated dish. (B) Seeding of HeLa cells (red) on top of the self-assembled 100% confluent Vero monolayer (ML). (C) Holomonitor M4 was used to image monolayer assembly and invasion for 24 h. (D) Illustration of the expected result, the HeLa cells seeded on top of the Vero monolayer infiltrate by searching for optimal invasion positions.*

Review of label-free monitoring of bacteria: From challenging practical applications to basic research perspectives

B. Péter, E. Farkas, S. Kurunczi, Z. Szittner, Sz. Bősze (ELTE), J. J. Ramsden (University of Buckingham, UK), I. Székács, R. Horváth

Novel biosensors already provide a fast way to detect the adhesion of whole bacteria (or parts of them), biofilm formation, and the effect of antibiotics (Fig. 6.9). Moreover, the detection sensitivities of recent sensor technologies are large enough to investigate molecular-scale biological processes. Usually, these measurements can be performed in real time without using labeling. Despite these excellent capabilities summarized in the present work, the application of novel, label-free sensor technologies in basic biological research is still rare; the literature is dominated by heuristic work, mostly monitoring the presence and amount of a given analyte. The aims of this review are (i) to give an overview of the present status of label-free biosensors in bacteria monitoring, and (ii) to summarize potential novel directions with biological relevancies to initiate future development. Optical, mechanical, and electrical sensing technologies are all discussed with their detailed capabilities in bacteria monitoring. [Ref. 6.9].
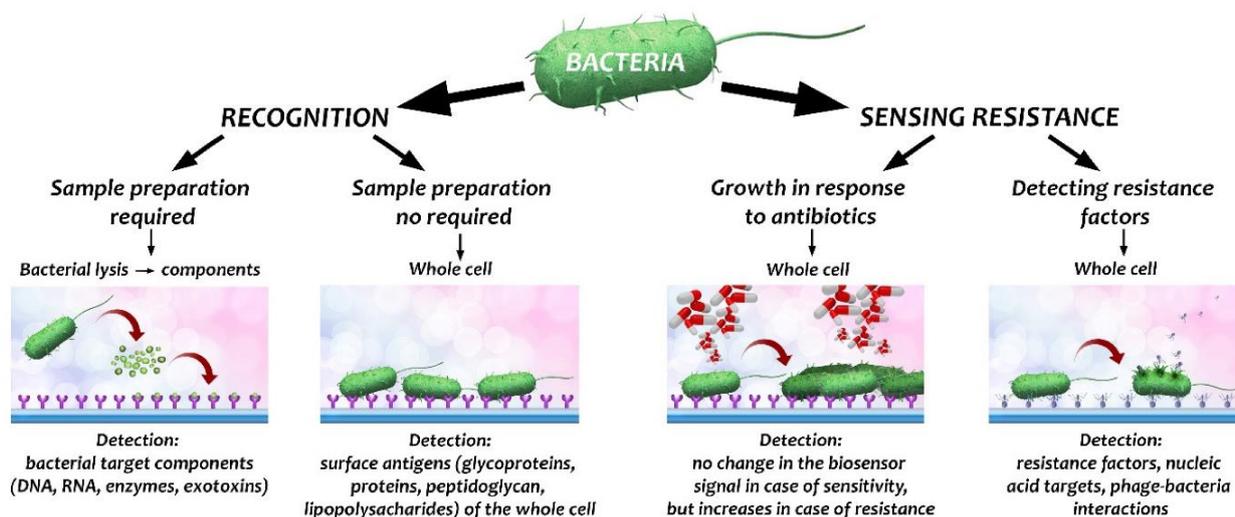
Figure 6.9. *Summary of the strategies of recognition of bacteria and ways of resistance sensing using biosensors. Sample preparation may be needed to lyse the bacteria (or otherwise disrupt them) to liberate the target bacterial components (first column); and preparation-free whole cell-based assays are in the second column. Few biosensors can sense antibiotic resistance as well. There are two possibilities: measuring and monitoring the growth of bacteria during antibiotic treatment (third column) or measuring resistance factor adhesion or bacteriophage– bacterium interaction.*

Prospects of fluidic force microscopy and related biosensors for medical applications

T. Gerecsei, B. Péter, R. Ungai-Salánki, S. Kurunczi, I. Székács, B. Szabó, R. Horváth

The biophysical characterization of cells is gaining momentum nowadays as more and more studies show that biomechanical parameters such as adhesion and stiffness carry relevance both in understanding and in diagnosing diseases. The revolution in the field sparked by atomic force microscopy has accelerated since the introduction of fluidic force microscopy roughly a decade ago. Unparalleled in versatility, it is easy to predict FluidFM to become the gold standard in single-cell manipulation (Fig. 6.10). It has become a common perception in biomedical sciences, especially in cancer research, hematology, and developmental biology to look at populations of cells as a distribution of various phenotypes and gene expression patterns rather than a homogeneous population of identical units. Thus the characterization of single-cells and the identification of subpopulations has gained importance, together with the methods that can be utilized to achieve these goals. The detachment, isolation, injection, and extraction of a wide variety of cell types with high viability has been demonstrated with FluidFM and the list of applications is expected to grow. In this book chapter, we presented and summarized FluidFM and related biosensors for medical applications [Ref. 6.10].
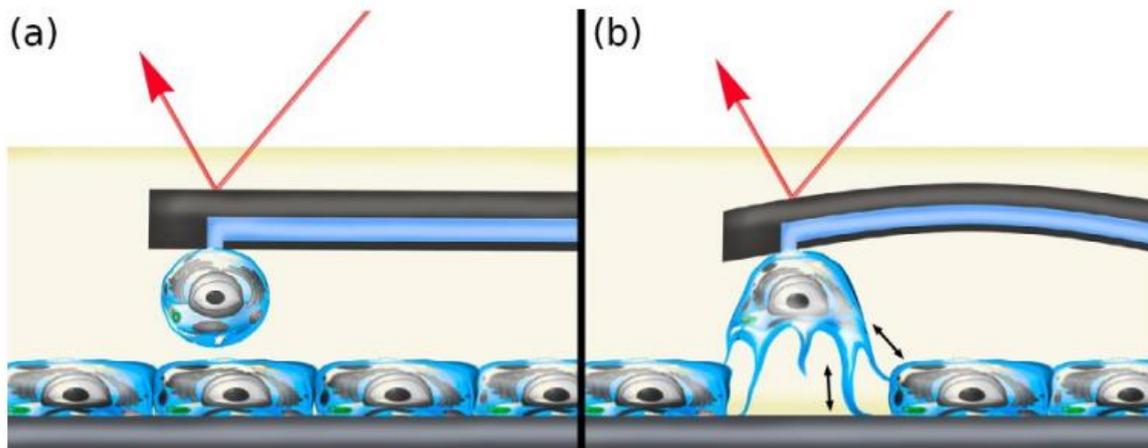
Figure 6.10. *Experimental setups using FluidFM. (A) The cell probe method can be used to study intercellular interaction by pushing the immobilized cell onto an adhered layer. (B) Individual cells can be torn out of a cell layer. Through this method, the cell–cell adhesion force can be determined in a closely packedcellular sheet.*

Cytotoxic effects of Roundup Classic and its components on NE-4C and MC3T3-E1 cell lines determined by biochemical and flow cytometric assays

M. Oláh (MATE), E. Farkas, I. Székács, R. Horváth, A. Székács (MATE)

Cytotoxic effects of the market leading broad-spectrum, synthetic herbicide product Roundup Classic, its active ingredient glyphosate (in a form of its isopropylamine (IPA) salt) and its formulating surfactant polyethoxylated tallowamine (POE-15) were determined on two murine cell lines, a neuroectodermal stem cell-like (NE-4C) and a high alkaline phosphatase activity osteoblastic cell line (MC3T3-E1). Cytotoxicity, genotoxicity, effects on cell viability and cell cycles were examined in five flow cytometry tests (Fig. 6.11), the two former of which were compared by the enzymatic-assay and the alkaline single cell gel electrophoresis (Comet) assay. All of the tests indicated the NE-4C cells being more sensitive, than the MC3T3-E1 cell line to the treatments with the target compounds. Higher sensitivity differences were detected in the viability test by flow cytometry (7–9-fold), than by the MTT assay (1.5–3-fold); in the genotoxicity test by the Comet assay (3.5–403-fold), than by the DNA-damage test (9.3–158-fold); and in the apoptosis test by the Annexin V dead cell kit (1.1–12.7-fold), than by the Caspase 3/7 kit (1–6.5-fold). Cell cycle assays indicated high count of cells (~70%) in the G0/G1 phase for MC3T3-E1 cells, than in NE-4C cell (~40%) after 24 h. The order of the inhibitory potency of the target substances has unequivocally been POE-15 > Roundup Classic > > glyphosate IPA salt [Ref. 6.11].
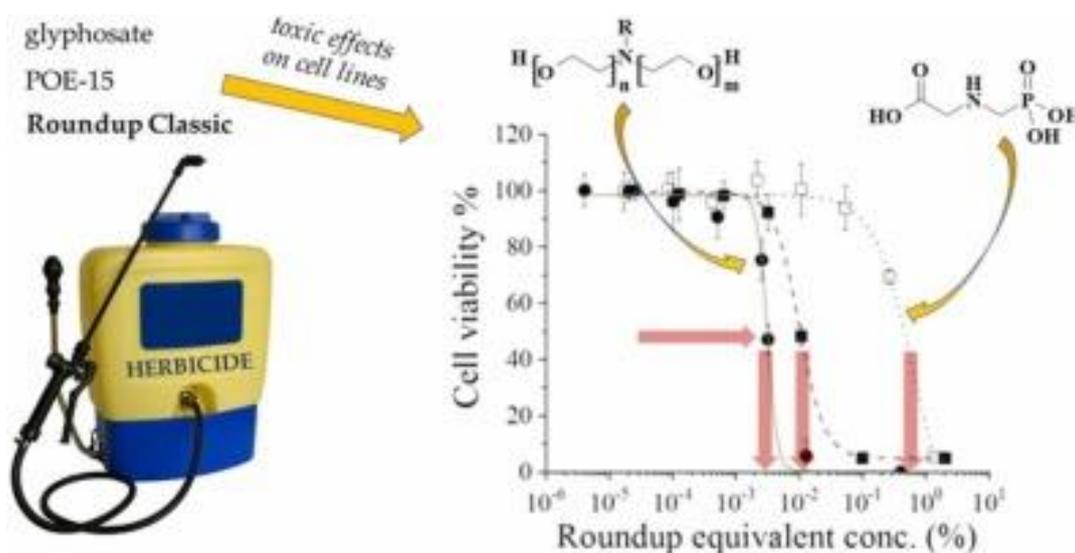
Figure 6.11. *Examination and analysis of the cytotoxic effect of herbicides.*

Comparative assessment of the inhibitory potential of the herbicide glyphosate and its structural analogs on RGD-specific integrins using enzyme-linked immunosorbent assays

B. Gémes (MATE), E. Takács (MATE), I. Székács, R. Horváth, A. Székács (MATE)

Transmembrane glycoprotein integrins play crucial roles in biochemical processes, and by their inhibition or activation, different signal pathways can be disrupted, leading to abnormal physiological functions. We have previously demonstrated the inhibitory effect of glyphosate herbicide's active ingredient on cell adhesion and its $\alpha v\beta 3$ integrin antagonist effect. Therefore, it appeared particularly exciting to investigate inhibition of glyphosate and its metabolites on a wider range of Arg-Gly-Asp (RGD) binding integrins, namely $\alpha v\beta 3$, $\alpha 5\beta 1$ and $\alpha llb\beta 3$. Thus, the purpose of this study was to assess how extended the inhibitory effect observed for glyphosate on the integrin $\alpha v\beta 3$ is in terms of other RGD integrins and other structurally or metabolically related derivatives of glyphosate.

Five different experimental setups using enzyme-linked immunosorbent assays were applied (Fig. 6.12): (i) $\alpha v\beta 3$ binding to a synthetic polymer containing RGD; (ii) $\alpha v\beta 3$ binding to its extracellular matrix (ECM) protein, vitronectin; (iii) $\alpha 5\beta 1$ binding to the above polymer containing RGD; (iv) $\alpha llb\beta 3$ binding to its ECM protein, fibrinogen and (v) $\alpha v\beta 3$ binding to the SARS-CoV-2 spike protein receptor binding domain. Total inhibition of $\alpha v\beta 3$ binding to RGD was detected for glyphosate and its main metabolite, aminomethylphosphonic acid (AMPA), as well as for acetylglycine on $\alpha 5\beta 1$ binding to RGD [Ref. 6.12].
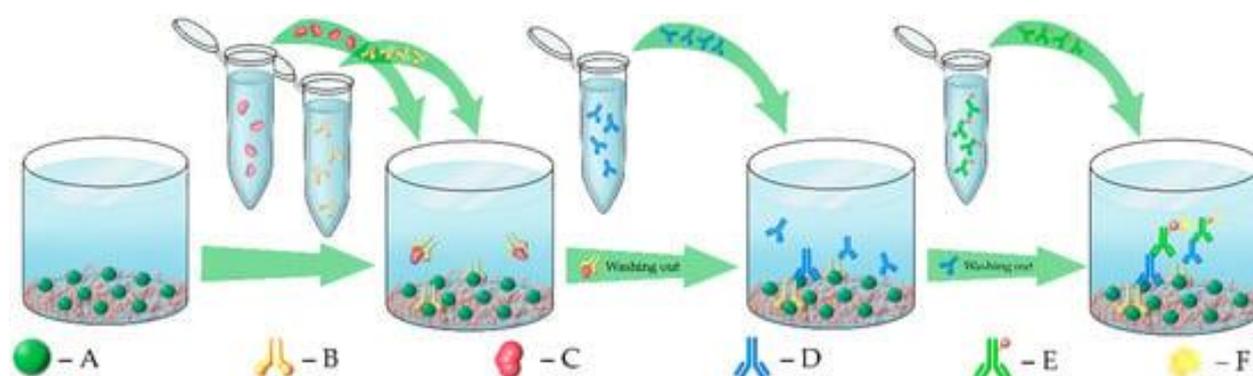
Figure 6.12 *Schematic illustration of the enzyme-linked immunosorbent assay (ELISA).*

Single-cell temporal transcriptomics from tiny cytoplasmic biopsies

R. Horváth

In a recent issue in Nature, Chen et al. [Ref. 6.13] present Live-seq, a single-cell transcriptomic profiling method using picoliter scale single-cell cytoplasmic biopsies instead of complete cell lysis. Since the cells quickly recover and basically remain unaffected after the cytoplasmic extraction, the authors transform single-cell RNA sequencing (scRNA-seq) from an end point to a temporal analysis platform. In our recent Spotlight article, this topic and results were discussed (Fig.6.13) [Ref. 6.14].
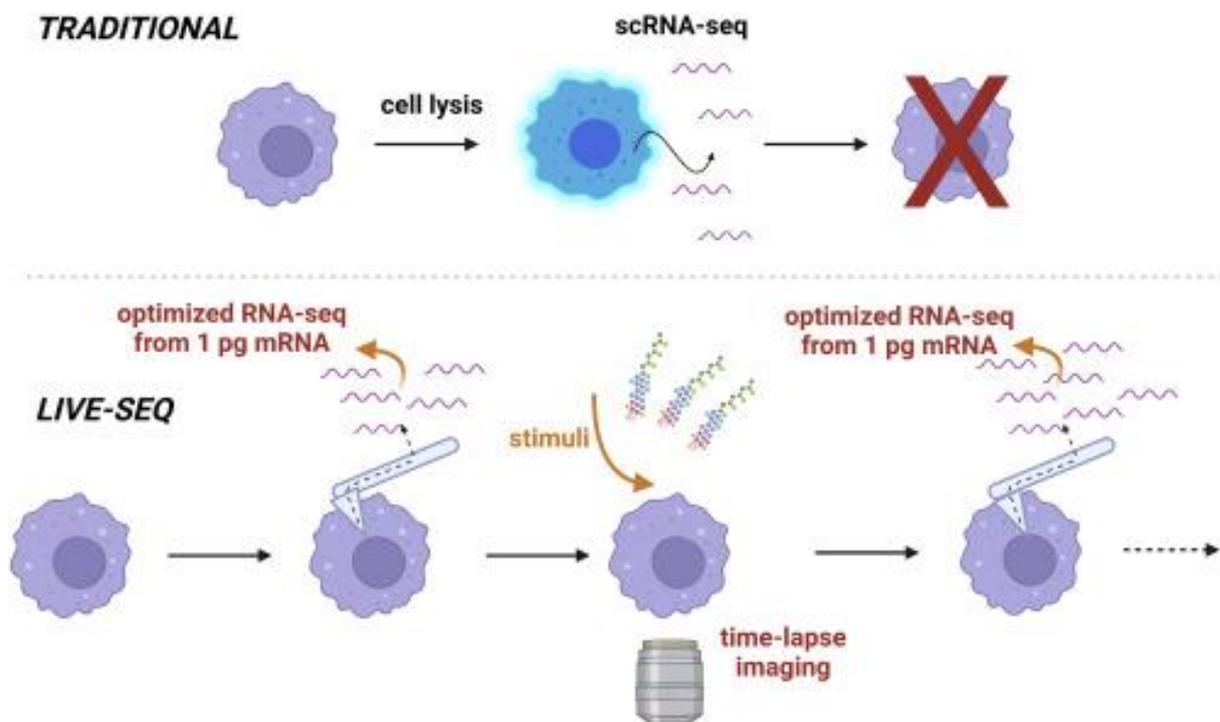

Figure 6.13. *Schematic comparison of traditional scRNA-seq and Live-seq*

Complex Systems Department

Head: Dr. Géza Ódor D.Sc., Scientific advisor

Research Staff:
- Balázs Király PhD
- István Borsos
- Zoltán Juhász PhD
- György Szabó D.Sc., professor emeritus
- Attila Szolnoki D.Sc.,
- Shengfeng Deng PhD
- István Papp PhD

Ph.D. students / Diploma workers:
- Katalin Kovács, LFZE diploma
- Krisztián Kiss, LFZE diploma
- Attila Kazsoki, BME PhD student
- Kristóf Benedek, BME MSc student

The research field of the Complex Systems Department is the investigation of complex systems by the methods of statistical physics in equilibrium as well as non-equilibrium states:

- Statistical physical models of relevance for game theory are studied using the tensor renormalization group method proposed by Levin and Nave, including the Blume-Capel model in an external magnetic field, which can be shown to be equivalent to the combination of an elementary coordination-type game and some elementary self-dependent games under the right conditions, making it a prime candidate for investigating the basic mechanics of the interplay between elementary game theoretic interactions.

- Theoretical investigation of multi-agent evolutionary game models studies processes supporting fair behavior of individuals by numerically analyzing mathematical models when a player's own interest opposes that of the community. Mathematical models have been used to investigate the effect of one kind of penalties, the combinations of the rules of strategy updates, and systems in which the income of the players is obtained from two or three interconnection systems (communities). The effects of special players, whose only duty is to watch the population and punish defectors was investigated and cyclic dominance like structures have been found. Self-organizing impact of averaged payoffs on the evolution of cooperation has also been studied.

- Synchronization blackout cascades analyses were performed in models appearing in the interconnected network of electric plants and high voltage consumers. They extended the investigation of the general characteristics of the Griffiths phase to inhomogeneous networks of Northwest US and Europe. The emergence of non-local cascade failures, concentrated at weak points of the networks has been shown. Traditional concepts and methods of statistical physics the universal properties of avalanche phenomena were analyzed in human brain models. These have provided local synchronization results showing close-to critical behavior in brain modules in agreement with fMRI experiments, even in the presence of periodic excitation fields.

- The critical behavior of Covid-type SIR models were also studied on 2 dimensional lattices in the presence of mobility of individuals. This breaks the symmetry of the SIR model, causing a different universal scaling behavior.

- The increase of folk music and genetic data sets implies the continuous improvement of algorithms to analyze them. Newly developed algorithms are able both to identify clusters and to follow the evolutionary inheritance of clusters, both in genetic (haplogroup) features and in popular characteristics of folk music tunes. Genetic studies have proven that the total weights of common haplogroups in the Hungarian population can be found at the level of 30% in Hungarian and 70% in bronze age population.

Quantification and statistical analysis of topological features of recursive trees

OTKA PD 138571

B. Király, I. Borsos, and G. Szabó

Our recent research into the structure and properties of payoff matrices in game theory has revealed that square matrices can be decomposed as linear combinations of just a handful of fundamentally different kinds of basis matrices that each represent archetypal interaction situations. Symmetry considerations can further simplify the picture: In particular, antisymmetric matrices consist only of hierarchical and cyclic components. We applied this insight to the by definition antisymmetric adjacency matrix representation of simple directed graphs, and thus found that they can be considered as linear combinations of star-like hierarchical and rock-paper-scissors-like cyclic basis graphs. Using the expansion coefficients of the elementary matrices, we have introduced various vectors and scalar products to quantify and characterize some local and global topological properties of the underlying graphs. For example, the elements of the vector **h** count the difference between the outgoing and incoming edges of each node, and its scalar product with itself, **h·h**, turns out to be proportional to the weight of the graph's hierarchical component.

We decided to begin testing the applicability and the usefulness of these quantities on recursive trees, because the presence of a unique root naturally designates a unique decomposition in the otherwise linearly dependent set of all elementary cyclic matrices. Moreover, the structural properties of recursive trees allowed us to determine analytically the averages of certain quantities over the set of same-sized recursive trees by induction. We focused our efforts on a number of promising scalar products that quantify the correlations between local measures derived from the leaf structure and the hierarchical and cyclic components of the adjacency matrix. In order to find out how effectively these measures can sort graphs into groups according to their isomorphism classes, we counted the number of different values these measures can take. We found that global measures that combine fundamentally different topological features have the highest resolving power, some of them can even correctly identify all isomorphism classes for smaller recursive trees, but we have found none that can keep up with the exponential increase in the number of isomorphism classes as the size of the graphs is increased. One way to further increase the resolving power of this approach is to use two or more suitably chosen global measures simultaneously, as illustrated by the figure on this page, which shows both joint and marginal distributions of 7-node trees over the values two such measures derived from the hierarchical, cyclical, and leaf structures of the graphs can take.
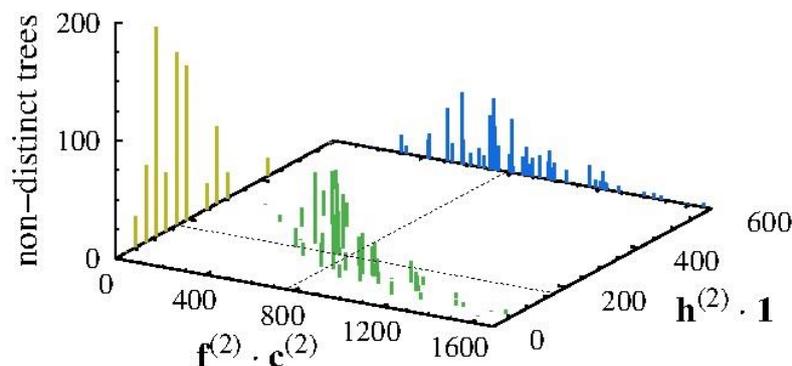
Figure 7.1. *Distribution of the number of recursive trees characterized by two measures, h(2)·1 and f(2)· c(2), for n=7. The marginal distributions are shown by vertical columns along the axes and the dash lines indicate their average values (quantitatively 168 and 770) over the whole set.*

Mercenary punishment in structured populations

H.-W. Lee, C. Cleveland, and A. Szolnoki

Punishing those who refuse to participate in common efforts is a known and intensively studied way to maintain cooperation among self-interested agents. But this act is costly, hence punishers who are generally also engaged in the original joint venture, become vulnerable, which jeopardizes the effectiveness of this incentive. As an alternative, we may hire special players, whose only duty is to watch the population and punish defectors. Such a police-like or mercenary punishment can be maintained by a tax-based fund. If this tax is negligible, a cyclic dominance may emerge among different strategies. When this tax is relevant then this solution disappears. In the latter case, the fine level becomes a significant factor that determines whether punisher players coexist with cooperators or alternatively with defectors. The maximal average outcome can be reached at an intermediate cost value of punishment. Our observations highlight that we should take special care when such kind of punishment and accompanying tax are introduced to reach a collective goal. [Ref.7.1]

The payoff values of different strategies, cooperator, defector, and punisher, originated from a game are the following:

$$\Pi_C = \frac{rc(N_c+1)}{N} - c - T \, ; \, \Pi_D = \frac{rcN_c}{N} - \beta N_P - T \, ; \, \Pi_P = \frac{rcN_c}{N} - GP + \frac{NT}{N_P+1} - T$$
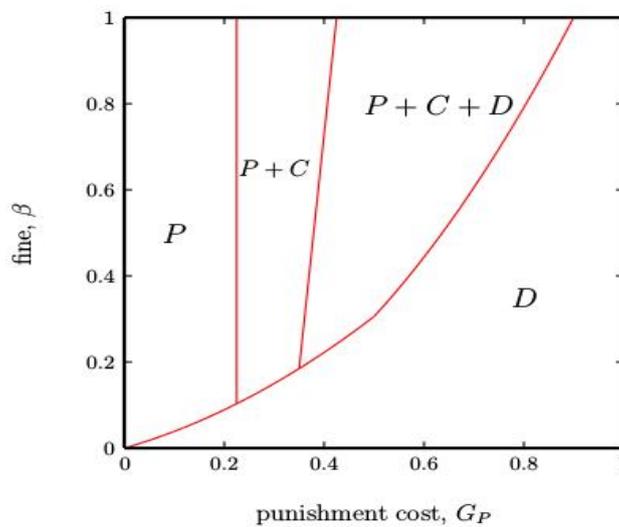
Figure 7.2. *Schematic phase diagram on the punishment cost – penalty plane obtained at r = 3, T = 0. Despite the lack of tax, cooperators can coexist with punishers at an intermediate cost value if the fine is high enough. When we weaken punishers further by increasing the punishment cost then a cyclic dominance emerges, where C→P→D→C is the rank among competing strategies. By increasing G_P further, this delicate balance is broken and defectors prevail*
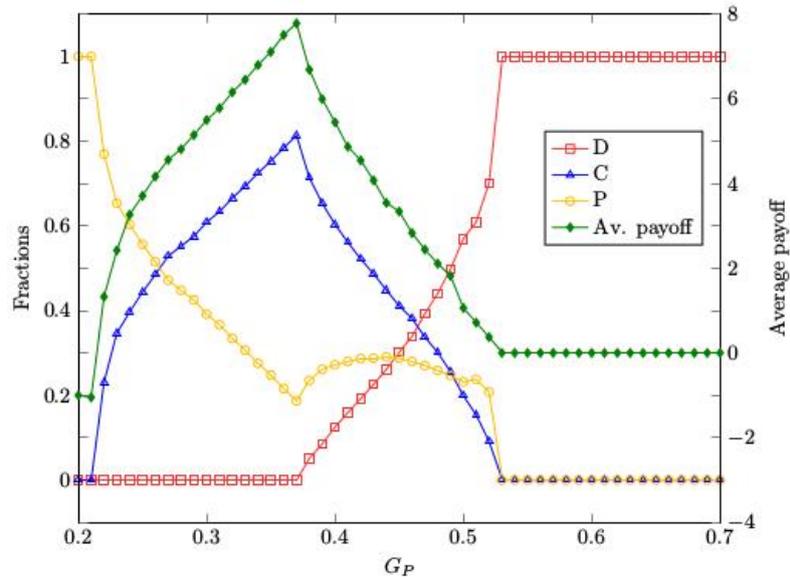
Figure 7.3. *Cross section of the phase diagram shown in Figure 1, as obtained for β = 0.4 fine value. Depicted are stationary fractions of the three competing strategies as a function of punishment cost. As we increase G_P, the system enters to P+C solution from full P state, then P+C+D state emerges, and finally it arrives to full D state. We also plotted the average payoff values of the population, which signs that there is an optimal G_P cost level of punishers which is necessary to reach the best collective income.*
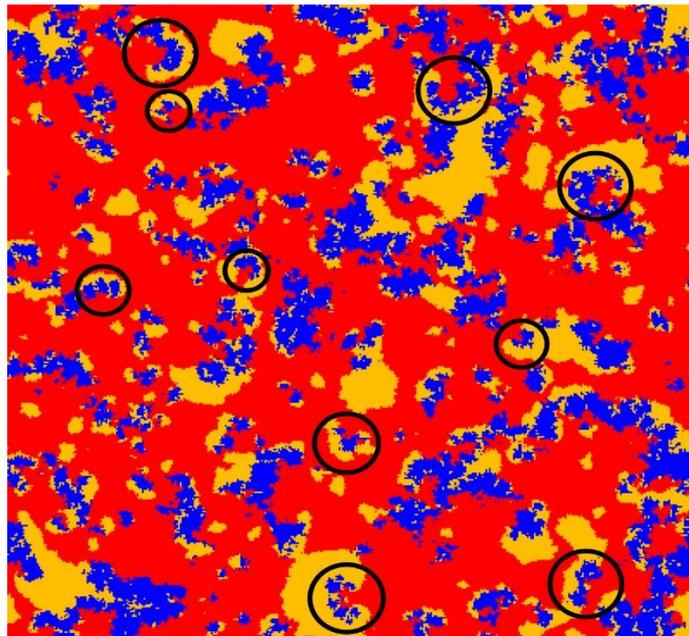
Figure 7.4. *Characteristic distribution of competing strategies in the P+C+D phase. Blue, red, and yellow colors denote players with C, D, and P strategy respectively. The rotating spiral patterns of invasion fronts between homogeneous domains signal clearly the cyclic dominance among three competing strategies. For clarity we marked them with black circles. The snapshot was taken at β = 0.4, T = 0, $G_P = 0.5$ in the stationary state where linear size was L = 400.*

The self-organizing impact of averaged payoffs on the evolution of cooperation

A. Szolnoki and M. Perc

According to the fundamental principle of evolutionary game theory, the more successful strategy in a population should spread. Hence, during a strategy imitation process a player compares its payoff value to the payoff value held by a competing strategy. But this information is not always accurate. To avoid ambiguity a learner may therefore decide to collect a more reliable statistic by averaging the payoff values of its opponents in the neighborhood, and makes a decision afterwards. This simple alteration of the standard microscopic protocol significantly improves the cooperation level in a population. Furthermore, the positive impact can be strengthened by increasing the role of the environment and the size of the evaluation circle. The mechanism that explains this improvement is based on a self-organizing process which reveals the detrimental consequence of defector aggregation that remains partly hidden during face-to-face comparisons. Notably, the reported phenomenon is not limited to lattice populations but remains valid also for systems described by irregular interaction networks. [Ref. 7.2]
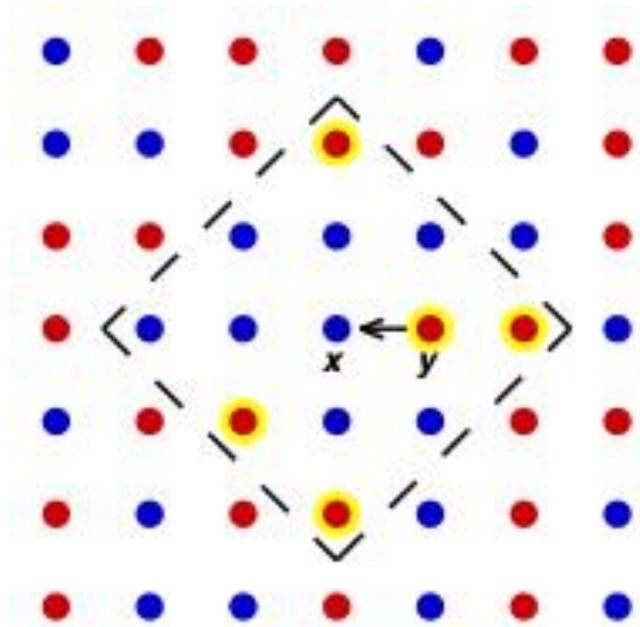
Figure 7.5. *As a learner, a cooperator (blue) player x tries to imitate the strategy of the defector (red) neighbor player y. To calculate the imitation probability player x considers not only the Π_y payoff of player y, but also the Π_{av} averaged payoff values of ball other defector players who are within the evaluation circle. The latter players are marked by yellow background while the border of evaluation circle around player x is marked by a dashed diamond. In this particular case $l_e = 2$ is applied, which means that all players whose distance from player x are not larger than 2 may contribute to Π_{av}, hence providing a more accurate statistics about the general success of s_y strategy. To calculate the effective payoff we apply $\Pi_w = q\Pi_{av} + (1 − q)\Pi_y$, where q is the control parameter determining how strongly our learner player trusts on the alternative source of information about the success of tempting strategy.*
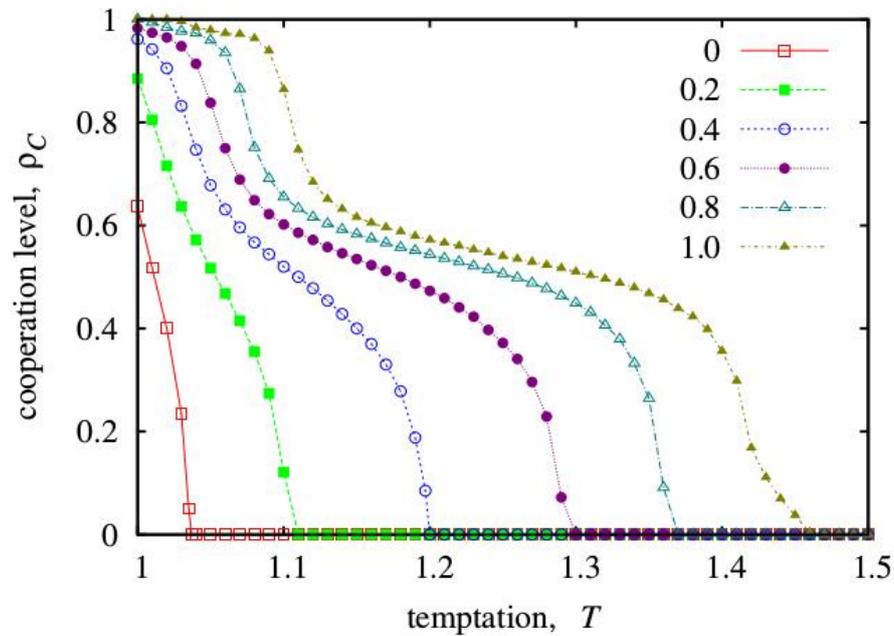
Figure 7.6. *Cooperation level in dependence of temptation value on a square lattice for different values of q obtained at $l_e = 2$. The values of q are marked in the legend. The curves suggest that the cooperation level can be improved significantly if the learner players give greater credit to payoff information obtained from the neighborhood instead of trusting to the neighboring model player exclusively. In other words, it is wiser to make a decision based not only a single information, but collecting more. By enlarging the size of the neighborhood from the extra information is collected the cooperation level can be lifted further even if the mentioned information has just a minor role on the decision making because of the small value of q. Interestingly, however, the reachable cooperation level saturates for large range of information circle.*

Synchronization dynamics on power grids in Europe and the United States

ELKH SA-44/2021

G. Ódor, B. Hartmann, S. Deng, J. Kelling

Dynamical simulation of the cascade failures on the Europe and United States (U.S.) high-voltage power grids has been done via solving the second-order Kuramoto equation. We show that synchronization transition happens by increasing the global coupling parameter K with metastable states depending on the initial conditions so that hysteresis loops occur. We provide analytic results for the time dependence of frequency spread in the large-K approximation and by comparing it with numerics of $d= 2, 3$ lattices, we find agreement in the case of ordered initial conditions. However, different power-law (PL) tails occur, when the fluctuations are strong.

After thermalizing the systems, we allow a single line cut failure and follow the subsequent overloads with respect to threshold values T. The PDFs $p(N_f)$ of the cascade failures exhibit PL tails near the synchronization transition point K_c. Near this, the exponents of the PLs for the U.S. power grid vary with T as $1.4<\tau<2.1$, in agreement with the empirical blackout statistics, while on the Europe power grid we find somewhat steeper PLs characterized by $1.4<\tau<2.4$. Below K_c, we find signatures of T-dependent PLs, caused by frustrated synchronization, reminiscent of Griffiths effects. Here we also observe stability growth following the blackout cascades, similar to intentional islanding, but for $K>K_c$ this does not happen. For $T<T_c$, bumps appear in the PDFs with large mean values, known as "dragon king" blackout events. We also analyze the delaying or stabilizing effects of instantaneous feedback or increased dissipation and show how local synchronization (r_i) behaves on geographic maps. [Ref. 7.3]
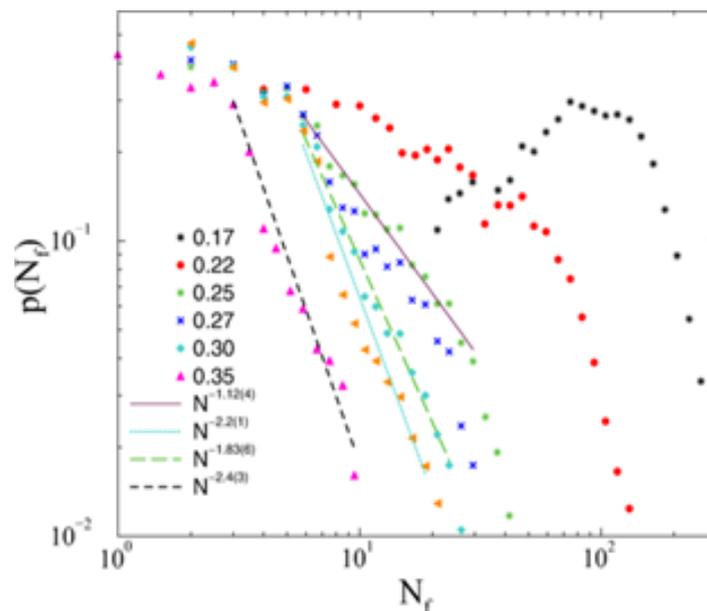
Figure 7.7. *Probability distribution of line failures for different thresholds for K=60 shown in the legends in case of the Europe-HV power grid. Dashed lines show power-law fits for the scaling region, determined by visual inspection. One can observe dragon king bumps for low threshold values.*

Figure 7.8. *Local Kuramoto results encoded by the color map as 1−r$_i$. Red corresponds low local synchronization, green to high synchronization. The width of gray edges is proportional to the amplitude of the power flow.*

Synchronization transitions on connectome graphs with external force

OTKA K 128989

G. Ódor, I. Papp, S. Deng, J. Kelling

We investigate the synchronization transition of the Shinomoto-Kuramoto model on networks of the fruit-fly and two large human connectomes. This model contains a force term (F), thus is capable of describing critical behavior in the presence of external excitations. By numerical solution we determine the crackling noise durations with and without thermal noise and show extended non-universal scaling tails, described by the exponent $2 < t_t < 2.8$, in contrast with the Hopf transition of the Kuramoto model, without the force $t_t = 3.1(1)$. Comparing phase and frequency order parameters we find different transition points and fluctuations peaks as in case of the Kuramoto model related to a crossover at Widom lines. Using the local order parameter values we also determine the Hurst (phase) and b (frequency) exponents and compare them with recent experimental results, obtained by fMRI. We show that these exponents, characterizing the auto-correlations are smaller in the excited system than in the resting state and exhibit module dependence. [Ref. 7.4]
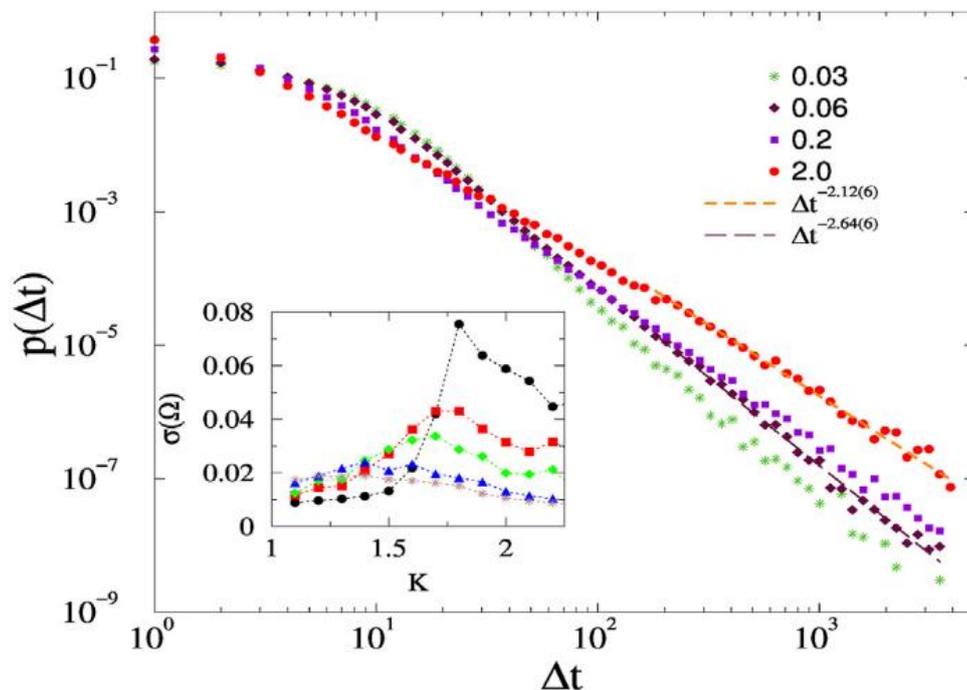
Figure 7.9. *Avalanche duration distributions on the fruit-fly connectome for different forces, shown by the legends and at K = 1.3 global coupling. Dashed lines are PL fits for Δt > 100. The inset shows the steady state σ(Ω) as the function of K, for excitation values F = 0.001, 0.0667, 0.1, 0.2, 0.3 (top to bottom).*
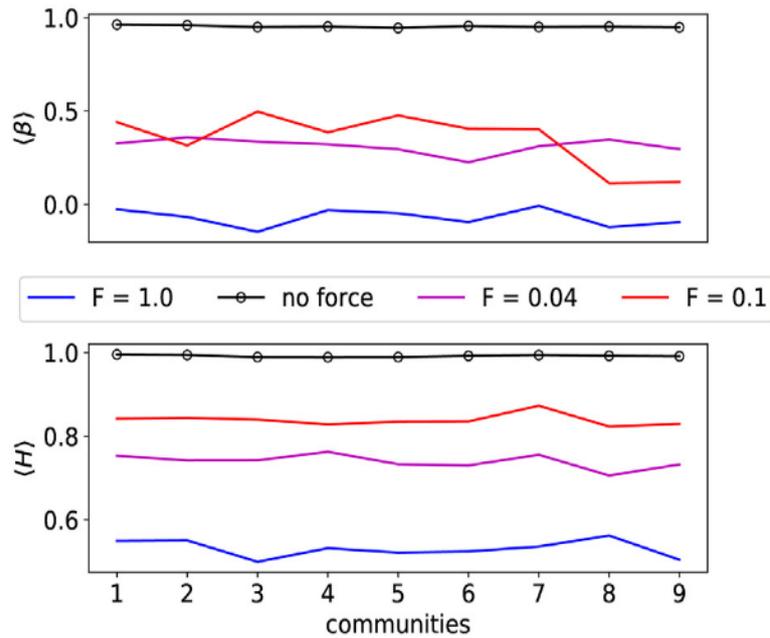
Figure 7.10. *Hurst and beta exponents of all fruit-fly connectome communities. In the forceless case at the critical Hopf transition coupling, the H exponent is the largest for every community. With forces these values drop for each community. This shows a resemblance with the rest and non-rest studies of different brain areas in [63], showing ⟨H⟩ ≈ 1.0 at resting state and ⟨H⟩ ≈ 0.7 at task driven states.*
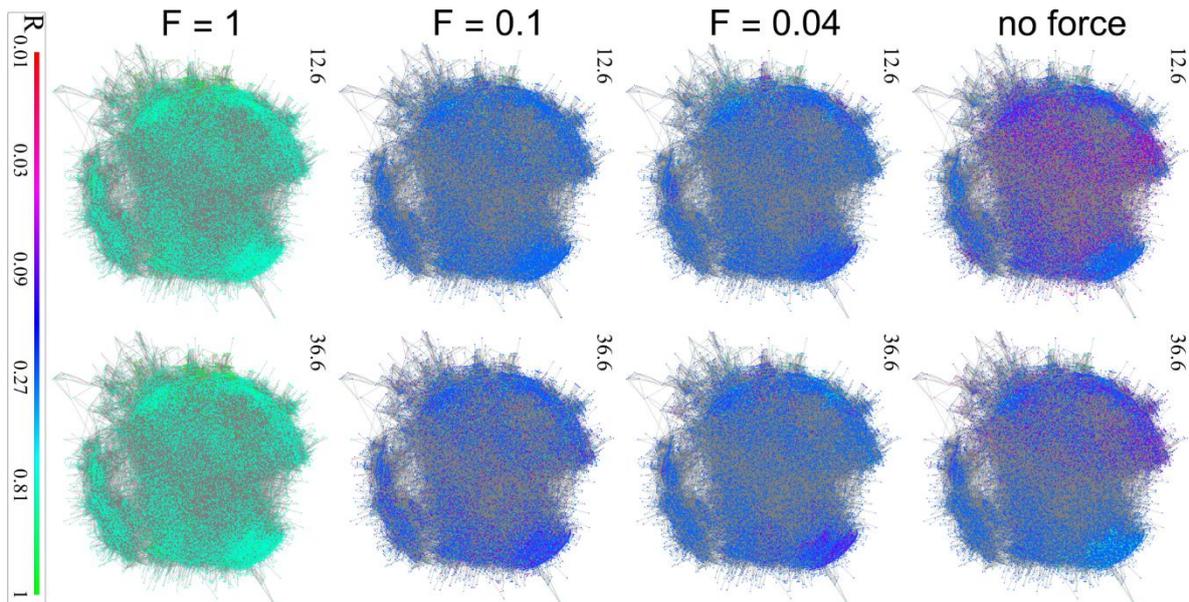
Figure 7.11. *Here we see the evolution of the local order parameters $R_i(t)$ of a sub-graph of the fruit-fly connectome at different time steps: t = 12.6, 36.6. The right column shows R_i map without a force, left columns the one with F = 1.0. Color-coding at the bottom provides $R_i(t)$ for all subfigures.*

Critical behavior of the diffusive susceptible-infected-recovered model

S. Deng and G. Ódor

The critical behavior of the non-diffusive susceptible-infected-recovered (SIR) model on lattices had been well established in virtue of its duality symmetry. By performing simulations and scaling analyses for the diffusive (SIRD) variant on the two-dimensional lattice, we show that diffusion (D) for all agents, while rendering this symmetry destroyed, constitutes a singular perturbation that induces asymptotically distinct dynamical and stationary critical behavior from the non-diffusive model. In particular, the manifested crossover behavior in the effective mean-square radius exponents reveals that slow crossover behavior in general diffusive multispecies reaction systems may be ascribed to the interference of multiple length scales and timescales at early times.
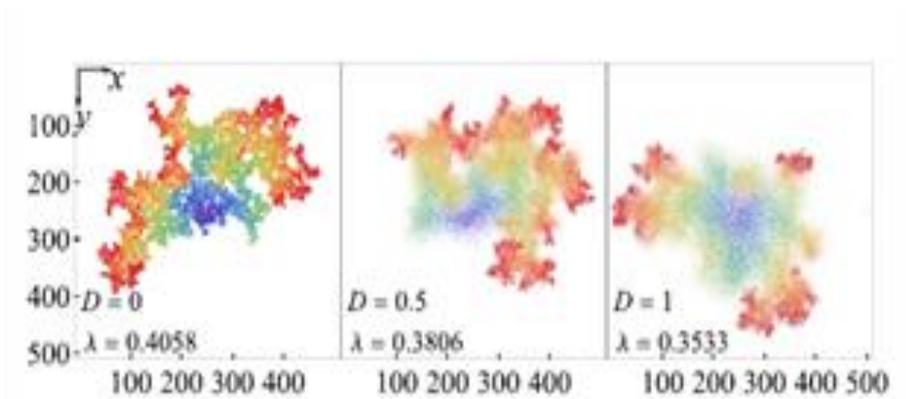
Figure 7.12. *Snapshots for the critical SIRD process with diffusion rates D = 0, 0.5, and 1 on a 500 × 500 lattice. The S and I species are colored in white and black. The rainbow spectrum beared by the R species, from blue to red, linearly marks their relative generating time.*
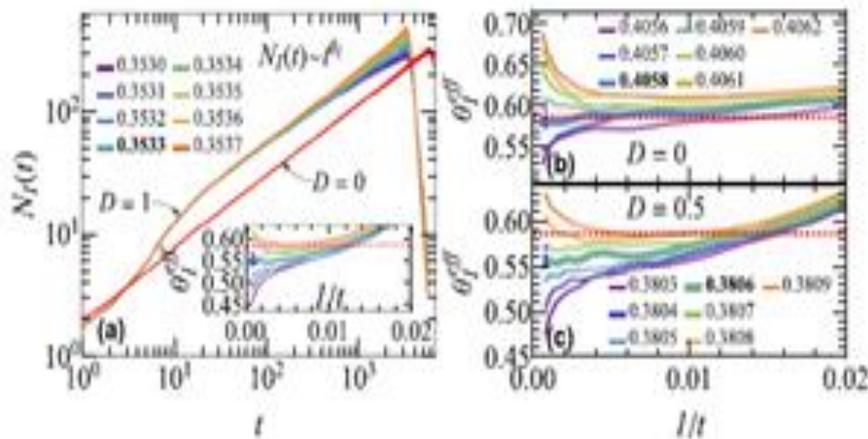
Figure 7.13. *Growth of the I population size $N_I(t)$ from a single infectious seed on a L=4001 square lattice in the vicinity of criticality for (a) D=1, and the evolution of the corresponding effective exponent θ_{eff} in the inset, in panel (b) for D=0, and in panel (c) for D= 0.5. For comparison, the red solid line in panel (a) depicts the critical $N_I(t)$ result for D=0. The critical points, emphasized by the thick curves, are estimated at infection probabilities $\lambda_c=0.4058(1)$, $\lambda_c=0.3806(1)$, and $\lambda_c=0.3533(1)$ for D=0, D=0.5, and D=1, respectively. The horizontal dashed red line indicates the SIR value. All results were averaged over 10^4 independent runs.*

REFERENCES

[Ref. 1.1] Regnault, N., Xu, Y., Li, MR. et al. Catalogue of flat-band stoichiometric materials. Nature 603, 824–828 (2022)

[Ref. 1.2] Hagymási, I. et al. Observation of competing, correlated ground states in the flat band of rhombohedral graphite Science Advances 2 Sep 2022 Vol 8, Issue 35 (2022)

[Ref. 1.3] Joucken, F. et al. Direct Visualization of Native Defects in Graphite and Their Effect on the Electronic Properties of Bernal-Stacked Bilayer Graphene. Nano Lett.21, 7100–7108 (2021)

[Ref. 1.4] Torche, A., Mauri, F., Charlier, J.-C. & Calandra, First-principles determination of the Raman fingerprint of rhombohedral graphiteM. Phys. Rev. Mater. 1, 041001 (2017)

[Ref. 1.5] W. Z. Zhuo, B. Lei, C. S. Zhu, Z. L. Sun, J. H. Cui, W. X. Wang, Z. Y. Wang, T. Wu, J. J. Ying, Z. J. Xiang, and X. H. Chen Thickness-dependent electronic structure in layered ZrTe5 down to the two-dimensional limit Phys. Rev. B 106, 085428 (2022)

[Ref. 1.6] Weng, H., Dai, X. & Fang, Z. ransition-Metal Pentatelluride ZrTe5 and HfTe5: A Paradigm for Large-Gap Quantum Spin Hall Insulators Phys. Rev. X 4, 011002 (2014)

[Ref. 1.7] Tajkov, Z., Nagy, D., Kandrai, K. et al. Revealing the topological phase diagram of ZrTe5 using the complex strain fields of microbubbles. npj Comput Mater 8, 177 (2022)

[Ref. 1.8] Magda, G., Pető, J., Dobrik, G. et al. Exfoliation of large-area transition metal chalcogenide single layers. Sci Rep 5, 14714 (2015)

[Ref. 1.9] Shim, J. et al. Controlled crack propagation for atomic precision handling of wafer-scale two-dimensional materials Science 362, 665–670 (2018)

[Ref. 2.1] N. Nagy, "Contact Angle Determination on Hydrophilic and Superhydrophilic Surfaces by Using r–θ-Type Capillary Bridges" LANGMUIR, vol. 35, iss. 15, 5202-5212, 2019.

[Ref. 2.2] N. Nagy, " Capillary Bridges on Hydrophobic Surfaces: Analytical ContactAngle Determination" LANGMUIR, vol. 38, iss. 19, 6201-6208, 2022.

[Ref. 2.3] J.B. Renkó, A. Romanenko, P.J. Szabó, A. Sulyok, P. Petrik, A. Bonyár, Analysis of structural and chemical inhomogeneity of thin films developed on ferrite grains by color etching with Beraha-I type etchant with spectroscopic ellipsometry and XPS, Journal of Materials Research and Technology. 18 (2022) 2822–2830. https://doi.org/10.1016/j.jmrt.2022.03.159.

[Ref. 2.4] J. Budai, Z. Pápa, P. Petrik, P. Dombi, Ultrasensitive probing of plasmonic hot electron occupancies, Nat Commun. 13 (2022) 6695.

[Ref. 2.5] A. Pálinkás, G. Kálvin, P. Vancsó, K. Kandrai, M. Szendrő, G. Németh, M. Németh, Á. Pekker, J.S. Pap, P. Petrik, K. Kamarás, L. Tapasztó, P. Nemes-Incze, The composition and structure of the ubiquitous hydrocarbon contamination on van der Waals materials, Nat Commun. 13 (2022) 6770.

[Ref. 2.6] Labadi, Z.: "Sensing Layer for Ni Detection in Water Created by Immobilization of Bioengineered Flagellar Nanotubes on Gold Surfaces" ACS BIOMATERIALS-SCIENCE & ENGINEERING, 3811 (2020)

[Ref. 2.7] Jankovics, H.: "Flagellin-based electrochemical sensing layer for arsenic detection in water"; SCIENTIFIC REPORTS 11(1), 3497 (2021)

[Ref. 2.8] D. Zámbó, D. Kovács, G. Südi, A. Deák, „Surface Modification of Gold Nanoprisms and Their Self-assembly with Nanospheres." PART & PART SYST CHARACT 2022, 2200197.

 [Ref. 2.9] Schlosser, A., Schlenkrich, J., Zámbó, D.*, Rosebrock, M., Graf, R. T., Escobar, G., Bigall, N. C.*, Interparticle Interaction Matters: Charge Carrier Dynamics in Hybrid Semiconductor–Metal Cryoaerogels. ADVANCED MATERIALS INTERFACES 2022, 9, 2200055.

[Ref. 2.10] F. Riesz, "Modelling of the backside pattern transfer in magic mirror (Makyoh) imaging," JOURNAL OF OPTICS, vol. 25, no. 2, art. 025602, 2023.

[Ref. 3.1] J. Gambino, Process Technology for Copper Interconnects Handbook of Thin Film Deposition (Fourth Edition) 2018, Pages 147-194 Elsevier Inc.

[Ref. 3.2] F. Misják, K.H. Nagy, P. Lobotka, and G. Radnóczi, J. Electron scattering mechanisms in Cu-Mn films for interconnect applicationsAppl. Phys. 116, (2014).

[Ref. 3.3] G. Sáfrán, "One-sample concept" micro-combinatory for high throughput TEM of binary films Ultramicroscopy 187, 50 (2018).

[Ref. 3.4] S. Behrangi, I. Sedláček, J. Štěrba, G. Suková, Zs. Czigány, V. Buršíková, P. Souček, V. Sochora, K. Balázsi, P. Vašina, Assessment of bactericidal and virucidal properties of some ZrN-Cu nanostructured coatings deposited by an industrial PVD system, Coatings 12 (2022) 1330

[Ref. 3.5] T. Stasiak, P. Souček, V. Buršíková, N. Koutná, Zs. Czigány, K. Balázsi, P. Vašina, Synthesis and characterization of the ceramic refractory metal high entropy nitride thin films from Cr-Hf-Mo-Ta-W system, Surface and Coatings Technology 449 (2022) 128987

[Ref. 3.6]. M. Hans, Zs. Czigány, D. Neuß, J. A. Sälker, H. Rueß, J. Krause, G.K. Nayak, D. Holec, J. M. Schneider, Probing the onset of wurtzite phase formation in (V,Al)N thin films by transmission electron microscopy and atom probe tomography, Surf. Coat. Technol. 442 (2022) 128235

[Ref. 3.7] G. Dravecz, T. Kolonits, L. Péter, Formation of LiNbO3 Nanocrystals Using the Solvothermal Method. Crystals 13(1), (2023). 77.

[Ref. 3.8] L. Kocsor, L. Kovács, L. Bencs, T. Kolonits, K. Lengyel, G. Bazsó, Zs. Kis, L. Péter Lithium oxide loss of lithium niobate nanocrystals during high-energy ball-milling. Journal of Alloys and Compounds, 909, (2022) 164713

[Ref. 3.9] A.S. Racz, Z. Fogarassy, U. Kentsch, P. Panjan, M. Menyhard Design and production of tungsten-carbide rich coating layers, Applied Surface Science, 586, 2022, 152818

[Ref. 3.10] A. S. Racz, Z. Kerner, M. Menyhard Corrosion resistance of tungsten carbide-rich coating layers produced by noble gas ion mixing, Applied Surface Science, 605, 2022, 154662

[Ref. 3.11] M. Serenyi, M. Racz and T. Lohner, Vacuum, 285 vol. 61, pp. 245-249, 2001.

[Ref. 3.12] G Sáfrán, N Szász, G Dobrik, B Kalas, M Serényi Smart gas dosage by a peristaltic pump for reactive RF sputtering of composition spread combinatorial hafnium-oxy-nitride layers Vacuum 182, 2020, 109675

[Ref. 3.13] S. Berg, H.-O. Blom, T. Larsson and C. Nender, " Journal of Vacuum 291 Science & Technology A: Vacuum, Surfaces, and Films, vol. 5, no. 2, pp. 202-207, 1987. 292

[Ref. 3.14] S. Berg and T. Nyberg, Fundamental understanding and modeling of reactive sputtering processes Materials Thin Solid Films, vol. 476, 293 pp. 215-230, 2005.

[Ref. 3.15] N. Hegedűs, Cs. Balázsi , T. Kolonits , D. Olasz, G. Sáfrán, M. Serényi and K. Balázsi Materials 2022, 15, 6313.

[Ref. 3.16] D. Olasz, Gy. Sáfrán, N. Szász, G. Huhn, N. Q. Chinh Indentation size effect in exceptionally hard AlCu thin films Materials Letters 330 (2023) 133409.

[Ref. 3.17] M Draissia, H Boudemagh and M Y Debli: Structure and Hardness of the Sputtered Al-Cu Thin Films System Phys. Scr. 69 (2004) 348.

[Ref. 3.18] Cowley J. M., Electron Diffraction Techniques, Oxford Uni. Press. Vol. 1. 1992

[Ref. 3.19] Xiaodong Zou, Electron Crystallography of Inorganic Structures – Theory and Practice, Chemical Communications, Stockholm University, 1995

[Ref. 3.20] H.M. Rietveld, (1967). Line Profiles of Neutron Powder–Diffraction Peaks for Structure Refinement. Acta Crystallogr 22, 151–152.

[Ref. 3.21] Zs. Czigány, & V.K. Kis., Acquisition and evaluation procedure to improve the accuracy of SAED. Microsc Res Tech (2022). 1–13.

[Ref. 3.22] P. Boullay, L. Lutterotti, D. Chateigner, & L. Sicard, Fast microstructure and phase analyses of nanopowders using combined analysis of transmission electron microscopy scattering patterns. Acta Crystallogr A70, (2014) 448–456.

[Ref. 3.23] G. Caglioti, A. Paoletti, & F. P. Ricci, Choice of collimators for a crystal spectrometer for neutron diffraction. Nucl Instrum 3, (1958) 223–228.

[Ref. 3.24] A. Singh, M. Gracheva, V. Kovács Kis, Á. Keresztes, M. Sági-Kazár, Máté; Müller, Brigitta ; Pankaczi, Fruzsina ; Ahmad, W ; Kovács, Krisztina; May, Zoltán et al. Apoplast utilisation of nanohaematite initiates parallel suppression of RIBA1 and FRO1&3 in Cucumis sativus. NANOIMPACT 29 Paper: 100444 , 12 p. (2023)

[Ref. 3.25] K. Balázsi, D. Varanasi, Zs. E. Horváth, M. Furkó, F. S. Cinar & C. Balázsi, Scientfic Reports,| (2022) 12:8250

[Ref. 4.1] Posa, L.; Hornung, P.; Torok, T. N.; Arjmandabasi, S.; Molnar, Gy.; Baji, Zs.; Dražić, G.; Halbritter, A.; Volk, J., Interplay of thermal and electronic effects in the Mott transition of ultrasmall VO2 phase change memory devices, submitted to ACS Applied Nano Materials

[Ref. 4.2] P.L. Neumann, J. Radó, J.M. Bozorádi, J. Volk, AlGaN/GaN Heterostructure Based 3-Dimensional Force Sensors, submitted to Micro and Nano Engineering Journal

[Ref. 5.1] Ferenc Bíró, András Deák, Csaba Dücső, Zoltán Hajnal, "Microheater with uniform surface temperature", Utility model: U 20 001150, registration number 5279

[Ref. 5.2] F. Bíró, A. Deák, I. Bársony, N. Samotev, Cs. Dücső, An analytical method to design annular microfilaments with uniform temperature, MICROSYSTEM TECHNOLOGIES (0946-7076 1432-1858): 28 (11) pp 2511-2528 (2022)

[Ref. 5.3] L. Harasztosi, I. A. Szabó, F. Biró, R. Gy. Kiss, G. Battistig, Microcalorimeter development and calibration based on a twin microheater platform, Proceedings of the 8th International Conference on Sensors and Electronic Instrumentation Advances, Korfu: International Frequency Sensor Association (IFSA) Publishing, pp 112-116 (2022)

[Ref. 5.4] J. Radó, R. Dekker; M. C. Louwerse, V. A. Henneken, M. Peters, P. Fürjes, Cs. Dücső, Force Sensor Chip With High Lateral Resolution for Artificial Skin and Surgical Applications, IEEE Sensors Journal, 22 (19) pp. 18359 – 18365, 2022

[Ref. 5.5] P. Fürjes, Tactile sensing and tissue recognition in Minimal Invasive Surgery - Smart laparoscopes and surgery robots, SEB2022 – Sustainable Electronics & Bioanalytics Workshop 2022, Tallinn, Estonia, 2022 (invited keynote)

[Ref. 5.6] J. M. Bozorádi, A. Nagy, J. Radó, P. Földesy, I. Bársony, G. Papp, Cs. Dücső, P. Fürjes, Characterisation tissue elasticity by MEMS force sensors, MNE-ES 2022 - Micro and Nano Engineering (MNE) & Eurosensors 2022 Conferences, Leuven, Belgium, 2022

[Ref. 5.7] A. Bányai, M. Varga, P. Fürjes, Filtration efficiencies of crossflow type microfilters for E.Coli separation, Mátrafüred International Meeting on Chemical Sensors 2022, Visegrád, Hungary, 2022

[Ref. 5.8] A. Bányai, E. L. Tóth, M. Varga, P. Fürjes, Geometry-Dependent Efficiency of Dean-Flow Affected Lateral Particle Focusing and Separation in Periodically Inhomogeneous Microfluidic Channels, SENSORS, 22 (9), 3474, 2022

[Ref. 5.9] E. Farkas, R. Tarr, T. Gerecsei, A. Saftics, K. D. Kovács, B. Stercz, J. Domokos, B. Peter, S. Kurunczi, I. Szekacs, A. Bonyár, A. Bányai, P. Fürjes, Sz. Ruszkai-Szaniszló, M. Varga, B. Szabó, E. Ostorházi, D. Szabó, R. Horváth, Development and

In-Depth Characterization of Bacteria Repellent and Bacteria Adhesive Antibody-Coated Surfaces Using Optical Waveguide Biosensing, BIOSENSORS 12 : 2 Paper: 56 , 20 p., 2022

[Ref. 5.10] L. Bató, P. Fürjes, A fluorescent detection method to measure the diffusion coefficients of proteins in a free-diffusion based microfluidic system, Lab-on-a-Chip and Microfluidics Europe 2022 Conference, Rotterdam, The Netherlands, 2022

[Ref. 5.11] L. Bató, P. Fürjes, Microfluidic device for single cell trapping and viability testing, Mátrafüred International Meeting on Chemical Sensors 2022, Visegrád, Hungary, 2022

[Ref. 5.12] A. Bányai, E. L. Tóth, P. Fürjes, Effects of channel morphology on magnetophoretic separation in microfluidic particle trapping, Lab-on-a-Chip and Microfluidics Europe 2022 Conference, Rotterdam, The Netherlands, 2022

[Ref. 5.13] Z. Szabó, V. Rakovics, B. Beiler, P. Fürjes, Wide emission-spectrum NIRLED based on in-chip efficient photon-recycling, ICEL 2022 – 13th International Conference of Electroluminescence and Optoelectronic Devices, London, UK, 2022

[Ref. 5.14] D. Bereczki, A. Füredi, P. Fürjes, Plate reader compatible microfluidic cuvette for UV-excited fluorescent spectroscopy, Lab-on-a-Chip and Microfluidics Europe 2022 Conference, Rotterdam, The Netherlands, 2022

[Ref. 5.15] D. Bereczki, A. Füredi, P. Fürjes, Platereader compatible microfluidic chambers for fluorescent spectroscopy, Mátrafüred International Meeting on Chemical Sensors 2022, Visegrád, Hungary, 2022

[Ref. 6.1] T. Gerecsei, R. Ungai-Salánki, A. Saftics, I. Derényi, R. Horvath, B. Szabó, „Characterization of the dissolution of water microdroplets in oil". COLLOIDS AND INTERFACES, vol. 6, 2022.

[Ref. 6.2] E. Farkas, R. Tarr, T. Gerecsei, A. Saftics, K. D. Kovács, B. Stercz, J. Domokos, B. Peter, S. Kurunczi, I. Szekacs, A. Bonyár, A. Bányai, P. Fürjes, Sz. Ruszkai-Szaniszló, M. Varga, B. Szabó, E. Ostorházi, D. Szabó, R. Horvath, „Development and in-depth characterization of bacteria repellent and bacteria adhesive antibody-coated surfaces using optical waveguide biosensing." BIOSENSORS, vol. 12, 2022.

[Ref. 6.3] N. Kanyo, K. D. Kovács, S. V. Kovács, B. Béres, B. Péter, I. Székács, R. Horvath, „Single-cell adhesivity distribution of glycocalyx digested cancer cells from high spatial resolution label-free biosensor measurement". MATRIX BIOLOGY PLUS, vol. 14, 2022.

[Ref. 6.4] B. Péter, N. Kanyo, I. Szekacs, A. Csampai, Sz. Bosze, R. Horvath, „Epigallocatechin-gallate tailors the cell adhesivity of fibronectin coatings in oxidation and concentration-dependent manner". MATERIALS ADVANCES, vol. 3, 2022.

[Ref. 6.5] Z. Szittner, B. Péter, S. Kurunczi, I. Székács, R. Horvath, „Functional blood cell analysis by label-free biosensors and single-cell technologies", ADVANCES IN COLLOID AND INTERFACE SCIENCE, vol. 308, 2022.

[Ref. 6.6] Á.G. Nagy, N. Kanyó, A. Vörös, I. Székács, A. Bonyár (BME), R. Horvath, „Population distributions of single-cell adhesion parameters during the cell cycle from high-throughput robotic fluidic force microscopy", SCIENTIFIC REPORTS, vol. 12, 2022.

[Ref. 6.7] Á. G. Nagy, I. Székács, A. Bonyár, R. Horvath, „Cell-substratum and cell-cell adhesion forces and single-cell mechanical properties in mono- and multilayer assemblies from robotic fluidic force microscopy",EUROPEAN JOURNAL OF CELL BIOLOGY, vol. 101, 2022

[Ref. 6.8] Á. G. Nagy, I. Székács, A. Bonyár, R. Horvath, „Simple and automatic monitoring of cancer cell invasion into an epithelial monolayer using label-free holographic microscopy", SCIENTIFIC REPORTS, vol. 12, 2022.

[Ref. 6.9] B. Péter, E. Farkas, S. Kurunczi, Z. Szittner, Sz. Bősze, J. J. Ramsden, I. Szekacs, R. Horvath, „Review of label-free monitoring of bacteria: From challenging practical applications to basic research perspectives", BIOSENSORS, vol. 12, 2022.

[Ref. 6.10] T. Gerecsei, B. Peter, R. Ungai-Salánki, S. Kurunczi, I. Szekács, B. Szabó, R. Horvath, „Prospects of fluidic force microscopy and related biosensors for medical applications", NANOBIOANALYTICAL APPROACHES TO MEDICAL DIAGNOSTICS, Woodhead Publishing Series in Biomaterials, 2022.

[Ref. 6.11] M. Oláh, E. Farkas, I. Székács, R. Horvath, A. Székács, „Cytotoxic effects of Roundup Classic and its components on NE-4C and MC3T3-E1 cell lines determined by biochemical and flow cytometric assays", TOXICOLOGY REPORTS, vol. 9, 2022.

[Ref. 6.12] B. Gémes, E. Takács, I. Székács, R. Horvath, A. Székács, „Comparative assessment of the inhibitory potential of the herbicide glyphosate and its structural analogs on RGD-specific integrins using enzyme-linked immunosorbent assays", INTERNATIONAL JOURNAL OF MOLECULAR SCIENCES, vol. 23, 2022.

[Ref. 6.13] W. Chen, O. Guillaume-Gentil, P.Y. Rainer, C.G. Gabelein, W. Saelens, V. Gardeux, A. Klaeger, R. Dainese, M. Zachara, T. Zambelli, et al., "Live-seq enables temporal transcriptomic recording of single cells", NATURE, vol. 608, 2022

[Ref. 6.14] R. Horvath, „Single-cell temporal transcriptomics from tiny cytoplasmic biopsies", CELL REPORTS METHODS, vol. 2, 2022.

[Ref. 7.1] H.-W. Lee, C. Cleveland, A. Szolnoki: Mercenary punishment in structured populations, Appl. Math. Comput. 417 (2022) 12679

[Ref. 7.2] A. Szolnoki, M. Perc: The self-organizing impact of averaged payoffs on the evolution of cooperation, NEW JOURNAL OF PHYSICS 23 (2021) 063068.

[Ref. 7.3] Géza Ódor, Shengfeng Deng, Bálint Hartmann, and Jeffrey Kelling: Synchronization dynamics on power grids in Europe and the United States, Phys. Rev. E 106 (2022) 034311.

[Ref. 7.4] G. Ódor, I. Papp, S. Deng, J. Kelling: Synchronization transitions on connectome graphs with external force Front. Phys. Sec. Complex Physical Systems Volume 11 – 2023

[Ref. 7.5] Shengfeng Deng and Géza Ódor: Critical behavior of the diffusive susceptible-infected-recovered model, Phys. Rev E 107 (2023) 014303

FULL LIST OF MFA PUBLICATIONS IN 2022

1.   M. Abdelmonem, D. Zambo, P. Rusch, A. Schlosser, L. F. Klepzig, and N. C. Bigall, "Versatile Route for Multifunctional Aerogels Including Flaxseed Mucilage and Nanocrystals," MACROMOLECULAR RAPID COMMUNICATIONS, vol. 43, no. 7, 2022.

2.   S. Amarjeet, K. K. Viktória, G. Maria, K. Áron, K. Krisztina, T. Gyula, H. Zoltán, F. Ferenc, K. Zoltán, and S. Ádám, "Apoplast utilisation of nanohaematite in the roots of Cucumis sativus," in Abtract Book of the 20th International Symposium on Iron Nutrition and Interactions in Plants, 2022, p. 29.

3.   Anita, L. T. Eszter, and F. Péter, "Effect of channel morphology on magnetic separtation in microfluidic particle trapping." 2022.

4.   Anita, V. Máté, and F. Péter, "Filtration efficiencies of crossflow type microfilters for E.Coli separation." 2022.

5.   Ayyubov, A. Vulcu, C. Berghian-Grosan, E. Tálas, I. Borbáth, I. E. Sajó, G. Sáfrán, J. Mihály, and A. Tompos, "Preparation of Pt electrocatalyst supported by novel, Ti(1−x)MoxO2-C type of composites containing multi-layer graphene," REACTION KINETICS MECHANISMS AND CATALYSIS, vol. 135, no. 1, pp. 49–69, 2022.

6.   Z. Baji, Z. Fogarassy, A. Sulyok, and P. Petrik, "Investigation of the Tetrakis(dimethylamino)hafnium and H2S ALD Process: Effects of Deposition Temperature and Annealing," SOLIDS, vol. 3, no. 2, pp. 258–270, 2022.

7.   K. Balázsi, D. Varanasi, Z. E. Horváth, M. Furkó, F. S. Cinar, and C. Balázsi, "Effect of the pressureless post-sintering on the hot isostatic pressed Al2O3 prepared from the oxidized AlN powder," SCIENTIFIC REPORTS, vol. 12, no. 1, 2022.

8.   K. Balázsi and C. Balázsi, "Application of sputtered ceramic TiC/a: C thin films with different structures by changing the deposition parameters," INTERNATIONAL JOURNAL OF APPLIED CERAMIC TECHNOLOGY, vol. 19, no. 2, pp. 753–761, 2022.

9.   K. Balázsi, "Katalin Balázsi, 2021 Acta Materialia Mary Fortune Global Diversity Medal Recipient," MATERIALIA, vol. 21, 2022.

10. Bányai, E. L. Tóth, M. Varga, and P. Fürjes, "Geometry-Dependent Efficiency of Dean-Flow Affected Lateral Particle Focusing and Separation in Periodically Inhomogeneous Microfluidic Channels," SENSORS, vol. 22, no. 9, 2022.

11. Bányász, I. Rajta, G. U. L. Nagy, N. Q. Khanh, V. Havránek, V. Vosecek, M. Fried, Z. Szabó, M. Veres, R. Holomb, L. Himics, and É. Tichy-Rács, "Characterisation of Channel Waveguides Fabricated in an Er3+-Doped Tellurite Glass Using Two Ion Beam Techniques," CHEMOSENSORS, vol. 10, no. 8, 2022.

12. M. Barbara, P. Beatrix, B. Imre, B. Szilvia, S. Inna, K. Sándor, and H. Robert, "Grating Coupled Interferometry (GCI) for kinetic interaction analysis of small molecules and their target proteins." 2022.

13. B. P. Barna, "Transzmissziós elekronmikroszkópba beépített kísérleti berendezéssel az innovatív vékonyrétegkutatás élvonalában. Barna Árpád munkásságáról," in A Magyar Mikroszkópos Társaság 2022 Konferenciájának Kivonatkönyve, 2022, pp. 108–115.

14. P. Beatrix, S. Inna, B. Szilvia, B. Imre, M. K. Gábor, and H. Robert, "Label-free discovery of natural compounds as target biomolecules in cellular adhesion and migration." 2022.

15. S. Behrangi, I. Sedláček, J. Štěrba, G. Suková, Z. Czigány, V. Buršíková, P. Souček, V. Sochora, K. Balázsi, and P. Vašina, "An Assessment of the Bactericidal and Virucidal Properties of ZrN-Cu Nanostructured Coatings Deposited by an Industrial PVD System," COATINGS, vol. 12, no. 9, 2022.

16. S. Bernadette, S. Christian, Z. Wenli, M. Rolf, D. Ulrich, S. Richard, D. Ján, B. Katalin, B. Csaba, and K. Andreas, "Influence of Graphene Type and Content on Friction and Wear of Silicon Carbide/Graphene Nanocomposites in Aqueous Environment," MATERIALS, vol. 15, no. 21, 2022.

17. Bertóti, S. Farah, A. Bulátkó, A. Farkas, J. Madarász, M. Mohai, G. Sáfrán, and K. László, "Nitrogen implantation into graphene oxide and reduced graphene oxides using radio frequency plasma treatment in microscale," CARBON, vol. 199, pp. 415–423, 2022.

18. S. Bin Anooz, Y. Wang, P. Petrik, M. de Oliveira Guimaraes, M. Schmidbauer, and J. Schwarzkopf, "High temperature phase transitions in NaNbO3 epitaxial films grown under tensile lattice strain," APPLIED PHYSICS LETTERS, vol. 120, no. 20, 2022.

19. F. Bíró, A. Deák, I. Bársony, N. Samotev, and C. Dücső, "An analytical method to design annular microfilaments with uniform temperature," MICROSYSTEM TECHNOLOGIES, vol. 28, no. 11, pp. 2511–2528, 2022.

20. K. T. Biró, G. Szakmány, L. Illés, Z. Kovács, I. Harsányi, and V. Szilágyi, "Archaeometric investigations on Lengyel culture (Late Neolithic-Early Copper Age) polished stone tools from the iconic Lengyel site (SW Hungary) (Poster S4-P10.1515)," in Book of Abstracts, 2022, pp. 108–108.

21. Bódis, I. Cora, Z. Fogarassy, M. Veres, and P. Németh, "High-temperature evolution of diamond-SiC composites," PROCESSING AND APPLICATION OF CERAMICS, vol. 16, no. 1, pp. 69–77, 2022.

22. Bonyár, M. Szalóki, A. Borók, I. Rigó, J. Kámán, S. Zangana, M. Veres, P. Rácz, M. Aladi, M. Kedves, Á. Szokol, P. Petrik, Z. Fogarassy, K. Molnár, M. Csete, A. Szenes, E. Tóth, D. Vas, I. Papp, G. Galbács, L. Csernai, T. Biró, and N. Kroó, "The

Effect of Femtosecond Laser Irradiation and Plasmon Field on the Degree of Conversion of a UDMA-TEGDMA Copolymer Nanocomposite Doped with Gold Nanorods," INTERNATIONAL JOURNAL OF MOLECULAR SCIENCES, vol. 23, no. 21, 2022.

23. G. Borbála, T. Eszter, S. Inna, F. Enikő, H. Robert, K. Szandra, and S. András, "A NEWLY IDENTIFIED SPECIFIC BIOLOGICAL ACTIVITY OF GLYPHOSATE – INHIBITION OF RGD-BINDING INTEGRINS," in Proceedings of the 28th International Symposium on Analytical and Environmental Problems, 2022, pp. 147–151.

24. J. Budai, Z. Pápa, P. Petrik, and P. Dombi, "Ultrasensitive probing of plasmonic hot electron occupancies," NATURE COMMUNICATIONS, vol. 13, no. 1, 2022.

25. S. F. Çınar, M. Mansoor, M. Cengiz, B. Apak, L. Yanmaz, K. Balazsi, Z. Fogarassy, B. Derin, G. Göller, and O. Yücel, "B4C Composites with a TiB2-C Core–Shell Microstructure Produced by Self-Propagating High-Temperature Synthesis-Assisted Spark Plasma Sintering," JOURNAL OF PHYSICAL CHEMISTRY C, vol. 126, no. 47, pp. 20114–20126, 2022.

26. Z. Czigány and K. V. Kovácsné, "Kalibrációs eljárás fejlesztése aberrációkorrigált Themis mikroszkópon a SAED pontosságának javítására," in A Magyar Mikroszkópos Társaság 2022 Konferenciájának Kivonatkönyve, 2022, pp. 133–136.

27. P. S. Dániel, Z. Dániel, Z. Zsolt, N. Rita, N. Norbert, and D. András, "Investigating the electric double layer directed self assembly of oppositely charged gold nanospheres," in Symposium on Materials Science, 2022, pp. 7–10.

28. Z. Dániel, "Nanoparticle gel networks as a novel platform in electrochemical sensing," in Symposium on Materials Science, 2022, pp. 15–19.

29. T. Defforge, A. Chaix, B. Kalas, M. Fried, P. Petrik, and G. Gautier, "Development of silicon nanoparticles for plasmonic sensing," PROGRESS IN BIOMEDICAL OPTICS AND IMAGING (PROCEEDINGS OF SPIE), vol. 11977, pp. 35–39, 2022.

30. B. F. de Oliveira and A. Szolnoki, "Competition among alliances of different sizes," CHAOS SOLITONS & FRACTALS, vol. 157, 2022.

31. G. Dobrik, P. Nemes-Incze, B. Majerus, P. Süle, P. Vancsó, G. Piszter, M. Menyhárd, B. Kalas, P. Petrik, L. Henrard, and L. Tapasztó, "Large-area nanoengineering of graphene corrugations hosting visible-frequency graphene plasmons," NATURE NANOTECHNOLOGY, vol. 17, no. 1, pp. 61–66, 2022.

32. Dodony, A. Rečnik, I. Dódony, and G. Sáfrán, "In situ TEM study of Ni-silicides formation up to 973K," JOURNAL OF ALLOYS AND COMPOUNDS, vol. 918, 2022.

33. Dódony, I. Dódony, and G. Sáfrán, "In situ TEM vizsgálatok nikkel-szilicid vékonyréteg rendszerben," in A Magyar Mikroszkópos Társaság 2022 Konferenciájának Kivonatkönyve, 2022, pp. 19–21.

34. D. Olasz, V. Kis, P. Petrik, B. Kalas, G. Sáfrán, "Microstructure of composition spread YTiO thin films," in Symposium on Materials Science, 2022, pp. 29–30.

35. T. Dózsa, J. Radó, J. Volk, Á. Kisari, A. Soumelidis, and P. Kovács, "Road abnormality detection using piezoresistive force sensors and adaptive signal models," IEEE TRANSACTIONS ON INSTRUMENTATION AND MEASUREMENT, vol. 71, 2022.

36. Dvurečenskij, A. Cigáň, P. Lobotka, G. Radnóczi, M. Škrátek, J. Benyó, E. Kováčová, M. Majerová, and J. Maňka, "Colloids of HEA nanoparticles in an imidazolium-based ionic liquid prepared by magnetron sputtering: Structural and magnetic properties," JOURNAL OF ALLOYS AND COMPOUNDS, vol. 896, 2022.

37. Efremova, I. Szenti, J. Kiss, Á. Szamosvölgyi, A. Sápi, K. Baán, L. Olivi, G. Varga, Z. Fogarassy, B. Pécz, Á. Kukovecz, and Z. Kónya, "NATURE of the Pt-COBALT-OXIDE SURFACE INTERACTION AND ITS ROLE IN the CO2 METHANATION," APPLIED SURFACE SCIENCE, vol. 571, 2022.

38. M. El-Tahawy, L. Péter, L. F. Kiss, J. Gubicza, Z. Czigány, G. Molnár, and I. Bakonyi, "Anisotropic magnetoresistance (AMR) of cobalt: hcp-Co vs. fcc-Co," JOURNAL OF MAGNETISM AND MAGNETIC MATERIALS, vol. 560, 2022.

39. Eniko, T. Robert, G. Tamás, S. Andras, D. K. Kinga, S. Balazs, D. Judit, P. Beatrix, K. Sandor, S. Inna, B. Attila, B. Anita, F. Péter, R.-S. Szilvia, V. Máté, S. Barnabás, O. Eszter, S. Dóra, and H. Robert, "Label-free optical biosensor method for detailed analysis of bacteria repellent and adhesive surfaces." 2022.

40. E. Farkas, R. Tarr, T. Gerecsei, A. Saftics, K. D. Kovács, B. Stercz, J. Domokos, B. Peter, S. Kurunczi, I. Szekacs, A. Bonyár, A. Bányai, P. Fürjes, S. Ruszkai-Szaniszló, M. Varga, B. Szabó, E. Ostorházi, D. Szabó, and R. Horvath, "Development and In-Depth Characterization of Bacteria Repellent and Bacteria Adhesive Antibody-Coated Surfaces Using Optical Waveguide Biosensing," BIOSENSORS, vol. 12, no. 2, 2022.

41. F. Z. Fedor, M. Madarász, A. Zátonyi, Á. Szabó, T. Lőrincz, V. Danda, L. Spurgin, C. Manz, B. Rózsa, and Z. Fekete, "Soft, Thiol-ene/Acrylate-Based Electrode Array for Long-Term Recording of Intracranial EEG Signals with Improved Biocompatibility in Mice," ADVANCED MATERIALS TECHNOLOGIES, vol. 7, no. 5, 2022.

42. Fórizs, K. Dévai, Z. Mráv, and K. V. Kovács, "Roman nanotechnology: a new dichroic glass fragment found in Hungary," in ISA2022 – 43rd International Symposium on Archaeometry, 2022, pp. 213–213.

43. M. Fried, R. Bogar, D. Takacs, Z. Labadi, Z. E. Horvath, and Z. Zolnai, "Investigation of Combinatorial WO3-MoO3 Mixed Layers by Spectroscopic Ellipsometry using Different Optical Models," NANOMATERIALS, vol. 12, no. 14, 2022.

44. M. Furko, Z. E. Horváth, O. Czömpöly, K. Balázsi, and C. Balázsi, "Biominerals Added Bioresorbable Calcium Phosphate Loaded Biopolymer Composites," INTERNATIONAL JOURNAL OF MOLECULAR SCIENCES, vol. 23, no. 24, 2022.

45. M. Furko, Z. E. Horváth, A. Sulyok, V. K. Kis, K. Balázsi, J. Mihály, and C. Balázsi, "Preparation and morphological investigation on bioactive ion-modified carbonated hydroxyapatite-biopolymer composite ceramics as coatings for orthopaedic implants," CERAMICS INTERNATIONAL, vol. 48, no. 1, pp. 760–768, 2022.

46. M. Gartner, M. Anastasescu, J. M. Calderon-Moreno, M. Nicolescu, H. Stroescu, C. Hornoiu, S. Preda, L. Predoana, D. Mitrea, M. Covei, V.-A. Maraloiu, V. S. Teodorescu, C. Moldovan, P. Petrik, and M. Zaharescu, "Multifunctional Zn-Doped ITO Sol–Gel Films Deposited on Different Substrates: Application as CO2-Sensing Material," NANOMATERIALS, vol. 12, no. 18, 2022.

47. Gémes, E. Takács, I. Székács, E. Farkas, R. Horvath, S. Klátyik, and A. Székács, "A glyphosate és szerkezeti analógjai antagonista hatásainak vizsgálata RGD-specifikus integrinekkel," Ökotoxikológia, vol. 4, no. 3–4, pp. 61–66, 2022.

48. Gémes, E. Takács, I. Székács, R. Horvath, and A. Székács, "Comparative Assessment of the Inhibitory Potential of the Herbicide Glyphosate and Its Structural Analogs on RGD-Specific Integrins Using Enzyme-Linked Immunosorbent Assays," INTERNATIONAL JOURNAL OF MOLECULAR SCIENCES, vol. 23, no. 20, 2022.

49. T. Gerecsei, B. Péter, R. Ungai-Salánki, S. Kurunczi, I. Székács, B. Szabó, and R. Horvath, "Prospects of fluidic force microscopy and related biosensors for medical applications," in Nanobioanalytical Approaches to Medical Diagnostics, 2022, pp. 1–28.

50. T. Gerecsei, R. Ungai-Salánki, A. Saftics, I. Derényi, R. Horvath, and B. Szabó, "Characterization of the Dissolution of Water Microdroplets in Oil," COLLOIDS AND INTERFACES, vol. 6, no. 1, 2022.

51. F. Giannazzo, S. E. Panasci, E. Schilirò, F. Roccaforte, A. Koos, M. Nemeth, and B. Pécz, "Esaki Diode Behavior in Highly Uniform MoS2/Silicon Carbide Heterojunctions," ADVANCED MATERIALS INTERFACES, vol. 9, no. 22, 2022.

52. K. Glowka, M. Zubko, P. Świec, K. Prusik, M. Szklarska, D. Chrobak, J. L. Lábár, and D. Stróż, "Influence of Molybdenum on the Microstructure, Mechanical Properties and Corrosion Resistance of Ti20Ta20Nb20(ZrHf)20−xMox (Where: x = 0, 5, 10, 15, 20) High Entropy Alloys," MATERIALS, vol. 15, no. 1, 2022.

53. M. Gracheva, Z. Klencsár, V. K. Kis, K. A. Béres, Z. May, V. Halasy, A. Singh, F. Fodor, Á. Solti, L. F. Kiss, G. Tolnai, Z. Homonnay, and K. Kovács, "Iron nanoparticles for plant nutrition: Synthesis, transformation, and utilization by the roots of Cucumis sativus," JOURNAL OF MATERIALS RESEARCH, 2022.

54. R. T. Graf, A. Schlosser, D. Zámbó, J. Schlenkrich, P. Rusch, A. Chatterjee, H. Pfnür, and N. C. Bigall, "Interparticle Distance Variation in Semiconductor Nanoplatelet Stacks," ADVANCED FUNCTIONAL MATERIALS, vol. 32, no. 24, 2022.

55. J. M. Griffin, J. Mathew, A. Gasparics, G. Vértesy, I. Uytdenhouwen, R. Chaouadi, and M. E. Fitzpatrick, "Machine-Learning Approach to Determine Surface Quality on a Reactor Pressure Vessel (RPV) Steel," APPLIED SCIENCES-BASEL, vol. 12, no. 8, 2022.

56. B. Gyarmati, S. Farah, A. Farkas, G. Sáfrán, L. M. Voelker-Pop, and K. László, "Long-Term Aging of Concentrated Aqueous Graphene Oxide Suspensions Seen by Rheology and Raman Spectroscopy," NANOMATERIALS, vol. 12, no. 6, 2022.

57. Hagymási, I. M. S. Mohd, Z. Tajkov, K. Márity, L. Oroszlány, J. Koltai, A. Alassaf, P. Kun, K. Kandrai, A. Pálinkás, P. Vancsó, L. Tapasztó, and P. Nemes-Incze, "Observation of competing, correlated ground states in the flat band of rhombohedral graphite," SCIENCE ADVANCES, vol. 8, no. 35, 2022.

58. K. Hajagos-Nagy, F. Misják, and G. Radnóczi, "Cu-Mn szilárd oldat rétegek mikroszerkezetének és morfológiájának kombinatorikus feltérképezése," in A Magyar Mikroszkópos Társaság 2022 Konferenciájának Kivonatkönyve, 2022, pp. 80–83.

59. M. Hans, Z. Czigány, D. Neuß, J. A. Sälker, H. Rueß, J. Krause, G. K. Nayak, D. Holec, and J. M. Schneider, "Probing the onset of wurtzite phase formation in (V,Al)N thin films by transmission electron microscopy and atom probe tomography," SURFACE AND COATINGS TECHNOLOGY, vol. 442, 2022.

60. L. Harasztosi, I. . Szabó, F. Biró, R. G. Kiss, and G. Battistig, "Microcalorimeter Development and Calibration Based on a Twin Micro-heater Platform," in Proceedings of the 8 th International Conference on Sensors and Electronic Instrumentation Advances, 2022, pp. 112–116.

61. L. Hegedűs, T. Nguyen, K. Lévay, K. László, G. Sáfrán, and A. Beck, "Poisoning and Reuse of Supported Precious Metal Catalysts in the Hydrogenation of N-Heterocycles, Part II: Hydrogenation of 1-Methylpyrrole over Rhodium," CATALYSTS, vol. 12, no. 7, 2022.

62. N. Hegedűs, C. Balázsi, T. Kolonits, D. Olasz, G. Sáfrán, M. Serényi, and K. Balázsi, "Investigation of the RF Sputtering Process and the Properties of Deposited Silicon Oxynitride Layers under Varying Reactive Gas Conditions," MATERIALS, vol. 15, no. 18, 2022.

63. N. Hegedüs, R. Lovics, M. Serényi, Z. Zolnai, P. Petrik, C. Balázsi, and K. Balázsi, "Interpretation of hydrogen incorporation into radio frequency sputtered amorphous silicon based on Berg modelling," VACUUM, vol. 202, 2022.

64. Holló, D. Zámbó, A. Deák, F. Rossi, R. Cucciniello, P. Lo Nostro, H. Nabika, B. Baytekin, I. Lagzi, and M. Itatani, "Effect of the Polarity of Solvents on Periodic Precipitation: Formation of Hierarchical Revert Liesegang Patterns," JOURNAL OF PHYSICAL CHEMISTRY B, vol. 126, no. 41, pp. 8322–8330, 2022.

65. Horváth, M. Németh, A. Beck, G. Sáfrán, G. Žerjav, and A. Pintar, "Study of Metal-Support Interactions in Different Ni-In/CeO2 Catalysts Designed for Methane Dry Reforming," in 28th Annual Meeting of the Slovenian Chemical Society, 2022.

66. Á. C. Horváth, S. Borbély, F. Mihók, P. Fürjes, P. Barthó, and Z. Fekete, "Histological and electrophysiological evidence on the safe operation of a sharp-tip multimodal optrode during infrared neuromodulation of the rat cortex," SCIENTIFIC REPORTS, vol. 12, no. 1, 2022.

67. R. Horvath, "Single-cell temporal transcriptomics from tiny cytoplasmic biopsies," CELL REPORTS METHODS, vol. 2, no. 10, 2022.

68. P. T. Hung, M. Kawasaki, A. Szabo, J. L. Labar, Z. Hegedus, and J. Gubicza, "Influence of Degree of Severe Plastic Deformation on Thermal Stability of an HfNbTiZr Multi-Principal Element Alloy Processed by High-Pressure Torsion," NANOMATERIALS, vol. 12, no. 19, 2022.

69. P. T. Hung, M. Kawasaki, J.-K. Han, Á. Szabó, J. L. Lábár, Z. Hegedűs, and J. Gubicza, "Thermal stability of nanocrystalline CoCrFeNi multi-principal element alloy: Effect of the degree of severe plastic deformation," INTERMETALLICS, vol. 142, 2022.

70. V. Ioannou-Sougleridis, S. Alafakis, B. Pécz, D. Velessiotis, N. Z. Vouroutzis, S. Ladas, M. Barozzi, G. Pepponi, and D. Skarlatos, "Post-metallization annealing and photolithography effects in p-type Ge/Al2O3/Al MOS structures," ECS JOURNAL OF SOLID STATE SCIENCE AND TECHNOLOGY, vol. 11, no. 4, 2022.

71. B. R. József, R. Alekszej, J. S. Péter, P. Péter, and B. Attila, "Analysis of the microstructure of color etched low carbon steel with spectroscopic ellipsometry," in Symposium on Materials Science, 2022, pp. 20–24.

72. Z. Juhász, A zene ősnyelve, 2nd ed. Pilisvörösvár: Fríg kiadó, 2022.

73. Z. Juhász, "Zenei ősnyelvek Eurázsia népzenei térképén és a magyar népzene," in Csodatévő szarvasnak ezer ága-boga, 2022, pp. 116–127.

74. Z. Juhász, "A magyar népzene a dallamtípusok és a haplocsoportok eloszlásainak tükrében," in Magyar Őstörténeti Műhelybeszélgetés, 2022, p. in press.

75. B. Kalas, G. Sáfrán, M. Serényi, M. Fried, and P. Petrik, "Scanning-resonance optical sensing based on a laterally graded plasmonic layer – optical properties of Ag x Al 1 − x in the range of x = 0 to 1," APPLIED SURFACE SCIENCE, vol. 606, 2022.

76. B. Kalas, G. Sáfrán, M. Serényi, K. Ferencz, M. Fried, and P. Petrik, "Surface-enhanced Kretschmann-Raether ellipsometry based on plasmonic, Bragg and waveguide structures," in Symposium on Materials Science, 2022, pp. 12–14.

77. B. Kalas, T. Defforge, G. Gautier, A. Chaix, M. Fried, and P. Petrik, "Development of advanced sensing materials and interface structures for in-situ bioellipsometry," PROCEEDINGS OF SPIE - THE INTERNATIONAL SOCIETY FOR OPTICAL ENGINEERING, vol. 11972, pp. 112–118, 2022.

78. N. Kanyo, K. D. Kovács, S. V. Kovács, B. Béres, B. Peter, I. Székács, and R. Horvath, "Single-cell adhesivity distribution of glycocalyx digested cancer cells from high spatial resolution label-free biosensor measurements," Matrix Biology Plus, vol. 14, 2022.

79. K. Kertész, G. Piszter, Z. Bálint, and L. P. Biró, "Boglárlepkék szerkezeti eredetű színei," FIRKA: AZ ERDÉLYI MAGYAR MŰSZAKI TUDOMÁNYOS TÁRSASÁG KIADVÁNYA FIATALOK RÉSZÉRE, vol. 31, no. 3, pp. 1–8, 2022.

80. K. Kertész, G. Piszter, Z. E. Horváth, D. Zámbó, A. Deák, and L. P. Biró, "Effect of Plasmonic Au and Ag/Au Nanoparticles and Sodium Citrate on the Optical Properties of Chitin-Based Photonic Nanoarchitectures in Butterfly Wing Scales," PHOTONICS, vol. 9, no. 8, 2022.

81. B. Király and H. Fort, "A game-theory-inspired decomposition of interspecific interaction matrices," EUROPHYSICS LETTERS, vol. 138, no. 2, 2022.

82. M. Kocsis, M. Szabados, S. B. Ötvös, G. F. Samu, Z. Fogarassy, B. Pécz, Á. Kukovecz, Z. Kónya, P. Sipos, I. Pálinkó, and G. Varga, "Selective production of imines and benzimidazoles by cooperative bismuth(III)/transition metal ion catalysis," JOURNAL OF CATALYSIS, vol. 414, pp. 163–178, 2022.

83. T. Kolonits, J. Gubicza, L. Péter, I. Bakonyi, and Z. Czigány, "Ciszteintartalmú elektrolitból leválasztott nikkel rétegek mikroszerkezete, keménysége és termikus stabilitása," in A Magyar Mikroszkópos Társaság 2022 Konferenciájának Kivonatkönyve, 2022, pp. 130–132.

84. K. V. Kovácsné, Z. Czigány, and Z. Kovács, "Nanokristályos anyagok Rietveld analízise elektrondiffrakciós mérések alapján," in A Magyar Mikroszkópos Társaság 2022 Konferenciájának Kivonatkönyve, 2022, pp. 126–129.

85. Z. Kovács, M. Fábián, N. Szász, I. Székács, and V. Kis-Kovacs, "Tracking the initial stage of bioactive layer formation on Si-Ca-Na-P oxide glasses by nanoindentation," JOURNAL OF NON-CRYSTALLINE SOLIDS, vol. 581, 2022.

86. O. Kürtössy, Z. Scherübl, G. Fülöp, I. E. Lukács, T. Kanne, J. Nygard, P. Makk, and S. Csonka, "Parallel InAs nanowires for Cooper pair splitters with Coulomb repulsion," NPJ QUANTUM MATERIALS, vol. 7, no. 1, 2022.

87. Lábár, B. Pécz, C. Francesca, N. Fabrice, Z. Zhen, Z. Shi-Li, and L. François, "A TEM szerepe a Qubitek fejlesztésében," in A Magyar Mikroszkópos Társaság 2022 Konferenciájának Kivonatkönyve, 2022, pp. 146–149.

88. L. Lábár, "DiffMap: A new free computer program to process scanned electron diffraction patterns," RESOLUTION AND DISCOVERY, vol. 6, no. 1, pp. 7–11, 2022.

89. Lázár, L. K. Varga, V. Kovács-Kis, S. Stichleutner, A. Tegze, and Z. Klencsár, "Electric explosion of amorphous iron alloy ribbons in water and in ethylene glycol," JOURNAL OF MATERIALS RESEARCH, 2022.

90. H.-W. Lee, C. Cleveland, and A. Szolnoki, "When costly migration helps to improve cooperation," CHAOS, vol. 32, no. 9, 2022.

91. H.-W. Lee, C. Cleveland, and A. Szolnoki, "Mercenary punishment in structured populations," APPLIED MATHEMATICS AND COMPUTATION, vol. 417, 2022.

92. Lengyel, G. Bazsó, A. I. Chumakov, D. L. Nagy, G. Hegedűs, D. Bessas, Z. E. Horváth, N. M. Nemes, M. A. Gracheva, E. Szilágyi, S. Sajti, and D. G. Merkel, "Synergy effect of temperature, electric and magnetic field on the depth structure of the FeRh/BaTiO3 composite multiferroic," MATERIALS SCIENCE AND ENGINEERING B - SOLID STATE MATERIALS FOR ADVANCED TECHNOLOGY, vol. 285, 2022.

93. Liu, Z. Xiao, X. Chen, and A. Szolnoki, "Early exclusion leads to cyclical cooperation in repeated group interactions," JOURNAL OF THE ROYAL SOCIETY INTERFACE, vol. 19, no. 188, 2022.

94. Z. Li, X. Chen, H.-X. Yang, and A. Szolnoki, "Game-theoretical approach for opinion dynamics on social networks," CHAOS, vol. 32, no. 7, 2022.

95. T. Lohner, A. Németh, Z. Zolnai, B. Kalas, A. Romanenko, N. Q. Khánh, E. Szilágyi, E. Kótai, E. Agócs, Z. Tóth, J. Budai, P. Petrik, M. Fried, I. Bársony, and J. Gyulai, "Disorder and cavity evolution in single-crystalline Ge during implantation of Sb ions monitored in-situ by spectroscopic ellipsometry," MATERIALS SCIENCE IN SEMICONDUCTOR PROCESSING, vol. 152, 2022.

96. R. Lo Nigro, P. Fiorenza, B. Pécz, and J. Eriksson, "Nanotechnology for Electronic Materials and Devices," NANOMATERIALS, vol. 12, no. 19, 2022.

97. H. Luong, T. T. Trung, T. T. Hong, N. H. Nam, M.-H. Phan, P. Jenei, J. L. Lábár, and J. Gubicza, "Relating the magnetic coercivity to the L10 ordered FePd phase in annealed FexPd100-x nanoparticles," APPLIED PHYSICS A - MATERIALS SCIENCE AND PROCESSING, vol. 128, no. 10, 2022.

98. Marianna, F. Enikő, S. Inna, H. Robert, K. Szandra, and S. András, "DETAILED CYTOTOXICITY ASSESSMENT OF THE FORMULATED HERBICIDE ROUNDUP CLASSIC AND ITS CONSTITUENTS," in Proceedings of the 28th International Symposium on Analytical and Environmental Problems, 2022, pp. 269–273.

99. G. I. Márk, P. Vancsó, and P. Nemes-Incze, "Transport properties of TMDC materials," in Eighth International Workshop Nanocarbon Photonics and Optoelectronics, 2022, pp. 19–19.

100. G. I. Márk, V. Péter, and M. Alexandre, "Wave Packet Dynamical Simulation of Magnetic Effects in 2D Materials." 2022.

101. K. Maroua H., H. Zsolt E., B. Katalin, and B. Csaba, "Eco-friendly preparation and structural characterization of calcium silicates derived from eggshell and silica gel," INTERNATIONAL JOURNAL OF APPLIED CERAMIC TECHNOLOGY, vol. in press, p. in press, 2022.

102. H. Máté, E. A. László, K. K. Viktória, and K. Zsolt, "Anizotrópia vizsgálata fogzománcban pásztázó elektronmikroszkópos és Raman spektroszkópos módszerekkel," in A Magyar Mikroszkópos Társaság 2022 Konferenciájának Kivonatkönyve, 2022, pp. 44–47.

103. H. Máté, K. Zsolt, E. A. László, K. K. Viktória, and R. Noémi, "Structural anisotropy in primary dental enamel and its relation to mechanical properties," in Szegedi Fogorvosnapok 2022. Szegedi Fogorvos Találkozó és Tudományos Konferencia, Magyar Gyermekfogászati és Fogszabályozási Társaság IX. Tóth Pál Vándorgyűlés, 2022, pp. 32–32.

104. M. Menyhárd, "Miért szükséges a felületfizika a TEM minta készítéséhez? Árpi (Barna Á.) emlékére," in A Magyar Mikroszkópos Társaság 2022 Konferenciájának Kivonatkönyve, 2022, pp. 116–117.

105. G. Merkel, G. Hegedüs, M. Gracheva, A. Deák, L. Illés, A. Németh, F. Maccari, I. Radulov, M. Major, A. I. Chumakov, D. Bessas, D. L. Nagy, Z. Zolnai, S. Graning, K. Sájerman, E. Szilágyi, and A. Lengyel, "A Three-Dimensional Analysis of Magnetic Nanopattern Formation in FeRh Thin Films on MgO Substrates: Implications for Spintronic Devices," ACS APPLIED NANO MATERIALS, vol. 5, no. 4, pp. 5516–5526, 2022.

106. W. Monika, M. Aneta, P. Agata, F. Enikő, S. Inna, and H. Robert, "Electrokinetic, viscoelastic and optical properties of the biocompatible multilayers based on polysaccharides – the impact of the films on the cell adhesion." 2022.

107. R. I. Mukhamadiarov, S. Deng, S. R. Serrao, P. Priyanka, L. M. Childs, and U. C. Tauber, "Requirements for the containment of COVID-19 disease outbreaks through periodic testing, isolation, and quarantine," JOURNAL OF PHYSICS A- MATHEMATICAL AND THEORETICAL, vol. 55, no. 3, 2022.

108. G. Nagy, N. Kanyo, A. Voros, I. Szekacs, A. Bonyar, and R. Horvath, "Population distributions of single-cell adhesion parameters during the cell cycle from high-throughput robotic fluidic force microscopy," SCIENTIFIC REPORTS, vol. 12, no. 1, 2022.

109. Á. G. Nagy, I. Székács, A. Bonyár, and R. Horvath, "Cell-substratum and cell-cell adhesion forces and single-cell mechanical properties in mono- and multilayer assemblies from robotic fluidic force microscopy," EUROPEAN JOURNAL OF CELL BIOLOGY, vol. 101, no. 4, 2022.

110. Á. G. Nagy, I. Székács, A. Bonyár, and R. Horvath, "Simple and automatic monitoring of cancer cell invasion into an epithelial monolayer using label-free holographic microscopy," SCIENTIFIC REPORTS, vol. 12, no. 1, 2022.

111. Nagy, "Capillary Bridges on Hydrophobic Surfaces: Analytical Contact Angle Determination," LANGMUIR, vol. 38, no. 19, pp. 6201–6208, 2022.

112. Nagy, N. Rohbeck, R. N. Widmer, Z. Hegedűs, J. Michler, L. Pethö, J. L. Lábár, and J. Gubicza, "Combinatorial Study of Phase Composition, Microstructure and Mechanical Behavior of Co-Cr-Fe-Ni Nanocrystalline Film Processed by Multiple-Beam-Sputtering Physical Vapor Deposition.," MATERIALS, vol. 15, no. 6, 2022.

113. Németh, H. Lancaster, C. Salzmann, K. McColl, Z. Fogarassy, L. Garvie, L. Illés, B. Pécz, M. Murri, F. Corà, R. Smith, M. Mezouar, C. Howard, and P. McMillan, "Shock-formed carbon materials with intergrown sp3- and sp2-bonded nanostructured units," PROCEEDINGS OF THE NATIONAL ACADEMY OF SCIENCES, vol. 119, no. 30, 2022.

114. G. Odor, "Nonuniversal power-law dynamics of susceptible infected recovered models on hierarchical modular networks (vol 103, 062112, 2021)," PHYSICAL REVIEW E: COVERING STATISTICAL NONLINEAR BIOLOGICAL AND SOFT MATTER PHYSICS (2016-), vol. 106, no. 2, 2022.

115. G. Ódor, S. Deng, B. Hartmann, and J. Kelling, "Synchronization dynamics on power grids in Europe and the United States," PHYSICAL REVIEW E: COVERING STATISTICAL NONLINEAR BIOLOGICAL AND SOFT MATTER PHYSICS (2016-), vol. 106, no. 3, 2022.

116. G. Ódor, G. Deco, and J. Kelling, "Differences in the critical dynamics underlying the human and fruit-fly connectome," PHYSICAL REVIEW RESEARCH, vol. 4, no. 2, 2022.

117. M. Oláh, E. Farkas, I. Székács, R. Horvath, S. Klátyik, and A. Székács, "A Roundup Classic gyomirtó szer és összetevői citotoxikus hatásainak vizsgálata," Ökotoxikológia, vol. 4, no. 3–4, pp. 54–60, 2022.

118. M. Oláh, E. Farkas, I. Székács, R. Horvath, and A. Székács, "Cytotoxic effects of Roundup Classic and its components on NE-4C and MC3T3-E1 cell lines determined by biochemical and flow cytometric assays," TOXICOLOGY REPORTS, vol. 9, pp. 914–926, 2022.

119. Olasz, G. Sáfrán, and Q. C. Nguyen, "AlCu mikrokombinatorikus vékonyrétegek mechanikai és szerkezeti tulajdonságainak összefüggései," in A Magyar Mikroszkópos Társaság 2022 Konferenciájának Kivonatkönyve, 2022, pp. 73–75.

120. Pálinkás, G. Kálvin, P. Vancsó, K. Kandrai, M. Szendrő, G. Németh, M. Németh, Á. Pekker, J. S. Pap, P. Petrik, K. Kamarás, L. Tapasztó, and P. Nemes-Incze, "The composition and structure of the ubiquitous hydrocarbon contamination on van der Waals materials," NATURE COMMUNICATIONS, vol. 13, no. 1, 2022.

121. Peter, N. Kanyo, I. Szekacs, A. Csampai, S. Bosze, and R. Horvath, "Epigallocatechin-gallate tailors the cell adhesivity of fibronectin coatings in oxidation and concentration-dependent manner," MATERIALS ADVANCES, vol. 3, no. 23, pp. 8684–8694, 2022.

122. Péter, E. Farkas, S. Kurunczi, Z. Szittner, S. Bősze, J. J. Ramsden, I. Szekacs, and R. Horvath, "Review of Label-Free Monitoring of Bacteria: From Challenging Practical Applications to Basic Research Perspectives," BIOSENSORS, vol. 12, no. 4, 2022.

123. P. Petrik and M. Fried, "Mapping and imaging of thin films on large surfaces," PHYSICA STATUS SOLIDI A-APPLICATIONS AND MATERIALS SCIENCE, vol. 219, no. 13, 2022.

124. T. T. Pham, P. Vancso, M. Szendro, K. Palotas, R. Castelino, M. Bouatou, C. Chacon, L. Henrard, J. Lagoute, and R. Sporken, "Higher-indexed Moire patterns and surface states of MoTe2/graphene heterostructure grown by molecular beam epitaxy," NPJ 2D MATERIALS AND APPLICATIONS, vol. 6, no. 1, 2022.

125. Piszter, G. Molnar, A. Palinkas, and Z. Osvath, "Graphene-Encapsulated Silver Nanoparticles for Plasmonic Vapor Sensing," NANOMATERIALS, vol. 12, no. 14, 2022.

126. Piszter, K. Kertész, D. Kovács, D. Zámbó, Z. Baji, I. Levente, G. Nagy, J. S. Pap, Z. Bálint, and L. P. Biró, "Spectral Engineering of Hybrid Biotemplated Photonic/Photocatalytic Nanoarchitectures," NANOMATERIALS, vol. 12, no. 24, 2022.

127. Piszter, K. Kertész, G. Sramkó, Z. Bálint, and L. P. Biró, "Structural colors of blue butterflies: from photonic nanoarchitectures to DNA," PROCEEDINGS OF SPIE - THE INTERNATIONAL SOCIETY FOR OPTICAL ENGINEERING, vol. 12214, 2022.

128. G. Piszter, K. Kertész, G. Nagy, Z. Baji, Z. Endre Horváth, Z. Bálint, J. Sándor Pap, and L. Péter Biró, "Spectral tuning of biotemplated ZnO photonic nanoarchitectures for photocatalytic applications," ROYAL SOCIETY OPEN SCIENCE, vol. 9, no. 7, 2022.

129. M. Poláček, P. Souček, M. Alishahi, N. Koutná, P. Klein, L. Zábranský, Z. Czigány, K. Balázsi, and P. Vašina, "Synthesis and characterization of Ta–B–C coatings prepared by DCMS and HiPIMS co-sputtering," VACUUM, vol. 199, 2022.

130. A.-M. Putz, O. I. Ivankov, A. I. Kuklin, V. Ryukhtin, C. Ianasi, M. Ciopec, A. Negrea, L. Trif, Z. E. Horváth, and L. Almásy, "Ordered mesoporous silica prepared in different solvent conditions: Application for Cu(II) and Pb(II) adsorption," GELS, vol. 8, no. 7, 2022.

131. A.-M. Putz, A. Len, L. Trif, Z. E. Horváth, and L. Almásy, "Imidazolium Ionic Liquids as Designer Solvents Confined in Silica Nanopores," GELS, vol. 8, no. 6, 2022.

132. S. Racz, Z. Fogarassy, U. Kentsch, P. Panjan, and M. Menyhard, "Design and production of tungsten-carbide rich coating layers," APPLIED SURFACE SCIENCE, vol. 586, 2022.

133. S. Racz, Z. Fogarassy, P. Panjan, and M. Menyhard, "Evaluation of AES depth profiles with serious artefacts in C/W multilayers," APPLIED SURFACE SCIENCE, vol. 582, 2022.

134. Racz, Z. Kerner, and M. Menyhard, "Corrosion resistance of tungsten-carbide-rich coating layers produced by noble gas ion mixing," APPLIED SURFACE SCIENCE, vol. 605, 2022.

135. G. Radnóczi, "TEM minták ionsugaras vékonyítása Barna Árpádnak, a módszer megalapozójának emlékére," in A Magyar Mikroszkópos Társaság 2022 Konferenciájának Kivonatkönyve, 2022, p. 103,118-105,120.

136. G. Z. Radnóczi, "Fókuszált ionsugárral készített minták tisztítása kis-energiás Ar+ ionnyalábbal," in A Magyar Mikroszkópos Társaság 2022 Konferenciájának Kivonatkönyve, 2022, pp. 121–121.

137. Rado, R. Dekker, M. C. Louwerse, V. A. Henneken, M. Peters, P. Furjes, and C. Ducso, "Force Sensor Chip With High Lateral Resolution for Artificial Skin and Surgical Applications," IEEE SENSORS JOURNAL, vol. 22, no. 19, pp. 18359–18365, 2022.

138. B. Renkó, A. Romanenko, P. J. Szabó, A. Sulyok, P. Petrik, and A. Bonyár, "Analysis of structural and chemical inhomogeneity of thin films developed on ferrite grains by color etching with Beraha-I type etchant with spectroscopic ellipsometry and XPS," JOURNAL OF MATERIALS RESEARCH AND TECHNOLOGY, vol. 18, pp. 2822–2830, 2022.

139. Revesz, M. Gajdics, M. Alifah, V. K. Kis, E. Schafler, L. K. Varga, S. Todorova, T. Spassov, and M. Baricco, "Thermal, Microstructural and Electrochemical Hydriding Performance of a Mg65Ni20Cu5Y10 Metallic Glass Catalyzed by CNT and Processed by High-Pressure Torsion," ENERGIES, vol. 15, no. 15, 2022.

140. Romanenko, E. Agócs, Z. Hózer, P. Petrik, and M. Serényi, "In-situ ellipsometry on the oxidation of zirconium at medium temperatures," in Symposium on Materials Science, 2022, pp. 25–28.

141. Romanenko, E. Agócs, Z. Hózer, P. Petrik, and M. Serényi, "Concordant element of the oxidation kinetics—Interpretation of ellipsometric measurements on Zr," APPLIED SURFACE SCIENCE, vol. 573, 2022.

142. E. P. Salvatore, K. Antal, S. Emanuela, D. F. Salvatore, G. Giuseppe, F. Patrick, R. Fabrizio, A. Simonpietro, C. Marco, M. G. Franco, S. Attila, N. Miklos, P. Béla, and G. Filippo, "Multiscale Investigation of the Structural, Electrical and Photoluminescence Properties of MoS2 Obtained by MoO3 Sulfurization," NANOMATERIALS, vol. 12, no. 2, 2022.

143. Schlosser, J. Schlenkrich, D. Zámbó, M. Rosebrock, R. T. Graf, C. G. Escobar, and N. C. Bigall, "Interparticle Interaction Matters: Charge Carrier Dynamics in Hybrid Semiconductor–Metal Cryoaerogels," ADVANCED MATERIALS INTERFACES, vol. 9, no. 12, 2022.

144. S. Shankar, D. Zalka, T. Szabó, E. Székely, M. Kőrösi, Z. Pászti, K. Balázsi, L. Illés, Z. Czigány, and R. Kun, "Supercritical carbon dioxide assisted synthesis of ultra-stable sulfur/carbon composite cathodes for Li– S batteries," MATERIALS TODAY CHEMISTRY, vol. 26, 2022.

145. J. Shen, W. Li, S. Deng, D. Xu, S. Chen, and F. Liu, "Machine learning of pair-contact process with diffusion," SCIENTIFIC REPORTS, vol. 12, no. 1, 2022.

146. J. Shen, F. Liu, S. Chen, D. Xu, X. Chen, S. Deng, W. Li, G. Papp, and C. Yang, "Transfer learning of phase transitions in percolation and directed percolation," PHYSICAL REVIEW E: COVERING STATISTICAL NONLINEAR BIOLOGICAL AND SOFT MATTER PHYSICS (2016-), vol. 105, no. 6, 2022.

147. Silva, I. Borbáth, K. Zelenka, I. Sajó, G. Sáfrán, A. Tompos, and Z. Pászti, "Effect of the reductive treatment on the state and electrocatalytic behavior of Pt in catalysts supported on Ti0.8Mo0.2O2-C composite," REACTION KINETICS MECHANISMS AND CATALYSIS, vol. 135, no. 1, pp. 29–47, 2022.

148. T. Sopcak, I. Shepa, M. Giretova, V. Kucharova, R. Sedlak, K. Balazsi, R. Stulajterova, and M. Streckova, "Influence of boron addition on the phase transformation, microstructure, mechanical and in-vitro cellular properties of bredigite-type coatings deposited by a spin coating technique," MATERIALS CHEMISTRY AND PHYSICS, vol. 283, 2022.

149. T. Stasiak, P. Souček, V. Buršíková, N. Koutná, Z. Czigány, K. Balázsi, and P. Vašina, "Synthesis and characterization of the ceramic refractory metal high entropy nitride thin films from Cr-Hf-Mo-Ta-W system," SURFACE AND COATINGS TECHNOLOGY, vol. 449, 2022.

150. Stucchi, D. Meroni, G. Safran, A. Villa, C. L. Bianchi, and L. Prati, "Noble Metal Promoted TiO2 from Silver-Waste Valorisation: Synergism between Ag and Au," CATALYSTS, vol. 12, no. 2, 2022.

151. Sulyok and K. Tőkési, "Surface and Bulk Plasmon Excitation on Aluminum Surface at Small to High Grazing Angles," ATOMS, vol. 10, no. 4, 2022.

152. K. Sun, Y. Liu, X. Chen, and A. Szolnoki, "Evolution of trust in a hierarchical population with punishing investors," CHAOS SOLITONS & FRACTALS, vol. 162, 2022.

153. Szabó, G. Novodárszki, F. Lónyi, L. Trif, Z. Fogarassy, J. Valyon, and R. Barthos, "Texture and morphology-directed activity of magnesia-silica mixed oxide catalysts of ethanol-to-butadiene reaction," JOURNAL OF MOLECULAR STRUCTURE, vol. 1259, 2022.

154. Á. Szamosvölgyi, T. Rajkumar, A. Sápi, I. Szenti, M. Ábel, J. F. Gómez-Pérez, K. Baán, Z. Fogarassy, E. Dodony, B. Pécz, S. Garg, J. Kiss, Á. Kukovecz, and Z. Kónya, "Interfacial Ni active sites strike solid solutional counterpart in CO2 hydrogenation," ENVIRONMENTAL TECHNOLOGY & INNOVATION, vol. 27, 2022.

155. P. Szekrenyes, C. Hamon, D. Constantin, and A. Deak, "Formation of kinetically trapped small clusters of PEGylated gold nanoparticles revealed by the combination of small-angle X-ray scattering and visible light spectroscopy," SOFT MATTER, vol. 18, no. 43, pp. 8295–8301, 2022.

156. Z. Szittner, B. Péter, S. Kurunczi, I. Székács, and R. Horváth, "Functional blood cell analysis by label-free biosensors and single-cell technologies," ADVANCES IN COLLOID AND INTERFACE SCIENCE, vol. 308, 2022.

157. Szolnoki and X. Chen, "Tactical cooperation of defectors in a multi-stage public goods game," CHAOS SOLITONS & FRACTALS, vol. 155, 2022.

158. Z. Tajkov, D. Nagy, K. Kandrai, J. Koltai, L. Oroszlany, P. Sule, Z. E. Horvath, P. Vancso, L. Tapaszto, and P. Nemes-Incze, "Revealing the topological phase diagram of ZrTe5 using the complex strain fields of microbubbles," NPJ COMPUTATIONAL MATERIALS, vol. 8, no. 1, 2022.

159. G. Tamás, V. Tamás, D. K. Kinga, P. Beatrix, K. Sándor, K. Anna, N. Krisztina, L. Dorina, V. V. Krisztina, L. Péter, S. Inna, I. B. Edit, and H. Robert, "Nanoinjection of fluorescent nanoparticles to single live cells by robotic fluidic force microscopy." 2022.

160. T. Török, K. Maár, I. G. Varga, and Z. Juhász, "A new linear combination method of haplogroup distribution central vectors to model population admixtures," MOLECULAR GENETICS AND GENOMICS, vol. 297, no. 3, pp. 889–901, 2022.

161. T. N. Török, J. G. Fehérvári, G. Mészáros, L. Pósa, and A. Halbritter, "Tunable, Nucleation-Driven Stochasticity in Nanoscale Silicon Oxide Resistive Switching Memory Devices," ACS APPLIED NANO MATERIALS, vol. 5, no. 5, pp. 6691–6698, 2022.

162. G. Vértesy, A. Gasparics, I. Szenthe, and I. Uytdenhouwen, "Investigation of the Influence of Neutron Irradiation on Cladded Nuclear Reactor Pressure Vessel Steel Blocks by Magnetic Adaptive Testing," APPLIED SCIENCES-BASEL, vol. 12, no. 4, 2022.

163. G. Vértesy, A. Gasparics, I. Szenthe, and S. Bilicz, "Magnetic Investigation of Cladded Nuclear Reactor Blocks," MATERIALS, vol. 15, no. 4, 2022.

164. G. Vértesy, A. Gasparics, and I. Szenthe, "Investigation of Potential Material Inhomogeneity in the Magnetically Detected Neutron-Irradiation-Generated Structural Degradation of Nuclear Reactor Pressure Vessel Steel," APPLIED SCIENCES-BASEL, vol. 12, no. 22, 2022.

165. K. K. Viktória, S. Attila, H. Máté, R. Noémi, and K. Zsolt, "TEM Study on the Nanostructure Change of Primary Dental Enamel Subjected to Mechanical and Chemical Surface Modifications," in Second InternatIonal conference on electron microscopy of nanostructures, 2022, pp. 154–155.

166. K. K. Viktoria, C. Zsolt, and K. Zsolt, "Microstructure Investigation of Nanocrystalline Materials Using Electron Diffraction Based Rietveld Analysis – Approximation of Instrumental Broadening," in Second InternatIonal conference on electron microscopy of nanostructures, 2022, pp. 98–99.

167. P. Villy, A. Kohut, A. Kéri, Á. Bélteki, G. Radnóczi, Z. Fogarassy, G. Z. Radnóczi, G. Galbács, and Z. Geretovszky, "Continuous spark plasma synthesis of Au/Co binary nanoparticles with tunable properties," SCIENTIFIC REPORTS, vol. 12, no. 1, 2022.

168. J. Volk, J. Radó, Z. Baji, and R. Erdélyi, "Mechanical Characterization of Two-Segment Free-Standing ZnO Nanowires Using Lateral Force Microscopy," NANOMATERIALS, vol. 12, no. 23, 2022.

169. Wallin and C. Balázsi, "'Fresh Potential for Multilayer Structures,'" INTERCERAM: INTERNATIONAL CERAMIC REVIEW, vol. 71, no. 1, pp. 14–17, 2022.

170. Wang and A. Szolnoki, "A reversed form of public goods game: equivalence and difference," NEW JOURNAL OF PHYSICS, vol. 24, no. 12, 2022.

171. Wang and A. Szolnoki, "Involution game with spatio-temporal heterogeneity of social resources," APPLIED MATHEMATICS AND COMPUTATION, vol. 430, 2022.

172. Wang, X. Chen, Z. Xiao, and A. Szolnoki, "Decentralized incentives for general well-being in networked public goods game," APPLIED MATHEMATICS AND COMPUTATION, vol. 431, 2022.

173. Y. Wang, T. Csanádi, Z. Fogarassy, B. Zhang, R. Sedlák, X. Wang, C. Zhang, J. Dusza, and M. J. Reece, "The role of Cr addition on the processing and mechanical properties of high entropy carbides," JOURNAL OF THE EUROPEAN CERAMIC SOCIETY, vol. 42, no. 13, pp. 5273–5279, 2022.

174. Wójcicka, Z. Fogarassy, A. Rácz, T. Kravchuk, G. Sobczak, and M. A. Borysiewicz, "Multifactorial investigations of the deposition process – Material property relationships of ZnO:Al thin films deposited by magnetron sputtering in pulsed DC, DC and RF modes using different targets for low resistance highly transparent films on unheated substrates," VACUUM, vol. 203, 2022.

175. Zaharescu, M. Anastasescu, H. Stroescu, J. M. Calderon-Moreno, N. Apostol, S. Preda, C. M. Vladut, S. Mihaiu, P. Petrik, and M. Gartner, "Comparative study of the dopants (Mn vs. V) influence on the properties of sol-gel ZnO films," JOURNAL OF SOL-GEL SCIENCE AND TECHNOLOGY, vol. 104, no. 1, pp. 67–77, 2022.

176. Zsolt and K. K. Viktória, "Calibration Procedure and Error Analysis to Improve the Accuracy of SAED in Aberration Corrected TEM," in Second InternatIonal conference on electron microscopy of nanostructures, 2022, pp. 100–101.

177. Zsurzsa, M. El-Tahawy, L. Péter, L. F. Kiss, J. Gubicza, G. Molnár, and I. Bakonyi, "Spacer Layer Thickness Dependence of the Giant Magnetoresistance in Electrodeposited Ni-Co/Cu Multilayers," NANOMATERIALS, vol. 12, no. 23, 2022.